Assessment and Development of Mitigation Strategies for Membrane Durability in Fuel Cells

by

Dilip Ramani

M.Sc., Arizona State University, 2014

Thesis Submitted in Partial Fulfillment of the
Requirements for the Degree of
Doctor of Philosophy

in the
School of Mechatronic Systems Engineering
Faculty of Applied Sciences

SIMON FRASER UNIVERSITY

Summer 2021

Declaration of Committee

Name:	**Dilip Ramani**
Degree:	**Doctor of Philosophy**
Title:	**Assessment and Development of Mitigation Strategies for Membrane durability in Fuel Cells**
Committee:	**Chair: Ramtin Rakhsha** Lecturer, Mechatronic Systems Engineering
	Erik Kjeang Supervisor Professor, Mechatronic Systems Engineering
	Steven Holdcroft Committee Member Professor, Department of Chemistry
	Lida Ghassemzadeh Committee Member Senior Research Scientist, Ballard Power Systems Inc.
	Gary Wang Examiner Professor, Mechatronic Systems Engineering
	James M. Fenton External Examiner Professor, Material Science and Engineering University of Central Florida

Abstract

Fuel cell membranes undergo simultaneous or individual chemical and mechanical degradation under dynamic fuel cell operating conditions. This combined stress development effect compromises the functionality of the membrane and ultimately, the overall durability of the fuel cell system. Therefore, it is critical to understand the underlying degradation mechanisms and failure modes under operational conditions. In this thesis, an extensive research methodology including accelerated stress tests, visualization techniques, and finite element modeling is adopted in order to understand and mitigate membrane degradation. The membrane characterization is facilitated using a non-invasive laboratory-based X-ray computed tomography (XCT) system for 3D visualization of membrane damage progression over the lifetime of the fuel cell. The 3D XCT approach is first applied to understand the degradation mechanism responsible for combined chemical and mechanical membrane degradation. The XCT approach is further expanded to 4D *in situ* visualisation through periodic same location tracking within a miniature operational fuel cell. Fuel cell membranes with mechanical reinforcements and chemical additives are tested as existing mitigation strategies for the isolated degradation stressors. Under pure chemical degradation, the chemically and mechanically reinforced membrane does not show membrane thinning or shorting sites and exceeds the lifetime of the non-reinforced membrane by 2x. The reinforced membrane also mitigated/delayed the crack development during pure mechanical degradation as compared to the non-reinforced membrane. However, significant membrane degradation is still observed and attributed to buckling and delamination mechanisms within the membrane electrode assembly (MEA). Mitigation of these mechanisms is demonstrated through two novel approaches proposed in this thesis: i) reduced surface roughness gas diffusion layers (GDLs); and ii) bonded MEAs. Both mitigation strategies are tested using the same experimental workflow and shown to provide substantial mitigation against fatigue driven mechanical membrane degradation via reduced membrane buckling, resulting in a doubling of the test lifetime in each case. Complementary finite element simulations corroborate the experimental findings and further estimate the critical GDL void sizes to prevent membrane buckling and the required interfacial MEA adhesion quality to stabilize the MEA for improved membrane durability.

Keywords: fuel cell; membrane degradation; durability; X-ray computed tomography; characterization; membrane fracture

Acknowledgements

First and foremost, I want to take this opportunity to express my sincere thanks and gratitude to my senior supervisor Dr. Erik Kjeang. It would have been impossible without his guidance and support all through my doctoral studies. His mentorship and clear vision enabled me to accomplish my work. I also would like to extend my sincere thanks to my other supervisors: Dr. Lida Ghassemzadeh and Dr. Steven Holdcroft for their useful insights and constructive inputs. Further, I would like to thank our funding agencies namely, Natural Sciences and Engineering Research Council (NSERC) of Canada, Canada Foundation for Innovation (CFI), British Columbia Knowledge Development Fund, and Ballard Power Systems through an Automotive Partnership Canada (APC) grant.

I want to extend my thanks and acknowledgement to my fellow graduate students at FCReL: Dr. Robin White- for his unbelievable innovation and knowledge, Dr. Yadvinder Singh- for all his compassionate deeds right from helping me settle in this country to technical assistance in drafting manuscripts, have been stunning. Mr. Francesco Orfino- for his happy spirit and approachable nature, which helped me bounce off ideas. Ms. Monica Dutta- who has always been prompt in helping to expedite get things done from Ballard and providing critical assistance all through the NXCT project.

I further would like to recognize and acknowledge the crucial technical assistance provided by the co-op students at FCReL: Ms. Marina Najm, Ms. Tylynn Haddow, Ms. Vivian Pan, Mr. Kevin Dahl, Mr. Mike Xu, Mr. Alex Boswell, and Mr. Matthew Wegener. I also thank the industrial partner of my research projects, Ballard Power Systems, for offering various forms of infrastructural and technical support. Finally, I would like to thank the other colleagues at FCReL for their help and guidance in several aspects of my research work, with the following individuals especially acknowledged: Dr. Narinder Singh Khattra, Dr. Alireza Sadeghi Alavijeh, Mr. Anish Pokhrel, Mr. Marvin Messing and Dr. Sebastian Eberhardt.

Table of Contents

List of Figures

List of Acronyms

AMST	Accelerated mechanical stress test
BOL	Beginning of life
CCL	Cathode catalyst layer
CCM	Catalyst coated membrane
COCV	Cyclic open circuit voltage
CV	Cyclic voltammetry
EIS	Electrochemical impedance spectroscopy
ELDT	Electrochemical leak detection test
EOL	End of life
ePTFE	Expanded polytetrafluoroethylene
FCReL	Fuel Cell Research Laboratory
FEM	Finite element model
GDL	Gas diffusion layer
HSR	High surface roughness
LSR	Low surface roughness
MEA	Membrane electrode assembly
OCV	Open circuit voltage
ORR	Oxygen reduction reaction
PEMFC	Proton exchange membrane fuel cell
PFSA	Perfluorosulfonic acid
RH	Relative humidity
SEM	Scanning electron microscopy
UTS	Ultimate tensile strength
XCT	X-ray computed tomography

Preface

The present thesis concentrates on mitigation approaches to improve the membrane durability in polymer electrolyte fuel cells. The thesis includes a combination of peer reviewed journal articles and unpublished manuscripts are included in the Appendix. The thesis has the following workflow:

Chapter 1: Introduction including the overview of existing works on membrane degradation mechanisms, composite membranes, technical aspects of the XCT approach and finite element modeling of the ionomer membrane.

Chapter 2: This chapter includes the synopsis of contributions, with excerpts from five full-length journal articles and manuscripts which are included in appendix (A-E) of the thesis. The five appendices are as follows

"***Characterization of Membrane Degradation Growth in Fuel Cells Using X-ray Computed Tomography***" authored by D. Ramani, Y. Singh, F. P. Orfino, M. Dutta, and E. Kjeang. Journal of The Electrochemical Society, 165 (6) F3200-F3208 (2018). Reproduced with permission from *J. Electrochem. Soc.*

"4D in situ visualization of mechanical degradation evolution in reinforced fuel cell membranes" authored by D. Ramani, Y. Singh, R. T. White, M. Wegener, F. P. Orfino, M. Dutta, and E. Kjeang. International Journal of Hydrogen Energy 45 (2020) 10089-10103. Reproduced with permission from *IJHE.*

"Four-dimensional in situ imaging of chemical membrane degradation in fuel cells" by D. Ramani, Y. Singh, R.T. White, T. Haddow, M. Wegener, F. P. Orfino, L. Ghassemzadeh, M. Dutta and E. Kjeang. Electrochimica Acta, 380 (2021) 138194. Reproduced with permission from Electrochimica Acta.

"Mitigation of Mechanical Membrane Degradation in Fuel Cells – Part 1: Gas Diffusion Layers with Low Surface Roughness" by D. Ramani, N.S. Khattra, Y. Singh, A. Mohseni-Javid, F.P. Orfino, M. Dutta and E. Kjeang. Accepted Manuscript (August 2021), Journal of Power Sources.

"Mitigation of Mechanical Membrane Degradation in Fuel Cells – Part 2: Bonded Membrane Electrode Assembly" by D. Ramani, N.S. Khattra, Y. Singh, F.P. Orfino, M. Dutta and E. Kjeang. Accepted Manuscript (August 2021), Journal of Power Sources.

Chapter 3: This chapter contains the overall conclusions of the contributions made and scope of possible future work.

Chapter 1.

Introduction

1.1. Objectives and Scope

The longevity of a fuel cell system is its ability to withstand irreversible degradation over time under different operating conditions [1]. The degradation of the ionomer membrane within the fuel cell system can directly impact the overall performance and durability. Hence, there is a necessity to understand the degradation mechanisms responsible for failures and address them with suitable mitigation approaches. The overall objective of this work is therefore to obtain a detailed understanding of degradation mechanisms in fuel cell membranes and evaluate possible mitigation strategies relevant to operational modes in automotive applications. In the present thesis, this is achieved through a sequence of experiments covering accelerated stress tests replicating operational scenarios, periodic tomographic characterization, mitigation concepts and complementary finite element analysis. In brief, the overall scope of this thesis includes the following approaches,

a) 3+1-D *ex situ* imaging of chemo-mechanical membrane degradation: Expand the 3D visualization methodology formerly demonstrated for membrane failure analysis to examine the growth of membrane degradation during the operational lifetime of fuel cells. The damage development within the membrane is correlated with the supplementary diagnostics parameters at different life stages.
b) 4-D *in situ* characterization of pure chemical degradation: Novel *in situ* visualization of same location within MEAs containing different fuel cell membrane types subjected to chemical degradation. To achieve the 4D visualization approach, a custom designed small scale fuel cell fixture is used to house the MEA and failures are brought about by pure chemical stressors of membrane degradation.
c) 4-D *in situ* characterization of pure mechanical degradation: Similar to b), periodic structural investigations of membrane damage evolution during pure

mechanical degradation procedure. MEA with reinforced membrane is used to test the mitigation against the mechanical stress cycling.

d) 4-D *in situ* characterization of mitigation of mechanical membrane degradation (Part I): A gas diffusion layer (GDL) with low surface roughness is applied as a novel MEA design strategy for mitigating mechanical membrane degradation. Correlative finite element investigation is adopted to ratify the experimental observations.

e) 4-D *in situ* characterization of mitigation of mechanical membrane degradation (Part II): In this mitigation approach, an adhesion improved MEA is investigated as a novel strategy to arrest membrane buckling during mechanical stress cycling. Similar to d), complementary finite element simulations are performed to corroborate experimental observations.

1.2. Background

Growing energy demands has led to increased dependency on fossil fuels. However, the use of fossil fuels leads to increased emission of green-house gases such as CO_2, N_2O, CH_4 and fluorinated gases, which leads to poor air quality and global warming. Global warming leads to changes in weather patterns, frequent droughts, and flooding around the world. One of the primary contributors to this environmental pollution is the transportation industry. Electrifying the transport system is one of the most important approaches to mitigate the air pollution.

Hydrogen-based fuel cells are one of the leading contenders for the substitution of internal combustion (IC) engines for automobile applications, owing to their noise-free, tidy, and dynamic operation [2]. The primary advantage of hydrogen fuel cells is that they require shorter refueling times and provide longer ranges as compared to the battery vehicles. Several automotive companies are actively working for large-scale adoption of fuel cells for automotive applications. In recent years, these programs have been tremendously boosted by extensive subsidies and public policy frameworks from their respective federal and state/provincial governments targeting massive decarbonization of the energy system.

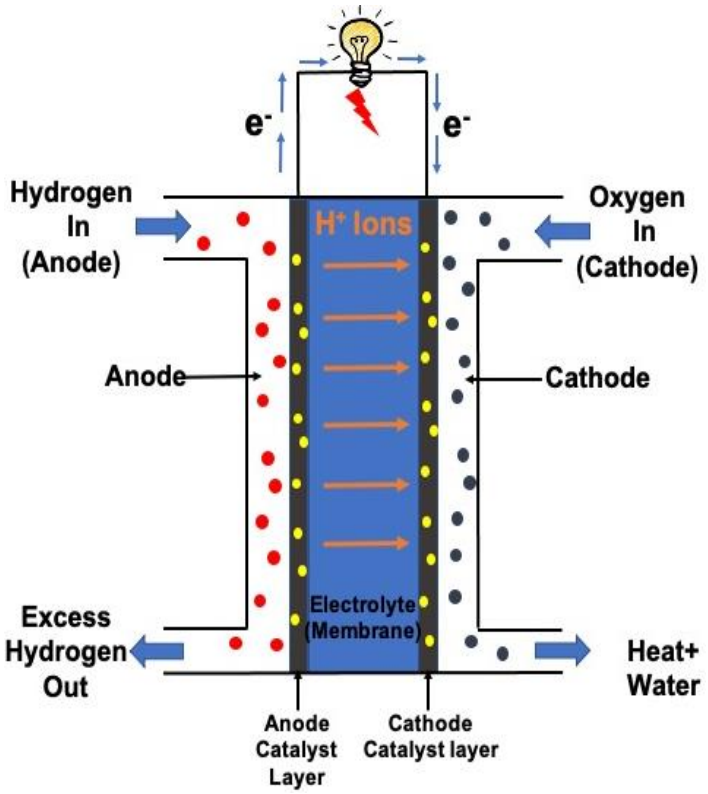

Figure 1.1. Schematic sketch of an operational PEMFC [3]**.**

A typical fuel cell produces electricity through an electrochemical process by converting hydrogen and oxygen into water (Figure 1.1). They operate much like a battery; except they do not require electrical recharging time and again. Proton exchange membrane fuel cell (PEMFC) among different types, are considered best suited for automotive operation due to high performance at low temperature range. Significant advancement has been made in PEMFC technology in the recent past primarily in the areas of improved volumetric and gravimetric specific power density and effective material utilization. However, the durability and lifetime of the PEMFCs has been a major research-intensive challenge for large scale commercial adoption of the technology. A PEMFC is fabricated in the form of membrane electrode assembly (MEA) which comprises of: (i) a central polymeric membrane, (ii) anode and cathode catalyst layers (CLs) composed of carbon-supported Pt and ionomer; and (iii) gas diffusion layers (GDLs), typically carbon paper coated with PTFE and a microporous layer [4]. During the operation, the H_2 gas supplied to the anode side diffuses through the GDL and oxidizes at the anode catalyst layer forming protons (H^+) and electrons (e^-). Meanwhile, air is supplied to the cathode side from where O_2 gas diffuses through the GDL to the cathode catalyst layer. The central

membrane facilitates the transport of protons but prevents the electron motion, which in-turn is pushed through the external circuit. The primary anode, cathode, and overall reactions of the operational fuel cell are outlined below in equations 1-3.

$$\text{Anode reaction (HOR):}\quad H_2 \Rightarrow 2H^+ + 2e^- \qquad E_o = 0\ V_{SHE} \tag{1}$$

$$\text{Cathode reaction (ORR):}\quad \tfrac{1}{2}\,O_2 + 2H^+ + 2e^- \Rightarrow H_2O \qquad E_o = 1.229\ V_{SHE} \tag{2}$$

$$\text{Overall reaction:}\quad H_2 + \tfrac{1}{2}\,O_2 \Rightarrow H_2O \qquad E_o = 1.229\ V \tag{3}$$

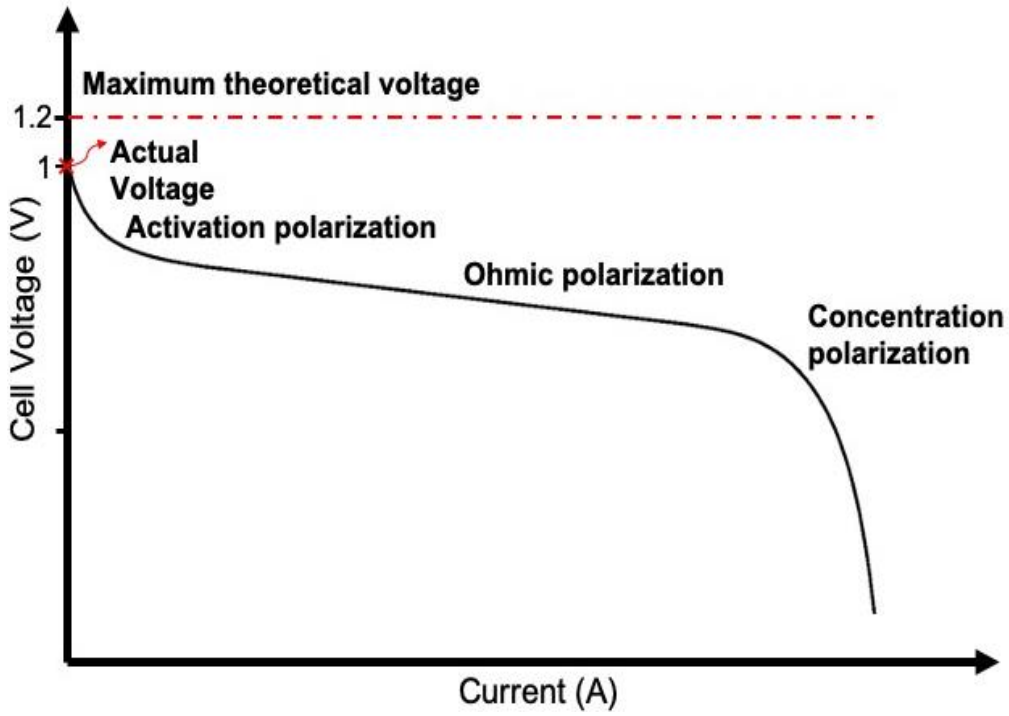

Figure 1.2. Typical polarization curve for a PEMFC with different losses such as activation, ohmic and concentration losses [5]**.**

The basic electrochemical potential of the fuel cell reaction restricts the voltage output to about 1 V for a single cell. For automotive applications, several cells can be connected together to build a stack, to achieve greater voltage and currents [4]. Under nominal conditions, the theoretical open-circuit voltage (OCV) of PEMFC is around 1.23 V as shown in Figure 1.2. However, the voltages generated tend to be typically less than 1 V due to the several losses which eventually influence the overall activity of the fuel cell. Though no current is taken under OCV state, there is still substantial voltage loss due to

reactant crossover and electron leakage across the ionomer membrane. And different types of losses show up at varying levels of current drawn. For instance, *activation losses* occur at the kinetic region i.e. at low current densities [4,6]. This is primarily due to the energy barrier related with the electrode reaction. The second type is the *ohmic loss*, which is proportional to the current and is mainly prevalent at the medium current density region. This loss is primarily attributed to the resistance of different fuel cell components such as the bipolar plates, electrodes, membrane, GDL, CLs and interfacial contacts which cause voltage loss and subsequent current density reduction [4]. The third type is the *mass transport loss*, which occurs at high current densities, when there is higher water generation. This could cause flooding thereby blocking the reactants to reach the MEA components [4,6]. This is the dominating loss at high current densities as it leads to major drop in cell voltage. In addition to these inherent losses, the deterioration of fuel cell materials in an operational set up could lead to more loss of overall efficiency. Furthermore, the reliability of the membrane is vital for achieving greater durability and longer lifetime of PEMFCs.

1.3. Membrane Degradation and Lifetime

Perfluorosulfonic acid (PFSA) ionomer membranes are generally used in the PEMFCs because of its high proton conductivity and chemical strength from the PTFE (polytetrafluoroethylene) backbone. The lifetime requirements prescribed by the US Department of Energy for fuel cell systems range from 8,000 hours for automotive, 25,000 hours for buses and 40,000 hours for stationary applications [7]. Under practical operating conditions, the fuel cell stack could undergo start-stop states, contaminants in fuel and air, freezing, humidity cycling, which compromise the chemical and mechanical stability of the fuel cell stack. However, there is a lack of evidence from the field and accurate models for lifespan estimation. Therefore, durable materials and fuel cell technologies that substantially surpass goals based on lab-scale accelerated reliability tests are required at this stage to reduce uncertainty.

For fuel cells to satisfy commercial requirements and compete with hybrid engines, it is important to enhance the membrane lifetime, which may affect the overall lifetime of an operational fuel cell. The operational conditions of the fuel cell can cause severe impact on the membrane leading to several damage features such as cracks, divots, tears,

pinholes and delamination [8,9]. These defects can compromise the basic functionality of the polymeric membrane and lead to early breakdown of the fuel cell.

The underlying degradation mechanisms must be carefully addressed in order to create new materials and technologies, which can help improve membrane longevity and thereby increase the overall performance of PEMFCs, by making them more robust and cost-effective. PFSA ionomer membranes under operational fuel cell conditions undergo three types of degradation mechanisms namely: i) thermal, ii) chemical, and iii) mechanical degradations [10,11]. The intensity of individual stressors is amplified by the presence of other stressors, which could lead to a combined synergistic effect [12].

1.3.1. Thermal Membrane Degradation

Thermal degradation of ionomer membranes is caused by thermal variations which occur at temperatures over 100°C [13,14]. The high temperature fluctuations over time, without proper humidification causes severe membrane breakdown leading to decomposition of main and side chains [15]. One mitigation approach that is used to lower the thermal degradation is to incorporate a cooling component which will help to regulate the temperature [3]. On the other hand, subfreezing temperature can impact the membrane during fuel cell operation. The frozen condition can lead increased contact resistance between the membrane and the adjoining CLs [1]. The impact of freezing can be reduced by purging excess water and thereby decrease the chance of ice formation [15].

1.3.2. Chemical Membrane Degradation

Chemical degradation in PFSA membranes diminishes the overall lifetime of the PEMFCs. The chemical degradation is brought by radical species. The first step to radical formation is the hydrogen peroxide (H_2O_2) byproduct during the oxygen reduction reaction (ORR) at the cathode [16],

$$O_2 + 2H^+ + 2e^- \Rightarrow H_2O_2 \quad (4)$$

The H_2O_2 developed on the cathode or via oxygen crossover at the anode can pass through the membrane and decay into $OH\cdot$ in the presence of Fe^{2+}. Presence of Fenton's reagents such as Fe^{2+} drives the formation of radicals.

$$Fe^{2+}\ H_2O_2 + H^+ \Rightarrow Fe^{3+} + OH\cdot + H_2O \quad (5)$$

Computational works have shown that during OCV hold, the chemical stressors can remain high during the Fe-ion redox cycle, which directly impacts the ionomer, thereby causing radical generation in the membrane [17,18]. The chemical radicals such as hydroxyl (•OH) and hydroperoxyl (•OOH) tend to attack weak chemical bonds in the molecular structure of the membrane ionomer [19–23]. The evidence can be observed as membrane material loss and fluoride presence in the effluent water exhaust [24]. Several factors such as high temperature, low relative humidity (RH), high cell potential, and high reactant gas pressures accelerate the radical species formation [11,12,25–27]. Especially for improved membrane lifetime and durability, adequate membrane humidification is critical. This is because the dry conditions create vulnerable scenario for higher H_2O_2 development, thereby increased membrane deterioration. In addition, the humidification influences the partial pressures of the reactant gases, membrane thickness and permeability [28,29]. The impact of radical attack is also observed as reduced mechanical strength of the membrane and damage development [30].

Chemically mitigated membranes have been designed to slow down or to prevent the chemical degradation. One approach is presence of Pt into the ionomer membrane. The Pt present in the CL can dissolve during the operational conditions of the fuel cell [31] or during the voltage cycling process [32] and can deposit in the ionomer membrane. This band of Pt in the membrane has shown a positive impact in improving longevity of the membrane. Another approach to mitigate the chemical degradation is by addition of $Ce^{3+/}Ce^{4+}$ ions into the ionomer [33,34]. Cerium oxide (CeO_2) nanoparticles can also be added into the MEA [33,35–38]. The cerium based additives are known to act as regenerative radical scavengers and protect the membrane under steady state OCV conditions and have demonstrated longer lifetime during durability test [33–35,39].

Different *in situ* characterization techniques such as electron spin resonance (ESR) [40,41] and fluorescence spectroscopy [42] have also demonstrated the effectiveness of cerium as a potent radical mitigator. Several other durability test results have shown that addition of cerium into the MEA can reduce membrane thinning, pinhole

development and fluoride emission rates (FERs) [33,35,36,43–46]. However, one major drawback of this approach is the mobile behaviour of the cerium, failing to realise the complete effectiveness of this approach. Especially, under completely saturated conditions where the cerium migrates more into the CL from the PEM [39].

1.3.3. Mechanical Membrane Degradation

Mechanical membrane degradation in an operational fuel setup is caused by the stress development in PFSA membranes owing to the compressed fuel cell assembly, complex operational conditions, and interplay of different MEA components. The membrane is hygroscopic in nature, and this tendency to absorb moisture is strongly dictated by temperature and RH [47]. Operational demands within the fuel cell stack lead to fluctuations in RH and temperature. This in-turn creates favorable conditions for in-plane compressive and tensile stress in the confined membranes due to cyclic swelling and shrinking under hydrated and dehydrated states, respectively [48,49]. This expansion and contraction behavior under constrained state at high temperature and varying humidities leads to hygrothermal fatigue, fracture and creep development [23,50,51]. The fatigue driven micro-cracks on the membrane facilitate high gas crossover, leading to failure in the early stages of fuel cell operation. This crossover of gases leads to combustion reaction of the gases causing local hotspots which increase the rate of degradation. Generally, RH variations lead to fatigue-based crack formation, which tend to develop in both through plane and in-plane directions [52,53]. The RH cycling at high temperatures also tends to alter the mechanical endurance of the membrane [54–56].

The catalyst coated membrane (CCM) is a sandwich structure with membrane and two adjacent CLs to form a composite structure. The CLs act as a reinforcement which improves the overall mechanical properties of the CCM as compared to the pure ionomer membrane [55,57]. Under similar tensile conditions, the CCM is more resistant to elastic deformation than the pure ionomer membrane [58]. The ionomer membrane demonstrates higher modulus under dry conditions as compared to CCM indicating underlying residual stress. The CCM is bounded by the GDLs within the fuel cell setup, which provides further lamination to prevent expansion in the in-plane direction.

The membrane fracture development process is a global phenomenon. The membrane fracture development location could be dictated by the MEA irregularities. In

other words, the MEA variation due to local defects could act as preferential sites for membrane failure. For instance, the electrode delamination could exacerbate the failure and the failure location correlated with the CL crack locations [10]. Kundu et al. [59] showed the defects observed at BOL could possibly be due to manufacturing and handling process. Improper contact during assembly could lead to clearances between CCM and GDL [60,61]. Though the MPL cracks/voids improve the fuel cell performance by reducing GDL liquid water saturation [62], these irregular locations could also make the adjoining CCM vulnerable to local damage.

The durability and endurance of the PFSA ionomer membranes can be improved by addition of mechanical reinforcements and chemical stabilizers [63]. By addition of reinforcement, the overall mechanical strength and dimensional stability of the membrane are improved. Furthermore, the PFSA reinforced membranes possess increased fracture resistance and improve the overall lifetime of the PEMFCs [64]. This enables the composite membrane to operate with lower thickness without compromising the overall functionality [65].

Commonly used composite membranes are Nafion XL fabricated by Dupont (Dupont) and GORE-SELECT membranes produced by W. L. Gore & Associates, Inc. The reinforcement layer helps to reduce the plastic deformation of the membrane and thereby suppress/delay the crack development process. Expanded polytetrafluoroethylene (ePTFE) have been used as a support material to contain a composite membrane. The reinforced membranes have also performed well in various operation conditions such as high voltage, varying humidity and freeze/thaw cycling [66]. Nafion XL, from DuPont is a common example of ePTFE reinforced PFSA membrane. This membrane consists of a central microporous PTFE-rich support layer sandwiched with ionomer layers on either side of the reinforcement. The pores of the ePTFE are filled with ionomer, creating a transport network across the thickness of the membrane [67]. This three-layered structure has shown to reduce the swelling in the in-plane direction as compared to the through-plane [67,68]. PFSA based reinforced membranes have demonstrated improved operational lifetime [69,70] during RH cycling procedure [71–73]. A previous work [74] compared the non-reinforced and reinforced PFSA membranes during RH cycling protocol and demonstrated that the reinforced membranes had 40% greater lifetime than the non-reinforced membranes [75]. Another recent work tested reinforced membranes under different RH cycling procedures [8,76]. Observations showed that the length and

frequency of the RH cycles plays a key role in deciding the membrane lifespan. Overall, major improvements in mechanical reliability have been observed with reinforced membranes. However, there is still a disparity in the chemical and chemo mechanical AST assessment literature for reinforced membranes.

1.3.4. Chemo-Mechanical Membrane Degradation

Fuel cell systems under real time operational conditions undergo mechanical and chemical degradation in sequence. As discussed previously, the chemical degradation directly reduces the hygrothermal expansion of the membrane [9,23], which alters the swelling and shrinking capacity during the *in situ* RH cycling process. Our group studied the combined chemical and mechanical degradation processes using accelerated stress tests (AST) protocols [22]. It was observed that the joint action leads to more rapid failures than the individual mechanisms. In addition, the effects of the fluoride emission, microscopy characterization and solid state nuclear magnetic resonance (NMR) spectroscopy results showed significant degradation in the polymer chain. Another team from our group [23] performed tensile experiments of the degraded MEA of combined mechanical and chemical cycling process. They observed severe decay in mechanical properties, which demonstrated the underlying impact of interaction between the chemical and mechanical stressors.

1.4. Accelerated Stress Tests and Diagnostic Tools

Large scale durability evaluation of new MEA materials can be expensive and time consuming. To overcome this, ASTs are typically adopted to expedite the degradation process associated with different components within the MEA [22,49]. Unlike field operation conditions, the ASTs are operated in a more controlled fashion such that the component specific degradation is replicated in a short period of time [15]. Hence, the ASTs facilitate to perform an accelerated lifetime analysis and based on the results suitable mitigation strategies can be designed. Standard AST protocols were defined by the US Department of Energy (DOE) for different MEA components such as catalyst, catalyst support and membrane [77,78]. As observed in several of the previous works [22,35,59,79–83], the AST is the most commonly adopted approach to understand the overall durability and lifetime of separate MEA parts.

Some of the common membrane stressors are RH cycling, steady state OCV, temperature, compressive stress, start-up and shut down cycling [15]. Generally, an OCV hold is the commonly used parameter to intensify the pure chemical degradation process in PFSA membranes [84–87]. At steady OCV, the reactant gases are at their maximum partial pressures, which accelerates the gas crossover and membrane deterioration. Under this condition, no fuel is consumed and hence, high gas crossover is possible and lead to peroxide formation and radical attack [1]. The impact of OCV operation on chemical degradation was studied by Wong et al. [18]. Results showed that the OCV operation creates favorable conditions for FeII ion formation which in turn accelerates the chemical degradation. Another implication of constant voltage test is the deterioration in mechanical properties of PFSA membranes [82,88]. Recently, Bhattacharya et al. [82] tried to establish a link between membrane mechanics and chemical degradation. They performed hygrothermal expansion tests and observed progressive deteriorations in the membrane mechanical properties with increasing pure chemical AST time. Additionally, the mechanical properties were compared with the loss of membrane and fluoride release, which helped to identify the underlying correlation between the mechanical and chemical stressors.

On the other hand, pure mechanical degradation is induced by aggressively fluctuating inlet gas humidity and nullifying any chemical stressors at elevated temperatures [23]. The cyclic RH variation results in fatigue induced membrane failure by means of cracks, tears, and pinholes, which causes gradual increase in gas crossover [59,89]. The structural damage features may experience accelerated growth due to local stress concentration, thus exacerbating the degradation and associated gas crossover [90]. The intermittent hygrothermal variations during the AST mimic the *in situ* conditions during automotive duty cycles. Overall, the basic idea of initiating individual chemical or mechanical membrane stressors using the ASTs remain standard. However, the experimental conditions selected during the ASTs may vary [8,24,51,91–93], which causes different degradation rates.

ASTs that combine both chemical and mechanical stressors, either in sequence or concurrently, have been developed in addition to the isolated ASTs that generate pure chemical or mechanical degradation [11,22,94]. The presence of combined mechanical and chemical stressors plays a key role in fastening the overall rate of membrane degradation. For instance, disintegrated ionomer structure due to chemical degradation

makes the membrane vulnerable for mechanical deterioration during mechanical degradation. Previously, our group adopted periodic chemical and mechanical stresses in a cyclic sequence, namely through the cyclic open circuit voltage (COCV) AST protocol. The findings revealed that the cumulative involvement of combined stressors substantially speed up the overall rate of membrane deterioration as compared to the individual stressors applied separately [22]. The key failure modes observed were uniform membrane thinning and pinholes formation. Tensile tests revealed the membrane becoming less ductile and more brittle with AST cycling. Various *in situ* diagnostic techniques may be appropriate or applicable for tracking the membrane health, based on the underlying stressor during the durability testing. For instance, a typical criterion for evaluating cell failure is gas crossover leakage through the membrane, which can be evaluated electrochemically using linear sweep voltammogram [95] or electrochemical leak detection test (ELDT) [22].

1.5. Failure Analysis

1.5.1. Post-mortem Studies

Early post-mortem studies related to fuel cell components have typically been performed using two-dimensional scanning electron microscopy (SEM). The SEM technique is carried out under vacuum conditions and performs 2D surface characterizations. Several previous works have adopted this approach to understand the morphological MEA features such as CL cracks [30,59,96,97]. Particularly, SEM studies based on ionomer membranes enabled to visualise the damage features in the cross-sections [98] and on the membrane surfaces [22] subjected to different types of stressors. However, the electron microscopy based characterisations have very limited scope and possess certain drawbacks such as destructive sample preparation which involves grinding, polishing etc. [22,99]. Especially considering the polymeric membrane is the central most component, the invasive sample preparation process could introduce artificial features. In addition, damage propagation in membrane is three dimensional in nature, hence SEM-based approach would not be able to capture this phenomenon.

1.5.2. X-ray computed tomography (XCT)

XCT approach is based on computerized techniques which enables to develop the overall 3D image of the internal components of an object. A large number of 2D images generated, also known as projections, are obtained at different angle to obtain one wholesome 3D image. In general, X-rays are a form of electromagnetic waves (wavelength 0.01 -10 nm) which possess high energy and can penetrate through most objects. A typical configuration of a laboratory XCT scanner is made of different components- i) X-ray source, ii) a rotating platform to support a sample, and iii) a detector; iv) a scintillator which converts X-ray photons into visible photons which are calculated as intensity. In addition, the X-ray lenses and Fresnel plates come as add-on to control the focus of the X-ray beam. Yet these add-ons are not adopted for nano-tomography because of their smaller sample size (only few microns), which reduces the scope of the study.

The density of the object under study is calculated from the attenuation coefficient that the X-ray beam penetrates through. The attenuation through the object follows the Beer-Lambert law, defined as

$$I = I_0 \, e^{-\mu t} \tag{6}$$

where I_0: X-ray intensity at the entry, I: X-ray intensity at the exit of the sample, t: thickness of the sample, μ: attenuation coefficient.

The contrast between the different materials depends on three factors, namely the density, the atomic number (Z), and energy of the X-ray beam. 3D imaging using XCT approach can be carried out in two ways i) laboratory-based scanners and ii) synchrotron X-ray beamlines. Though synchrotron enables fast scans with high resolution, lab based XCT facilitates for longer scan times owing to less damaging X-rays.

1.5.3. XCT Characterization of Fuel cell Components

To overcome the drawbacks of 2D microscopy techniques, 3D XCT based characterization has recently been pursued to perform more comprehensive failure analysis of degraded fuel cell parts. XCT studies on various MEA parts such as catalyst layers [99–101] and GDL [102–104] have been performed. Particularly, the GDL's

fundamental composition-dependent transport characteristics such as diffusivity, porosity and permeability, can be obtained from 3D XCT data [105,106]. In contrast, the catalysts layers are composed of Pt particles that possess high mass density which provides better contrast as compared to the other MEA materials. In addition to the component characterization, the XCT approach can also be used to study the liquid water distribution, transport paths and flooding which have direct impact on the performance of the fuel cell [107–109].

Membrane characterization based on XCT has been limited as compared to the GDL and electrodes [90,110–112]. 3D XCT characterisation of membranes has the potential benefit of resolving the 3D nature of membrane damage, although the method is complicated by the lower attenuation of the PFSA membranes and its central location within the MEA. Recently, our team developed a comprehensive failure analysis approach to understand the membrane degradation process using 3D XCT based non-destructive imaging. Singh et al. [113,114] performed 3D failure analysis of membrane parts affected by different types of operational stressors, facilitated by lab-based XCT. These novel works provided critical insights and new outcomes, such as different types of crack morphologies produced under combined chemical/mechanical stressors and membrane thinning and associated electrode shorting sites under pure chemical degradation. Further, Singh *et al.* [115] expanded the 3D failure analysis to 4D *in situ* characterization to study the structural changes of the non-reinforced PFSA membrane during pure mechanical degradation procedure. This novel methodology facilitated for a detailed probe to understand the critical stages of membrane degradation which ultimately led to failure.

1.6. Finite element modeling (FEM)

As detailed in previous sections, membrane fracture growth is caused by synchronous hygrothermal and cyclic loading at high temperature, which create favorable conditions for fatigue development [54]. However, it is not possible to measure the mechanical stress development on the membrane in the *in situ* fuel cell environment. To overcome this, numerical approaches have been adopted as they provide more versatile and inexpensive options to obtain the stress and related parameters inside a fuel cell. FEM is one of the most appropriate methods where the results can be correlated and coupled with the experimental findings. Kusoglu *et al.* [116,117] employed a FEM based model to study the *in situ* stress development during mechanical degradation process and

they further expanded this approach to understand the crack initiation principles. FEM based studies can be used as membrane lifetime prediction tool [118]. For instance, Khorasany *et al.* [119] put forth a robust FEM based model to simulate the fatigue lifetime of pure ionomer membranes under a variety of operating conditions. The model was equipped with additional capability to predict the dimensional distribution of the membrane life under fatigue conditions. Complementary experimental framework and FEM studies to understand the crack development phenomenon in reinforced membranes was performed [120,121]. Results showed preferential crack development under gas flow-fields sections for mechanically reinforced membranes during the mechanical degradation process. Singh *et al.* [58] performed crack propagation experiments in various conditions and incorporated the results into an FEM based semi analytical model. This model was based on Paris law and included elastic-viscoplastic material behavior. The model predicted the fatigue crack development and life of the membrane under mechanical loading conditions. Later, the experimental and modelling framework was extended to CCMs [122]. *Ex situ* characterisation of the CCMs was performed under a variety of environmental conditions and the results were incorporated into the FEM model. The fatigue crack development behaviour was compared against the pure membrane and results showed that the catalyst coating acted as a reinforcement against fracture development under similar loading conditions. In addition, stress distribution maps and directions were obtained using the FEM simulations, which showed the effect of deformities on the CCM. Similar frameworks could be extended into studying the degradation mechanisms of the CCM under *in situ* operation.

1.7. Mitigation Schemes

One particular degradation mechanism during mechanical cycling process is the wrinkled deformation of the MEA. This wrinkled deformation is caused by the in-plane membrane swelling which causes the CCM into buckle into the void regions where there is low compressive force, for example under the channel region which is the underlying reason for this deformation [123]. In addition, the low compressive force is also observed under imperfect geometry of the GDL surface and the irregular MPL structures [61]. The repeated swelling and the shrinking process leads to crack development on the catalyst surface due to strain aggregation [96,124]. The location of the catalyst cracks is vulnerable to membrane crack development due to PEM plastic deformation. Two novel mitigation

approaches to reduce the mechanical membrane degradation are proposed and studied in this work, namely:

i. Gas diffusion layers with low surface roughness (LSR)

ii. Adhesion improved MEAs

Both approaches are studied using a multi-physics finite element model under the hygro-thermo-mechanical fuel cell operation. The present study uses the base model developed by Dr. Narinder S. Khattra [125]. This work is based on a multi-physics finite element fuel cell model which was established to identify the membrane response during different conditions of fuel cell operation. In the present work, this model is modified to incorporate the effect of contact interaction between the CCM and GDL. The simulation domain of the model consists of a two-dimensional plane strain representation of one half of the miniaturized fuel cell geometry, taking into account the cell symmetry**.** The model consists of the polymer membrane sandwiched between the catalyst and gas diffusion layers from both sides. The material properties used for the membrane are based on a previously developed modified version of constitutive G'Sell-Jonas model [126], which takes into consideration the viscoelastic-plastic constitutive response of the membrane and further accounts for its time, temperature, and humidity dependent behavior. The catalyst layers are modeled as linear elastic and assumed to be bonded with the membrane. The GDLs are modeled as linear elastic orthotropic and the interface between the GDL and CCM permits relative sliding. The GDL substrate and MPL is modeled as a single entity with uniform properties. Thermal expansion is considered for all components, whereas membrane is the only component assumed to incur hygral swelling.

Chapter 2.

Synopsis of Contributions

All contributions from this dissertation are from the project titled "*NXCT Fuel Cell Project: Four-Dimensional In Situ Visualization of Fuel Cell Degradation*". This was a collaborative project between scientists and engineers at Ballard Power Systems Inc. and researchers of the Fuel Cell Research Laboratory (FCReL) at Simon Fraser University. The principal investigator of this project was Prof. Erik Kjeang. The primary emphasis of this thesis is to assess and develop mitigation strategies for membrane durability in fuel cell applications. The author of the present thesis is the lead researcher and first author of five major contributions as detailed below. In this regard, the current dissertation includes a summary of five journal publications and manuscripts as detailed in Appendix A-E. Appendix A, B and C are published in journals, while Appendix D and E are written in manuscript forms which are planned to be submitted for journal publication.

2.1. Characterization of Membrane Degradation Growth in Fuel Cells Using X-ray Computed Tomography

Fuel cell membranes under operational conditions undergo synergistic mechanical and chemical degradation. This leads to membrane cracks, tears, thinning and pinholes, causing to contemplate the main functionality of the membrane. To study this mechanism, our FCReL team has extensively adopted a non-invasive 3D XCT approach to characterize the membrane degradation. The overall objective of this particular study is to extend the 3D visualization approach previously demonstrated by Singh *et al.* [113] for membrane failure analysis to characterize the growth of membrane degradation over its practical lifetime in fuel cells. Partially degraded MEAs extracted after different stages of combined chemical and mechanical membrane degradation were visualized using the NXCT Versa system and the degradation evolution was studied by mapping the 3D structural/morphological changes. The MEAs used in this work were extracted by Dr. Chan Lim *et al*. [22], from their previously published journal article. This group also tracked a suite of *in situ* diagnostics such as OCV results, hydrogen leak rate, and tensile mechanical properties. These global parameters were correlated to the damage development at the same life stages as inferred by XCT.

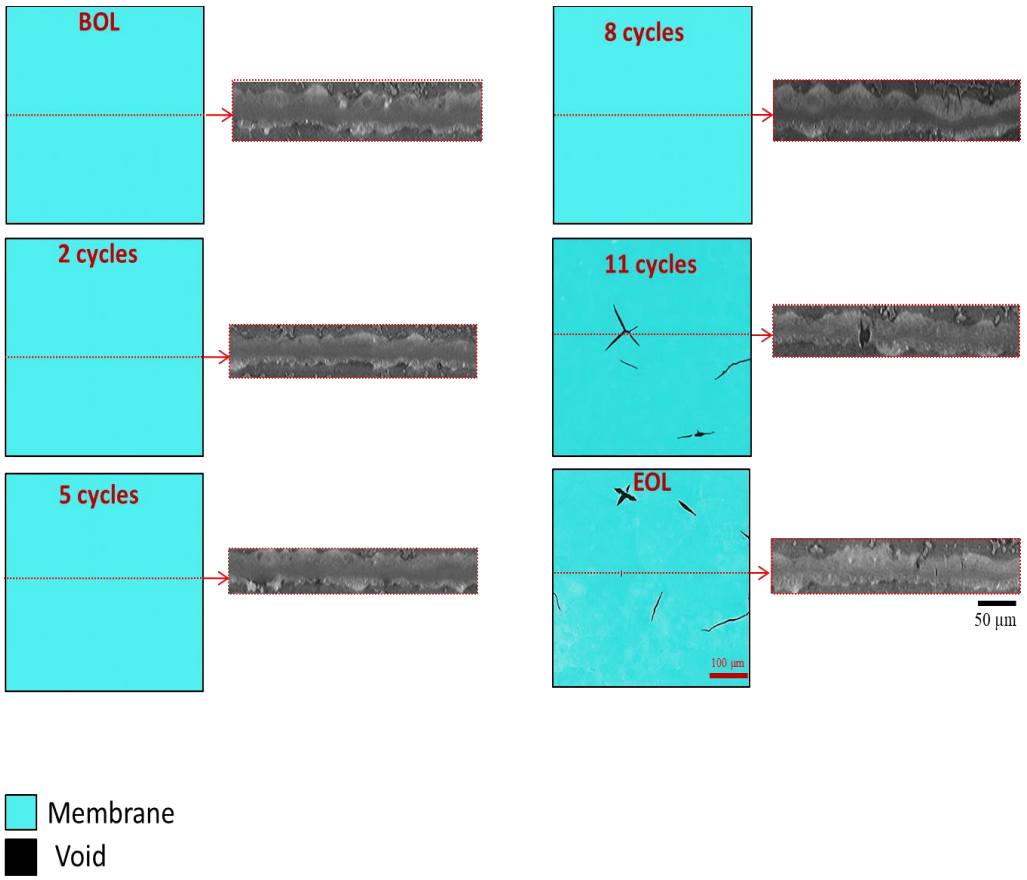

Figure 2.1. Representative planar XCT views of the segmented membrane in MEAs extracted after different life stages of COCV AST cycling. Virtual cross-sectional views (in grey scale) of the MEAs, taken along the annotated dashed lines in the planar views, are also shown in the inset [127].[1]

XCT tomographic datasets obtained after different cycling stages included 1601 projections with 15 s per projection to achieve optimum intensity (around 5500 counts) at the central membrane region. The 2D images obtained at different angles were reconstructed using the ZEISS XMReconstructor ® software. The full 3D data set enabled a comprehensive analysis of membrane cracks which demonstrated no through thickness membrane cracks during the initial phase of the COCV cycling (***Figure 2.1***). However, major membrane crack development initiated at the later stages of the AST cycling procedure. This advent of crack initiation and propagation showed good agreement/correlation with the global *in situ* results such as rise in crossover gas leakage and OCV decay close to the end of life (EOL). The structural connectivity of membrane

[1] Image reprinted from an open access article in *Journal of The Electrochemical Society,* Vol. 165, F3200-F3208, © 2018.

damage with the adjoining CL cracks was investigated to decode the crack development mechanism active within the membrane. Three distinct membrane crack morphologies (I-, Y- and X-shaped) were identified to have developed. Out of the three, the X-shaped cracks were deemed most severe due to their high cross-sectional area at the junction. Further, the X-cracks were seen to extend through the adjoining catalyst layers, facilitating major gas leaks across the membrane. Membrane tensile test results after different life stages demonstrated reduction in tensile strength and rise in elastic modulus which again correlated to the membrane crack development process in the later stages of degradation. This unique analysis of the evolution of membrane degradation with a 3-D perspective enabled important new knowledge regarding the critical stages of degradation and damage development in the membrane. The advent of crack initiation and propagation was in good agreement with *in situ* diagnostic parameters.

Detailed information of this work is provided in **Appendix A** [127].

2.2. Four-dimensional *in situ* Imaging of Chemical Membrane Degradation in Fuel Cells

As discussed in the previous sections, the intensity of mechanical degradation is accelerated by the presence of chemical stressors during the fuel cell operation. One approach to improve the membrane lifetime is to adopt reinforced/ composite membranes. The reinforcement/mitigation of the membrane could possibly be of two different types, i) Mechanically reinforced membrane: central reinforcement layer such as ePTFE layer [67,128], ii) Chemically mitigated membrane: addition of radical scavengers into the membrane [33,34]. Previously, our group developed a four dimensional (4D) based approach using XCT to study the evolution of CL degradation within an operational fuel cell [129]. The time-resolved 4D *in situ* methodology was achieved by adopting a custom designed miniature fuel cell that was originally designed and developed by Dr. Robin T. White [129–131]. However, for the present work the MEAs were fabricated as gas diffusion electrodes (GDEs) as compared to the previous CCM based designs, and the focus was shifted from CL degradation to membrane degradation.

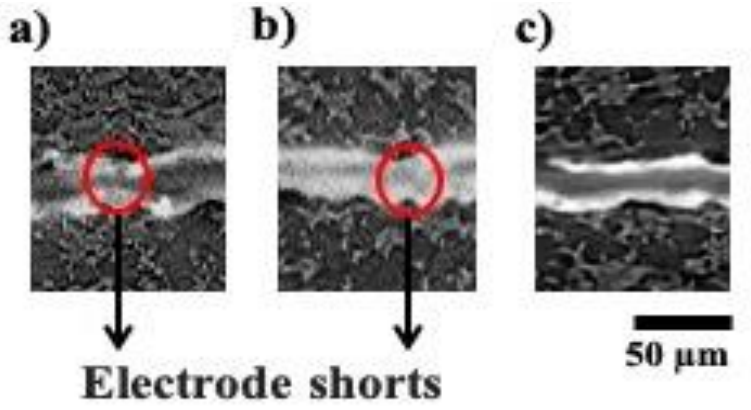

Figure 2.2. Cross-sectional membrane locations displaying electrode short sites for a) non-reinforced and b) mechanically reinforced membrane, while c) the chemically and mechanically reinforced membrane did not display any shorts [132].

The overall objective of this study was to adopt the 4D *in situ* XCT approach to understand the growth of pure chemical membrane degradation in fuel cells and evaluate previously developed mitigation approaches. Periodic 3D visualization of the same MEA location is performed at various life stages affected by chemical stressors within a miniature X-ray transparent fuel cell assembly [54]. Three MEA design types were studied within the fuel cell set up: MEA with i) Type I (non-reinforced); ii) Type II (mechanically reinforced); and iii) Type III (chemically and mechanically mitigated) membranes. The AST protocol included a constant open circuit voltage at 75°C and 30% RH maintained under anode H_2 gas at 0.3 slpm and cathode air at 0.5 slpm. Whereas the present author conducted the experiments for the two mitigated membranes (Types II and III), the AST protocol was originally developed and tested for the baseline non-reinforced membrane (Type I) by Dr. Yadvinder Singh.

Results showed that upon application of the AST, the membranes free of any radical scavenging additives, i.e., non-reinforced and mechanically reinforced membranes, showed decay in OCV and increase in crossover currents and eventually leading to membrane failure. The XCT cross-sectional images (**Figure 2.2**) demonstrated preferential local thinning spots under lands and global membrane thinning for Type I and II membranes, while no cracks or pinholes were observed. Another novel finding is that the several localized membrane thinning locations under lands lead to short formation. Quantitively, over 90% of the shorts were under the land region demonstrating the connection of the clamping pressures in short development. Interestingly, even the ePTFE

layer (Type II) did not prevent the short formation. On the contrary, the chemically and mechanically mitigated membrane showed minimal thinning, and negligible OCV changes. This highlights the regenerative radical scavenging effect of its cerium additive to mitigate the chemical stressors. Overall, the outcomes of this research showcase the strong capabilities of XCT imaging towards improving the scientific understanding of membrane degradation in fuel cells by revealing the underlying mechanisms and failure modes, with key implications for fuel cell durability.

Detailed information of this work is provided in **Appendix B** or [132].

2.3. 4D *in situ* Visualization of Mechanical Degradation Evolution in Reinforced Fuel Cell Membranes

The overall objective of this journal publication is to understand the underlying failure mechanisms and mode of a mechanically reinforced membrane (Nafion XL) during the pure mechanical degradation process. Similar to 2.2, a 4D *in situ* approach, where an operational small fuel cell is characterized within a micro-XCT system. The pure mechanical degradation of the reinforced membrane was brought about by a sequence of humidity cycles composed of supersaturated wet phase (150% RH) and a subsequent dry phase (0% RH), both of 2 min duration at 80°C cell temperature. To eliminate any chemical stressors, the cycling was performed under 0.5 slpm N_2 gas and electrochemical diagnostics were avoided. The X-ray transparent fixture was visualized at beginning of life (BOL) and after 2000, 3000, 4000, and 4500 cycles (EOT (end of test)) using a ZEISS Xradia 520 Versa XCT system. In addition, the fixture was imaged under ‘wet’ and ‘dry’ conditions at EOL, to discern the membrane swelling and shrinking after degradation. The tomographic datasets obtained at different cycling stages included 1601 projections with 5 s per projection to achieve optimum intensity (around 5500 counts) at the central membrane region. A custom membrane segmentation procedure was adopted in this study. This procedure was developed by Dr. Robin T. White [107] in ImageJ [133] as a macro language to enable automated segmentation of both CLs from the MEA, and thus, broaden the scope for membrane study. The segmented membrane enabled to perform a slice by slice inspection to understand the extent of damage within the membrane at various life stages, using Dragonfly software (non-commercial version 2.0) [134].

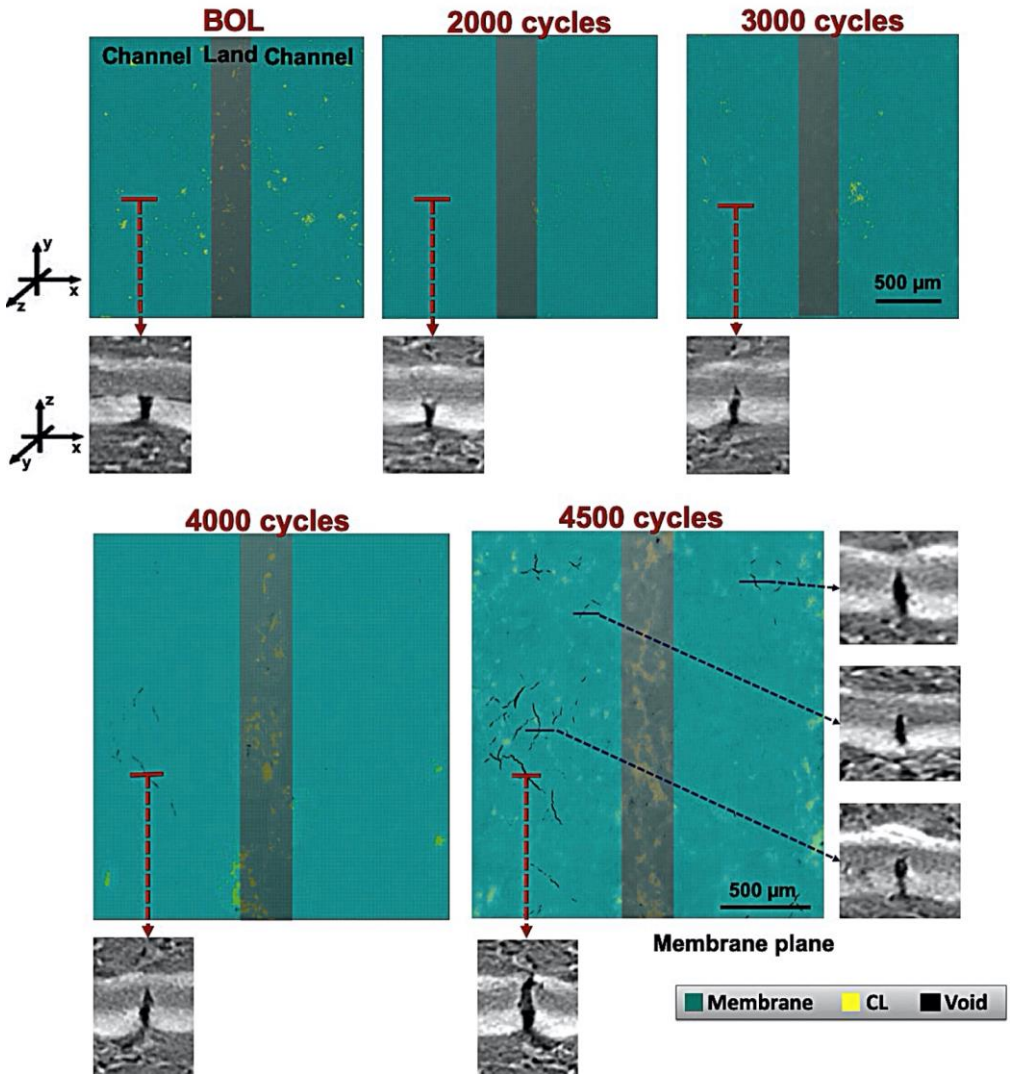

Figure 2.3. Periodic same location tracking of the reinforced membrane plane at various life stages during pure mechanical membrane degradation caused by wet/dry cycling [128].[2]

Results showed that the key failure mode due to the mechanical stressors i.e., the repetitive wet/dry cycling was through-thickness membrane cracks. Micro-cracks developed between 2000 to 4000 cycles on the membrane surface. All the micro cracks were confined to the PFSA ionomer section during this cycling phase. With further cycling, the micro-cracks grew to through thickness crack extending across entire thickness between 4000 to 4500 cycles, as shown in ***Figure 2.3***. The combined impact of interfacial delamination and electrode cracks was evident during the membrane crack development

[2] Adapted from *International journal of hydrogen energy*, Vol. 45, 10089-10103, ©2020 with permission from *Elsevier*.

process. In comparison with the non-reinforced membrane [115], the degradation rate was 2-3X lower owing to greater fracture resistance with the help of central ePTFE layer with the membrane. This shows the mitigatory impact of using reinforced membrane over non-reinforced against pure mechanical degradation. The *in situ* imaging of wet and dry states showed the through plane membrane swelling and associated crack closure in the later stages of the degradation. Overall, the 4D XCT approach provided novel insights into the reinforced membrane degradation by capturing the key failure modes and the associated mechanisms during different developmental stages.

Detailed information of this work is provided in **Appendix C** [128].

2.4. Mitigation of Mechanical Membrane Degradation in Fuel Cells – Part 1: Gas Diffusion Layers with Low Surface Roughness

As illustrated in section 2.3, the MEA defects and irregularities are known to be the main source of local membrane degradation during the pure mechanical degradation [128]. Previously, Dr. Yadvinder Singh adopted pure mechanical AST and showed that the pre-existing MEA features such as CL cracks and delamination played a critical part in the local crack development [115], and explicitly assessed the impact of CL crack density on membrane failure [135]. This work, conducted on non-reinforced CCM based MEAs, showed the dominant role of local buckling deformation on the membrane fracture when GDLs/MPLs containing large void spaces are utilized in an MEA. The buckling mechanism as revealed by XCT was deemed the underlying reason, where the CCM buckled into large GDL pores causing a significant number of membrane fractures. The GDL is known to have uneven surface and the contour of the substrate leads to deformations within the MEA [96]. The MPL layer within the GDL acts as a buffer layer to mitigate the MEA deformation. Hence, it is hypothesized that a smoother MPL with low surface roughness (LSR), i.e., with low number of cavities or voids, could help achieve uniform contact between the CCM and GDL and act as a buffer layer. The overall objective of this work is to use 4D *in situ* XCT characterization to explore the potential for mitigation of mechanical membrane degradation by adopting a GDL configuration with LSR. The MEA comprised of CCM with Nafion® NR211 membrane and SGL Sigracet® 29BC GDL used on both anode and cathode sides without bonding. This GDL constitutes of nonwoven carbon paper coated with thick MPL and low surface roughness, LSR, as

desired for this work. Results were assessed against an equivalent MEA with high surface roughness (HSR) GDL subjected to the same experimental procedure.

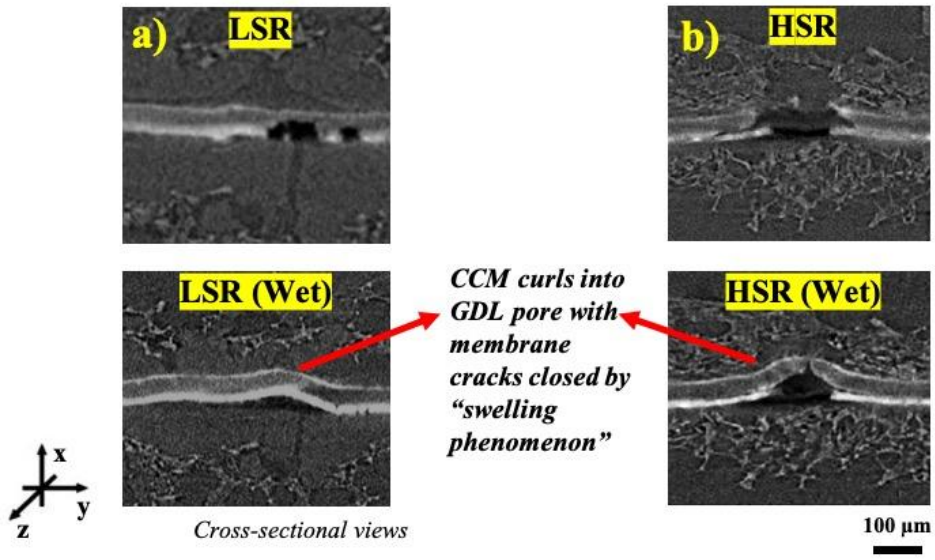

Figure 2.4. Cross-sections of MEAs with a) LSR GDL [136] **and b) HSR GDL** [135] **imaged during ambient and wet conditions after EOT. The EOT for LSR MEA was 4000 wet/dry cycles, while that for HSR MEA was 2000 wet/dry cycles.**

Results demonstrated the significant interaction between MPL deformities and membrane crack locations for LSR and HSR MEA configurations. However, the crack density and crack area were considerably lower for LSR GDL as compared to HSR. In addition, the relatively lower density and different geometry of MPL cracks in the LSR GDL was observed to reduce the severity of CCM buckling (and associated membrane fracture) as its bulge height in the MPL cracks was lower. For instance, **Figure 2.4** shows the cross-sectional images of the EOT dry and wet structure of the MEAs with LSR and HSR GDLs, respectively. The preferential crack formation was noticed under the uncompressed channel regions while strongly interacting with the MPL deformities, due to the thick MPL layer of the HSR GDL. Overall, the severity of membrane buckling was substantially reduced by adoption of the smoother GDL, contributing 2X greater lifetime [135]. A 2D multi-physics finite element model was developed to simulate the hygro-thermo-mechanical *in situ* fuel cell operation. The membrane deformation was accompanied by a rise in the effective plastic strain in the regions of major deformation. The modeling results revealed that the critical GDL pore radius for CCM buckling to occur was ~80 µm, which is consistent with the experimental observations of membrane crack formation under the

adopted AST conditions. In addition to this, the bulge height and the effective plastic strain on the catalyst layer dictates the buckling behavior of the membrane. The relatively lower density and different geometry of MPL cracks in the LSR GDL was observed to reduce the severity of CCM buckling (and associated membrane fracture) as its bulge height in the MPL cracks is lower, as observed in the wet images of **Figure 2.4**. Overall, the improvement in GDL surface demonstrates substantial mitigation effect against fatigue-driven mechanical membrane degradation and failure, which is also corroborated by the numerical simulation results.

Further details of this work are provided in **Appendix D** [136].

2.5. Mitigation of Mechanical Membrane Degradation in Fuel Cells – Part 2: Bonded Membrane Electrode Assembly

The GDL pores facilitate membrane cracks through wrinkle deformation as a key failure mode during pure mechanical membrane degradation [135]. The free CCM movement into such pores is known to cause elevated local stress and facilitate crack development. Hence as a novel second mitigation, the objective of this work is to achieve uniform CL-GDL bonding via improved MEA lamination in order to evade delamination and mitigate the CCM buckling. The bonded MEA was fabricated by hot pressing the CCM and GDL's at 150ºC for 3 mins using a Instron® 5569 equipment. The bonded MEA was subjected to similar experimental workflow as used in Section 2.4, consisting of miniature fuel cell fixture and non-invasive XCT visualization during life stages of a wet/dry cycling AST [115,128]. Fundamental support of the experimental findings is provided with complementary FEM based numerical simulations.

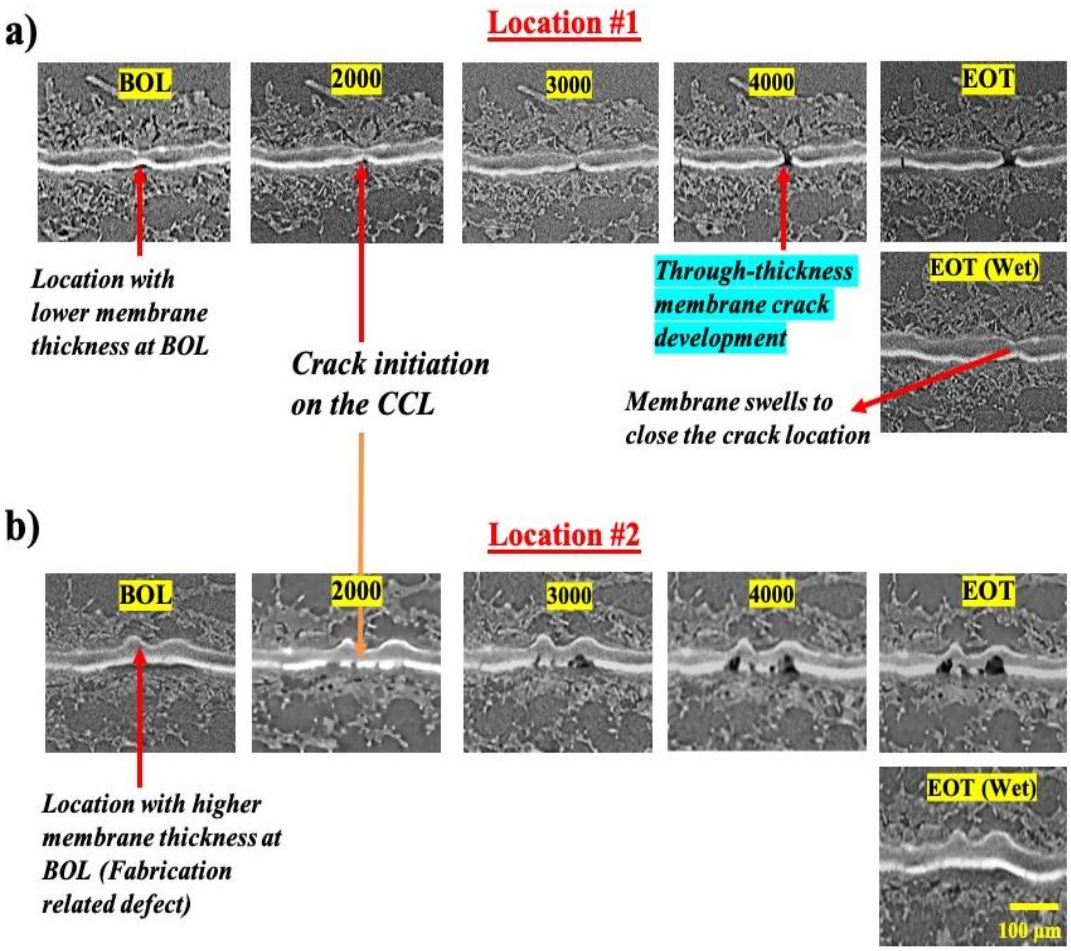

Figure 2.5. Membrane crack development observed under two locations (a & b) with fabrication related deformities (EOT = 4500 cycles) [137]**.**

In this work, substantial crack development was observed after an AST lifetime of 4500 cycles (EOT). Similar to part 1 [136], through-thickness membrane cracks were the key failure mode during mechanical degradation induced through wet/dry cycling procedure. On contrary to part 1, a decreasing CCL crack density trend was noticed with cycling, possibly due to crack merging. On closer observation, GDL fiber intrusion at the CCM surface was discovered to induce CCL crack development and ultimately leading to membrane cracks. Another membrane crack mechanism observed was due to MEA fabrication deformities i.e., locations with lower and excessively higher local membrane thickness (Figure 2.5). Complementary FE simulations demonstrated that with increasing adhesion at the CCM-GDL interfaces, the effective plastic strain was found to decrease significantly for all GDL void sizes. Based on the simulation results, improved adhesion decreases the sliding interaction at the CCM-GDL interface and thereby, reduces the buckling into the GDL void. Overall, the adhesion improved architecture facilitates to slow

down the overall membrane degradation rate during the mechanical cycling and thereby enhance the membrane durability.

Further details of this work are provided in **Appendix E** [137].

Chapter 3.

Conclusions and Future work

The present dissertation addresses the membrane lifetime and durability in PEMFCs. Membrane durability is one of the main technical challenges for the commercial propagation of this technology for transportation applications. This thesis is an effort to characterize the effects of various degradation processes of PFSA ionomer membranes and mitigation techniques to minimize the rate of decay in the physical integrity of the membranes.

3.1. Conclusions

Non-destructive 3D XCT characterization comes as a pioneering methodology to perform a detailed analysis to understand the intermediate degradation stages during practical operation of fuel cell membranes. Chemical and mechanical degradation mechanisms independently play important roles in aggravating membrane breakdown, while the combined involvement of combined mechanisms greatly accelerates the overall rate of degradation. Initially, the combined effect of chemical and mechanical degradation was characterized as a baseline. Based on the results, mitigation strategies were assessed and developed to negate the individual effects of pure chemical and mechanical degradation processes, collectively targeting high combined chemical and mechanical membrane durability in fuel cells.

The non-reinforced, baseline MEAs degraded to different levels of combined chemical and mechanical membrane degradation were characterized using micro-XCT. The global *in situ* diagnostic results of increasing crossover gas leakage and OCV decay were in good agreement with the XCT results. In addition to the two membrane crack shapes (I- and Y-shaped) reported previously, a third distinct X-shaped crack morphology was observed to have developed. Severe membrane thinning of around 60% of the thickness was measured at EOL, with magnified thinning at the inlet regions. Tensile test results showed increasing membrane stiffening and brittleness with the cycling procedure. This underlined the effect of chemical stressors in damaging the membrane resilience for further degradation under mechanical stress.

The 3D membrane failure analysis was extended to four dimensional (4D) *in situ* visualization to study the membrane damage development under isolated types of degradation stressors. The 4D XCT approach was achieved by observing the same MEA location at different stages of degradation time. This methodology was first applied to examine pure chemical degradation of three different types of membranes namely i) non-reinforced; ii) mechanically reinforced; and iii) chemically and mechanically mitigated membranes.

XCT observations showed global membrane thinning for non-reinforced and mechanically reinforced membranes. Several locations showed electrode shorting sites under the land regions, preceded by excessive thinning due to the chemical stressors. Hence, the land regions demonstrated shorts due to mechanical stresses caused by clamping pressure which can accelerate electrode shorting. The ePTFE layer in the chemical additive free reinforced membrane was not sufficient to negate this short development. In contrast, the co-mitigated membrane sustained significantly longer test duration without failures such as shorts or significant membrane thinning, highlighting the scavenging effect against the radicals. The regenerative radical effect of Ce cation additive is thus deemed a key strategy to mitigate the chemical stressors.

Next, the same 4D *in situ* visualization methodology was applied to examine the mitigative effect of mechanical membrane reinforcement against pure mechanical membrane degradation induced by wet/dry cycling. Results demonstrated that membrane crack propagation is the dominant failure mode during the pure mechanical degradation process for both non-reinforced and reinforced membranes. Notably however, the reinforced membrane extended the test lifetime by approximately 2x compared to that of the non-reinforced baseline membrane. Membrane-catalyst layer delamination and catalyst layer cracks were identified as the preceding drivers of local membrane failure. As expected, the central ePTFE reinforcement layer enhanced the overall fracture resistance of the membrane which in turn delayed the crack development process as compared to non-reinforced membranes. Moreover, membrane crack closure and opening were observed, facilitated by *in situ* XCT imaging during wet and dry states, respectively. The systematic XCT approach enabled novel views for mechanical degradation in reinforced membranes and will act as guide for more developments in the future works.

As additional measures to mitigate mechanical membrane degradation, two novel mitigation strategies were developed and assessed using 4D *in situ* XCT approach. In the first approach, 4D *in situ* visualization of pure mechanical membrane degradation process was carried out using a small-scale fuel cell fixture consisting of MEA with LSR GDLs. Results showed the underlying membrane failure mode during the wet/dry cycling AST was membrane fracture which was preceded by CCL fracture associated with locally elevated stress and strain. The buckling deformation of the MEA with low surface roughness was significantly suppressed compared to the high surface roughness MEA, owing to the thick and smooth MPL of the low surface roughness MEA. Complementary FEM simulations showed that cyclic CCM buckling onto the GDL cavities led to a state of tension-compression, causing crack development at the CL and membrane surfaces. In addition, the membrane's simulated bulge height and effective plastic strain were found to be related to the critical geometry-dependent buckling behavior of the membrane. The simulation results also revealed that the critical GDL pore radius for CCM buckling to occur was ~80 μm, which is consistent with the experimental observations of membrane crack formation under the adopted AST conditions. Overall, this novel approach showed significant mitigation on mechanical membrane degradation contributing to 2x greater lifetime as compared to HSR GDL MEA.

The second approach for mitigation of mechanical membrane degradation in the two-part series focused on component interaction effects within an MEA with non-reinforced membrane. This was achieved by establishing uniform CL-GDL bonding in order to evade delamination and CCM buckling. Similar to Part 1 [136], the key membrane failure mode associated with the repetitive wet/dry cycles was development of through-thickness membrane cracks. On comparison with a non-bonded baseline MEA, the bonded MEA showed 2x lower rate of degradation which was attributed to the improved interfacial contact and arresting the CCM movement facilitated by the bonding procedure. The primary root causes of failure were now associated with bonding irregularities and impingement of GDL fibers. Complementary FEM simulations showed that an increase in the CCM-GDL frictional coefficient, which is representative of the interfacial adhesion quality, substantially decreases the effective plastic strain within the membrane during CCM swelling and buckling into adjacent GDL void spaces. With improved MEA bonding, the CL crack and membrane crack development can be delayed or even completely stopped, which enhances the membrane lifetime and durability.

3.2. Suggested Future Works

The current findings have shown a pathway to improve the fuel cell performance, particularly focusing on membrane lifetime and durability. A comprehensive suite of novel XCT approach, complementary diagnostic tools and finite element models can further improve the understanding of membrane degradation processes. Based on the observations and results, the following future work is suggested.

- Adopt the 4D *in situ* approach to characterize the combined chemical and mechanical degradation process for both reinforced and non-reinforced membranes. This will provide further insights into understanding the mitigation effect.
- The morphological characterization of the *in situ* behavior of the membrane within an operational MEA could be extended to study the startup/shut down under freezing conditions to typify the cold weather.
- Optimizing the MEA bonding process to minimize unintended defects, can offer further potential improvements in overall membrane durability and lifetime.
- Cost evaluation of different mitigation strategies demonstrated in this work, including fuel cell performance assessment, possible interactions with other failure modes, and their cost and compatibility with high volume manufacturing.

References

[1] Wu J, Yuan XZ, Martin JJ, Wang H, Zhang J, Shen J, et al. A review of PEM fuel cell durability: Degradation mechanisms and mitigation strategies. Journal of Power Sources 2008;184:104–19. doi:10.1016/j.jpowsour.2008.06.006.

[2] Larminie J, Dicks A. Fuel cell systems explained. 2003. doi:10.1002/9781118878330.

[3] Venkatesan SV. Investigation of Mesoscopic Degradation Phenomena in Fuel Cells. Simon Fraser University 2017:1–153.

[4] Mench MM. Fuel Cell Engines. John Wiley and Sons; 2008. doi:10.1002/9780470209769.

[5] Yu D, Yuvarajan S. Electronic circuit model for proton exchange membrane fuel cells. Journal of Power Sources 2005;142:238–42. doi:https://doi.org/10.1016/j.jpowsour.2004.09.041.

[6] Basualdo MS, Feroldi D, Outbib R. PEM Fuel Cells with Bio-Ethanol Processor Systems A Multidisciplinary Study of Modelling, Simulation, Fault Diagnosis and Advanced Control / edited by Marta S. Basualdo, Diego Feroldi, Rachid Outbib. 1st ed. 20. Springer London : Imprint: Springer; 2012.

[7] U.S. Department of Energy DCCAST. DOE Technical Targets for Polymer Electrolyte Membrane Fuel Cell Components | Department of Energy. Http://Www1EereEnergyGov/Hydrogenandfuelcells/Pdfs/ Component_durability_may_2010Pdf 2010. https://energy.gov/eere/fuelcells/doe-technical-targets-polymer-electrolyte-membrane-fuel-cell-components#mea (accessed February 4, 2017).

[8] Mukundan R, Baker AM, Kusoglu A, Beattie P, Knights S, Weber AZ, et al. Membrane Accelerated Stress Test Development for Polymer Electrolyte Fuel Cell Durability Validated Using Field and Drive Cycle Testing. Journal of The Electrochemical Society 2018;165:F3085–93. doi:10.1149/2.0101806jes.

[9] Alavijeh AS, Khorasany RMH, Nunn Z, Habisch A, Lauritzen M, Rogers E, et al. Microstructural and Mechanical Characterization of Catalyst Coated Membranes Subjected to In Situ Hygrothermal Fatigue. Journal of The Electrochemical Society 2015;162:F1461–9. doi:10.1149/2.0471514jes.

[10] Tavassoli A, Lim C, Kolodziej J, Lauritzen M, Knights S, Wang GG, et al. Effect of catalyst layer defects on local membrane degradation in polymer electrolyte fuel cells. Journal of Power Sources 2016;322:17–25. doi:10.1016/j.jpowsour.2016.05.016.

[11] Gittleman CS, Coms FD, Lai YH. Membrane Durability: Physical and Chemical Degradation. In: Mench M, Kumbur EC, Veziroglu TN, editors. Polymer Electrolyte Fuel Cell Degradation, Cambridge MA: Academic Press; 2012, p. 15–88.

[12] Rodgers MP, Bonville LJ, Kunz HR, Slattery DK, Fenton JM. Fuel cell perfluorinated sulfonic acid membrane degradation correlating accelerated stress testing and lifetime. Chemical Reviews 2012;112:6075–103. doi:10.1021/cr200424d.

[13] El-kharouf A, Chandan A, Hattenberger M, Pollet BG. Proton exchange membrane fuel cell degradation and testing: review. Journal of the Energy Institute n.d.;85:188–200. doi:10.1179/1743967112Z.00000000036.

[14] Marrony M, Barrera R, Quenet S, Ginocchio S, Montelatici L, Aslanides A. Durability study and lifetime prediction of baseline proton exchange membrane fuel cell under severe operating conditions. Journal of Power Sources 2008;182:469–75. doi:https://doi.org/10.1016/j.jpowsour.2008.02.096.

[15] Zhang S, Yuan X, Wang H, Mérida W, Zhu H, Shen J, et al. A review of accelerated stress tests of MEA durability in PEM fuel cells. International Journal of Hydrogen Energy 2009;34:388–404. doi:10.1016/j.ijhydene.2008.10.012.

[16] Wroblowa HS, Yen-Chi-Pan, Razumney G. Electroreduction of oxygen: A new mechanistic criterion. Journal of Electroanalytical Chemistry and Interfacial Electrochemistry 1976;69:195–201. doi:https://doi.org/10.1016/S0022-

0728(76)80250-1.

[17] Wong KH, Kjeang E. Macroscopic In-Situ Modeling of Chemical Membrane Degradation in Polymer Electrolyte Fuel Cells. Journal of The Electrochemical Society 2014;161:F823–32. doi:10.1149/2.0031409jes.

[18] Wong KH, Kjeang E. Mitigation of Chemical Membrane Degradation in Fuel Cells: Understanding the Effect of Cell Voltage and Iron Ion Redox Cycle. ChemSusChem 2015;8:1072–82. doi:10.1002/cssc.201402957.

[19] Ghassemzadeh L, Holdcroft S. Quantifying the structural changes of perfluorosulfonated acid ionomer upon reaction with hydroxyl radicals. Journal of the American Chemical Society 2013;135:8181–4.

[20] Ghassemzadeh L, Peckham TJ, Weissbach T, Luo X, Holdcroft S. Selective formation of hydrogen and hydroxyl radicals by electron beam irradiation and their reactivity with perfluorosulfonated acid ionomer. Journal of the American Chemical Society 2013;135:15923–32.

[21] Danilczuk M, Coms FD, Schlick S. Visualizing Chemical Reactions and Crossover Processes in a Fuel Cell Inserted in the ESR Resonator: Detection by Spin Trapping of Oxygen Radicals, Nafion-Derived Fragments, and Hydrogen and Deuterium Atoms. J Phys Chem B 2009;113:8031.

[22] Lim C, Ghassemzadeh L, Van Hove F, Lauritzen M, Kolodziej J, Wang GG, et al. Membrane degradation during combined chemical and mechanical accelerated stress testing of polymer electrolyte fuel cells. Journal of Power Sources 2014;257:102–10. doi:10.1016/j.jpowsour.2014.01.106.

[23] Sadeghi Alavijeh A, Goulet MA, Khorasany RMH, Ghataurah J, Lim C, Lauritzen M, et al. Decay in mechanical properties of catalyst coated membranes subjected to combined chemical and mechanical membrane degradation. Fuel Cells 2015;15:204–13. doi:10.1002/fuce.201400040.

[24] Macauley N, Alavijeh AS, Watson M, Kolodziej J, Lauritzen M, Knights S, et al. Accelerated membrane durability testing of heavy duty fuel cells. Journal of the

Electrochemical Society 2015;162:F98–107. doi:10.1149/2.0671501jes.

[25] Coms FD. The Chemistry of Fuel Cell Membrane Chemical Degradation Frank D. Coms General Motors Corporation, Fuel Cell Research Labs, 10 Carriage Street, Honeoye Falls, NY 14472, USA. ECS Trans 2008;16:235–55. doi:10.1149/1.2981859.

[26] Healy J, Hayden C, Xie T, Olson K, Waldo R, Brundage M, et al. Aspects of the chemical degradation of PFSA ionomers used in PEM fuel cellsx. Fuel Cells 2005;5:302–8. doi:10.1002/fuce.200400050.

[27] COLLIER A, WANG H, ZIYUAN X, ZHANG J, WILKINSON D. Degradation of polymer electrolyte membranes. International Journal of Hydrogen Energy 2006;31:1838–54. doi:10.1016/j.ijhydene.2006.05.006.

[28] Williams M V, Kunz HR, Fenton JM. Operation of Nafion ®-based PEM fuel cells with no external humidification: influence of operating conditions and gas diffusion layers. Journal of Power Sources 2004;135:122–34. doi:10.1016/j.jpowsour.2004.04.010.

[29] UCHIDA H, UENO Y, HAGIHARA H, WATANABE M. Self-humidifying electrolyte membranes for fuel cells: Preparation of highly dispersed TiO2 particles in Nafion 112. Journal of the Electrochemical Society 2003;150:A57–62.

[30] Huang X, Solasi R, Zou YUE, Feshler M, Reifsnider K, Condit D, et al. Mechanical Endurance of Polymer Electrolyte Membrane and PEM Fuel Cell Durability. J Polym Sci Part B Polym Physics 2006;44:2346–57.

[31] Macauley N, Ghassemzadeh L, Lim C, Watson M, Kolodziej J, Lauritzen M, et al. Pt Band Formation Enhances the Stability of Fuel Cell Membranes. ECS Electrochemistry Letters 2013;2:F33–5. doi:10.1149/2.007304eel.

[32] Xie J, Wood DL, More KL, Atanassov P, Borup RL. Microstructural Changes of Membrane Electrode Assemblies during PEFC Durability Testing at High Humidity Conditions. Journal of the Electrochemical Society 2005;152:A1011. doi:10.1149/1.1873492.

[33] Pearman BP, Mohajeri N, Brooker RP, Rodgers MP, Slattery DK, Hampton MD, et al. The degradation mitigation effect of cerium oxide in polymer electrolyte membranes in extended fuel cell durability tests. J Power Sources 2013;225:75–83.

[34] Pearman BP, Mohajeri N, Slattery DK, Hampton MD, Seal S, Cullen DA. The chemical behavior and degradation mitigation effect of cerium oxide nanoparticles in perfluorosulfonic acid polymer electrolyte membranes. Polymer Degradation and Stability 2013;98:1766–72. doi:10.1016/j.polymdegradstab.2013.05.025.

[35] Lim C, Alavijeh AS, Lauritzen M, Kolodziej J, Knights S, Kjeang E. Fuel Cell Durability Enhancement with Cerium Oxide under Combined Chemical and Mechanical Membrane Degradation. ECS Electrochemistry Letters 2015;4:F29–31. doi:10.1149/2.0081504eel.

[36] Baker AM, Wang L, Johnson WB, Prasad AK, Advani SG. Nafion membranes reinforced with ceria-coated multiwall carbon nanotubes for improved mechanical and chemical durability in polymer electrolyte membrane fuel cells. Journal of Physical Chemistry C 2014;118:26796–802. doi:10.1021/jp5078399.

[37] Wang L, Advani SG, Prasad AK. Self-Hydrating Pt/CeO2-Nafion Composite Membrane for Improved Durability and Performance. ECS Electrochemistry Letters 2014;3:F30–2. doi:10.1149/2.007405eel.

[38] Wang L, Advani SG, Prasad AK. Degradation reduction of polymer electrolyte membranes using CeO 2 as a free-radical scavenger in catalyst layer. Electrochimica Acta 2013;109:775–80. doi:10.1016/j.electacta.2013.07.189.

[39] Baker AM, Mukundan R, Spernjak D, Judge EJ, Advani SG, Prasad AK, et al. Cerium Migration during PEM Fuel Cell Accelerated Stress Testing. Journal of The Electrochemical Society 2016;163:F1023–31. doi:10.1149/2.0181609jes.

[40] Danilczuk M, Schlick S, Coms FD. Cerium(III) as a Stabilizer of Perfluorinated Membranes Used in Fuel Cells: In Situ Detection of Early Events in the ESR Resonator. Macromolecules n.d.;42:8943–9. doi:10.1021/ma9017108.

[41] Danilczuk M, Perkowski AJ, Schlick S. Ranking the Stability of Perfluorinated Membranes Used in Fuel Cells to Attack by Hydroxyl Radicals and the Effect of Ce(III): A Competitive Kinetics Approach Based on Spin Trapping ESR. Macromolecules n.d.;43:3352–8. doi:10.1021/ma1001386.

[42] Venkateshkumar Prabhakaran, Christopher G. Arges, Vijay Ramani. Investigation of polymer electrolyte membrane chemical degradation and degradation mitigation using in situ fluorescence spectroscopy. Proceedings of the National Academy of Sciences - PNAS n.d.;109:1029–34. doi:10.1073/pnas.1114672109.

[43] Trogadas P, Parrondo J, Ramani V. Degradation Mitigation in Polymer Electrolyte Membranes Using Cerium Oxide as a Regenerative Free-Radical Scavenger. Electrochemical and Solid-State Letters 2008;11:B113. doi:10.1149/1.2916443.

[44] Wang L, Advani SG, Prasad AK. Degradation reduction of polymer electrolyte membranes using CeO2 as a free-radical scavenger in catalyst layer. Electrochimica Acta n.d.;109:775–80. doi:10.1016/j.electacta.2013.07.189.

[45] Wilson MS, Garzon FH, Borup RL, Stewart SM, Datye A. Ceria and Doped Ceria Nanoparticle Additives for Polymer Fuel Cell Lifetime Improvement. ECS Transactions 2014;64:403–11. doi:10.1149/06403.0403ecst.

[46] Coms FD, Liu H, Owejan JE. Mitigation of Perfluorosulfonic Acid Membrane Chemical Degradation Using Cerium and Manganese Ions. ECS transactions, vol. 16, n.d., p. 1735–47. doi:10.1149/1.2982015.

[47] Lu Z, Lugo M, Santare MH, Karlsson AM, Busby FC, Walsh P. An experimental investigation of strain rate, temperature and humidity effects on the mechanical behavior of a perfluorosulfonic acid membrane. Journal of Power Sources 2012;214:130–6. doi:10.1016/j.jpowsour.2012.04.094.

[48] Büchi FN, Srinivasan S. Operating Proton Exchange Membrane Fuel Cells Without External Humidification of the Reactant Gases. Journal of The Electrochemical Society 1997;144:2767. doi:10.1149/1.1837893.

[49] Knights SD, Colbow KM, St-Pierre J, Wilkinson DP. Aging mechanisms and

lifetime of PEFC and DMFC. Journal of Power Sources 2004;127:127–34. doi:10.1016/j.jpowsour.2003.09.033.

[50] Khorasany RMH, Sadeghi Alavijeh A, Kjeang E, Wang GG, Rajapakse RKND. Mechanical degradation of fuel cell membranes under fatigue fracture tests. Journal of Power Sources 2015;274:1208–16. doi:10.1016/j.jpowsour.2014.10.135.

[51] Lai Y-H, Mittelsteadt CK, Gittleman CS, Dillard DA. Viscoelastic Stress Analysis of Constrained Proton Exchange Membranes Under Humidity Cycling. Journal of Fuel Cell Science and Technology 2009;6:021002. doi:10.1115/1.2971045.

[52] Aindow TT, O'Neill J. Use of mechanical tests to predict durability of polymer fuel cell membranes under humidity cycling. J Power Sources 2011;196:3851–4.

[53] Khorasany RMH, Goulet M-A, Alavijeh AS, Kjeang E, Wang GG, Rajapakse RKND. On the constitutive relations for catalyst coated membrane applied to in-situ fuel cell modeling. Journal of Power Sources 2014;252:176–88. doi:10.1016/j.jpowsour.2013.11.087.

[54] Goulet M-A, Arbour S, Lauritzen M, Kjeang E. Water sorption and expansion of an ionomer membrane constrained by fuel cell electrodes. Journal of Power Sources 2015;274:94–100. doi:10.1016/j.jpowsour.2014.10.040.

[55] Goulet M-A, Khorasany RMH, De Torres C, Lauritzen M, Kjeang E, Wang GG, et al. Mechanical properties of catalyst coated membranes for fuel cells. Journal of Power Sources 2013;234:38–47. doi:10.1016/j.jpowsour.2013.01.128.

[56] Khorasany RMH, Sadeghi Alavijeh A, Kjeang E, Wang GG, Rajapakse RKND. Mechanical degradation of PFSA membranes in polymer electrolyte membrane fuel cells under fatigue fracture tests. J Power Sources 2015;274:1208–16.

[57] Khorasany RMH, Singh Y, Sadeghi Alavijeh A, Kjeang E, Wang GG, Rajapakse RKND. Fatigue properties of catalyst coated membranes for fuel cells: Ex-situ measurements supported by numerical simulations. International Journal of Hydrogen Energy 2016;41:8992–9003. doi:10.1016/j.ijhydene.2016.04.042.

[58] Singh Y, Khorasany RMH, Sadeghi Alavijeh A, Kjeang E, Wang GG, Rajapakse RKND. Ex situ measurement and modelling of crack propagation in fuel cell membranes under mechanical fatigue loading. International Journal of Hydrogen Energy 2017;42:19257–71.

[59] Kundu S, Fowler MW, Simon LC, Grot S. Morphological features (defects) in fuel cell membrane electrode assemblies. Journal of Power Sources 2006;157:650–6. doi:10.1016/j.jpowsour.2005.12.027.

[60] Lai YH, Li Y, Rock JA. A novel full-field experimental method to measure the local compressibility of gas diffusion media. Journal of Power Sources 2010;195:3215–23. doi:10.1016/j.jpowsour.2009.11.122.

[61] Hizir FE, Ural SO, Kumbur EC, Mench MM. Characterization of interfacial morphology in polymer electrolyte fuel cells: Micro-porous layer and catalyst layer surfaces. Journal of Power Sources 2010;195:3463–71. doi:10.1016/j.jpowsour.2009.11.032.

[62] Gostick JT, Ioannidis MA, Fowler MW, Pritzker MD. On the role of the microporous layer in PEMFC operation. Electrochemistry Communications 2009;11:576–9. doi:10.1016/j.elecom.2008.12.053.

[63] Jao TC, Jung G Bin, Kuo SC, Tzeng WJ, Su A. Degradation mechanism study of PTFE/Nafion membrane in MEA utilizing an accelerated degradation technique. International Journal of Hydrogen Energy 2012;37:13623–30. doi:10.1016/j.ijhydene.2012.02.035.

[64] Lin Q, Liu Z, Wang L, Chen X, Shi S. Fracture property of Nafion XL composite membrane determined by R-curve method. Journal of Power Sources 2018;398:34–41. doi:10.1016/j.jpowsour.2018.07.052.

[65] Shim J, Ha HY, Hong SA, Oh IH. Characteristics of the Nafion ionomer-impregnated composite membrane for polymer electrolyte fuel cells. Journal of Power Sources 2002;109:412–7. doi:10.1016/S0378-7753(02)00106-4.

[66] Zhu X, Zhang H, Liang Y, Zhang Y, Luo Q, Bi C, et al. Challenging reinforced

composite polymer electrolyte membranes based on disulfonated poly(arylene ether sulfone)-impregnated expanded PTFE for fuel cell applications. Journal of Materials Chemistry 2007;17:386–97. doi:10.1039/b611690f.

[67] Shi S, Weber AZ, Kusoglu A. Structure/Property Relationship of Nafion XL Composite Membranes. Journal of Membrane Science 2016;516:123–34. doi:10.1016/j.memsci.2016.06.004.

[68] Tang Y, Karlsson AM, Santare MH, Gilbert M, Cleghorn S, Johnson WB. An experimental investigation of humidity and temperature effects on the mechanical properties of perfluorosulfonic acid membrane. Materials Science and Engineering: A 2006;425:297–304. doi:https://doi.org/10.1016/j.msea.2006.03.055.

[69] Dubau L, Castanheira L, Chatenet M, Maillard F, Dillet J, Maranzana G, et al. Carbon corrosion induced by membrane failure: The weak link of PEMFC long-term performance. International Journal of Hydrogen Energy n.d.;39:21902–14. doi:10.1016/j.ijhydene.2014.07.099.

[70] De Moor G, Bas C, Charvin N, Moukheiber E, Niepceron F, Breilly N, et al. Understanding Membrane Failure in PEMFC: Comparison of Diagnostic Tools at Different Observation Scales. Fuel Cells (Weinheim an Der Bergstrasse, Germany) n.d.;12:356–64. doi:10.1002/fuce.201100161.

[71] Cleghorn SJC, Mayfield DK, Moore DA, Moore JC, Rusch G, Sherman TW, et al. A polymer electrolyte fuel cell life test: 3 years of continuous operation. Journal of Power Sources 2006;158:446–54. doi:https://doi.org/10.1016/j.jpowsour.2005.09.062.

[72] Li Y, Dillard DA, Case SW, Ellis MW, Lai Y-H, Gittleman CS, et al. Fatigue and creep to leak tests of proton exchange membranes using pressure-loaded blisters. Journal of Power Sources 2009;194:873–9. doi:https://doi.org/10.1016/j.jpowsour.2009.06.083.

[73] Grohs JR, Li Y, Dillard DA, Case SW, Ellis MW, Lai Y-H, et al. Evaluating the time

and temperature dependent biaxial strength of Gore-Select® series 57 proton exchange membrane using a pressure loaded blister test. Journal of Power Sources 2010;195:527–31. doi:https://doi.org/10.1016/j.jpowsour.2009.07.054.

[74] Tang HL, Pan M, Wang F. A mechanical durability comparison of various perfluocarbon proton exchange membranes. Journal of Applied Polymer Science 2008;109:2671–8. doi:10.1002/app.28343.

[75] Rodgers MP, Bonville LJ, Mukundan R, Borup R, Ahluwalia R, Beattie P, et al. Perfluorinated sulfonic acid membrane and membrane electrode assembly degradation correlating accelerated stress testing and lifetime testing. ECS Transactions, vol. 58, Electrochemical Society Inc.; 2013, p. 129–48. doi:10.1149/05801.0129ecst.

[76] Chen J, Goshtasbi A, Soleymani AP, Ricketts M, Waldecker J, Xu C, et al. Effects of cycle duration and test hardware in relative humidity cycling of a polymer electrolyte membrane. Journal of Power Sources 2020;476. doi:10.1016/j.jpowsour.2020.228576.

[77] Energy USD of. USCAR FUEL CELL TECH TEAM CELL COMPONENT ACCELERATED STRESS TEST PROTOCOLS FOR PEM FUEL CELLS n.d.

[78] Benjamin TG. Membrane and MEA Accelerated Stress Test Protocols 2007.

[79] Panha K, Fowler M, Yuan X-Z, Wang H. Accelerated durability testing via reactants relative humidity cycling on PEM fuel cells. Applied Energy 2012;93:90–7. doi:10.1016/j.apenergy.2011.05.011.

[80] Lai Y-H, Rahmoeller KM, Hurst JH, Kukreja RS, Atwan M, Maslyn AJ, et al. Accelerated Stress Testing of Fuel Cell Membranes Subjected to Combined Mechanical/Chemical Stressors and Cerium Migration. Journal of The Electrochemical Society 2018;165:F3217–29. doi:10.1149/2.0241806jes.

[81] Cheng TTH, Rogers E, Young AP, Ye S, Colbow V, Wessel S. Effects of crossover hydrogen on platinum dissolution and agglomeration. Journal of Power Sources 2011;196:7985–8. doi:10.1016/j.jpowsour.2011.05.034.

[82] Bhattacharya S, Leung J, Lauritzen M V., Kjeang E. Isolated chemical degradation induced decay of mechanical membrane properties in fuel cells. Electrochimica Acta 2020;352:136489. doi:10.1016/j.electacta.2020.136489.

[83] Kang J, Kim J. Membrane electrode assembly degradation by dry/wet gas on a PEM fuel cell. International Journal of Hydrogen Energy 2010;35:13125–30. doi:10.1016/j.ijhydene.2010.04.077.

[84] Patil YP, Jarrett WL, Mauritz KA. Deterioration of mechanical properties: A cause for fuel cell membrane failure. Journal of Membrane Science 2010;356:7–13. doi:10.1016/j.memsci.2010.02.060.

[85] Yoon W, Huang X. Study of Polymer Electrolyte Membrane Degradation under OCV Hold Using Bilayer MEAs. Journal of the Electrochemical Society 2010;157:B599. doi:10.1149/1.3305965.

[86] Endoh E, Terazono S, Widjaja H, Takimoto Y. Degradation Study of MEA for PEMFCs under Low Humidity Conditions. Electrochemical and Solid-State Letters 2004;7:A209. doi:10.1149/1.1739314.

[87] Wahdame B, Candusso D, François X, Harel F, Péra M-C, Hissel D, et al. Comparison between two PEM fuel cell durability tests performed at constant current and under solicitations linked to transport mission profile. International Journal of Hydrogen Energy 2007;32:4523–36. doi:10.1016/j.ijhydene.2007.03.013.

[88] Patil Y, Sambandam S, Ramani V, Mauritz K. Model Studies of the Durability of a Titania-Modified Nafion Fuel Cell Membrane. Journal of the Electrochemical Society 2009;156:B1092. doi:10.1149/1.3169512.

[89] Kusoglu A, Santare MH, Karlsson AM. Aspects of fatigue failure mechanisms in polymer fuel cell membranes. Journal of Polymer Science, Part B: Polymer Physics 2011;49:1506–17. doi:10.1002/polb.22336.

[90] Kreitmeier S, Schuler GA, Wokaun A, Büchi FN. Investigation of membrane degradation in polymer electrolyte fuel cells using local gas permeation analysis.

Journal of Power Sources 2012;212:139–47. doi:10.1016/j.jpowsour.2012.03.071.

[91] Huang X, Solasi R, Zou Y, Feshler M, Reifsnider K, Condit D, et al. Mechanical endurance of polymer electrolyte membrane and PEM fuel cell durability. Journal of Polymer Science Part B: Polymer Physics 2006;44:2346–57. doi:10.1002/polb.20863.

[92] Sompalli B, Litteer BA, Gu W, Gasteiger HA. Membrane Degradation at Catalyst Layer Edges in PEMFC MEAs. Journal of The Electrochemical Society 2007;154:B1349. doi:10.1149/1.2789791.

[93] Sadeghi Alavijeh A, Venkatesan SV, Khorasany RMH, Kim WHJ, Kjeang E. Ex-situ tensile fatigue-creep testing: A powerful tool to simulate in-situ mechanical degradation in fuel cells. Journal of Power Sources 2016;312:123–7.

[94] Crum M, Liu W. Effective Testing Matrix for Studying Membrane Durability in PEM Fuel Cells: Part 2. Mechanical Durability and Combined Mechanical and Chemical Durability. Electrochemical Society Transactions 2006;3:541–50.

[95] Inaba M, Kinumoto T, Kiriake M, Umebayashi R, Tasaka A, Ogumi Z. Gas crossover and membrane degradation in polymer electrolyte fuel cells. Electrochimica Acta n.d.;51:5746–53. doi:10.1016/j.electacta.2006.03.008.

[96] Kai Y, Kitayama Y, Omiya M, Uchiyama T, Kato M. Crack Formation in Membrane Electrode Assembly Under Static and Cyclic Loadings. Journal of Fuel Cell Science and Technology 2013;10:021007.

[97] Zhang J, Tang Y, Song C, Zhang J, Wang H. PEM fuel cell open circuit voltage (OCV) in the temperature range of 23. Journal of Power Sources 2006;163:532–7. doi:10.1016/j.jpowsour.2006.09.026.

[98] Zhang Z, Shi S, Lin Q, Wang L, Liu Z, Li P, et al. Exploring the role of reinforcement in controlling fatigue crack propagation behavior of perfluorosulfonic-acid membranes. International Journal of Hydrogen Energy 2018;43:6379–89. doi:10.1016/j.ijhydene.2018.02.034.

[99] Pfrang A, Veyret D, Janssen GJM, Tsotridis G. Imaging of membrane electrode assemblies of proton exchange membrane fuel cells by X-ray computed tomography. Journal of Power Sources 2011;196:5272–6. doi:10.1016/j.jpowsour.2010.09.020.

[100] Pokhrel A, El Hannach M, Orfino FP, Dutta M, Kjeang E. Failure analysis of fuel cell electrodes using three-dimensional multi-length scale X-ray computed tomography. Journal of Power Sources 2016;329:330–8. doi:10.1016/j.jpowsour.2016.08.092.

[101] Litster S, Epting WK, Wargo EA, Kalidindi SR, Kumbur EC. Morphological analyses of polymer electrolyte fuel cell electrodes with nano-scale computed tomography imaging. Fuel Cells 2013;13:935–45. doi:10.1002/fuce.201300008.

[102] Andisheh-Tadbir M, Orfino FP, Kjeang E. Three-dimensional phase segregation of micro-porous layers for fuel cells by nano-scale X-ray computed tomography. Journal of Power Sources 2016;310:61–9. doi:10.1016/j.jpowsour.2016.02.001.

[103] Odaya S, Phillips RK, Sharma Y, Bellerive J, Phillion AB, Hoorfar M. X-ray Tomographic Analysis of Porosity Distributions in Gas Diffusion Layers of Proton Exchange Membrane Fuel Cells. Electrochimica Acta 2015;152:464–72. doi:10.1016/j.electacta.2014.11.143.

[104] James JP, Choi H-W, Pharoah JG. X-ray computed tomography reconstruction and analysis of polymer electrolyte membrane fuel cell porous transport layers. International Journal of Hydrogen Energy 2012;37:18216–30. doi:10.1016/j.ijhydene.2012.08.077.

[105] Becker J, Flückiger R, Reum M, Büchi FN, Marone F, Stampanoni M. Determination of Material Properties of Gas Diffusion Layers: Experiments and Simulations Using Phase Contrast Tomographic Microscopy. Journal of The Electrochemical Society 2009;156:B1175. doi:10.1149/1.3176876.

[106] Becker J, Schulz V, Wiegmann A. Numerical Determination of Two-Phase Material Parameters of a Gas Diffusion Layer Using Tomography Images. Journal

of Fuel Cell Science and Technology 2008;5:021006. doi:10.1115/1.2821600.

[107] White RT, Eberhardt SH, Singh Y, Haddow T, Dutta M, Orfino FP, et al. Four-dimensional joint visualization of electrode degradation and liquid water distribution inside operating polymer electrolyte fuel cells. Scientific Reports 2018:1–12. doi:10.1038/s41598-018-38464-9.

[108] Markötter H, Manke I, Krüger P, Arlt T, Haussmann J, Klages M, et al. Investigation of 3D water transport paths in gas diffusion layers by combined in-situ synchrotron X-ray radiography and tomography. Electrochemistry Communications 2011;13:1001–4. doi:10.1016/j.elecom.2011.06.023.

[109] Markötter H, Alink R, Haußmann J, Dittmann K, Arlt T, Wieder F, et al. Visualization of the water distribution in perforated gas diffusion layers by means of synchrotron X-ray radiography. International Journal of Hydrogen Energy 2012;37:7757–61. doi:10.1016/j.ijhydene.2012.01.141.

[110] Kreitmeier S, Michiardi M, Wokaun A, Büchi FN. Factors determining the gas crossover through pinholes in polymer electrolyte fuel cell membranes. Electrochimica Acta 2012;80:240–7. doi:10.1016/j.electacta.2012.07.013.

[111] Lau SH, Chiu WKS, Garzon F, Chang H, Tkachuk A, Feser M, et al. Non invasive, multiscale 3D X-Ray characterization of porous functional composites and membranes, with resolution from MM to sub 50 NM. Journal of Physics: Conference Series 2009;152:012059. doi:10.1088/1742-6596/152/1/012059.

[112] Garzon FH, Lau SH, Davey JR, Borup R. Micro And Nano X-Ray Tomography Of PEM Fuel Cell Membranes After Transient Operation. ECS Transactions, vol. 11, ECS; 2007, p. 1139–49. doi:10.1149/1.2781026.

[113] Singh Y, Orfino FP, Dutta M, Kjeang E. 3D visualization of membrane failures in fuel cells. Journal of Power Sources 2017;345:1–11. doi:10.1016/j.jpowsour.2017.01.129.

[114] Singh Y, Orfino FP, Dutta M, Kjeang E. 3D Failure Analysis of Pure Mechanical and Pure Chemical Degradation in Fuel Cell Membranes. Journal of The

Electrochemical Society 2017;164:1331–41. doi:10.1149/2.0451713jes.

[115] Singh Y, White RT, Najm M, Haddow T, Pan V, Orfino FP, et al. Tracking the evolution of mechanical degradation in fuel cell membranes using 4D in situ visualization. Journal of Power Sources 2019:224–37. doi:10.1016/j.jpowsour.2018.11.049.

[116] Kusoglu A, Karlsson AM, Santare MH, Cleghorn S, Johnson WB. Mechanical response of fuel cell membranes subjected to a hygro-thermal cycle. Journal of Power Sources 2006;161:987–96. doi:10.1016/j.jpowsour.2006.05.020.

[117] Kusoglu A, Karlsson AM, Santare MH, Cleghorn S, Johnson WB. Mechanical behavior of fuel cell membranes under humidity cycles and effect of swelling anisotropy on the fatigue stresses. Journal of Power Sources 2007;170:345–58. doi:10.1016/j.jpowsour.2007.03.063.

[118] Kusoglu A, Santare MH, Karlsson AM. Aspects of fatigue failure mechanisms in polymer fuel cell membranes. J Polym Sci Part B Polym Physics 2011;49:1506–17.

[119] Khorasany RMH, Kjeang E, Wang GG, Rajapakse RKND. Simulation of ionomer membrane fatigue under mechanical and hygrothermal loading conditions. Journal of Power Sources 2015;279:55–63. doi:10.1016/j.jpowsour.2014.12.133.

[120] Ding G, Santare MH, Karlsson AM, Kusoglu A. Numerical evaluation of crack growth in polymer electrolyte fuel cell membranes based on plastically dissipated energy. Journal of Power Sources 2016;316:114–23. doi:10.1016/j.jpowsour.2016.03.031.

[121] Ding G, Karlsson AM, Santare MH. Numerical evaluation of fatigue crack growth in polymers based on plastically dissipated energy. International Journal of Fatigue 2017;94:89–96. doi:10.1016/j.ijfatigue.2016.09.012.

[122] Singh Y, Khorasany RMH, Kim WHJ, Alavijeh AS, Kjeang E, Rajapakse RKND, et al. Ex situ characterization and modelling of fatigue crack propagation in catalyst coated membrane composites for fuel cell applications. International Journal of

Hydrogen Energy 2019;44:12057–72. doi:10.1016/j.ijhydene.2019.03.108.

[123] Kleemann J, Finsterwalder F, Tillmetz W. Characterisation of mechanical behaviour and coupled electrical properties of polymer electrolyte membrane fuel cell gas diffusion layers. Journal of Power Sources 2009;190:92–102. doi:10.1016/j.jpowsour.2008.09.026.

[124] Uchiyama T, Kato M, Yoshida T. Buckling deformation of polymer electrolyte membrane and membrane electrode assembly under humidity cycles. Journal of Power Sources 2012;206:37–46. doi:10.1016/j.jpowsour.2012.01.073.

[125] Singh N, Bhattacharya S, Lauritzen M V, Kjeang E. Residual fatigue life modeling of fuel cell membranes. Journal of Power Sources 2020;477:228714. doi:10.1016/j.jpowsour.2020.228714.

[126] Sell CG, Hiver IM, Poinsot C. POLYETHYLENE IN UNIAXIAL TENSION 1996:75–82.

[127] Ramani D, Singh Y, Orfino FP, Dutta M, Kjeang E. Characterization of Membrane Degradation Growth in Fuel Cells Using X-ray Computed Tomography. Journal of The Electrochemical Society 2018;165:F3200–8. doi:10.1149/2.0251806jes.

[128] Ramani D, Singh Y, White RT, Wegener M, Orfino FP, Dutta M, et al. 4D in situ visualization of mechanical degradation evolution in reinforced fuel cell membranes. International Journal of Hydrogen Energy 2020;45:10089–103. doi:10.1016/j.ijhydene.2020.02.013.

[129] White RT, Wu A, Najm M, Orfino FP, Dutta M, Kjeang E. 4D in situ visualization of electrode morphology changes during accelerated degradation in fuel cells by X-ray computed tomography. Journal of Power Sources 2017;350:94–102. doi:10.1016/j.jpowsour.2017.03.058.

[130] White RT, Orfino FP, Hannach M El, Luo O, Dutta M, Young AP, et al. 3D Printed Flow Field and Fixture for Visualization of Water Distribution in Fuel Cells by X-ray Computed Tomography. Journal of The Electrochemical Society 2016;163:F1337–43. doi:10.1149/2.0461613jes.

[131] White RT, Najm M, Dutta M, Orfino FP, Kjeang E. Communication—Effect of Micro-XCT X-ray Exposure on the Performance of Polymer Electrolyte Fuel Cells. Journal of The Electrochemical Society 2016;163:1206–8. doi:10.1149/2.0751610jes.

[132] Ramani D, Singh Y, White RT, Haddow T, Wegener M, Orfino FP, et al. Four-dimensional in situ imaging of chemical membrane degradation in fuel cells. Electrochimica Acta 2021;380:138194. doi:10.1016/j.electacta.2021.138194.

[133] ImageJ 2017:https://imagej.net.

[134] Dragonfly 2.0, Object Research Systems (ORS) Inc., http://www.theobjects.com/dragonfly. 2017.

[135] Y. Singh, R. T. White, M. Najm , A. Boswell, F. P. Orfino MD and EK. Mitigation of Mechanical Membrane Degradation in Fuel Cells by Controlling Electrode Morphology — a 4D in-situ Structural Characterization. Journal of The Electrochemical Society 2021;168.

[136] Ramani D, Khattra NS, Singh Y, Mohseni-Javid A, Orfino FP, Dutta M and KE. Mitigation of Mechanical Membrane Degradation in Fuel Cells – Part 1: Gas Diffusion Layers with Low Surface Roughness. Journal of Power Sources (Accepted Manuscript) 2021.

[137] Ramani D, Khattra NS, Singh Y, Orfino FP, Dutta M and KE. Mitigation of Mechanical Membrane Degradation in Fuel Cells – Part 2: Bonded Membrane Electrode Assembly. Journal of Power Sources (Accepted Manuscript) 2021.

Appendix A.

Characterization of Membrane Degradation Growth in Fuel Cells Using X-ray Computed Tomography

JES Focus Issue on Proton Exchange Membrane Fuel Cell (PEMFC) Durability

Characterization of Membrane Degradation Growth in Fuel Cells Using X-ray Computed Tomography

Dilip Ramani,[1] Yadvinder Singh,[1,*] Francesco P. Orfino,[1] Monica Dutta,[2] and Erik Kjeang [1,**,z]

[1] Fuel Cell Research Laboratory (FCReL), School of Mechatronic Systems Engineering, Simon Fraser University, Surrey BC V3T 0A3, Canada
[2] Ballard Power Systems, Burnaby BC V5J 5J8, Canada

Perfluorosulfonic acid ionomer membranes are subjected to simultaneous chemical and mechanical degradation under fuel cell operation. Despite the importance of membrane durability, the understanding of its structural degradation and failure modes has been considerably restricted by conventional 2D imaging. In this work, non-invasive micro X-ray computed tomography (XCT) is adopted to visualize the 3D membrane decay at different life stages during combined chemical and mechanical degradation. A detailed survey exhibits damage density of 6 and 10 cracks per mm^2 observed at the near-final and final end of life stages respectively. Through-thickness membrane cracks with unbranched I-shaped cracks and Y- and X- shaped cracks with one and two branches respectively are observed. The observed damage development at each life stage is correlated to supplementary diagnostic data including hydrogen leak rate, open circuit voltage, and tensile strength. In particular, large X-shaped cracks formed due to embrittlement from underlying chemical degradation are deemed to have a critical impact on the eventual failure development by facilitating large hydrogen leaks. Overall, the comprehensive 3D perspective enabled by XCT imparts new knowledge pertaining to the degradation process, and could also be extended to other fuel cell failure modes and degradation mechanisms.

 [DOI: 10.1149/2.0251806jes]

Manuscript submitted December 21, 2017; revised manuscript received February 21, 2018. Published March 23, 2018. *This paper is part of the JES Focus Issue on Proton Exchange Membrane Fuel Cell (PEMFC) Durability.*

Polymer electrolyte membrane fuel cells (PEMFCs) are conceived by many as the prime contenders to replace internal combustion (IC) engines for automotive applications owing to their clean and efficient operation.[1] The use of fuel cells in vehicles however poses high demands on cost effectiveness and durability.[2,3] Durability of a fuel cell system is its capacity to resist permanent deterioration in performance under a range of operating conditions over time.[4] The United States Department of Energy lifetime targets for fuel cell systems vary from 8,000 hours for cars to 25,000 hours for buses and 40,000 hours for stationary application.[5] Although the lifetime targets for automotive applications are lower than for stationary applications, the highly dynamic nature of operating conditions such as startup/shutdown and load cycling creates an additional challenge.

The membrane electrode assembly (MEA) represents the core of a fuel cell and includes an ion-conducting polymeric membrane, two catalyst layers (anode and cathode), and two gas diffusion layers (GDLs).[6] In a typical PEMFC, the membrane is sandwiched between the two electrodes and transports protons while simultaneously preventing crossover of reactant gases and electrons. Therefore, the functional requirements for an effective membrane are high protonic conductivity, negligible reactant gas permeability and electronic conductivity, and high thermal, mechanical, and chemical stability.[7] The most commonly used membranes for PEMFCs are perfluorosulfonic acid (PFSA) ionomer membranes such as Nafion (DuPont) due to their electrical insulation property and chemical strength from the polytetrafluoroethylene (PTFE) backbone.[8] Nevertheless, membrane failure remains an important factor influencing the overall fuel cell durability and reliability.

PFSA ionomer membranes are known to undergo two main types of degradation during regular fuel cell operation, namely chemical and mechanical degradation. Chemical degradation is generated by the action of hydroxyl (•OH) and hydroperoxyl (•OOH) radical species initiated from hydrogen peroxide formed as a by-product of the oxygen reduction reaction. Factors which accelerate this mechanism are high temperature, low relative humidity, high cell potential, and high reactant gas pressures.[7–9] The evidence of this mechanism is observed as fluoride release from ionomer chain scission and bulk membrane thinning due to the associated material loss. Additionally, the constrained membrane in an assembled fuel cell encounters mechanical degradation with in-plane tension resulting from shrinkage under dehydrated conditions[10] and in-plane compression during swelling under wet conditions.[11] This fluctuating hygrothermal stress pattern leads to physical damage development in the form of fatigue, cracks,[12] creep,[13] and pinholes.[14,15] Furthermore, the membrane strength and stiffness are reduced with progressive humidity cycling.[16,17] Chemical and mechanical degradation mechanisms separately play key roles in aggravating membrane failure whereas the coupled presence of combined mechanisms significantly accelerates the overall rate of degradation.[18] In particular, the disintegrated ionomer structure resulting from advanced chemical degradation renders the membrane prone to rapid failure when subjected to subsequent mechanical stress.

Laboratory based testing of fuel cell components through their entire lifetime is time consuming and costly. To overcome this, accelerated stress testing (AST) is utilized to generate failure modes observed in field operation in a compressed time period by applying enhanced levels of stress.[19] This is done by adjusting operating conditions such as humidity, temperature, cell voltage, and current density to accelerate the degradation rate.[20] Standard ASTs for membrane degradation were established by the US Department of Energy (DOE). Open circuit voltage (OCV) hold and relative humidity cycling are used to exacerbate chemical and mechanical degradation, respectively.[21] However, automotive fuel cell use conditions involve combined chemical and mechanical stressors acting simultaneously due to dynamic load fluctuations. The combined effect of these mechanisms was thoroughly studied by our group by adopting a cyclic open circuit voltage (COCV) AST protocol[22] that applies periodic chemical and mechanical stresses in a cyclic pattern. The results showed that combined stressors aggravate the overall membrane degradation rate and lead to earlier failure than for separate application of chemical or mechanical stress.

*Electrochemical Society Student Member.
**Electrochemical Society Member.
zE-mail: ekjeang@sfu.ca

Post mortem failure analysis of MEA components is generally based on 2D imaging by scanning electron microscope (SEM). For instance, Kundu et al.[23] investigated the presence of catalyst layer cracks prior to operation using SEM. SEM was used to capture the growth of circular voids on the membrane surface during chemical degradation.[24] Membrane ruptures initiated by chemical and mechanical degradation were observed to have smooth and rough fracture surfaces, respectively.[19] An in-depth SEM survey demonstrated significant membrane thinning and the presence of circular damage features termed as "pinholes" in membranes subjected to combined mechanical and chemical degradation.[22] However, the sample preparation for SEM is destructive in nature which involves grinding and polishing. This invasive procedure could introduce critical artefacts, especially on the soft membrane. Furthermore, SEM is limited to 2D surface or cross-sectional views and requires vacuum conditions. As an alternative imaging technique, X-ray computed tomography (XCT) has gained considerable interest in various facets of fundamental fuel cell materials research. Several studies have used XCT for characterization of fuel cell components such as diffusion layers[25–30] and catalyst layers[31–33] as well as for liquid water visualization.[34–36] Furthermore, the technique has also been successfully used to resolve fuel cell membranes. Recently, Singh et al.[37] successfully adopted the XCT technique to develop a unique 3D failure analysis framework for fuel cell membranes. This 3D failure analysis approach was demonstrated for pure chemical, pure mechanical, and combined chemical and mechanical degradation[37,38] and unraveled important new findings which were thus far not attainable with conventional 2D imaging. These findings include the presence of multiple crack development mechanisms based on the interaction of chemical and mechanical stressors and the identification of electrode shorting sites arising from severe chemical degradation and associated membrane thinning. The 3D approach also enabled accurate quantification of damage feature dimensions and density.

The objective of the present work is to extend the 3D visualization approach previously demonstrated for membrane failure analysis to study the growth of membrane degradation over its practical lifetime in fuel cells. Partially degraded MEAs subjected to different stages of combined chemical and mechanical membrane degradation are analyzed for this purpose by application of micro-XCT. This non-destructive visualization strategy facilitates an accurate investigation of the critical stages of membrane degradation which ultimately lead to failure. Changes in structural features such as membrane thickness and damage morphologies associated with the growth of membrane degradation are carefully evaluated. Of particular interest are membrane cracks, which were recently discovered as the dominant membrane failure mode under combined chemical and mechanical degradation. The membrane damage development observed by XCT is correlated to a suite of supplementary diagnostic data comprising of open circuit voltage, hydrogen leak rate, and tensile mechanical properties measured at the same life stages. This enables comprehensive understanding of the structure-property-performance relationships associated with membrane degradation in fuel cells.

Experimental

Materials and test apparatus.—Anode and cathode gas diffusion electrodes (GDE) were fabricated by coating a fine micro porous layer of PTFE and carbon black on a non-woven carbon paper GDL substrate followed by a top coating of a catalyst layer consisting of carbon-supported platinum catalyst and perfluorosulfonic acid ionomer. Subsequently, MEAs were assembled using a hot-pressing technique. In this process, a non-reinforced perfluorosulfonic acid membrane of Nafion NRE211 type was sandwiched between the anode and cathode GDEs.[39] The edges of the fabricated MEAs were covered with adhesive films on each side to curtail unwanted localized electrochemical and mechanical deterioration in these regions during operation. The fabricated MEAs were then placed into a research-scale stack consisting of five 45 cm^2 cells separated by graphitic bipolar plates designed to achieve consistent one-dimensional conditions over the entire active area. The stack was uniformly compressed at 60 psig using a pressurized bladder type compression hardware. Gas flow rates were 2 slpm H_2 (fuel) and 4 slpm air (oxidant) per cell, and were set high to maintain a uniform operating environment throughout the length of the MEA. To maintain uniform reactant gas pressure and minimize pressure drops from inlet to outlet, flow field plates with parallel co-flow straight channels were utilized. Internal and external gas leak tests were performed by pressurizing dead end fluid sections and gauging any gas transfer across the compartments. An initial conditioning for 12 h was performed using pure hydrogen and air at anode and cathode respectively to initiate electrochemical activation by drawing a constant current density.[22]

Accelerated stress testing.—Accelerated stress testing (AST) is a well-established tool for reducing the time required for replicating the failure modes encountered during field operation.[40] In this work, a membrane specific AST, known as the cyclic open circuit voltage (COCV) AST protocol,[22] was used to accelerate combined chemical and mechanical degradation. Each AST cycle comprises of an initial OCV hold phase at high temperature and low relative humidity (RH) followed by a set of wet/dry cycles in N_2 environment. These cycles are repeated until membrane failure is reached based on a criterion of >10 sccm per cell of internal gas leak suggested by the US Department of Energy.[41] Further details concerning the COCV AST are provided elsewhere.[18,22] In order to characterize the membrane structural features and properties at different stages of degradation, MEAs were extracted from the stack after conditioning (denoted as beginning of life (BOL)) and after two, five, eight, eleven, and thirteen (end of life (EOL)) AST cycles. Separate samples were prepared from these extracted MEAs to be analyzed by XCT and tensile traction tests, respectively.

In situ diagnostics.—The membrane health at the end of each COCV AST cycle was examined by evaluating the hydrogen leak rate from the anode to the cathode by means of an in situ electrochemical leak detection test (ELDT). The test was performed by measuring the OCV before and after applying a small hydrogen overpressure 48 kPa in a pure hydrogen/air (anode/cathode) condition. The AST cycling was stopped when the ΔV value exceeded 40 mV per cell, which corresponds to the present membrane failure criterion of hydrogen gas crossover >0.16 $cm^3 s^{-1}$ from anode to cathode.[22] The OCV of each cell in the stack was also measured in conjunction with the ELDT data to further understand the impact of the hydrogen leaks on the cell performance at the various life stages.

X-ray computed tomography.—X-ray imaging was performed using a laboratory based micro XCT system (*ZEISS Xradia 520 Versa*, Carl Zeiss X-ray Microscopy). Two square-shaped 2 × 2 cm^2 MEA samples from each of the inlet, middle, and outlet regions at the various life stages from BOL to EOL were manually cut using a scalpel. It should be noted that the samples prepared for XCT visualization at different life stages came from different MEAs that had been subjected to various levels of degradation. Accordingly, this work does not represent same location tracking of a given MEA. Each MEA sample was fastened to a rigid polycarbonate plastic film using an adhesive 3 M scotch tape. The plastic backed sample was placed on the rotation stage with a clip type holder. The source and detector distances were set to 17 and 14 mm, respectively, measured from the holder position. The electron accelerating voltage and power used for the X-ray source during the tomographic scans were 80 kV and 7 W, respectively. This beam setting was used in conjunction with an air filter to acquire better contrast between the internal MEA components. The imaging parameters were tuned to obtain a pixel resolution of 0.67 μm in a 0.66 × 0.66 mm^2 field of view (FOV). The FOV for imaging was aligned with the center of the sample to avoid any deformation or artifacts at the edges from the manual slitting procedure. Each tomography scan required approximately 11 h of exposure time for 1,601 projections with 15 s per projection across a complete 360° rotation. The exposure time per projection was selected to accomplish the

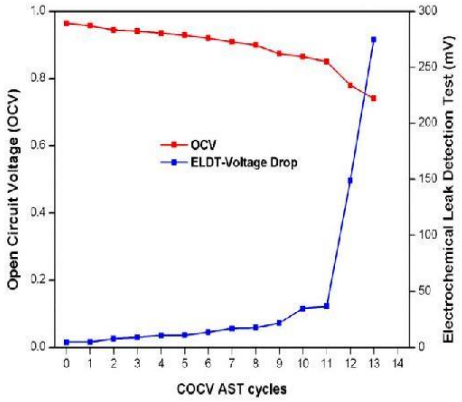

Figure 1. Open circuit cell voltage (OCV) and electrochemical leak detection test (ELDT) voltage differential as a function of the number of COCV AST cycles.

desired level of intensity (generally 5,000 counts) at the membrane region. Subsequently, the obtained 2D radiographs were reconstructed using ZEISS *XMReconstructor* software. The membrane structural features were visualized and segmented using Dragonfly Pro from Object Research Systems (ORS). This was achieved by partitioning the original gray scale values of the 2D images into catalyst layer, membrane and void phase using manual procedure. The data presented in the following sections represent the collective results of six tomographic scans (two each at inlet, middle, and outlet locations) for each degradation stage unless otherwise stated.

Tensile traction test.—The tensile mechanical properties of the membrane were characterized using an electromechanical tester (Instron 5569). The MEA samples extracted at the different life stages were initially equilibrated at room temperature over a period of 24 h after removal. The samples were then cut using a plotter-cutting procedure, where ribbon shaped MEA sub-samples of 5 mm width and 50 mm length were obtained. The anode and cathode GDLs were carefully peeled off from the specimen while the catalyst layers remained adhered to the membrane. This obtained catalyst coated membrane sub-sample was fitted in the tensile clamps of the tester with a primary grip separation length of 30 mm. The tensile traction tests were performed at 23°C and 38% RH at a fixed strain rate of 0.01 min^{-1}.

Results and Discussion

The cyclic OCV (COCV) accelerated stress test (AST) used in this work was designed to simulate and accelerate conjoint chemical and mechanical membrane degradation mechanisms known to occur during regular fuel cell stack operation. The results reported in this section collectively represent an examination of membrane damage observed at six different stages of membrane life throughout the same AST experiment, based on MEA samples extracted after stack conditioning (beginning of life (BOL)) and after two, five, eight, eleven, and thirteen (EOL) cycles. The end of life (EOL) MEA sample under study failed after thirteen COCV AST cycles by exceeding a given threshold hydrogen leak rate across the membrane.

Hydrogen leaks and voltage decay.—The overall membrane health at each life stage was monitored by estimating the hydrogen leaks via an electrochemical leak detection test (ELDT) and the open circuit voltage (OCV) of each cell. The obtained data are given in in Figure 1 as a function of the number of COCV AST cycles. At the initial stage and up to eleven AST cycles, the OCV decay rate was estimated to a moderate level of 8.7 mV per cycle. However, post eleven cycles until EOL the OCV decay rate increased several folds to 62 mV per cycle. The cumulative OCV decay at EOL is nearly 20% of its BOL value, which is very close to the OCV-based failure criterion prescribed by DOE for MEA Chemical Stability AST protocol. The 20% OCV reduction was seen to correlate reasonably well with the ELDT results which indicated a gradually increasing hydrogen leaks across the membrane due to the combined chemical and mechanical membrane degradation process. However, the exponential rise in the hydrogen leak rate exhibited between twelfth cycle and EOL is remarkable, thus signifying the event of membrane failure. Major hydrogen leaks were detected after thirteen AST cycles (EOL) in accordance with the MEA failure criterion of the COCV AST. From our previous experience with a larger format MEA test fixture, a significant gas leak across the membrane is known to cause an ELDT $\Delta V > 30$ mV, and may be attributed to convective hydrogen transfer across the newly developed physical defects in the membrane (e.g., through-thickness cracks or holes).[22] The increased gas crossover through the degraded membrane was responsible for the concurrent OCV decay due to mixed electrode potentials.[18]

Damage growth.—XCT visualization of MEAs at different stages of degradation provides an exclusive opportunity to characterize the damage growth trends in the structure/morphology of the MEA over time. This is achieved in the present work by acquiring 3D virtual images of different MEAs that have been degraded to different life stages under combined chemical and mechanical membrane degradation. The 3D reconstructed images lend themselves to be translated and/or rotated across the three coordinate axes (x, y, and z) to comprehensively study the sample of interest from various perspectives, as demonstrated in our previous work.[37] Here, Figure 2 shows the representative virtual planar view of segmented membrane at each life stage with supporting cross-sectional views of the MEAs at BOL and EOL.

Membrane cracks were the dominant damage feature observed in the planar images acquired during the cycling procedure. Through-thickness membrane cracks, which penetrate completely through the membrane and provide a direct convective path between the opposite electrodes (see inset for eleven cycles in Figure 2), are expected to be the dominant contributors to the overall hydrogen crossover leakage. No through-thickness membrane cracks were detected in the MEAs extracted post conditioning until the end of eight AST cycles. The first through-thickness membrane cracks were identified after eleven cycles and would have formed between the ninth and eleventh cycle. At EOL (thirteen cycles), a greater frequency of similar operational membrane cracks was observed. The extent or reach of these cracks in the through-plane direction can be detected from the cross-sectional views by moving the cross-sections between the two extremities of a crack; thus, a thorough examination of crack morphology can be conducted. The 3D datasets acquired by XCT also lend themselves to detailed numerical analysis of the membrane and MEA structure at each life stage.

The initial analysis performed pertains to damage features confined to each layer in the MEA. This approach helps to study the overall rise in damage features in each layer throughout the degradation process. The number of damage features is represented in terms of damage density, which is a key failure analysis metric defined as the number of damage features (e.g., cracks) per unit area of the MEA.[37] In the present study, damage features observed are confined to only membrane cracks. Figure 3 shows a statistical plot of the measured crack density within the membrane and catalyst layers (CLs) at each life stage. The ionomer membrane is elastic in nature and expected to be crack-free upon manufacturing. Here, the membrane analyzed at BOL post conditioning was indeed completely crack free. However, sizeable membrane cracks developed during the later stages of degradation. The overall membrane damage density of through-thickness membrane cracks after eleven and thirteen cycles was 6.1 and 10.3 cracks/mm^2, respectively. For eleven cycles and EOL only, a more traditional non-dimensional crack density parameter was calculated to simultaneously characterize both the number and size of membrane

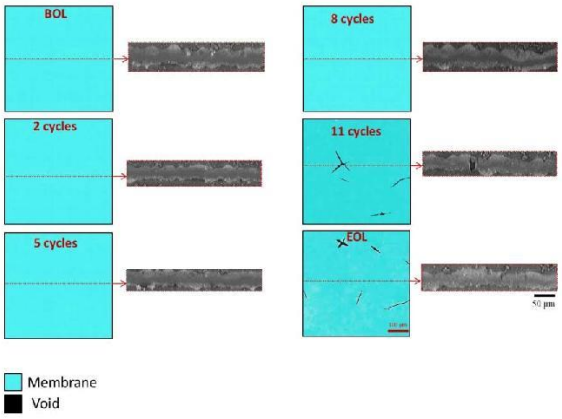

Figure 2. Representative virtual planar view of the segmented membrane at each life stage, illustrating the growth of degradation with COCV AST cycling. Virtual cross-sectional views (in gray scale) of the MEAs, taken along the annotated dashed lines in the planar views, are also shown in the inset. The 2D planar and cross-sectional views were obtained from the 3D reconstructed images of each MEA analyzed by XCT. The legend applies to the segmented planar membrane views only.

damage due to cracking with a single parameter with respect to AST cycling. This crack density parameter Γ, defined in a previous work by Lu et al.,[42] can be determined from the following relationship:

$$\Gamma = \frac{\sum_{i=1}^{N} li^2}{A} \quad [1]$$

where A is the planar survey area; l_i is the length of the i^{th} through-thickness membrane crack; and N is the total number of through-thickness membrane cracks within the survey area. This non-dimensional crack density parameter was found to increase by 70% from a value of 2.7 at eleven cycles to 4.8 at thirteen cycles (or EOL), which closely resembles the membrane damage density based on the number of cracks only. The membrane crack development can be attributed to the combined chemical and mechanical stressors active during the COCV AST cycling, which have previously been shown to induce crack dominated membrane failure at the EOL state.[37] In contrast to the membrane, the CLs are prone to crack development during fabrication, handling, and installation,[23] and were therefore seen to have pre-operational cracks at both the anode and cathode (Figure 3). These CL cracks can introduce local stress points with cycling where the cracks may propagate further. However, in the present study the CL crack density did not increase considerably until after eleven cycles, when a rise in the number of CL cracks was experienced in conjunction with the formation of membrane cracks. At EOL, the CL crack density increased approximately four times as compared to BOL. This increasing trend of CL cracks correlates to the membrane crack development trend with substantial new CL cracks formed during the late stages of membrane degradation possibly due to the cyclic swelling and contraction of the attached membrane. Our group previously reported interaction between membrane and catalyst layers (CLs) cracks at the point of membrane failure;[37,38] however, the direction and developmental stages of such cracks interaction effects are not yet known.

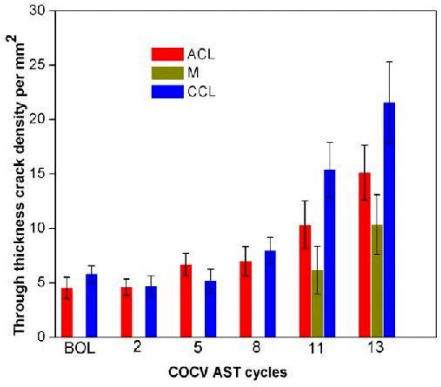

Figure 3. Change in individual through-thickness crack densities of all MEA layers, i.e. anode catalyst layer (ACL), membrane (M), and cathode catalyst layer (CCL), from beginning-of-life (BOL) to thirteen COCV AST cycles or end-of-life (EOL).

Membrane - catalyst layer interaction.—The non-invasive XCT based analysis approach provides an exclusive opportunity to identify the 3D interaction between membrane and catalyst layers at various life stages in the context of damage development. Furthermore, the 3D visualization capability enables a thorough examination of the structural connectivity of cracks between the MEA layers and can therefore yield more reliable results than any previous 2D studies. Based on their reach in the through-plane direction within the MEA, the membrane cracks can be categorized into: (a) Exclusive cracks confined within the membrane only (M); and (b) Non-exclusive cracks that extend into and penetrate through the adjoining CLs (A + M; M + C; A + M + C where A and C represents anode and cathode catalyst layers respectively).[37] Based on this assumption, 36% and 50% of the through-thickness membrane cracks were found to be exclusively confined to membrane at the end of eleven AST cycles and EOL, respectively. This confirms significant formation of membrane cracks that don't seem to develop as a result mechanical stress concentration effects that are typically believed to associated with adjacent CL cracks, but rather due to some underlying chemical stressors that reduce the mechanical strength of the membrane at these later stages of degradation. These results are consistent with our previous work,[37] where roughly 50% of the membrane cracks identified at EOL were confined within the membrane. The remaining Non-exclusive cracks are further quantified in terms of their interaction with anode and cathode CLs, respectively. *Interaction ratio* of Non-exclusive cracks is defined as the number of Non-exclusive membrane cracks associated with a given CL (e.g. A + M for anode and M + C for cathode) to the total number of cracks (Exclusive + Non-exclusive) in that CL

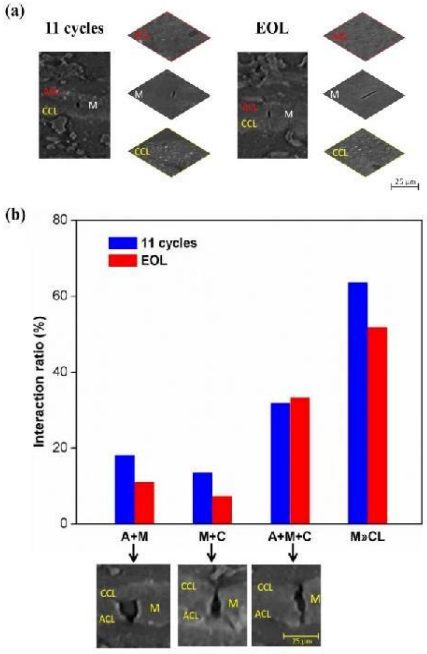

Figure 4. (a) Exclusive membrane cracks illustrated by cross-sectional and sliced images of the cathode catalyst layer (CCL), membrane (M), and anode catalyst layer (ACL) components of the MEA. (b) Obtained ratio of membrane crack interaction with adjoining catalyst layers at eleven AST cycles and end-of-life (EOL) (M: Membrane; A + M: Anode catalyst layer + Membrane; M + C: Membrane + Cathode catalyst layer; A + M + C: Anode catalyst layer + Membrane + Cathode catalyst layer). The crack interactions covered in (b) are further illustrated with cross-sectional images shown in the insets.

at any life stage. However, for the Non-exclusive cracks that span the entire MEA thickness (A + M + C), the individual interaction with CL cannot be clearly established. The calculated interaction ratio between membrane cracks and CL cracks after eleven AST cycles and at EOL is shown in Figure 4. The anode and cathode interactions occur at similar frequency as seen in the A + M and M + C data in Figure 4, respectively. However, most of the Non-exclusive cracks penetrate both of the CLs (roughly 30%; A + M + C in Figure 4) at each of the examined life stages. Such cracks are deemed as most critical to the overall failure as they open a convective passage for major gas leaks across the MEA. One possible scenario that may induce these features is that a CL crack (in either anode or cathode) may gradually propagate into the membrane with AST cycling, and may further extend into the opposite CL, thereby creating a through-thickness MEA crack. Previously reported works have shown a strong propensity of membrane crack development at the site of CL cracks, which is likely a result of mechanical stress concentration at such locations due to localized loss of mechanical reinforcement from the CL.[16,38] Given the significant presence of exclusive membrane cracks, however, there is also a likelihood that a membrane crack may initiate first and then propagate outwards forming these A + M + C (and even A + M and M + C) features. These possibilities are still deemed hypothetical in the current work, since we are analyzing different MEAs at each life stage.

Membrane crack morphologies.—Adoption of 3D XCT for imaging various life stages of MEA samples subjected to combined chemical and mechanical degradation enables to track the underlying degradation mechanism by analyzing the shapes of the membrane damage features. Three distinct planar crack shapes were observed to have developed for through-thickness membrane cracks during the AST cycling. Membrane cracks which propagated as a single entity formed I-shaped structures, while the branched cracks consisting of three and four branches formed Y and X-shaped morphologies, respectively. Singh et al.[37] previously reported the presence of I- and Y-shaped cracks at the EOL stage, using a similar methodology. Interestingly, the present study uncovered a new X-shaped crack morphology which could be attributed to a more advanced state of local membrane degradation in the present work under the auspices of combined chemical and mechanical degradation. Previous post-mortem studies within our group[37,38] have shown that the branching effect in membrane cracks during their planar propagation is absent under pure mechanical degradation, and an underlying chemical degradation is required to induce crack branching. In the present analysis, the intermediate stages are studied to understand the branching effect with increasing degradation. A detailed analysis of the frequency of each crack shape at near-final and final life stages is shown in Figure 5. All three crack shapes were present at each of the two life stages. The most common crack shape at both life stages was the I-shape, although the sharp rise in overall crack density observed between eleven cycles and EOL (Figure 3) is attributed to increasing frequencies of both I-shaped and X-shaped cracks. All the Y-shaped cracks at the end of eleven cycles were observed to be Exclusive membrane cracks. However, at EOL the Y-shaped cracks were a mix of Exclusive and Non-exclusive cracks which shows the effect of mechanical stress concentration at later stages of the cycling. In addition, it is worth noting that all X-shaped cracks at both life stages were Non-exclusive (mainly A + M + C) extending through the entire thickness of the MEA. The overall rise in X-shaped cracks could potentially be due to crack collision. For example, new X-cracks could have propagated from the interaction of existing Y-cracks with the single entity I-shaped cracks or from interaction of multiple I-cracks. Another possible mechanism is that a fourth branch may have formed at the internal junction of a Y-crack. The fundamental origin of both X and Y cracks is likely attributed to increasing membrane embrittlement during the COCV AST cycling.[18,22] In general, crack branching is the most important characteristic of dynamic brittle fracture.[43] This change in material property causes greater stress intensity around the existing crack tips.[44] The stress accumulation against the material directly in front of the crack tip moves against the advancing crack. This diverts the strain energy away from the crack symmetry line and into the

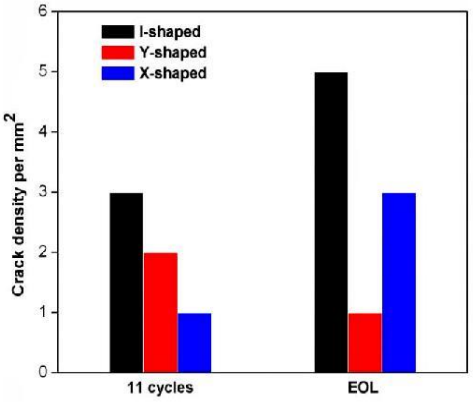

Figure 5. Frequency of the three different membrane crack morphologies identified at eleven AST cycles and EOL.

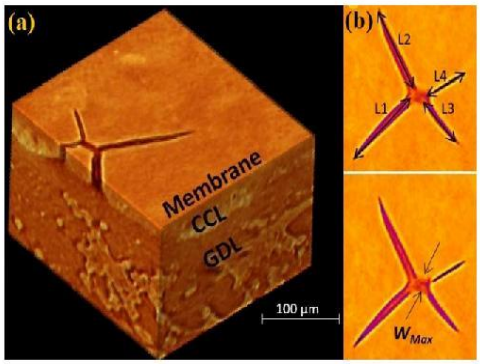

Figure 6. Reconstructed false color tomogram of an EOL MEA showing virtual (a) 3D and (b) 2D planar views of an X-shaped membrane crack interacting with the adjacent cathode catalyst layer (CCL). The cathode gas diffusion layer (GDL) is also shown in (a) for reference. The membrane crack length and maximum width measurement procedures using the planar views are illustrated in (b).

crack surfaces creating damage propagation away from the line. The damage movement, seen as roughness on the crack surface, modifies the strain energy around the crack tip. This phenomenon leads to preferential crack growth directions that branch from the original crack line. However, analyzing the evolution of individual crack shapes during AST cycling is beyond the scope of the present study.

A detailed approach adopted for dimensional measurements of I- and Y-shaped membrane crack morphologies was reported in our previous work.[37] Here, this approach was extended to X-cracks. A typical X-shaped crack comprises of four branches connected to a central junction or cavity. Figure 6a shows the 3D virtual view of such a membrane crack interacting with an adjacent catalyst layer crack. The cumulative crack length of an X-shaped morphology was determined by addition of the individual in-plane branch lengths, i.e., $L_1 + L_2 + L_3 + L_4$ (Figure 6b). This length measurement approach is consistent to that of I- and Y-shaped cracks; however, the maximum width measurement of X-cracks was performed by measuring the maximum diameter of the "central cavity" rather than the width of an individual branch. The planar 2D view which displayed the greatest crack extension (both length and width) within the plane of the membrane was selected in Figure 6 to illustrate this strategy. The cumulative mean branch length and average maximum width of different membrane morphologies were computed at eleven AST cycles and EOL (Figure 7). The average lengths of I- and Y-shaped cracks at eleven cycles was around 50–60 μm while the average maximum width was 6–10 μm. At same stage, the X-shaped morphology propagated as long slender cracks (≈200 μm) and almost similar width as other shapes. With increased cycling (EOL), there was moderate rise observed in branch lengths for all morphologies. However, a drastic rise in average maximum width of X-shaped cracks at EOL was observed. As we know, all X-shaped cracks were Non-exclusive (A + M + C) in nature, which makes them the most dominant morphology in membrane failure. This is owing to the large central width (craters), which facilitate major gas leaks without obstruction across the membrane leading to rapid MEA failure. The 6X times greater width at EOL (primarily due to X-shaped) proves a critical pointer to majority of leaks and OCV drop measured at EOL (Figure 1). The present approach has thus established an approach to accurately correlate the global performance trends with micro scale damage features.

In a previously reported work on combined chemical and mechanical membrane degradation, Lim et al.[22] observed a pinhole density of five counts per 3 cm^2 area, with diameter of around 100 μm using SEM post-mortem study. Pinholes are known as key physical defects which facilitate greater hydrogen leaks across the membrane. As a

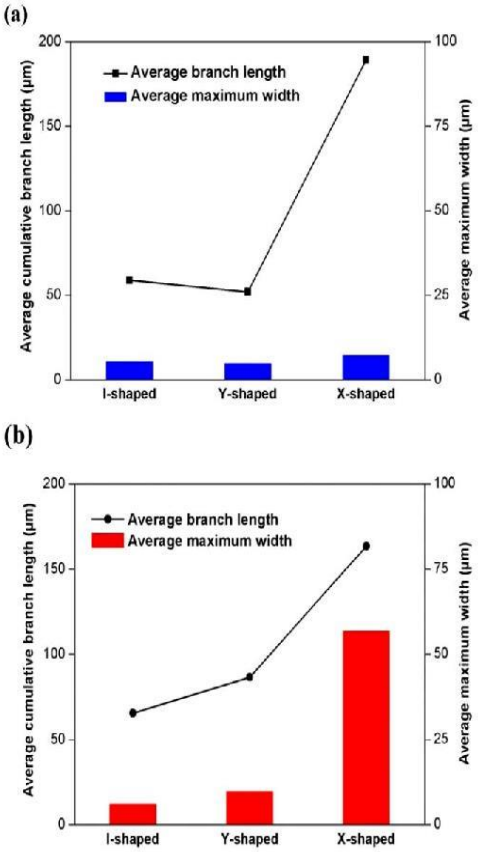

Figure 7. Measured mean cumulative membrane crack length and average maximum width of I-, Y-, and X-shaped cracks identified at (a) eleven AST cycles and (b) EOL.

comparison, in terms of "central cavity" X-cracks, ≈3 cracks/mm^2 were observed at EOL in the present work. This central cavity could very well be interpreted as a "pinhole" when observed using 2D SEM methodology. The 3D analysis facilitated by XCT has enabled to identify these peculiar features, which is an important, novel contribution of this work.

Membrane thinning.—Membrane thinning was prevalent in the COCV AST degraded MEA samples and is considered as an evidence of global chemical degradation caused by radical attack. Similar to our previous work, the average membrane thickness across six virtual 2D cross-sectional views (as shown in the insets of Figure 2) was numerically computed using standard image processing software at each life stage. Significant, progressive membrane thinning was observed on the degraded samples as a function of the number of AST cycles, as shown in Figure 8a. The original membrane thickness was retained during initial conditioning and slight thinning of around 13% of the BOL thickness occurred until the end of five AST cycles. However, the thinning rate accelerated post five cycles and 40% of membrane thickness reduction was observed after eight cycles. At EOL, 59% thinning was observed. Singh et al.[37] observed 48% membrane thinning after ten COCV AST cycles, which resulted in an earlier failure than in the present work. The more advanced thinning in the present case is log-

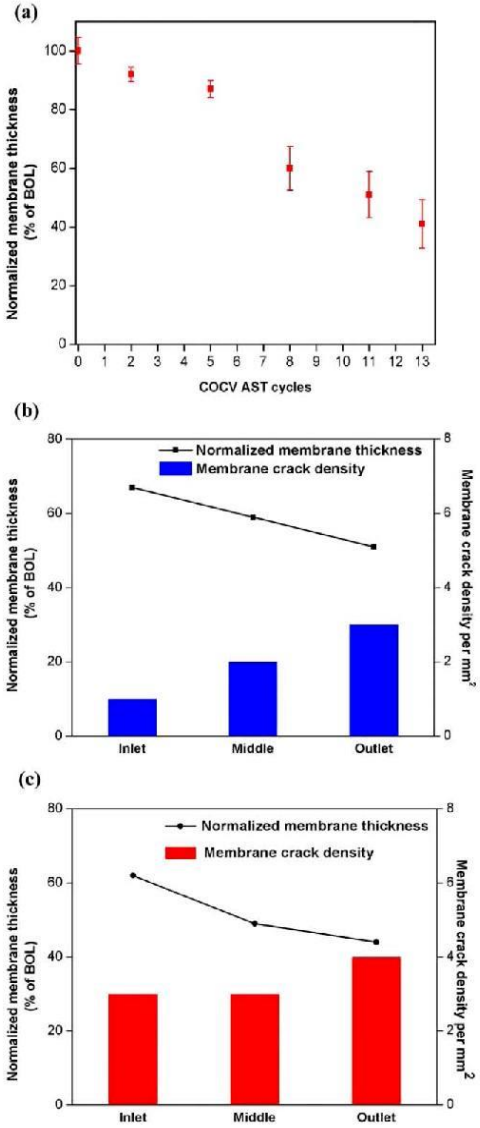

Figure 8. (a) Normalized membrane thickness as a function of COCV AST cycles; and distribution of membrane thickness and number of through-thickness membrane crack density per mm^2 across the inlet, middle, and outlet regions of the MEAs extracted after (b) eleven cycles and (c) EOL.

ical considering the additional cycles experienced at EOL (13). Lim et al.[22] reported 52% thinning (at EOL reached after thirteen cycles; measured by SEM) occurring at a linear rate of 4% per cycle for a similar COCV AST experiment. The difference could be due to the smaller domain used for XCT visualization whereas SEM evaluations represent the average thickness mapped across the entire active area. The membrane thinning observed occurred non-uniformly across the MEA with outlet regions experiencing ~20% higher average thinning than inlet regions at both eleven cycles and EOL (Figure 6b). This trend is consistent with the results reported by Macauley et al.,[19] for a milder combined chemical and mechanical degradation. Figure 6b also illustrates the distribution of the through-thickness membrane cracks identified across the MEA. The measured crack density at the inlet, middle, and outlet locations correlates well with the severity of membrane thinning at both life stages, which suggests that membrane thinning, i.e., global chemical degradation, is an important underlying factor for the observed crack development. This can be attributed to reduced mechanical strength associated with elevated chemical degradation in these locations.

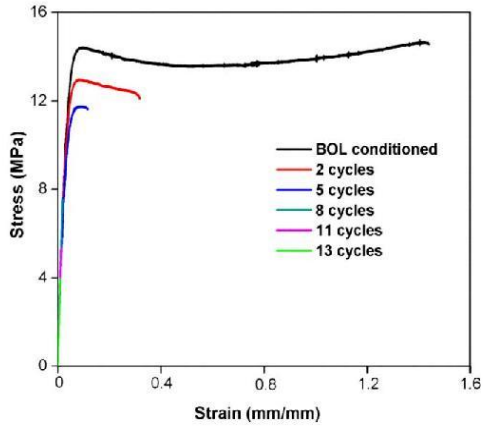

Figure 9. Stress-strain curves measured at 23°C and 38% RH from membrane samples extracted at/after BOL, two, five, eight, eleven, and thirteen COCV AST cycles.

Tensile properties.—The mechanical properties of the membranes were measured at each of the life stages during combined chemical and mechanical degradation by performing tensile traction tests at 23°C and 38% RH. The tests were done on membranes with attached catalyst layers, since it was not possible to separate these layers from the membrane after fuel cell operation; however, the mechanical properties of the specimen are still expected to be dominated by the membrane.[45] The obtained stress-strain curves are shown in Figure 9, wherein the stress was calculated by normalizing the applied force against the actual membrane thickness obtained separately from the cross-sectional images at each life stage using XCT image analysis. This is important in the present study where the membrane thickness varies with degradation, as shown earlier. Moreover, the membrane was assumed to be the main load bearing part of the specimen (neglecting the load sharing of the catalyst layers).

The conditioned BOL membrane exhibited ductile behavior with strain hardening, as expected. Rapid reduction in elongation was observed due to degradation throughout the various life stages. As noted in the previous sections, no membrane cracks were observed until after eight AST cycles. The initial decay in mechanical strength (primarily ductility) is therefore attributed to ionomer molecular degradation and chain disentanglement caused by the chemical stressors. After merely five AST cycles, the specimen fractured immediately after the yield point. With continued membrane degradation, the fracture stress decreased below the yield point where the material remained in the viscoelastic region. The fracture toughness, given by the area under the stress-strain curve representing the total amount of energy required for fracture, dropped rapidly during the initial five AST cycles. Membrane chain scission and reduction in molecular weight due

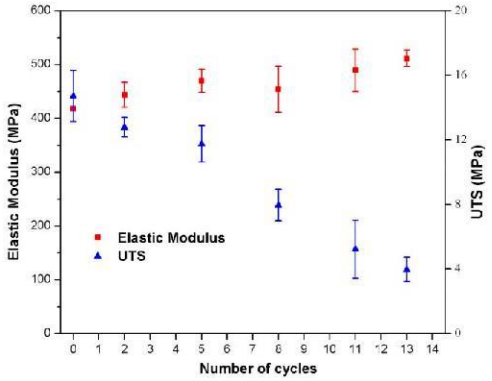

Figure 10. Degradation induced changes in elastic modulus and ultimate tensile stress (UTS) as a function of COCV AST cycles.

to chemical degradation are expected to weaken the macromolecular entanglements thereby causing ductile to brittle transition, as observed in the curves. During the second half of the experiment (from five to thirteen cycles), the fracture energy was negligible due to specimen failure before reaching the yield point.

Fundamentally, the elastic modulus defines the resistance of the material against elastic deformation. This is determined from the maximum slope of the stress-strain curves in the initial viscoelastic region. The elastic modulus was observed to increase slightly from BOL to EOL (Figure 10). This mild rise in elastic modulus during the cycling procedure indicates the stiffening of ionomer material supposedly caused by chemical degradation of the ionomer chains. The trend is logical with the transition of material behavior in the viscoelastic region i.e. ductile to brittle behavior. This shift in fundamental material behavior is seen to correlate well with the membrane thinning which is another indicator of bulk chemical degradation as observed in Figure 8a.

The maximum stress from each stress-strain curve was recorded as the ultimate tensile stress (UTS) and depicted in Figure 10 as a function of AST cycles. The UTS was found to decrease in a linear pattern from BOL to EOL, where the membrane had lost around 70% of its initial stress tolerance under room conditions. Given the similarity to the linear trends observed for thinning and modulus, the decay in UTS was also attributed to global chemical degradation which leads to reductions in polymer molecular weight and main chain length in agreement with previous literature.[22] Moreover, the overall impact of the molecular changes is likely exacerbated by the application of mechanical stress during the wet/dry cycles, acting to disentangle the ionomer bundles and split the ionic clusters. Notably, the small UTS resulting in tensile failure of heavily degraded membranes would likely be equivalent to the stress generated in situ during wet/dry cycling, where actual failures were evident by means of mechanically driven cracks. The significant drop in UTS from eight to eleven AST cycles is therefore likely the key underlying factor for crack formation during this period, as evidenced by XCT. Earlier, our group[18,22] has shown that gradual embrittlement and reduction in the mechanical strength of the membrane accompanies the combined chemical and mechanical degradation during COCV AST cycling. This change in the basic character of the material drives the differences in crack development process at various stages of the combined cycling process. The nature of degradation mechanism could be a key indicator determining the crack shape at different life stages. Once formed, these cracks would not experience much remaining resistance in the material to crack propagation and would therefore grow rapidly toward membrane failure, as detected after thirteen AST cycles.

Conclusions

Traditional 2D imaging techniques, such as SEM, are limited to surface views and cross-sectional snapshots of the MEA structure. The non-destructive X-ray computed tomography (XCT) comes as a breakthrough approach for conducting a comprehensive study to understand the intermediate degradation stages of fuel cell membranes. The present work discovered new fundamental insight regarding the growth of combined chemical and mechanical membrane degradation in fuel cells by application of a 3D perspective using laboratory based XCT. Global in-situ diagnostic results showed moderate rise in crossover gas leakage and OCV decay rate until 85% life stage while drastic rise was observed close to the end of life (EOL). This correlated well with the XCT results which showed that major membrane crack development initiated during the later stages of the cycling procedure i.e. between 70–85% life. Rise in Exclusive Membrane cracks without any structural connectivity with adjoining CL cracks shows the presence of an independent crack development mechanism active within the membrane. In addition to the existing two membrane crack modes (I- and Y-shaped) reported in literature, a third distinct X-shaped crack morphology was observed to have developed. These cracks could have propagated from the interaction of existing Y-cracks with the single entity I-shaped cracks or from interaction of multiple I-cracks. It is also possible that the fourth branch may have formed at the internal junction of a Y-crack, for instance during crack propagation into the adjoining CLs. Consistent rise in membrane crack width of branched entities could lead to overall membrane failure by facilitating high crossover across the damaged membrane. Non-uniform membrane thinning across the MEA was observed with gas inlet regions at both 85% life and EOL experiencing higher average thinning than outlet regions. Membrane tensile test results exhibited mild rise in elastic modulus and significant decay in tensile strength, which proves the stiffening behavior and increased membrane brittleness with degradation. This rise in brittleness can be attributed to underlying chemical degradation thereby reducing membrane resistance to mechanical degradation, i.e. the membrane resistance to crack growth.

The presently adopted XCT methodology is shown to be highly effective to identify and measure MEA damage features during fuel cell degradation, in this case the rise of membrane cracks at different life stages. Given the good compatibility of XCT with full MEAs, the present methodology could be further extended to other degradation mechanisms and alternate MEA designs. Furthermore, the new understanding developed around membrane failure mechanisms could prove useful in devising effective mitigation strategies, leading to enhanced fuel cell durability.

Acknowledgments

Funding for this research was provided by the Natural Sciences and Engineering Research Council of Canada, Canada Foundation for Innovation, British Columbia Knowledge Development Fund, and Ballard Power Systems through an Automotive Partnership Canada grant. This research was undertaken, in part, thanks to funding from the Canada Research Chairs program. The authors thank Chan Lim, Lida Ghassemzadeh, Erin Rogers, Mike Lauritzen, and Marina Najm for technical support.

ORCID

Erik Kjeang https://orcid.org/0000-0002-1373-5212

References

1. J. Larminie and A. Dicks, *Fuel Cell Systems Explained*, second ed., John Wiley & Sons Ltd. UK (2003).
2. M. F. Mathias, R. Makharia, H. A. Gasteiger, J. J. Conley, T. J. Fuller, C. J. Gittleman, S. S. Kocha, D. P. Miller, C. K. Mittelsteadt, T. Xie, S. G. Yan, and P. T. Yu, *Electrochem. Soc. Interface*, **14**, 24 (2005).

3. M. M. Mench, *Fuel Cell Engines*, 1st ed., p. 9, John Wiley & Sons, Inc., Hoboken, NJ, USA (2008).
4. J. Wu, X. Z. Yuan, J. J. Martin, H. Wang, J. Zhang, J. Shen, S. Wu, and W. Merida, *J. Power Sources*, **184**, 104 (2008).
5. U.S. Department of Energy, *http://www1.eere.energy.gov/hydrogenandfuelcells/pdfs/component_durability_may_2010.pdf* (2010).
6. N. Yousfi-Steiner, P. Mocoteguy, D. Candusso, and D. Hissel, *J. Power Sources*, **194**, 130 (2009).
7. J. Dunwoody and D. C. Leddy, *Electrochem. Soc Interface*, **14**, 21 (2005).
8. F. D. Coms, *ECS Trans*, **16**, 235 (2008).
9. J. Healy, C. Hayden, T. Xie, K. Olson, R. Waldo, M. Brundage, H. Gasteiger, and J. Abbott, *Fuel Cells*, **5**, 302 (2005).
10. F. N. Büchi and S. Srinivasan, *J. Electrochem. Soc.*, **144**, 2767 (1997).
11. S. D. Knights, K. M. Colbow, J. St-Pierre, and D. P. Wilkinson, *J. Power Sources*, **127**, 127 (2004).
12. Y. P. Patil, W. L. Jarrett, and K. A. Mauritz, *J. Memb. Sci.*, **356**, 7 (2010).
13. A. Sadeghi Alavijeh, R. M. H. Khorasany, A. Habisch, G. G. Wang, and E. Kjeang, *J. Power Sources*, **285**, 16 (2015).
14. R. M. H. Khorasany, M.-A. Goulet, A. S. Alavijeh, E. Kjeang, G. G. Wang, and R. K. N. D. Rajapakse, *J. Power Sources*, **252**, 176 (2014).
15. S. Zhang, X. Z. Yuan, J. Ng, C. Hin, H. Wang, J. Wu, K. A. Friedrich, and M. Schulze, *J. Power Sources*, **195**, 1142 (2010).
16. A. S. Alavijeh, R. M. H. Khorasany, Z. Nunn, A. Habisch, M. Lauritzen, E. Rogers, G. G. Wang, and E. Kjeang, *J. Electrochem. Soc.*, **162**, F1461 (2015).
17. M. A. Goulet, S. Arbour, M. Lauritzen, and E. Kjeang, *J. Power Sources*, **274**, 94 (2015).
18. A. Sadeghi Alavijeh, M. A. Goulet, R. M. H. Khorasany, J. Ghataurah, C. Lim, M. Lauritzen, E. Kjeang, G. G. Wang, and R. K. N. D. Rajapakse, *Fuel Cells*, **15**, 204 (2015).
19. N. Macauley, A. S. Alavijeh, M. Watson, J. Kolodziej, M. Lauritzen, S. Knights, G. Wang, and E. Kjeang, *J. Electrochem. Soc.*, **162**, F98 (2014).
20. S. J. Bae, S. J. Kim, J. I. Park, J.-H. Lee, H. Cho, and J.-Y. Park, *Int. J. Hydrogen Energy*, **35**, 9166 (2010).
21. M. P. Rodgers, L. J. Bonville, H. R. Kunz, D. K. Slattery, and J. M. Fenton, *Chem. Rev.*, **112**, 6075 (2012).
22. C. Lim, L. Ghassemzadeh, F. Van Hove, M. Lauritzen, J. Kolodziej, G. G. Wang, S. Holdcroft, and E. Kjeang, *J. Power Sources*, **257**, 102 (2014).
23. S. Kundu, M. W. Fowler, L. C. Simon, and S. Grot, *J. Power Sources*, **157**, 650 (2006).
24. H. Tang, S. Peikang, S. P. Jiang, F. Wang, and M. Pan, *J. Power Sources*, **170**, 85 (2007).
25. J. P. James, H.-W. Choi, and J. G. Pharoah, *Int. J. Hydrogen Energy*, **37**, 18216 (2012).
26. S. Odaya, R. K. Phillips, Y. Sharma, J. Bellerive, A. B. Phillion, and M. Hoorfar, *Electrochim. Acta*, **152**, 464 (2015).
27. C. Tötzke, G. Gaiselmann, M. Osenberg, J. Bohner, T. Arlt, H. Markötter, A. Hilger, F. Wieder, A. Kupsch, B. R. Müller, M. P. Hentschel, J. Banhart, V. Schmidt, W. Lehnert, and I. Manke, *J. Power Sources*, **253**, 123 (2014).
28. N. Khajeh-Hosseini-Dalasm, T. Sasabe, T. Tokumasu, and U. Pasaogullari, *J. Power Sources*, **266**, 213 (2014).
29. I. V. Zenyuk, D. Y. Parkinson, L. G. Connolly, and A. Z. Weber, *J. Power Sources*, **328**, 364 (2016).
30. M. Andisheh-Tadbir, F. P. Orfino, and E. Kjeang, *J. Power Sources*, **310**, 61 (2016).
31. A. Pokhrel, M. El Hannach, F. P. Orfino, M. Dutta, and E. Kjeang, *J. Power Sources*, **329**, 330 (2016).
32. S. Litster, W. K. Epting, E. A. Wargo, S. R. Kalidindi, and E. C. Kumbur, *Fuel Cells*, **13**, 93 (2013).
33. R. T. White, A. Wu, M. Najm, F. P. Orfino, M. Dutta, and E. Kjeang, *J. Power Sources*, **350**, 94 (2017).
34. H. Markötter, R. Alink, J. Haußmann, K. Dittmann, T. Arlt, F. Wieder, C. Tötzke, M. Klages, C. Reiter, H. Riesemeier, J. Scholta, D. Gerteisen, J. Banhart, and I. Manke, *Int. J. Hydrogen Energy*, **37**, 7757 (2012).
35. P. Krüger, H. Markötter, J. Haußmann, M. Klages, T. Arlt, J. Banhart, C. Hartnig, I. Manke, and J. Scholta, *J. Power Sources*, **196**, 5250 (2011).
36. I. V. Zenyuk, D. Y. Parkinson, G. Hwang, and A. Z. Weber, *Electrochem. commun.*, **53**, 24 (2015).
37. Y. Singh, F. P. Orfino, M. Dutta, and E. Kjeang, *J. Power Sources*, **345**, 1 (2017).
38. Y. Singh, F. P. Orfino, M. Dutta, and E. Kjeang, *J. Electrochem. Soc.*, **164**, 1331 (2017).
39. A. P. Young, J. Stumper, S. Knights, and E. Gyenge, *J. Electrochem. Soc.*, **157**, B425 (2010).
40. B. Sompalli, B. A. Litteer, W. Gu, and H. A. Gasteiger, *J. Electrochem. Soc.*, **154**, B1349 (2007).
41. U. S. Department of Energy, https://www1.eere.energy.gov/hydrogenandfuelcells/pdfs/component_durability_may_2010.pdf.
42. Z. W. Lu, M. H. Santare, A. M. Karlsson, F. C. Busby, and P. Walsh, *J. Power Sources*, **245**, 543 (2014).
43. M. Ramulu and A. S. Kobayashi, *Int. J. Fract.*, **27**, 187 (1985).
44. F. Bobaru and G. Zhang, *Int. J. Fract.*, 1 (2016).
45. M. A. Goulet, R. M. H. Khorasany, C. De Torres, M. Lauritzen, E. Kjeang, G. G. Wang, and N. Rajapakse, *J. Power Sources*, **234**, 38 (2013).

Appendix B.

Four-dimensional *In situ* Visualization of Chemical Degradation in Fuel Cell Membranes

Electrochimica Acta 380 (2021) 138194

Contents lists available at ScienceDirect

Electrochimica Acta

journal homepage: www.elsevier.com/locate/electacta

Four-dimensional *in situ* imaging of chemical membrane degradation in fuel cells

D. Ramani[a,1], Y. Singh[a,1], R.T. White[a], T. Haddow[a], M. Wegener[a], F.P. Orfino[a], L. Ghassemzadeh[b], M. Dutta[b], E. Kjeang[a,*]

[a] Fuel Cell Research Laboratory (FCReL), Simon Fraser University, 250-13450 102 Avenue, Surrey, BC V3T0A3, Canada
[b] Ballard Power Systems, 9000 Glenlyon Parkway, Burnaby, BC V5J5J8, Canada

ARTICLE INFO

Article history:
Received 23 December 2020
Revised 18 March 2021
Accepted 19 March 2021
Available online 25 March 2021

Keywords:
Fuel cell
X-ray imaging
Mechanically and chemically reinforced membranes
Electrode shorting
Chemical degradation

ABSTRACT

Chemical membrane degradation is considered a key impeding issue for durability of polymer electrolyte fuel cells. Chemical additives have been developed to mitigate this phenomenon by preventing radical attack and associated membrane thinning. In this work, a 4D *in situ* X-ray visualization approach is adopted to examine the pure chemical degradation effects of non-reinforced, mechanically reinforced, and mechanically and chemically reinforced fuel cell membranes. The 4D approach is achieved by non-invasive, identical location 3D (x, y, z) imaging of the fuel cell at different lifetime stages (t). Observations show that local membrane thinning culminating in electrode-shorting under land regions is the key failure mode for non-reinforced and mechanically reinforced membranes without chemical additives. The ePTFE layer within the mechanically reinforced membrane does not prevent electrode shorts and exhibits divot formation. Preferential shorts under the land regions show that mechanical stresses due to clamping pressure can accelerate electrode shorting at advanced stages of chemical degradation. In contrast, the mechanically and chemically reinforced membrane sustains significantly longer test duration without failure and significant membrane thinning, highlighting the radical scavenging effect. No membrane pinhole or crack development is observed in any of the three membranes, suggesting that such failures require additional mechanical degradation.

1. Introduction

Perfluorosulfonic acid (PFSA) ionomer membranes are a key component used in hydrogen-based polymer electrolyte fuel cells. PFSA ionomer membranes possess several critical properties, including high ionic conductivity, electrical insulation, and reactant permeation resistance, which enable efficient fuel cell operation. However, ionomer membranes are susceptible to different forms of degradation [1,2] under regular fuel cell operating conditions. Degradation-induced failure of the membrane could lead to hydrogen leak across the fuel cell's membrane electrolyte assembly (MEA). The membrane degradation may occur due to chemical and mechanical stresses which can act individually or synergistically [3–5]. During fuel cell operation, the hygroscopic membrane experiences frequent changes in water content that induce expansion/contraction cycles which create mechanical stress on the membrane [6]. This stress could potentially initiate cracks [7], creep [8], delamination [9], and tears on the membrane. The impact of mechanical degradation may be exacerbated by the presence of chemical stressors in the form of radical chemical species generated during operation. The chemical stressors can be triggered by various factors such as high cell voltage, metal ion contamination, and elevated temperature which lead to radical formation [10,11]. These radicals attack the membrane ionomer including the main chain carboxylic acid end groups and side chain sulfonic acid groups [12–14] and progressively alter the ionomer structure via unzipping, scission, and fragmentation events [15,16]. Chemical membrane degradation in fuel cells can be detected by fluoride emission and membrane thickness measurements, which are indicative of the membrane's material loss. Excessive local membrane thinning could also induce electrode shorting that may affect both performance and durability [17]. The chemical degradation leads to a fragile ionomer architecture, thereby causing weakened locations on the membrane, which are susceptible to further damage from mechanical stresses caused by hygrothermal fluctuations [4,5].

Significant recent progress in membrane material design for fuel cells has contributed to enhanced membrane durability and

* Corresponding author.
E-mail address: ekjeang@sfu.ca (E. Kjeang).
[1] These authors contributed equally to this work.

https://doi.org/10.1016/j.electacta.2021.138194
0013-4686/

performance. More durable membranes can be achieved by increasing their thickness, thus increasing the gas crossover resistance and reducing the chemical degradation rate [2]. Mechanical stability can be enhanced by means of composite structures featuring a reinforcement layer made from a mechanically stronger material than the PFSA ionomer, e.g., expanded polytetrafluoroethylene (ePTFE) [18,19]. Another approach of mitigating chemical degradation is the addition of a regenerative radical scavenger, such as the Ce^{3+}/Ce^{4+} redox system, into the membrane [20,21] or catalyst layers [22]. Ceria (CeO_2) is well known to be a promising additive to protect the PFSA ionomer membrane against radical attack at open circuit voltage (OCV) conditions of accelerated stress tests (ASTs) as well as under more benign durability test conditions [20,21,23,24]. Cerium stabilized membranes under chemical AST conditions resulted in lower fluoride emission rates and reduced membrane thinning compared to MEAs without cerium [25–27]. Thus, cerium containing MEAs have shown extended AST lifetimes, which confirms their superior *in situ* durability. Migration of mobile cerium ions, however, still remains a critical challenge to the sustained effectiveness of this mitigation strategy [24].

Characterization studies pertinent to ionomer membrane degradation typically employed cross-sectional visualization using electron or X-ray microscopy. For instance, membrane deformation upon MEA fabrication [28–31] or improper alignment due to excessive compression [32] has been observed. Lim et al. [3] adopted scanning electron microscopy (SEM) morphological analysis which showed that the membrane experienced uniform thinning under combined chemical and mechanical degradation and eventually developed pinholes. This was deemed the primary reason for hydrogen crossover leaks and ultimate MEA failure. Mukundan et al. [33] studied SEM micrographs post steady-state OCV AST at 30% RH and 90°C of an MEA with a reinforced Nafion XL membrane, which failed after ~250 h of operation. The SEM micrographs showed significant global membrane thinning without through-thickness cracking or catalyst layer delamination. Singh et al. [17,34] developed an X-ray computed tomography (XCT) based visualization technique to perform 3D failure analysis of MEAs subjected to pure mechanical, pure chemical, and combined chemical/mechanical ASTs. They discovered various forms of membrane fracture as the dominant failure mode, except for the case of pure chemical degradation where membrane cracks were absent. Ramani et al. [35] used a similar 3D visualization approach to understand the membrane damage at different stages of the fuel cell lifetime and correlated the observations to a suite of *in situ* diagnostic data. This visualization strategy revealed new insight into the critical stages of membrane fracture which ultimately affected its failure. Recently, our group expanded this approach to four-dimensional (4D) *in situ* visualization to examine the identical-location progression of damage growth in the cathode catalyst layer during voltage cycling [36] and in the membrane during pure mechanical membrane degradation [37]. Thus, a critical understanding of membrane crack initiation and growth over the MEA lifetime was achieved.

The objective of the present work is to apply the XCT-based 4D *in situ* imaging methodology to investigate the mechanism and evolution of pure chemical degradation in unmitigated and chemically/mechanically mitigated fuel cell membranes. The research scope includes 4D examination of three representative types of fuel cell membranes: (i) non-reinforced; (ii) mechanically reinforced; and (iii) mechanically and chemically reinforced membranes subjected to accelerated pure chemical membrane degradation conditions in a small-scale fuel cell compatible with *in situ* imaging by XCT. Additionally, a suite of complementary *in situ* electrochemical diagnostic techniques is periodically applied to monitor MEA and membrane health. XCT-based 3D datasets are obtained at periodic stages of degradation to facilitate identical location tracking and analysis of membrane morphology as a function of degradation time and enable the characterization of the damage evolution in the examined membranes.

Table 1
Specifications of the three membrane types being studied.

Membrane	Description
Non-reinforced	No chemical or mechanical mitigation
Mechanically reinforced	ePTFE layer for mechanical reinforcement, no chemical additives
Mechanically and chemically reinforced	ePTFE layer for mechanical reinforcement, and cerium as radical scavenger

2. Experimental

2.1. Materials and assembly

Small-scale MEAs were fabricated in this work using PFSA ionomer membranes and anode and cathode gas diffusion electrodes (GDEs) of dimensions 9 mm × 4 mm. The GDEs were prepared by coating a gas diffusion layer (GDL) substrate made of non-woven carbon paper with a carbon black and PTFE containing microporous layer and a catalyst layer with carbon supported Pt electrocatalyst and PFSA ionomer [37]. Three GDE-based MEAs with non-reinforced, mechanically reinforced, and mechanically and chemically reinforced membranes, respectively, were assembled with consistent anode/cathode GDE material used across all types. A brief description of each membrane type is given in Table 1. The miniature MEAs were hot pressed on an Instron® 5569 mechanical tester at 150°C and 1.4 MPa constant compression pressure [19,37]. To limit the GDL compression to 20 ± 5%, polyimide Kapton® sheets were used as gaskets, which also acted as sealant.

To enable operation under AST conditions and perform *in situ* XCT imaging, an in-house designed, X-ray transparent miniature fuel cell fixture was employed [38]. The design of this fixture was down-sized from larger scale technical cells and optimized to meet the specific requirements of this research for non-invasive imaging with sufficiently high resolution (~1 μm pixel size), a field of view (FOV) covering most of the fuel cell active area, and adequate image contrast between all MEA and flow field plate components. The flow field plates of the fixture were designed accordingly with two parallel flow channel and prepared by CNC machining of a block of compressed carbon/graphite with cured resin, which allows good X-ray transmission, heat transfer, and sealing of hydrogen and air gas compartments when the assembly is compressed. Further information on the materials, function, and implementation of the custom fixture is available in previous reports [36–39].

2.2. Electrochemical diagnostics

The custom fixture which houses the miniature fuel cell was operated using a fuel cell test station (Scribner 850C). Initially, a set of cyclic voltammetry scans were performed from 0.1 to 1.0 V to clean the cathode catalyst layer with H_2/N_2 flows at the anode and cathode with 0.2/0.5 slpm flow rates at 75°C and 100% RH. Activation of the MEA was achieved in the fuel cell setup by drawing constant 500 mA/cm^2 current density for 20 h at 75°C and 100% RH with anode/cathode H_2/air gas flow rates of 0.2/0.5 slpm. Periodic *in situ* electrochemical diagnostics were measured to track the effects of the applied pure chemical membrane degradation conditions as a supplement to *in situ* XCT imaging to visualize the membrane. The crossover current density, representing hydrogen crossover flux, was determined electrochemically from

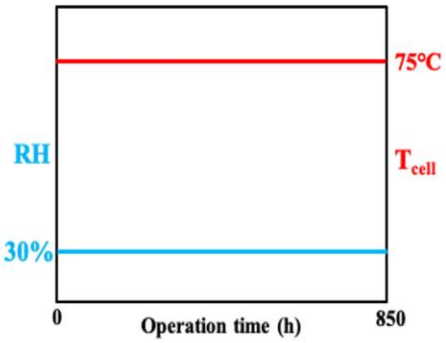

Fig. 1. Schematic of the constant OCV AST applied to induce rapid chemical membrane degradation.

the y-intercept of the linear fit between measured current density and applied voltage (0.3–0.5 V) acquired under 0.6 slpm H_2/0.5 slpm N_2 flow at 70°C and 100% RH. Additionally, three fuel cell polarization curves were measured at 70°C, 100% RH H_2/air and averaged at each life stage.

2.3. Accelerated stress testing (AST)

The presently used AST was adopted from the standard US Department of Energy protocol for accelerated chemical membrane degradation [40], with minor modifications in conditions to facilitate operation inside the custom fuel cell fixture. The AST protocol featured a steady-state OCV hold at high temperature (75°C) and low RH (30%) conditions, while supplying anode H_2 gas at 0.3 slpm and cathode air at 0.5 slpm, as illustrated in Fig. 1. The constant OCV AST protocol applied here was intended to mimic the typical idle operation of fuel cell vehicles, which induces chemical degradation through radical attack of the ionomer membrane. Except for the diagnostics described above, no mechanical stress cycles or other forms of mechanical degradation were applied in order to isolate the effect of chemical membrane degradation. The test was continued until membrane failure occurred, as detected by either 200 mV OCV loss or rise in the crossover current density by > 20 mA/cm^2.

2.4. X-ray computed tomography (XCT) imaging

A state-of-the-art, lab-based micro-XCT system (ZEISS Xradia 520 Versa) was used to characterize the 3D structure of the multilayered MEA and flow field plates of the miniature fuel cell fixture. The Versa 520 is an innovative XCT system, employing X-ray microscopy methods to achieve sub-micrometer resolutions for relatively large specimens (mm to cm) that can be leveraged for *in situ* fuel cell imaging. For this study, a specific X-ray energy flux irradiating the assembled fixture was achieved by choosing an electron accelerating voltage of 80 kV and a power of 7 W, with a low energy filter. The tomography scans comprised of 1,601 projections with 7 s X-ray exposure to obtain the required intensity (5000 counts) at the membrane region of the sample. The projections were taken across 190° rotation from −95° to +95° with increased density at the extremities by application of high aspect ratio tomography (HART) for optimum image quality. The tomographic datasets were subjected to center shift and beam hardening correction followed by numerical 3D reconstruction in ZEISS XMReconstructor® software. Fig. 2 illustrates a sample MEA cross-sectional view post reconstruction, virtually extracted from the tomography dataset. Good contrast between all MEA layers as well as the pore phase and flow field plates were achieved. For the purposes of the present work, periodic 3D tomographic data were acquired at identical locations within the miniature fuel cell fixture, covering a 3.2 mm × 3.2 mm FOV of the MEA. The X-ray beam is polychromatic, with a maximum beam energy of 80 keV. A pixel resolution of 1.59 µm was obtained by positioning the fuel cell fixture 27 mm from the X-ray source and 30 mm from the detector. For the execution of 4D *in situ* imaging, with the fourth dimension representing degradation time, the fuel cell was subjected to the aforementioned AST protocol for pure chemical membrane degradation. The fuel cell fixture was subjected to a certain number of AST hours and then installed in the micro-XCT system for 3D imaging of identical MEA locations at periodic intervals, thus enabling 4D visualization of the degrading membrane with respect to time from fabrication to failure. To characterize the membrane structural features at different stages of degradation, the same FOV of the small-scale fuel cell fixture was visualized using XCT at the beginning of life (BOL) and after various life stages of the AST procedure. This experimental procedure was repeated for each of the three fuel cell membranes listed in Table 1.

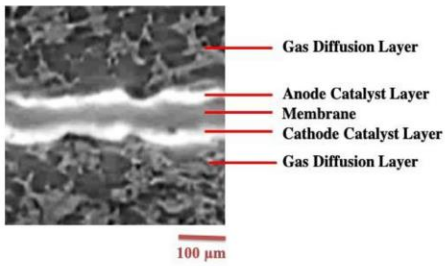

Fig. 2. Reconstructed cross-sectional XCT perspective of the miniature fuel cell, revealing the internal components of the MEA.

2.5. Image processing

Initially, the greyscale image datasets consisting of different MEA layers were cropped exclusively to the catalyst layers and membrane portion. Subsequently, a 2D median filtering was used to reduce the overall noise and enable segmentation accuracy to the representative cross section. Manual threshold was applied to obtain binary datasets. Further details of the procedure are available in [17]. The noise-free 2D cross-sectional images were used to compute the average membrane thickness measurements. This was performed using ImageJ [41], an open source software, by computing the membrane thickness across six 2D virtual locations of each life stage [35]. The tomographic data obtained were also used to generate virtual planar maps of electrode shorting defined by direct contact (zero separation) between the anode and cathode catalyst layers. The shorting maps were generated at the EOT stage of each MEA by adopting ImageJ.

3. Results and Discussion

The steady-state OCV AST protocol applied herein is known to induce elevated levels of predominant chemical degradation on the fuel cell membranes by constantly maintaining high cell temperature, low RH, and high cell voltage. The results reported in the upcoming sections collectively represent the structural and electrochemical characterization of AST-induced membrane damage observed on three separate MEAs fabricated with non-reinforced,

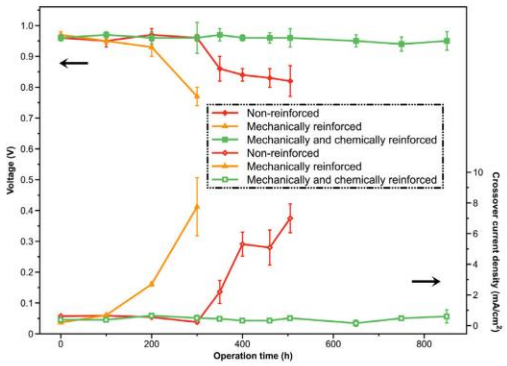

Fig. 3. Fuel cell OCV and hydrogen crossover current density for MEAs with three different types of membranes, as a function of steady-state OCV AST operation time.

mechanically reinforced, and mechanically and chemically reinforced membranes. The MEA health of the small-scale fuel cells was tracked at different stages of the same AST procedure. MEA failure was observed for non-reinforced and mechanically reinforced membranes after 500 and 300 h of operation, respectively. The AST of the mechanically and chemically reinforced membrane was terminated after 850 h of operation, i.e., after nearly three times the lifetime of the mechanically reinforced membrane, without reaching failure as per the criteria described in the 'Experimental' section.

3.1. OCV and crossover current density

OCV measure is a critical evaluation parameter for assessing the overall membrane health during the AST procedure as it degrades the membrane and initiates gas leaks across the membrane due to membrane thinning, electrode shorts, cracks, and pinholes. In the present work, the overall MEA health at various stages of AST operation was tracked by periodic OCV and hydrogen crossover current density measurements. The recorded data are illustrated as a function of hours of steady-state OCV AST operation in Fig. 3. For the non-reinforced baseline membrane, at the initial stage and until 300 h of operation, the OCV decay rate was negligible. However, between 300 and 350 h, an abrupt OCV drop of around 100 mV was noticed, which coincided with the rise in gas crossover at the same stage. After 350 h, the OCV decay was linear (0.25 mV/h) and reached 0.8 V after 500 h. For this membrane, the OCV loss trend was consistent with the rise in hydrogen crossover current density through the membrane due to the pure chemical membrane degradation process. The mechanically reinforced membrane showed earlier failure after 300 h, which could be attributed to its thinner structure. The OCV and crossover trends for this membrane were otherwise similar to those of the non-reinforced membrane. As seen for both non-reinforced and mechanically reinforced membranes, high gas crossover across the membrane suggests the presence of ruptures/cracks supportive of local convective gas flow. This gas crossover was likely responsible for the concurrent OCV decay caused by mixed electrode potentials. The mechanically and chemically reinforced membrane had stable OCV and minimal crossover for 850 h, after which the test was terminated. This suggests that the mechanisms that induced failure in the other two membranes were likely absent or significantly stifled when ePTFE reinforcement and radical scavengers were present together in the membrane.

3.2. Micro-structural investigation

The impact of radical attack, induced during the chemical membrane degradation, can alter the ionomer morphology, thereby reducing its ion exchange capacity and proton conductivity. Hence, a direct consequence of chemical degradation is membrane thinning due to material loss. The 4D *in situ* XCT visualization performed in this work facilitates parallel examination of both planar and cross-sectional perspectives within the fuel cell MEA for a comprehensive characterization of features associated with its degradation and failure. This examination was achieved in the present work for the three experimental runs with different membrane types by periodically acquiring 3D virtual images at different life stages during the pure chemical membrane degradation AST. The 3D datasets provided access to several 2D cross-sectional images with sufficient resolution to quantify the membrane thickness in its native environment inside the fuel cell and characterize the evolution of membrane thickness as a function of degradation time [17,35,36].

Representative same location virtual cross-sectional views of the conditioned BOL, intermediate, and end of test (EOT) lifetime stages of the three MEAs are shown in Fig. 4. The XCT images provided adequate contrast between all internal MEA components for all three membrane types, such that any component specific or component interactive structural degradation effects could be observed. Careful examination of the images demonstrated several local membrane thinning sites under the land region at the EOT stage for the non-reinforced and mechanically reinforced membranes. However, no such local thinning sites were observed under the channels for either of the two MEAs. No cracks or other features in the adjoining catalyst layers were observed that could have otherwise accelerated the thinning; hence, the external clamping pressure acting predominantly on the land regions of the MEA was likely the accelerating factor for locally elevated membrane thinning under the lands. Even the mechanically reinforced membrane, which is known to embody a mechanically reinforcing ePTFE layer, still failed to prevent thinning under the land section. On the contrary, the mechanically and chemically reinforced membrane displayed negligible thinning under both land and channel regions.

The global membrane thickness data in Fig. 5a show significant thinning of the non-reinforced and mechanically reinforced membranes as compared to the mechanically and chemically reinforced membrane at the two degraded states. For the non-reinforced membrane, slight thinning of 14% was measured after 350 h (intermediate stage) of AST operation. The rate of thinning was higher during the late stage of degradation and reached 26% at EOT (failure). The mechanically reinforced membrane showed only 9% thinning after 100 h of operation and 41% thinning at EOT (failure), which similarly demonstrates a non-linear thinning behavior with higher decay rate between the intermediate and EOT stages. On the contrary, the mechanically and chemically reinforced membrane demonstrated significantly lower rate of thinning with only ~5% thickness loss at EOT. Overall, the three types of membrane showed progressive membrane thinning [35] though at different intensity of degradation. Ionomer membranes under chemical stressors are known to decompose causing global membrane thinning leading to high gas crossover and eventual membrane failure [42]. Early failure in the mechanically reinforced membrane was attributed to a relatively lower membrane thickness as well as lack of Ce additives. Significant thinning of the membrane was observed at EOT for this case owing to severe scission of main and side chains of the ionomer [3]. Negligible changes in local features were noticed for the mechanically and chemically reinforced membrane. Mukundan et al. [33] used SEM micrographs and thinning data to show that Nafion XL membrane, which contains Ce-based radical scavengers as well as mechanical reinforcement, re-

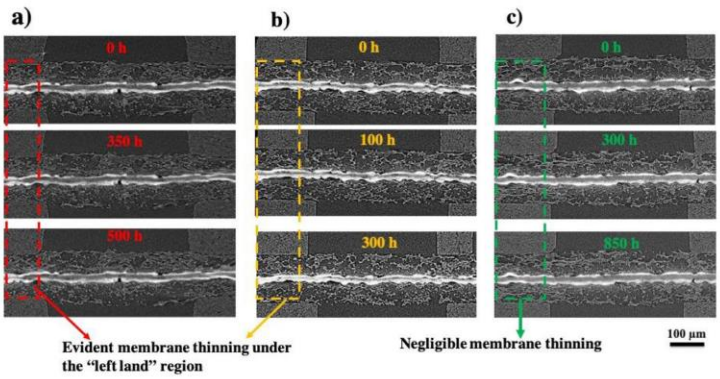

Fig. 4. Cross-sectional identical location MEA images obtained by XCT at beginning, intermediate, and end of test lifetime stages for separate MEAs with (a) non-reinforced, (b) mechanically reinforced, and (c) mechanically and chemically reinforced membranes. The highlighted areas indicate local thinning for the non-reinforced and mechanically reinforced membranes under the flow field land, whereas negligible thinning is observed for the mechanically and chemically reinforced membrane.

duced thinning by a factor of 3x during OCV AST compared to the Ce-free ionomer membranes. The present findings using a miniature fuel cell are consistent with this published work and reaffirm the effective mitigation capacity of Ce additives of reinforced fuel cell membranes against chemical membrane degradation. As an additional contribution of the present work, spatially resolved membrane thinning under land and channel regions can be identified using the same location cross-sectional MEA images at each stage of degradation. Fig. 5b shows the relative membrane thickness loss under land and channel regions of the three membrane types at EOT. The non-reinforced membrane showed 28% loss under the lands and 22% loss under the channels, whereas the mechanically reinforced membrane showed a higher loss of 46% under the lands and 37% under the channels. The mechanically and chemically reinforced membrane, which did not fail during the AST, demonstrated low thinning of ~7% under the lands and ~4% under the channels. Hence, all three membrane types showed amplified membrane thinning under the lands compared to the channel regions. Such differences between channel and land regions were not observed at BOL.

Radical attack on membranes causes changes in ionomer structure and thickness, thereby leading to less durable membrane [43]. The weakened polymer leads to favorable conditions for divots, cracks, and pinholes in the advanced stages of the cycling. Our previous post-mortem failure analysis investigation of non-reinforced membrane in a larger, technical-scale fuel cell had shown similar global and locally elevated membrane thinning accompanied by electrode shorting and absence of cracks when subjected to pure chemical degradation [17]. This finding is consistent with the present study, as no visible cracks, pinholes, or micro cracks were identified in any of the membranes. Furthermore, no major delamination within the MEAs was noticed. The mechanically reinforced membrane, however, displayed one minor "divot" like feature at EOT (under land region) as shown in Fig. 6. The divot was situated at a local membrane thin spot free of electrode cracks. The PFSA and ePTFE layers were all degraded at this location, thus compromising the structural barrier to gas crossover. The mechanically and chemically reinforced membrane showed no such divots, despite the much longer runtime, suggesting that divot formation can be delayed or prevented with the use of radical scavengers to mitigate chemical degradation.

The unique 4D *in situ* XCT visualization methodology facilitates in-depth visual and numerical analysis of degradation phenomena, which for the purposes of the present work enables detailed characterization of electrode shorting post membrane degradation. Electrode shorting is caused by the direct contact of the anode and cathode electrodes in the absence of the central membrane. The electrode shorting compromises the fuel cell performance and causes local hot spots in the vicinity of the shorts which are susceptible for damage formation with further degradation. While overall electrode shorting can be detected electrochemically [2], it has not been visualized inside an operational fuel cell to date. No electrode shorting was observed at BOL or any intermediate life stage; hence, these stages are not presented here. Fig. 7 illustrates the virtual planar maps of the electrode shorting sites of the three membrane configurations at EOT. Complementary cross-sectional views under the right, middle, and left land regions are provided to understand the 3D features of the electrode shorting sites within the MEA. The planar shorting maps show significant development of shorts in both non-reinforced and mechanically reinforced membranes, with the largest and most frequent shorts in the mechanically reinforced membrane. Detailed numerical analysis for each type of membrane was used to quantify the frequency and average size of the shorting sites. For the non-reinforced membrane, the average size of the short was 310 μm with a frequency of 5 shorts/mm^2, whereas the mechanically reinforced membrane showed a smaller mean short size of 120 μm with a much greater frequency of 100 shorts/mm^2. Previous post mortem studies with XCT on large scale cells showed that over 5% of the membrane area had shorting sites [17]. This correlates reasonably well with the present observations as roughly 3% and <1% of the membrane area displayed shorting sites for the mechanically reinforced and non-reinforced membranes, respectively. Interestingly, the distribution of the shorting sites was more concentrated under the left and right land regions, with over 90% of the electrode shorts located under lands. This suggests that the clamping pressure under the land regions had a significant influence on the location of shorting sites. This finding correlates with the results of Fig. 5b, where elevated membrane thinning was identified under the lands. Similar to our previous work [17], the shorting sites observed in the present work were attributed to severe membrane thinning due to chemical stressors, rather than specific features or defects in the adjacent electrodes. For the mechanically reinforced membrane, the shorting sites were more frequent owing to the thinner membrane. The widespread presence of shorts with this membrane demonstrates that the central ePTFE layer was no more

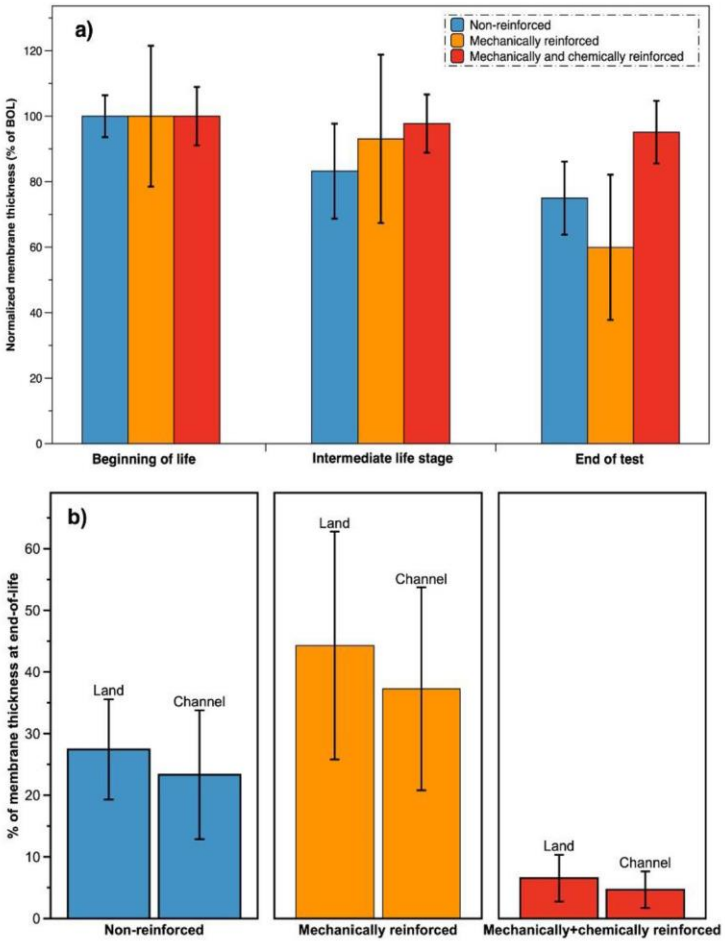

Fig. 5. (a) Normalized global membrane thickness calculated from the XCT images at different lifetime stages. The error bars represent the standard deviation of the measured thickness. (b) Membrane thickness loss under land and channel regions at the EOT stage for all three membranes.

intact, even in the absence of mechanical degradation. Overall, frequent shorting sites and severe membrane thinning in the absence of membrane cracks shows that pure chemical membrane degradation is a critical stressor which could lead to early membrane failure. This is corroborated by the failure of the mechanically reinforced membrane despite its mechanical reinforcement. Most notably however, the mechanically and chemically reinforced membrane did not develop any visible shorting sites. This shows the importance of the chemical additives/mitigation to achieve durability with thinner membranes.

3.3. Performance characterization

The measured fuel cell polarization curves obtained for the three membrane types at different stages of OCV AST operation are displayed in Fig. 8. As can be observed for the cell with non-reinforced membrane, the performance loss in the mass transport regime is pronounced after 350 h, which is additional to the OCV loss discussed earlier. The majority of the performance losses were incurred during the first 350 h, with only minor additional loss in the kinetic region at EOT. Considering the progressive membrane thinning, OCV drop, and increased gas crossover after 350 h, the performance drop observed here is logical. Considering that the high temperature, low humidity, and high cell potential conditions of the AST are favorable for ionomer scission, the mass transport loss observed at high current densities is likely due to ionomer fragment deposition in the GDL [3]. The GDLs are generally fabricated to be hydrophobic to facilitate water transport into the flow channels and avoid flooding of the MEA. This hydrophobic nature and functionality are likely compromised in the event of deposition of hydrophilic ionomer fragments originating from

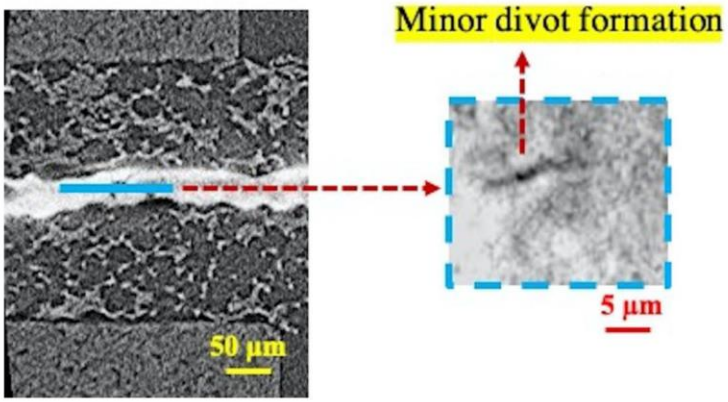

Fig. 6. Cross-sectional and planar views of a divot in the membrane plane at EOT for the mechanically reinforced membrane.

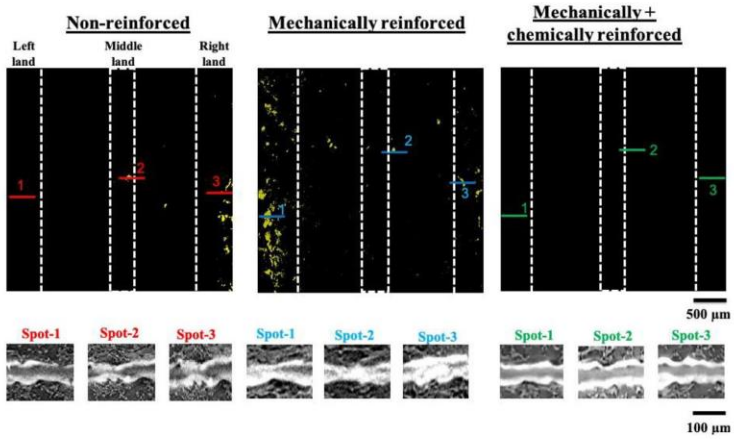

Fig. 7. Planar virtual electrode shorting maps at the membrane plane of EOT MEAs with non-reinforced, mechanically reinforced, and mechanically and chemically reinforced membranes. Shorting sites are shown in yellow color whereas black color indicates regions with retained membrane. Insets illustrate the corresponding cross-sectional views at the lines marked in the planar views under the left, middle, and right land regions (For interpretation of the references to color in this figure legend, the reader is referred to the web version of this article.).

the membrane, thereby increasing the mass transport related voltage loss at high current densities. It is further possible that the prolonged application of OCV AST also induced degradation in the ionomer phase of the catalyst layers which may have contributed additional ohmic and mass transport resistance. It is noteworthy that the cell with mechanically reinforced membrane had lower performance than the non-reinforced cell at both BOL and EOT; this membrane demonstrated major performance losses in the activation, ohmic, and mass transport regimes at EOT. The low BOL performance of this cell may in part be due to its small size and relatively large cell-to-cell variability in performance. As observed from the XCT images (Fig. 4), the membrane undergoes thinning presumably due to the loss of material in one or both of the PFSA layers around the central ePTFE reinforcement layer. Whereas this membrane thinning is expected to 'geometrically' lower the membrane's overall resistance to proton transport, the net increase observed in the ohmic losses is likely from a higher counteracting effect on the PFSA layer's ion exchange capacity due to its chemical degradation. Reduced proton conductivity in the catalyst layer ionomer may affect kinetics as well. The low EOT performance may also be influenced by the widespread electrode shorts resulting from membrane degradation. Contrastingly, only a minor performance drop was observed in the cell with mechanically and chemically reinforced membrane at EOT. This cell maintained good performance throughout 850 h of harsh chemical stress. Given that this membrane is both chemically and mechanically mitigated, it is expected to last longer than the other membranes, which based on the present results can be primarily attributed to its cerium content. Furthermore, the lower mass transport loss of this membrane compared to the non-reinforced and mechanically reinforced membranes was due to fewer ionomer fragments released into the other MEA components.

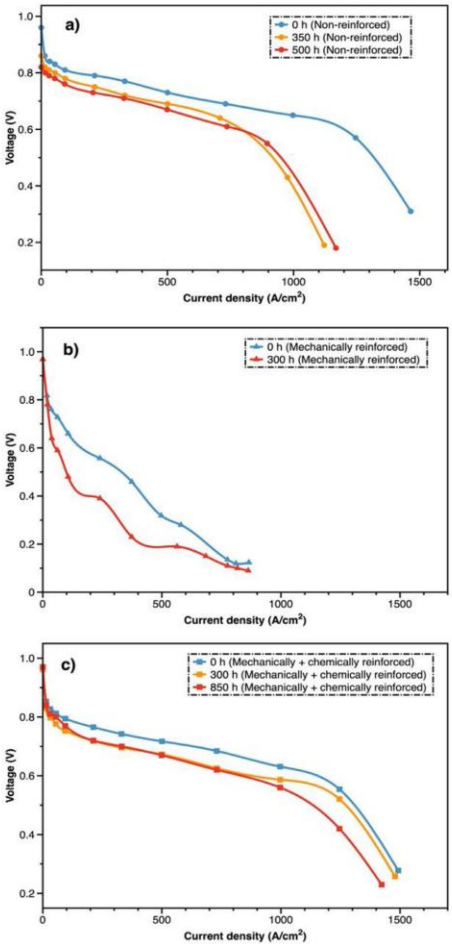

Fig. 8. Fuel cell polarization curves for MEAs with (a) non-reinforced, (b) mechanically reinforced, and (c) mechanically and chemically reinforced membranes at different stages of OCV AST operation.

4. Conclusions

The present study used a comprehensive 4D *in situ* visualization approach based on XCT to perform periodic structural investigations of identical locations within MEAs comprising of different fuel cell membrane types subjected to chemical degradation. The experiments utilized a custom miniature fuel cell fixture, wherein the failures were generated through pure chemical modes of membrane degradation by means of an OCV hold AST. Upon application of the AST, the membranes free of any radical scavenging additives, i.e., non-reinforced and mechanically reinforced membranes, showed decay in OCV and increase in hydrogen crossover current eventually leading to membrane failure. Microstructural observations showed preferential local thinning spots under lands and global membrane thinning for both membranes, whereas cracks and pinholes were absent. The locally amplified membrane thinning preceded the eventual formation of shorts due to localized absence of membrane material and associated loss of electrode separation. More than 90% of the shorts occurred under the lands, indicating that the clamping pressure had a strong influence on their formation. The ePTFE layer in the chemical additive free membrane did not prevent the short formation. In contrast, the mechanically and chemically reinforced membrane did not show major degradation or shorts even after 850 h of AST operation, highlighting the regenerative radical scavenging effect of its cerium additive to mitigate the chemical stressors. The observed phenomenon further suggests that mechanical stresses, even in the absence of mechanical degradation, may influence the local shorting events and by extension, the lifetime of the membrane when subjected to chemical degradation. Consequently, in order to maintain or enhance membrane durability with thinner membranes, radical scavengers in the form of chemical additives are likely essential. Overall, the outcomes of this research showcase the strong capabilities of XCT imaging towards improving the scientific understanding of membrane degradation in fuel cells by revealing the underlying mechanisms and failure modes, with key implications for fuel cell durability.

Declaration of Competing Interest

The authors declare no conflict of interest.

Acknowledgments

This research was supported by Automotive Partnership Canada, Canada Foundation for Innovation, British Columbia Knowledge Development Fund, Natural Sciences and Engineering Research Council of Canada, Ballard Power Systems, and Canada Research Chairs. W. L. Gore & Associates, Inc. is acknowledged for additional support.

References

[1] M.P. Rodgers, R.P. Brooker, N. Mohajeri, L.J. Bonville, H.R. Kunz, D.K. Slattery, J.M. Fenton, Comparison of proton exchange membranes degradation rates between accelerated and performance tests, J. Electrochem. Soc. 159 (2012) F338–F352, doi:10.1149/2.040207jes.
[2] C.S. Gittleman, F.D. Coms, Y.H. Lai, Membrane durability: physical and chemical degradation, in: M. Mench, E.C. Kumbur, T.N. Veziroglu (Eds.), Polymer Electrolyte Fuel Cell Degradation, Academic Press, Cambridge MA, 2012, pp. 15–88.
[3] C. Lim, L. Ghassemzadeh, F. Van Hove, M. Lauritzen, J. Kolodziej, G.G. Wang, S. Holdcroft, E. Kjeang, Membrane degradation during combined chemical and mechanical accelerated stress testing of polymer electrolyte fuel cells, J. Power Sources 257 (2014) 102–110, doi:10.1016/j.jpowsour.2014.01.106.
[4] N. Macauley, A.S. Alavijeh, M. Watson, J. Kolodziej, M. Lauritzen, S. Knights, G. Wang, E. Kjeang, Accelerated membrane durability testing of heavy duty fuel cells, J. Electrochem. Soc. 162 (2015) F98–F107, doi:10.1149/2.0671501jes.
[5] A. Sadeghi Alavijeh, M.A. Goulet, R.M.H. Khorasany, J. Ghataurah, C. Lim, M. Lauritzen, E. Kjeang, G.G. Wang, R.K.N.D. Rajapakse, Decay in mechanical properties of catalyst coated membranes subjected to combined chemical and mechanical membrane degradation, Fuel Cells 15 (2015) 204–213, doi:10.1002/fuce.201400040.
[6] R.M.H. Khorasany, E. Kjeang, G.G. Wang, R.K.N.D. Rajapakse, Simulation of ionomer membrane fatigue under mechanical and hygrothermal loading conditions, J. Power Sources 279 (2015) 55–63, doi:10.1016/j.jpowsour.2014.12.133.
[7] Y.P. Patil, W.L. Jarrett, K.A. Mauritz, Deterioration of mechanical properties: a cause for fuel cell membrane failure, J. Membr. Sci. 356 (2010) 7–13, doi:10.1016/j.memsci.2010.02.060.
[8] R.M.H. Khorasany, M.A. Goulet, A.S. Alavijeh, E. Kjeang, G.G. Wang, R.K.N.D. Rajapakse, On the constitutive relations for catalyst coated membrane applied to *in-situ* fuel cell modeling, J. Power Sources 252 (2014) 176–188, doi:10.1016/j.jpowsour.2013.11.087.
[9] A.S. Alavijeh, R.M.H. Khorasany, Z. Nunn, A. Habisch, M. Lauritzen, E. Rogers, G.G. Wang, E. Kjeang, Microstructural and mechanical characterization of catalyst coated membranes subjected to *in situ* hygrothermal fatigue, J. Electrochem. Soc. 162 (2015) F1461–F1469, doi:10.1149/2.0471514jes.
[10] J. Wu, X.Z. Yuan, J.J. Martin, H. Wang, J. Zhang, J. Shen, S. Wu, W. Merida, A review of PEM fuel cell durability: degradation mechanisms and mitigation strategies, J. Power Sources 184 (2008) 104–119, doi:10.1016/j.jpowsour.2008.06.006.
[11] M.P. Rodgers, L.J. Bonville, H.R. Kunz, D.K. Slattery, J.M. Fenton, Fuel cell perfluorinated sulfonic acid membrane degradation correlating accelerated stress testing and lifetime, Chem. Rev. 112 (2012) 6075–6103, doi:10.1021/cr200424d.

[12] F.D. Coms, The chemistry of fuel cell membrane chemical degradation, ECS Trans. 16 (2008) 235–255, doi:10.1149/1.2981859.
[13] L. Ghassemzadeh, K. Kreuer, J. Maier, K. Mu, Chemical degradation of nafion membranes under mimic fuel cell conditions as investigated by solid-state NMR spectroscopy, J. Phys. Chem. C 114 (2010) 14635–14645, doi:10.1021/jp102533v.
[14] L. Ghassemzadeh, K.D. Kreuer, J. Maier, K. Müller, Evaluating chemical degradation of proton conducting perfluorosulfonic acid ionomers in a Fenton test by solid-state 19F NMR spectroscopy, J. Power Sources 196 (2011) 2490–2497, doi:10.1016/j.jpowsour.2010.11.053.
[15] K.H. Wong, E. Kjeang, Macroscopic *in-situ* modeling of chemical membrane degradation in polymer electrolyte fuel cells, J. Electrochem. Soc. 161 (2014) F823–F832, doi:10.1149/2.0031409jes.
[16] K.H. Wong, E. Kjeang, Mitigation of chemical membrane degradation in fuel cells: understanding the effect of cell voltage and iron ion redox cycle, ChemSusChem 8 (2015) 1072–1082, doi:10.1002/cssc.201402957.
[17] Y. Singh, F.P. Orfino, M. Dutta, E. Kjeang, 3D failure analysis of pure mechanical and pure chemical degradation in fuel cell membranes, J. Electrochem. Soc. 164 (2017) 1331–1341, doi:10.1149/2.0451713jes.
[18] S. Shi, A.Z. Weber, A. Kusoglu, Structure/property relationship of nafion XL composite membranes, J. Membr. Sci. 516 (2016) 123–134, doi:10.1016/j.memsci.2016.06.004.
[19] D. Ramani, Y. Singh, R.T. White, M. Wegener, F.P. Orfino, M. Dutta, E. Kjeang, 4D *in situ* visualization of mechanical degradation evolution in reinforced fuel cell membranes, Int. J. Hydrog. Energy 45 (2020) 10089–10103, doi:10.1016/j.ijhydene.2020.02.013.
[20] B.P. Pearman, N. Mohajeri, R.P. Brooker, M.P. Rodgers, D.K. Slattery, M.D. Hampton, D.A. Cullen, S. Seal, The degradation mitigation effect of cerium oxide in polymer electrolyte membranes in extended fuel cell durability tests, J. Power Sources 225 (2013) 75–83.
[21] B.P. Pearman, N. Mohajeri, D.K. Slattery, M.D. Hampton, S. Seal, D.A. Cullen, The chemical behavior and degradation mitigation effect of cerium oxide nanoparticles in perfluorosulfonic acid polymer electrolyte membranes, Polym. Degrad. Stab. 98 (2013) 1766–1772, doi:10.1016/j.polymdegradstab.2013.05.025.
[22] L. Wang, S.G. Advani, A.K. Prasad, Degradation reduction of polymer electrolyte membranes using CeO_2 as a free-radical scavenger in catalyst layer, Electrochim. Acta 109 (2013) 775–780, doi:10.1016/j.electacta.2013.07.189.
[23] C. Lim, A.S. Alavijeh, M. Lauritzen, J. Kolodziej, S. Knights, E. Kjeang, Fuel cell durability enhancement with cerium oxide under combined chemical and mechanical membrane degradation, ECS Electrochem. Lett. 4 (2015) F29–F31, doi:10.1149/2.0081504eel.
[24] A.M. Baker, R. Mukundan, D. Spernjak, E.J. Judge, S.G. Advani, A.K. Prasad, R.L. Borup, Cerium migration during PEM fuel cell accelerated stress testing, J. Electrochem. Soc. 163 (2016) F1023–F1031, doi:10.1149/2.0181609jes.
[25] M.S. Wilson, F.H. Garzon, R.L. Borup, S.M. Stewart, A. Datye, Ceria and doped ceria nanoparticle additives for polymer fuel cell lifetime improvement, ECS Trans. 64 (2014) 403–411, doi:10.1149/06403.0403ecst.
[26] L. Wang, S.G. Advani, A.K. Prasad, Self-hydrating Pt/CeO2-nafion composite membrane for improved durability and performance, ECS Electrochem. Lett. 3 (2014) F30–F32, doi:10.1149/2.007405eel.
[27] C. Bi, H. Dai, H. Zhang, S. Xiao, Y. Zhang, Z. Mai, Y. Zhang, X. Li, Degradation location study of proton exchange membrane at open circuit operation, J. Power Sources 195 (2010) 5305–5311, doi:10.1016/j.jpowsour.2010.03.010.
[28] Q. Meyer, N. Mansor, F. Iacoviello, P.L. Cullen, R. Jervis, D. Finegan, C. Tan, J. Bailey, P.R. Shearing, D.J.L. Brett, Investigation of hot pressed polymer electrolyte fuel cell assemblies via X-ray computed tomography, Electrochim. Acta 242 (2017) 125–136, doi:10.1016/j.electacta.2017.05.028.
[29] J. Hack, T.M.M. Heenan, F. Iacoviello, N. Mansor, Q. Meyer, P. Shearing, N. Brandon, D.J.L. Brett, A structure and durability comparison of membrane electrode assembly fabrication methods: self-assembled versus hot-pressed, J. Electrochem. Soc. 165 (2018) 3045–3052, doi:10.1149/2.0051806jes.
[30] T.M.M. Heenan, C. Tan, J. Hack, D.J.L. Brett, P.R. Shearing, Developments in X-ray tomography characterization for electrochemical devices, Mater. Today 31 (2019) 69–85, doi:10.1016/j.mattod.2019.05.019.
[31] Q. Meyer, Y. Zeng, C. Zhao, *In situ* and operando characterization of proton exchange membrane fuel cells, Adv. Mater. 31 (2019) 1–25, doi:10.1002/adma.201901900.
[32] N. Kulkarni, M.D.R. Kok, R. Jervis, F. Iacoviello, Q. Meyer, P.R. Shearing, D.J.L. Brett, The effect of non-uniform compression and flow-field arrangements on membrane electrode assemblies - X-ray computed tomography characterisation and effective parameter determination, J. Power Sources 426 (2019) 97–110, doi:10.1016/j.jpowsour.2019.04.018.
[33] R. Mukundan, A.M. Baker, A. Kusoglu, P. Beattie, S. Knights, A.Z. Weber, R.L. Borup, Membrane accelerated stress test development for polymer electrolyte fuel cell durability validated using field and drive cycle testing, J. Electrochem. Soc. 165 (2018) F3085–F3093, doi:10.1149/2.0101806jes.
[34] Y. Singh, F.P. Orfino, M. Dutta, E. Kjeang, 3D visualization of membrane failures in fuel cells, J. Power Sources 345 (2017) 1–11, doi:10.1016/j.jpowsour.2017.01.129.
[35] D. Ramani, Y. Singh, F.P. Orfino, M. Dutta, E. Kjeang, Characterization of membrane degradation growth in fuel cells using X-ray computed tomography, J. Electrochem. Soc. 165 (2018) F3200–F3208, doi:10.1149/2.0251806jes.
[36] R.T. White, A. Wu, M. Najm, F.P. Orfino, M. Dutta, E. Kjeang, 4D *in situ* visualization of electrode morphology changes during accelerated degradation in fuel cells by X-ray computed tomography, J. Power Sources 350 (2017) 94–102, doi:10.1016/j.jpowsour.2017.03.058.
[37] Y. Singh, R.T. White, M. Najm, T. Haddow, V. Pan, F.P. Orfino, M. Dutta, E. Kjeang, Tracking the evolution of mechanical degradation in fuel cell membranes using 4D *in situ* visualization, J. Power Sources (2019) 224–237, doi:10.1016/j.jpowsour.2018.11.049.
[38] R.T. White, F.P. Orfino, M. El Hannach, O. Luo, M. Dutta, A.P. Young, E. Kjeang, 3D printed flow field and fixture for visualization of water distribution in fuel cells by X-ray computed tomography, J. Electrochem. Soc. 163 (2016) F1337–F1343, doi:10.1149/2.0461613jes.
[39] R.T. White, D. Ramani, S. Eberhardt, M. Najm, F.P. Orfino, M. Dutta, E. Kjeang, Correlative X-ray tomographic imaging of catalyst layer degradation in fuel cells, J. Electrochem. Soc. 166 (2019) 914–925, doi:10.1149/2.0121913jes.
[40] U.S.Department of Energy, Multi-Year Res. Dev. Demonstr. Plan, Chapter 3.4 Fuel Cells (2017) https://energy.gov/sites/prod/files/2017/05/f34/fcto_myrdd_fuel_cells.pdf.
[41] ImageJ, https://imagej.net (2017) 987–1104, doi:10.1021/acs.chemrev.6b00159.
[42] S. Kreitmeier, M. Michiardi, A. Kusoglu, A.Z. Weber, New Insights into Perfluorinated Sulfonic-Acid Ionomers, Chemical Reviews 117 (2017) 987–1104, doi:10.1021/acs.chemrev.6b00159.
[43] S. Kreitmeier, M. Michiardi, A. Wokaun, F.N. Büchi, Factors determining the gas crossover through pinholes in polymer electrolyte fuel cell membranes, Electrochimica Acta 80 (2012) 240–247, doi:10.1016/j.electacta.2012.07.013.

Appendix C.

4D *In situ* Visualization of Mechanical Degradation Evolution in Reinforced Fuel Cell Membranes

[DOI: https://doi.org/10.1016/j.ijhydene.2020.02.013]

INTERNATIONAL JOURNAL OF HYDROGEN ENERGY 45 (2020) 10089–10103

Available online at www.sciencedirect.com

ScienceDirect

journal homepage: www.elsevier.com/locate/he

4D *in situ* visualization of mechanical degradation evolution in reinforced fuel cell membranes

Dilip Ramani [a], *Yadvinder Singh* [a], *Robin T. White* [a], *Matthew Wegener* [a], *Francesco P. Orfino* [a], *Monica Dutta* [b], *Erik Kjeang* [a,*]

[a] *Fuel Cell Research Lab (FCReL), School of Mechatronic Systems Engineering, Simon Fraser University, 250-13450 102 Avenue, Surrey, BC, V3T 0A3, Canada*

[b] *Ballard Power Systems, 9000 Glenlyon Parkway, Burnaby, BC, V5J 5J8, Canada*

HIGHLIGHTS

- 4D *in situ* XCT is adopted to track mechanical degradation of reinforced membranes.
- The *in situ* process of fatigue crack propagation is revealed.
- Degradation mechanisms of reinforced and non-reinforced membranes are compared.
- Catalyst layer cracks and delamination are identified as key drivers of fracture.

GRAPHICAL ABSTRACT

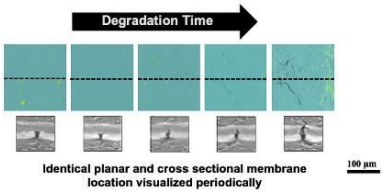

ARTICLE INFO

Article history:
Received 10 December 2019
Received in revised form
29 January 2020
Accepted 3 February 2020
Available online 22 February 2020

Keywords:
Reinforced membrane
Fuel cell
Fracture
Crack
Visualization
X-ray computed tomography

ABSTRACT

Composite ionomer membranes with ePTFE reinforcement have been developed to improve operational durability of polymer electrolyte fuel cells by creating a more mechanically robust membrane electrode assembly. The present objective is to determine the morphological damage evolution of a reinforced membrane subjected to pure mechanical degradation by wet/dry cycling in a fuel cell. Identical-location four-dimensional *in situ* visualization by X-ray computed tomography is used to reveal the progressive degradation stages from initiation via propagation to failure. The observed degradation process is dominated by fatigue driven membrane fracture which is primarily confined under the channel area. When compared to degradation of non-reinforced membranes, the results for the reinforced membrane demonstrate similar non-linear progression of membrane fracture, but at 2-3x lower rate due to the improved fracture resistance of ePTFE reinforcement. Membrane-catalyst layer delamination and catalyst layer cracks are identified as preceding drivers of local membrane fracture, while wet and dry phase *in situ* imaging demonstrates hydration induced through-plane swelling of 30% and widespread crack closure at advanced degradation states. Overall, these results provide new understanding of mechanical degradation in composite membranes and prospective directions for further durability enhancements.

* *Corresponding author.*
E-mail address: ekjeang@sfu.ca (E. Kjeang).

https://doi.org/10.1016/j.ijhydene.2020.02.013

Introduction

Polymer electrolyte fuel cells (PEFCs) are an important substitute to fossil fuel combustion in vehicle applications, considering their zero emissions at the point of use, long range, and rapid refueling characteristics. However, a key technological challenge is to extend the operational durability of fuel cells, which is influenced by the functional integrity of the ionomer membrane [1,2]. Perfluorosulfonic acid (PFSA) ionomer membranes such as Nafion™ are generally used in PEFCs owing to their low operational temperature, high proton conductivity, and capability to act as electrical insulator and gas barrier between electrodes [3]. This functionality may be compromised by a variety of stressors that arise during dynamic duty cycle operations, potentially resulting in loss of gas separation and/or electrode shorting [4–7]. The membrane is subjected to two main types of degradation during PEFC operation. Firstly, chemical degradation is initiated by radical species such as hydroxyl (•OH) radicals generated as a by-product of the fuel cell reaction. The impact of chemical degradation is known to be accelerated by several factors, including elevated temperature, high cell potential, high reactant gas pressure, and low relative humidity (RH) [8,9]. Secondly, mechanical degradation of fuel cell membranes is caused by in-plane tensile stress due to constrained contraction under dehydrated conditions [10] and compressive stress due to constrained expansion under saturated conditions [11], culminating in hygrothermal fatigue and creep [4,12]. The specific degradation mechanisms are isolated experimentally in order to evaluate material stability and analyze the fundamental aspects of individual degradation processes. Mode specific accelerated stress tests (ASTs) are hence developed to benchmark membrane stability in PEFCs under pure chemical or pure mechanical stress. For instance, pure mechanical stress is induced through cyclic tension with low RH and compression with high RH at elevated temperatures [12]. The cyclic RH results in fatigue induced membrane failure by means of cracks, tears, and pinholes, which causes gradual increase in gas crossover [13,14]. The structural damage features may experience accelerated growth due to local stress concentration, thus exacerbating the degradation and associated gas crossover [15].

One way to enhance the endurance of ionomer membranes is to introduce mechanical reinforcement in the form of a composite. This enhances the mechanical strength and dimensional stability while suppressing crack initiation and plastic deformation. Expanded-polytetrafluoroethylene (ePTFE) has been used as a supporting material for composite proton exchange membranes in various operating environments with voltage, humidity, and freeze/thaw cycling [16]. One such type of ePTFE reinforced PFSA membrane is Nafion XL by DuPont. This membrane is reinforced with a central microporous PTFE-rich support layer filled with ionomer which facilitates water transport pathways across the membrane thickness [17]. Its sandwich structure provides excellent mechanical strength and enhanced proton conductivity facilitated by the outer Nafion layers [18]. This structural modification has shown a two-fold increase in yield strength and modulus [19] and reduced in-plane swelling as compared to the thickness direction [17,20]. Consequently, the reinforced membrane is comparatively stable during RH cycling in fuel cells, thereby increasing membrane lifetime and durability [21–23]. Tang et al. [24] compared pure Nafion membrane and PTFE/Nafion reinforced membranes subjected to RH cycling tests. The results showed that the cyclic stresses due to water uptake and shrinkage were lower for the reinforced membranes which extended the lifetime by 40% over the non-reinforced analogue [25]. Furthermore, the mechanical durability of composite membranes subjected to varying humidity swings from 0%, 50%, or 80% RH to 150% RH showed that the time to failure increased with lower magnitude swings [26].

Preliminary failure analysis studies pertinent to ionomer membranes were typically carried out using two-dimensional (2D) visualization techniques, such as optical and electron microscopy. For instance, Huang et al. [27] adopted cross-sectional scanning electron microscopy (SEM) to image non-reinforced membranes degraded via humidity cycling. Observations suggested that fractures may develop at crazing locations at the catalyst layer (CL)—membrane interface and then propagate into the membrane. Membrane crack development associated with pure mechanical stressor showed critical interaction between the membrane and CL, while the membrane thinning was negligible [28]. Early studies of reinforced membranes adopted SEM to characterize PFSA/ePTFE composite layers post manufacturing [29]. Cross-sectional SEM images before and after accelerated chemical degradation test revealed membrane thinning [30]. Non-uniform thinning trend was observed with almost 30% thickness reduction at either side of the reinforced layer. Wu et al. [31] used cross-sectional electron microscopy techniques to image the interfaces between the ionomer, catalyst, and PTFE layers post combined RH and load cycling procedure. Results showed severe thinning of ionomer layers and disappearing ionomer layer on the cathode side with delamination or cracks along the interfacial regions. Zhang et al. [32] used SEM to examine the membrane sample post fatigue crack propagation experiments and observed two major features, namely interfacial delamination and crack development in the exterior ionomer layers.

Although SEM and transmission electron microscopy (TEM) imaging can be used to identify the structure and morphology of membrane electrode assembly (MEA) components at high resolution, they are both destructive and 2D in nature, which restricts their investigative scope. To overcome this shortcoming, X-ray computed tomography (XCT) was proposed as an alternative technique to perform failure analysis of various fuel cell components. Several XCT works have specifically characterized gas diffusion layers [33–35], electrodes [36–38] and liquid water distribution during fuel cell operation [39,40]. XCT has also been adopted to understand GDL compression under various configurations [41–44] and the effects of MEA fabrication methods such as hot pressing [45,46].

Recently, the XCT approach has benefitted the membrane failure analysis by yielding new insights using reconstructed three-dimensional (3D) virtual images of the internal MEA features, which enables a comprehensive analysis of

membrane damage [47,48] with quantifiable metrics for the structural evaluation of membrane degradation and inter-component interaction of membrane cracks. This approach was adopted for non-reinforced membranes failed using pure chemical, pure mechanical, and combined chemical/mechanical membrane stressors. These studies provided critical insights and several new findings such as multiple disparate crack types formed under combined chemical/mechanical stressors and severe electrode shorting sites and related membrane thinning under pure chemical degradation. Ramani et al. [49] extended this 3D failure analysis to study the membrane damage development over the fuel cell lifetime, and correlated the structural changes with a suite of additional diagnostic results measured at corresponding life stages. This unique approach allowed for a detailed probe to understand the pivotal phases of membrane degradation which ultimately lead to failure. Several other significant features such as changes in membrane thickness, damage shapes, and structures linked with the progression of degradation were discovered. More recently, an XCT-enabled four-dimensional (4D) *in situ* visualization technique was developed to study the evolution of damage development in fuel cell electrodes [50]. This study adopted a small scale fixture which housed an operational fuel cell that facilitated the non-invasive *in situ* visualization [51]. Overall, the study concluded that the electrochemical diagnostics of the miniature fuel cell were in agreement with previous measurements obtained using a large technical cell [52]. Hence, the small-scale fixture was adopted to perform AST cycling procedures.

Singh et al. [53] followed a similar methodology and tracked the identical membrane location to understand the progress of damage development due to pure mechanical degradation. Periodic XCT visualization of the same MEA location during various life stages enabled tracking of membrane damage interaction with other fuel cell components as well as measurement of *in situ* crack propagation rates as a function of cycling time. Overall, these systematic investigations provided novel insights related to the membrane crack initiation and propagation process. However, XCT based visualization has not yet been applied to reinforced fuel cell membranes.

As discussed earlier, the reinforced composite membrane possesses an ePTFE mesh in the membrane core and is hence structurally different from a non-reinforced membrane. The associated degradation processes are therefore also likely to differ. The objective of the present work is to apply the 4D *in situ* XCT technique to a fuel cell with a reinforced membrane in order to determine the pure mechanical degradation process over its lifetime. Periodic 3D visualization of the same MEA location is performed at various life stages affected by wet/dry cycling in a customized X-ray transparent fuel cell assembly [54]. Key degradation mechanisms responsible for mechanical deterioration of reinforced membranes as a function of wet/dry cycling can thus be identified. The composite membrane crack development phenomenon is examined using methodical investigations to understand the initiation, propagation, and interplay with adjacent fuel cell components. Furthermore, the membrane crack development phenomenon will be compared with non-reinforced membranes.

Experimental

Materials

Fuel cell MEAs were assembled using a Nafion XL reinforced PFSA ionomer membrane flanked by anode and cathode gas diffusion electrodes (GDEs) of 9 mm × 4 mm dimensions. The GDEs were prepared by spray-coating a fine microporous layer comprising of carbon black and PTFE and a CL comprising of Pt/C and PFSA ionomer on a gas diffusion layer of non-woven carbon paper type. The membrane and GDEs were hot pressed for 3 min under 1.4 MPa at 150 °C on an Instron® 5569 mechanical tester to form MEAs. Sealing of the MEAs was facilitated using polyimide gaskets. Further details on the materials used for MEA preparation are detailed elsewhere [53].

Test apparatus and operation

As illustrated in Fig. 1, a custom designed small-scale fuel cell fixture was adopted in this study to facilitate AST operation and *in situ* XCT imaging [51]. The miniature size of the fuel cell MEA and fixture enabled acceptable X-ray signal-to-noise ratio and optimum resolution and field of view for the purpose of this study. The flow-field plates were CNC machined from X-ray transparent compressed carbon/graphite with healed adhesive featuring high electrical and thermal conductivity and low gas permeability. This comprised of two parallel, straight flow field channels of 1 mm width separated by a 250 μm center land region. Further details concerning the functionality, parts, and connections of the fixture are detailed elsewhere [50,51,54]. The fuel cell setup was regulated using a modified Greenlight Innovation® G40 fuel cell test station.

Accelerated stress testing

The small-scale fuel cell fixture was subjected to *in situ* hygrothermal stress cycles by means of a modified version of the accelerated mechanical stress test (AMST) protocol [28]. Briefly, the protocol applies a series of humidity cycles composed of a supersaturated wet phase (150% RH) and a subsequent dry phase (0% RH), both of 2 min duration at 80 °C cell temperature under 0.5 slpm N_2 gas flow. The same N_2 gas condition was used on both anode and cathode sides to maintain inert conditions for the membrane and avoid unwanted gradients. To characterize the membrane structure across multiple stages of degradation, the identical field of view of the fixture was visualized by XCT at beginning of life (BOL) and periodically after various numbers of AST cycles. To avoid the interaction of chemical stressors, *in situ* electrochemical diagnostics such as cyclic voltammetry, electrochemical leak detection tests (ELDT), and polarization curves were not performed. This ensured that only pure mechanical membrane degradation was maintained.

X-ray computed tomography

The thin, central portion of the X-ray transparent fuel cell fixture was visualized using a ZEISS Xradia 520 Versa XCT

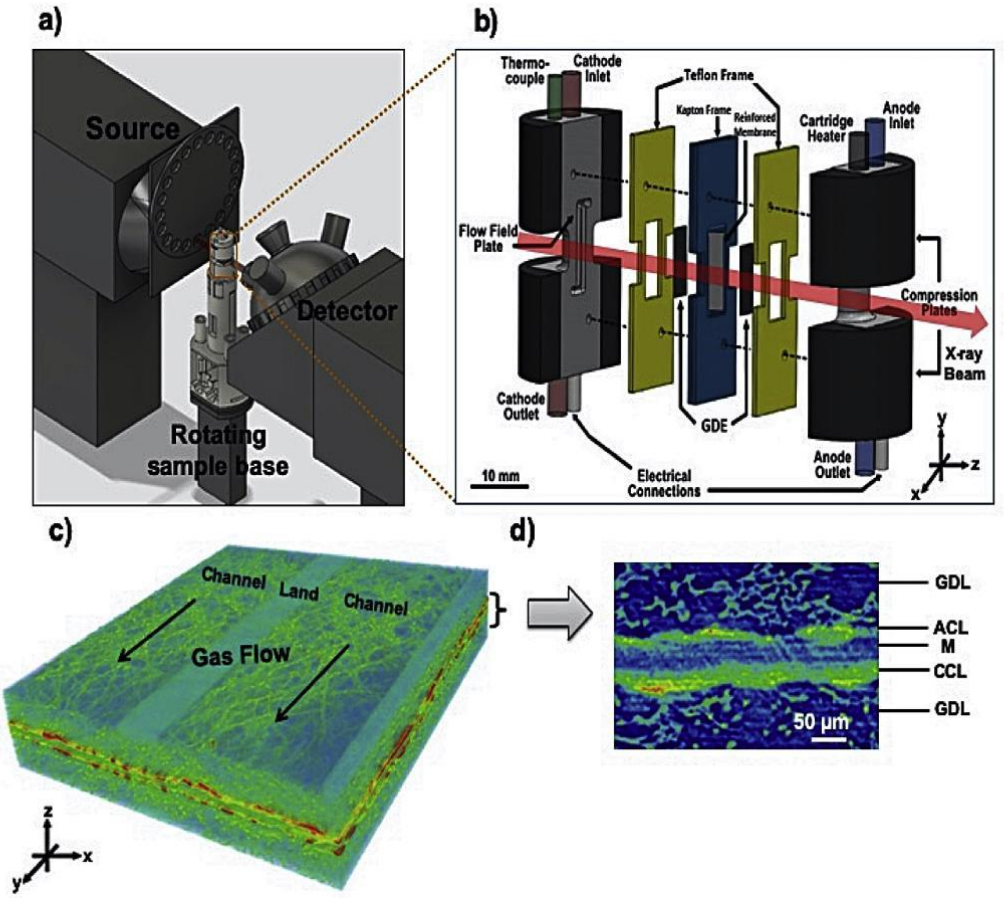

Fig. 1 – a) Schematic configuration of X-ray source and detector with small-scale fuel cell fixture mounted for XCT imaging; b) exploded view of small-scale fixture components, reproduced from Ref. [50] copyright (2017), with permission from Elsevier; c) false color tomogram of the 3D XCT reconstruction of the fuel cell; and d) virtually extracted cross-sectional perspective of the MEA illustrating various components (gas diffusion layer (GDL); anode catalyst layer (ACL); membrane (M); and cathode catalyst layer (CCL)). (For interpretation of the references to color, the reader is referred to the web version of the article.)

scanner. This XCT system employs X-ray microscopy methods to achieve sub-micrometer resolution from moderate to large specimens (mm to cm). The accelerating electron voltage and power employed for this study were 80 kV and 7 W, respectively, coupled with a low energy X-ray filter. The fuel cell fixture was mounted on the sample stage 27 mm from the X-ray source and 30 mm from the detector, which provided 1.59 μm pixel resolution. Each tomography scan included 1601 projections with 5 s per projection to achieve nominal intensity (around 5500 counts) at the membrane area. The sample was rotated around its own axis from −95° and +95° for an overall rotation of 190°. To improve the overall image quality, the frequency of projection was increased at the angular projection limits by high aspect ratio tomography (HART). Post-acquisition, the 2D image stack was reconstructed into a 3D tomography data set using ZEISS XMReconstructor® software with application of center shift and beam hardening correction. The pixel intensity of the obtained tomography was scaled against the greyscale values of the graphite flow field plates and air in order to aid i) identification of the different components within the MEA and fuel cell fixture and ii) detectability of degradation induced changes. Repetitive XCT acquisitions of an identical location 3.2 mm × 3.2 mm field of view located at the inlet region of the MEA were captured at periodic stages of the cycling procedure. Each tomography acquisition was performed under a constant uninterrupted N_2 flow at 0.3 slpm at room temperature and ambient dew point through both anode and cathode

compartments, prior to which a 2-h equilibrium period was maintained. The complete acquisition procedure had a cumulative X-ray exposure time of ~25 h, consisting six sets of periodic tomography scans. At the end of test (EOT) stage, acquisition was performed under both wet and dry conditions. The functional workflow of the procedure is detailed as follows: The small-scale fixture was placed inside the XCT system with the gas lines connected to the test station and purged with 0.3 slpm N_2 in both compartments. The test station was maintained at 60 °C dew point; however, the gas lines were exposed to ambient room temperature and thereby cooled prior to reaching the fuel cell fixture. This established a supersaturated environment inside the fixture, defined as the 'wet' condition. Following imaging, the test station was switched to ambient temperature and the flow was increased to 0.5 slpm N_2 for about 4 h in both compartments to remove liquid water and achieve an equilibrated 'dry' state for the identical-location dry scan under continuous N_2 flow.

To understand the impact of X-ray irradiation on the mechanical properties of the Nafion XL membranes used in this work, a separate verification experiment was designed as illustrated in Appendix A. Although minor embrittlement of the post-yield mechanical properties was detected following full X-ray exposure, the failure modes and degradation mechanisms observed in the present study are not anticipated to be affected. However, the post-yield embrittlement may somewhat reduce the number of fatigue cycles to failure. It is noteworthy that the photon flux produced by the laboratory-based XCT system in the present study is roughly four orders of magnitude lower than that of synchrotron radiation (SR) [54]. This enables longer X-ray exposure without extensive damage to material and performance, unlike the SR exposure which may cause major damage even within a few minutes of irradiation [55].

Membrane segmentation

The 3D tomography data obtained by XCT provide concurrent access to planar and cross-sectional virtual views of the MEA structure, which broadens the scope for membrane study. However, direct membrane segmentation is not viable due to similarity of greyscale values with surrounding features such as cracks, air, gas diffusion layers, etc. An oblique method is adopted to overcome this limitation, by using the CL boundaries to extract the membrane. This was aided by the pixel intensity scaling by graphite and air, providing a stable reference unaltered by degradation, followed by 2D median filtering to reduce noise and assist segmentation accuracy. Fig. 2 shows a sample filtered 2D greyscale image of the cross-sectional view of the MEA obtained using open source image software, ImageJ [56]. Segmentation of the CLs followed procedures established in Ref. [50] to produce binary data constituting void and solid phases. Initially, a custom script was composed in ImageJ macro language to facilitate automated segmentation of anode and cathode CLs from the MEA, as detailed elsewhere [57]. Following the CL segmentation, the isolated dataset of the membrane was obtained using a custom membrane segmentation tool developed in our group [57]. This tool uses the separated CLs to create interpreted boundaries representing the membrane-electrode interfaces to segment out the membrane. The final 2D isolated view of the membrane is illustrated in Fig. 2. The image also explains the comprehensive image processing procedure to obtain the final output. The fully segmented membrane enables a standardized through thickness slice-by-slice analysis to examine the extent of structural damage during the various phases of degradation. Dragonfly software (non-commercial version 2.0) [58] was used to visualize and inspect the slice-by-slice 2D images, thus interrogating the precise extent of structural membrane degradation at each stage throughout the lifetime.

Results and discussion

Investigation of mechanical membrane degradation mechanisms in reinforced, composite fuel cell membranes was pursued by applying wet/dry cycles to the small-scale fuel cell fixture and visualizing an identical location periodically by XCT until failure was reached. Identical membrane locations within the MEA obtained at BOL and after 2000, 3000, 4000, and

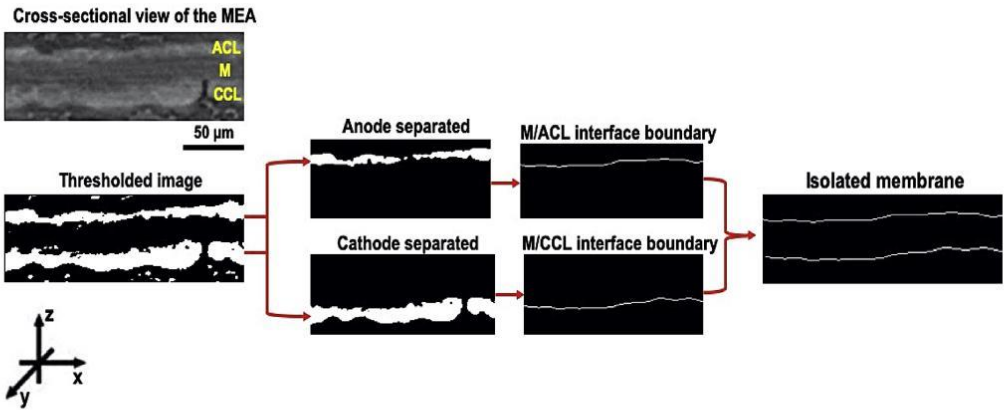

Fig. 2 – Stepwise image processing scheme from fully reconstructed MEA through CL separation to isolated membrane.

4500 (EOT) AST cycles were examined through the planar and cross-sectional internal views. In real time, the AST duration was 300 h, excluding the interruptions for imaging and diagnostics. The EOT MEA was visualized under both wet and dry conditions to further discern the swelling and drying nature of the degraded membrane. The results obtained for reinforced membranes were also compared to equivalent experimental results for non-reinforced membranes to elucidate the explicit effect of the ePTFE reinforcement on the mechanical degradation pattern.

Membrane damage initiation and growth

Fig. 3 displays the typical planar views of the segmented reinforced membrane at various life stages from BOL to 4500 cycles (EOT). The fresh BOL membrane was observed to have a uniform, defect-free structure at the single micrometer scale resolution and mostly remained free of measurable damage until 2000 cycles. Fatigue based micro-cracks were initiated between 2000 and 4000 cycles in the PFSA ionomer portion of the membrane and further grew into through-thickness

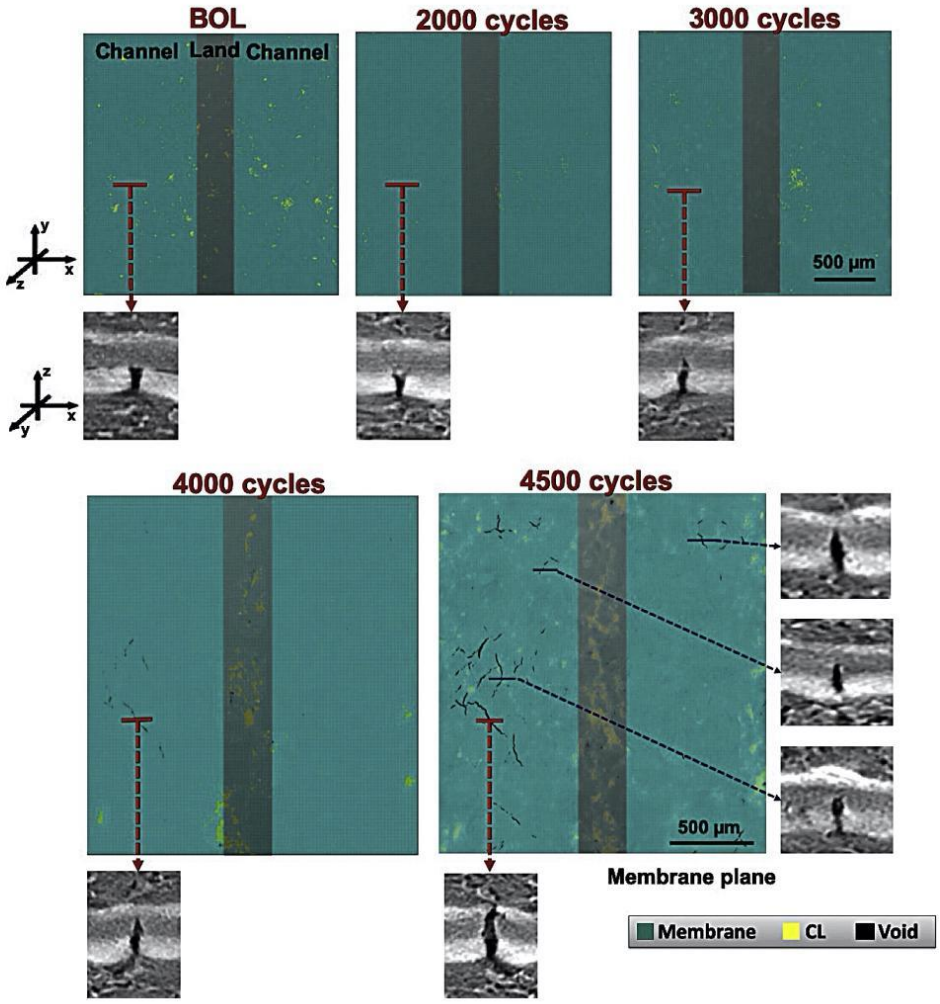

Fig. 3 – Periodic identical-location tracking of reinforced membrane plane at various life stages during pure mechanical membrane degradation caused by wet/dry cycling. The insets show the corresponding cross-sectional views of the MEA at the indicated membrane locations. (For interpretation of the references to color, the reader is referred to the web version of the article.)

membrane cracks between 4000 and 4500 cycles. The 'through-thickness' cracks that reach through the entire thickness of the membrane are of particular concern due to their ability to carry substantial reactant gas cross-over rates and are therefore indicative of membrane failure.

The dominant damage feature during pure mechanical degradation of non-reinforced membranes was observed to be membrane crack development [48]. This is similar to the present work where membrane cracks dominate the mechanical degradation and critical failure mode of reinforced fuel cell membranes. The fatigue process of PFSA ionomer membranes is known to consist of two main stages, namely membrane crack initiation and crack propagation [4,59,60]. The crack initiation occurs earlier in the degradation process, whereas the initiated cracks propagate gradually in the later stages of degradation. Previous work by Singh et al. [53] adopted similar 4D visualization of the mechanical degradation of a non-reinforced membrane (Nafion NR211). Results showed minor membrane crack formation in the initial period of cycling until 1500 cycles. Most of the membrane cracks developed within the membrane penetrated completely through the thickness between 1500 and 2000 cycles, i.e., representing rapid damage growth within 500 cycles. Thus, it is concluded that the damage induced by fatigue-driven membrane degradation follows a non-linear progression in time for both reinforced and non-reinforced membranes. The favorable effect of mechanical reinforcement is found to be a delay in the onset of this rapid crack development phase, occurring 2-3x cycles later than for the non-reinforced analogue. The delayed membrane crack development is due to the increased fracture resistance of the ePTFE layer present at the center of the reinforced membrane which thereby extends the mechanical durability of the fuel cell. Previous work with the Nafion XL membrane studied the membrane strength through the essential work of fracture method and showed that the increased fracture resistance is associated with the stabilizing effect of the central ePTFE mesh [61]. The cross-sectional image locations indicated by purple lines in Fig. 3 show partial membrane cracks after 4500 cycles. These frequently occurring partial membrane cracks extend from the membrane surface to the ePTFE layer (the reader is referred to Appendix B for the exact location of the ePTFE layer within the membrane) where the high fracture resistance of the reinforcement suppresses the through-thickness crack growth [17]. The gradual development of membrane cracks observed during the 2000–4000 cycling period is consistent with this mechanism. However, full through-thickness membrane cracks were nevertheless observed after 4500 cycles, for instance at the location marked in red in Fig. 3.

XCT imaging facilitates non-invasive characterization without MEA disassembly, which renders it a suitable technique for understanding the differences between the land and channel regions under the flow field plates. High susceptibility to crack formation under the channel portion was observed. This is attributed to the higher in-plane tensile stress within the membrane under the channel, which renders this location the likely site for early stage fatigue induced crack formation in the membrane. This tensile stress is induced by confined drying during the dry phase of the applied wet/dry cycling, as reported in our previous work [48].

A comprehensive numerical analysis of the membrane and CLs at each life stage is achieved using the 3D datasets acquired by XCT. Damage in the MEA layers is characterized by damage density, which is outlined as the number of cracks per unit area of the MEA [47,49]. The detectable and measurable through-thickness crack density within the membrane and CLs at each cycling stage is shown in Fig. 4. As noted previously, the membrane was crack free at BOL, post assembly, and developed sizeable through-thickness cracks at advanced stages of degradation. In contrast, both anode and cathode CLs had pre-existing cracks at BOL due to fabrication, handling, and installation. These pre-operational cracks induce local stress concentration points in the membrane under wet/dry cycling where membrane cracks may initiate and grow over time. At EOT, the CL crack density had approximately doubled in relation to the pre-existing crack density at BOL. Several new CL cracks were observed to have formed during the later stages of membrane degradation possibly due to the underlying cyclic swelling and shrinkage of the adjoining membrane. The overall membrane damage density of the through-thickness cracks post 4000 and 4500 cycles was observed to be 4 and 11 cracks/mm^2, with average crack width of 3 and 5 μm and average crack length of 15 and 35 μm, respectively. The amount of convective gas leaks across the membrane is influenced by the overall *crack area* on the membrane surface, which considers both the density and dimensions of the cracks. The *crack area* for the present study was 14% at 4000 cycles and more than doubled to 32% at 4500 cycles. This fatigue crack growth (FCG) at 4500 cycles could be attributed to the presence of several interrelated micro cracks (high local crack density) which led to increased crack propagation rate. In other words, the partial cracks at once are ruptured and merge together to form through-thickness cracks, which were previously blocked by the intact ePTFE layer. Our previous work with non-reinforced membranes [53] showed 3 cracks/mm^2 located under the channel region after 2000 cycles, whereas the present study did not show any through-thickness membrane cracks at this cycling stage. On

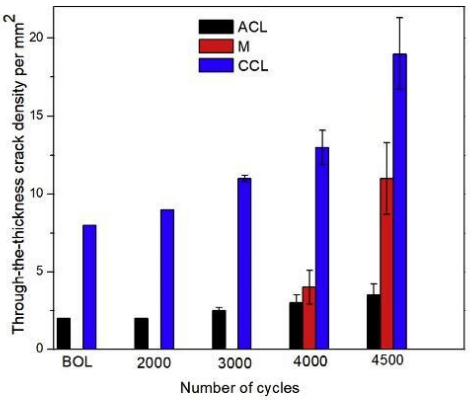

Fig. 4 – Measured through-thickness crack density of the individual MEA layers from BOL to 4500 AST cycles or EOT.

the contrary, the total *crack area* and *crack density* for the non-reinforced membranes did not vary significantly from 2000 to 2200 cycles, owing to crack closure phenomenon.

Membrane crack interaction with local CL cracks and delamination

The non-invasive XCT visualization technique applied at various life stages facilitates 4D investigation of the interaction between membrane and CL cracks. This approach facilitates a detailed understanding of the structural connectivity of local degradation features between the MEA layers, which provides useful insights into their development process. To understand the role of CL cracks in the membrane degradation process, a freshly prepared MEA with pre-existing anode and cathode CL cracks was used, which provides comprehensive assessment of various crack interaction events. The present results show that all membrane cracks

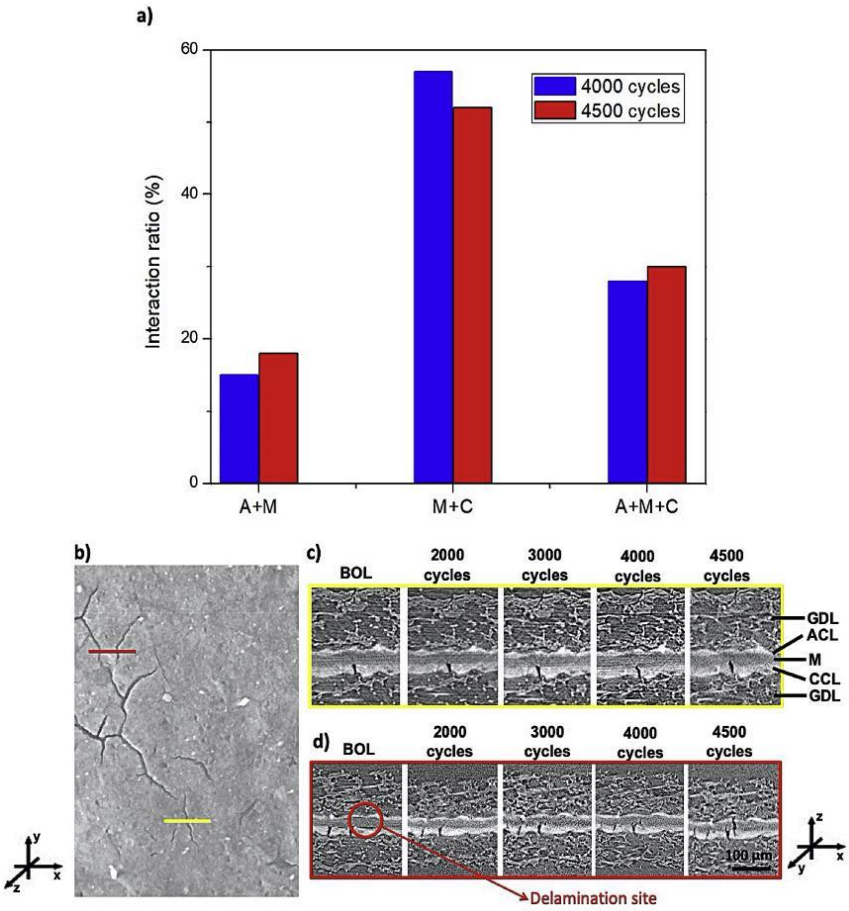

Fig. 5 – a) Interaction ratio of the through-thickness membrane cracks at 4000 and 4500 AST cycles classified based on their through-plane connectivity with adjacent anode and cathode CLs; b) planar view of a section of the cathode CL at BOL, showing a network of pre-existing CL cracks; c) degradation progression at the cross-sectional plane indicated by the yellow line in b), showing partial crack growth into the membrane; and d) degradation progression at the cross-sectional plane indicated by the red line in b), showing membrane crack growth at the membrane-cathode CL delamination site. (For interpretation of the references to color, the reader is referred to the web version of the article.) (A+M: through-thickness crack interacting with anode CL; M+C: through-thickness crack interacting with cathode CL; A+M+C: through-thickness crack interacting with both CLs)

interacted with pre-existing CL cracks, showing a strong membrane-CL interaction leading to mechanically induced cracks during RH cycling. In other words, all the membrane cracks initiated and developed from the pre-existing CL crack sites. These observations are in agreement with the previous reports of membrane-CL crack interaction under mechanical degradation of both reinforced [62] and non-reinforced membranes [48]. As illustrated by the crack interaction data in Fig. 5a, 30% of the through-thickness membrane cracks extended into both CL layers after 4000 and 4500 cycles. Through-thickness cracks extending across the entire CL layers and membrane are considered to be the most influential to the complete breakdown as they lead to convective gas crossover flow across the MEA. None of the membrane cracks were limited only in the membrane layer at these cycling stages, which shows the absence of chemical degradation and dominance of pure mechanical stressors during the RH-cycling AST. More than 50% interaction was observed for M+C type of cracks showing the strong involvement of the cathode CL in the membrane crack formation process. A typical network of pre-existing CL cracks present at BOL is illustrated in the planar cathode CL image in Fig. 5b. When the wet/dry cycling was applied, the membrane cracks initiated in the outer ionomer layer (cathode side). For instance, the cathode CL crack indicated by the yellow line in Fig. 5c was found to induce cracks in the ionomer layer and further propagated into the remainder of the membrane. This observation shows that the membrane cracks were formed due to locally elevated mechanical fatigue stress at the CL cracks. However, further propagation of these cracks was restricted by the membrane reinforcement layer. The hydrophobic ePTFE material would not undergo swelling/shrinking during wet/dry cycling while the hygroscopic ionomer material undergoes both. This creates additional stresses on the outer layers which are more susceptible for crack initiation and growth. The strength of the reinforcement layer was explored by Zhang et al. [32] using *ex situ* fatigue crack propagation tests. The results showed that the low rate of crack

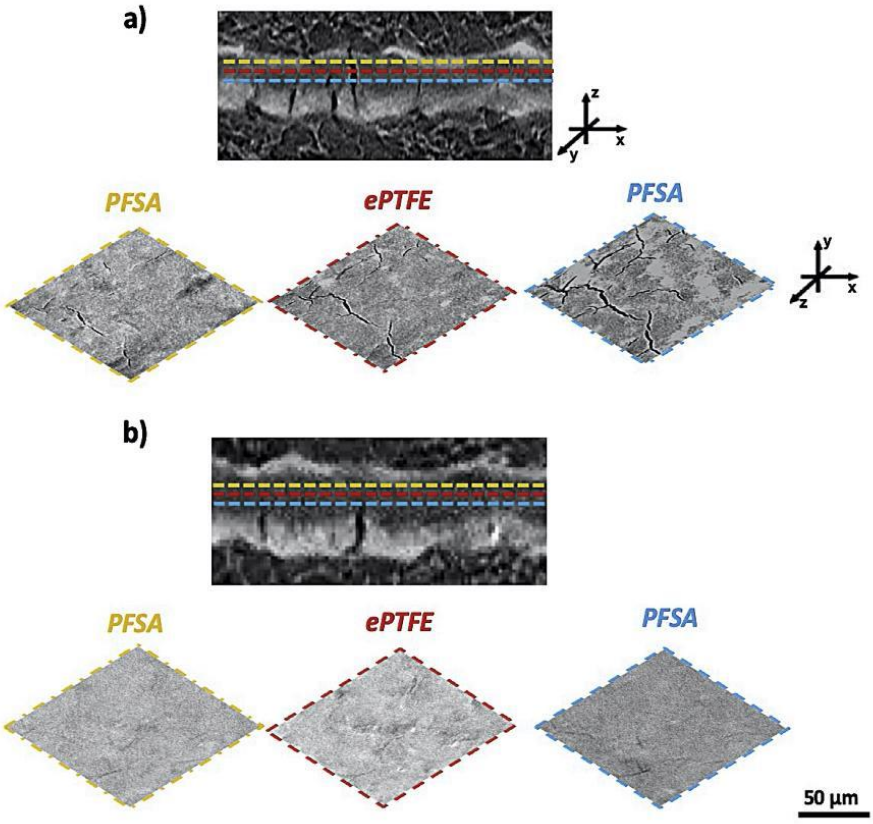

Fig. 6 – Cross-sectional views extracted from XCT images of the degraded MEA after 4500 wet/dry cycles in the a) dry and b) wet states, illustrating the presence and absence of membrane cracks, respectively. Planar views at the indicated planes within the PFSA ionomer and ePTFE membrane layers are appended.

propagation was achieved through a fibre bridging mechanism. This enabled the ePTFE fibres to bear some of the membrane load and the load encountered at the crack edge was immensely reduced. Likewise, Fig. 5c illustrates a delamination site between membrane and cathode CL (denoted by the red circle) present at BOL. After 2000 RH cycles, the delamination site was no longer visible with no detectable gap between membrane and CL, presumably due to creep of ionomer into the delaminated void space. At 3000 cycles, minor membrane cracks initiated at the original delamination site. With further cycling, several new membrane cracks initiated from adjacent CL cracks in the delamination region and the previously formed micro-cracks grew further. After 4500 cycles, the first through-thickness, membrane spanning crack was formed at the delamination site. The joint influence of interfacial delamination and electrode cracks observed in the crack development of the reinforced membrane is consistent with the previously reported results for non-reinforced membrane [53], highlighting the similarities in interaction effects between the two membrane materials.

In situ visualization of membrane swelling and shrinking behavior

The XCT-based visualization methodology adopted herein allows for *in situ* imaging to study membrane dimensions in the wet and dry states, which could provide insights into the structural dynamics associated with the wet/dry cycling AST. Fig. 6 shows the cross-sectional and layer by layer planar views of the same location during wet and dry phase post 4500 cycles. These images were captured at fully equilibrated hydration levels under N_2 flow, as described in the experimental section. During the 'wet' state, all the membrane cracks closed completely as a result of ionomer swelling and associated expansion of the membrane. Previously, similar "crack closure" phenomenon was observed by Singh et al. [53] during the 'dry' phase of the non-reinforced membranes, which was attributed to dynamic in-plane stress redistribution during the spatially evolving crack network. The redistribution leads to change in the complex stress fields thereby leading to membrane crack closure. In addition, cracks may experience plasticity-induced closure due to residual compressive stress originating from the 'wet' phase. On the contrary, the 'dry' state in the present study showed distinct open membrane cracks due to membrane dehydration and tensile stresses. This could be attributed to the ePTFE reinforcement which restricts the dry state crack closure and stress redistribution phenomenon. The present systematic experiment has also demonstrated that the applied humidity level directly impacts the membrane swelling and the closure of membrane cracks.

The membrane thickness expanded approximately 30% from dry to wet state, while there was no noticeable variation in the CL thicknesses. This excessive through-plane swelling is due to the high-water uptake of the PFSA ionomer in the membrane. For reference, the through-plane thickness of the non-reinforced PFSA ionomer membrane held in a similar fixture exhibited 25% membrane expansion during fuel cell operation compared to the dry condition [51]. This is in reasonable agreement with the present results, though through-plane expansion is amplified in the reinforced membrane due to its more confined in-plane expansion. The novel *in situ* XCT approach enabled to capture this swelling/shrinking mechanism as well as the crack closure effect for the first time for reinforced fuel cell membranes. In terms of crack closure, the continuous viability of fuel cell operation after membrane crack formation could thus conceivably be extended by ensuring adequate membrane hydration in order to close the pathways for reactant gas cross-over [63,64].

Conclusions

4D *in situ* imaging of reinforced membrane degradation was accomplished using a custom-built small-scale fuel cell fixture, which facilitated accelerated mechanical stress testing and non-invasive XCT visualization during different stages of degradation. The *in situ* approach enabled tracking of the creation and propagation of damage in reinforced fuel cell membranes and generated new insight related to its mechanical degradation mechanisms. Through-thickness membrane cracks were the main failure mode resulting from extensive, repetitive wet/dry cycling. This outcome was consistent with previous reports for non-reinforced membranes albeit with 2-3x lower rate of degradation, which was attributed to the improved fracture resistance facilitated by ePTFE reinforcement. The mechanical failure was preceded by fatigue-driven, non-linear crack initiation and propagation, featuring more progressive crack growth than for non-reinforced membranes. The local membrane fracture was driven by CL cracks and membrane-CL delamination that were pre-existing at the BOL stage. The *in situ* imaging also facilitated observation of a hygral expansion induced crack closure phenomenon in the "wet" state and distinct open membrane cracks in the "dry" state; closure of cracks in the dry state were not observed and likely restricted by the ePTFE reinforcement. Overall, the new findings demonstrate the distinct advantage of lab based XCT technology in gaining an improved fundamental understanding of reinforced membrane degradation by capturing critical failure modes and mechanisms at their different developmental stages.

Acknowledgements

Funding for this research was provided by the Natural Sciences and Engineering Research Council of Canada, Canada Foundation for Innovation, British Columbia Knowledge Development Fund, and Ballard Power Systems through an Automotive Partnership Canada grant. This research was undertaken, in part, thanks to funding from the Canada Research Chairs program. We acknowledge Marina Najm, Mike Xu, Kevin Dahl, and Alex Boswell for technical support.

Appendix A. Effect of X-ray irradiation on the reinforced membrane

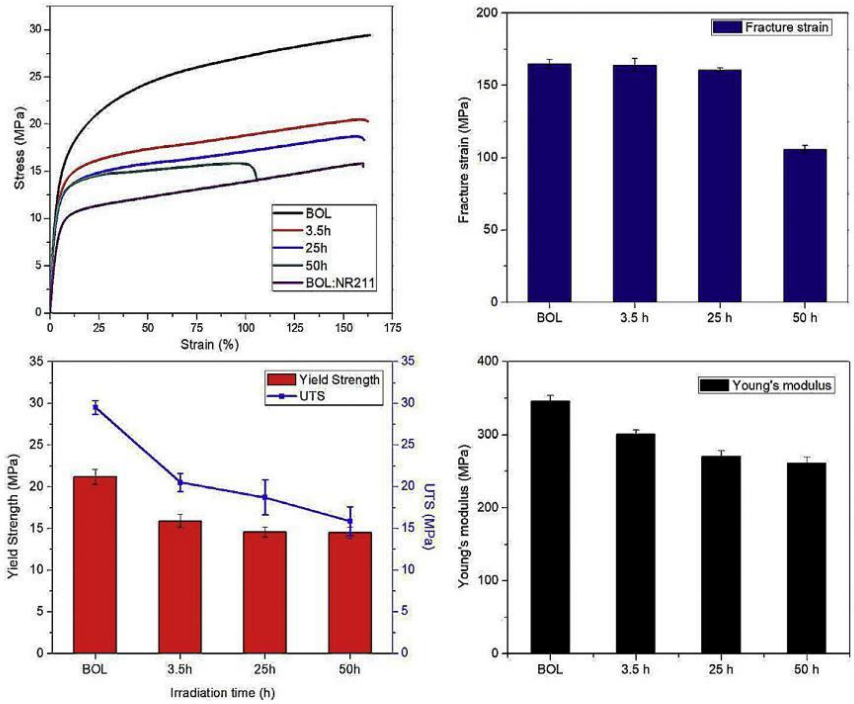

Fig. A1 – Tensile stress-strain curves and derived tensile properties of CCM samples prepared from Nafion XL reinforced membrane. The data were measured on a dynamic mechanical analyzer at room conditions of 23 °C and 50% RH at 0.01 min^{-1} strain rate before and after X-ray exposure for 3.5, 25, and 50 h on a ZEISS Xradia 520 Versa® micro-XCT system. An additional unexposed data set for non-reinforced NR211 is provided for reference.

Catalyst coated membrane (CCM) samples fabricated with Nafion XL membranes were installed in the small-scale fuel cell fixture and exposed to X-ray irradiation, after which *ex situ* tensile tests were done to assess the impact of X-ray damage on the mechanical properties of the reinforced membrane during the 4D *in situ* analysis. Adopting the same imaging parameters as for the *in situ* studies, the CCM samples were exposed to 3.5, 25, and 50 h of tomographic scans. Post exposure, the CCM samples were carefully disassembled, and tensile measurements were performed on a dynamic mechanical analyzer (TA Instruments Q800 DMA). The experimental conditions of the tensile testing procedure are detailed elsewhere [53]. As a baseline condition, a supplementary test was performed on a CCM sample which was not exposed to X-rays, but still assembled-disassembled in the small-scale fixture for consistency with the treatment of other samples. Fig. A1 illustrates the stress-strain curves acquired from the tensile testing procedure and the calculated mechanical properties, viz. Young's modulus (E), yield strength (YS), fracture strain, and ultimate tensile stress (UTS), against the duration of X-ray exposure. Results show that no changes in mechanical behavior occurred during initial fuel cell assembly. The primary effect of the ePTFE layer on the mechanical response (compared to non-reinforced Nafion NR211) is the expanded 'rollover yielding'

regime over a wider range of strain increment. Post exposure, a direct immediate impact of X-ray damage on UTS, E, and YS after 3.5 h of exposure (typically one tomography scan) is noted. The moderate drop in UTS, E, and YS indicates reduced mechanical strength of the ePTFE reinforcement, which directly impacts the fatigue lifetime of the composite membrane. Only a 3% decrease in fracture strain until 25 h is observed, suggesting negligible embrittlement with up to 160% strain still sustained. However, from 25 to 50 h exposure, more substantial embrittlement of the membrane occurred. The X-ray exposure induced decay in stress-strain curves and mechanical properties of the ePTFE reinforced membrane may thus be expected to affect the rate of mechanical degradation, potentially resulting in faster failures in the present work compared to regular, unexposed *in situ* conditions. Even after 50 h exposure, however, the Nafion XL membrane is still stronger than an unexposed NR211 membrane up to 100% strain (Fig. A1), suggesting that the X-ray exposure does not fully eliminate its mechanical reinforcement capacity. Furthermore, the changes experienced by the membrane are negligible within the relatively low stress range expected to occur during *in situ* wet/dry cycling. Accordingly, distinctions between the degradation processes of reinforced and non-reinforced membranes, as discussed in this work, would still be detectable with the adopted 4D visualization methodology. Most importantly, several key features that are generally applicable to membranes (both reinforced and non-reinforced), such as the interplay between the MEA components, underlying failure modes, and degradation mechanisms are not considerably altered. It is still clarified that the sensitivity of the mechanical response of the ePTFE reinforced membrane to X-ray exposure is significantly higher compared to homogenous PFSA ionomer membranes and should be considered while designing similar experiments involving the use of reinforced membranes.

Appendix B. Contrast enhancing procedure

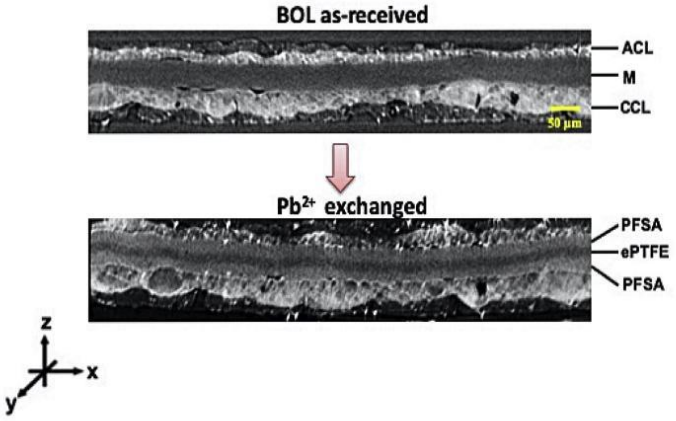

Fig. B1 – Cross-sectional XCT image of a BOL catalyst coated membrane sample made from Nafion XL membrane: a) as-received; and b) post Pb^{2+} exchange.

The XCT imaging contrast is provided by attenuation of materials, which is dependent on their density, thickness (material specific), as well as attenuation coefficients (material and X-ray energy specific). The attenuation of the ePTFE and PFSA ionomer layers in a composite membrane are similar, thus making it difficult to discern the respective layers. To overcome this, an *ex situ* analysis was performed wherein fresh CCM samples made from Nafion XL membrane were soaked in saturated lead acetate solution for 48 h. This procedure was intended to enhance the image contrast of the ionomer portions of the membrane by Pb^{2+} ion exchange at the protonic sites [65]. Next, the sample was rinsed with deionized water to expel excess residual lead acetate and dried for 24 h at room temperature. The dried sample was secured to a stiff polycarbonate plastic sheet using 3M adhesive scotch tape. This plastic supported sample was clipped on to a holder and installed on the XCT stage for imaging. XCT imaging showed the phase-separated dark (low-attenuating) PTFE-rich central layer surrounded by two bright (high-attenuating) hydrophilic ion-rich, contrast enhanced layers. Fig. B1 shows the sandwich arrangement of the membrane, which clearly depicts the central microporous PTFE-rich support layer (~10 μm) impregnated on each side with a dense PFSA ionomer layer (~10 μm).

REFERENCES

[1] Mench MM. Fuel cell engines. John Wiley and Sons; 2008. https://doi.org/10.1002/9780470209769.
[2] Wang Y, Chen KS, Mishler J, Cho SC, Adroher XC. A review of polymer electrolyte membrane fuel cells: technology,

applications, and needs on fundamental research. Appl Energy 2011;88:981–1007. https://doi.org/10.1016/j.apenergy.2010.09.030.
[3] Coms FD. The chemistry of fuel cell membrane chemical degradation Frank D. Coms general motors corporation, fuel cell research labs, 10 carriage Street, Honeoye Falls, NY 14472, USA. ECS Trans 2008;16:235–55. https://doi.org/10.1149/1.2981859.
[4] Khorasany RMH, Sadeghi Alavijeh A, Kjeang E, Wang GG, Rajapakse RKND. Mechanical degradation of fuel cell membranes under fatigue fracture tests. J Power Sources 2015;274:1208–16. https://doi.org/10.1016/j.jpowsour.2014.10.135.
[5] Sadeghi Alavijeh A, Khorasany RMH, Habisch A, Wang GG, Kjeang E. Creep properties of catalyst coated membranes for polymer electrolyte fuel cells. J Power Sources 2015;285:16–28. https://doi.org/10.1016/j.jpowsour.2015.03.082.
[6] Macauley N, Alavijeh AS, Watson M, Kolodziej J, Lauritzen M, Knights S, et al. Accelerated membrane durability testing of heavy duty fuel cells. J Electrochem Soc 2015;162:F98–107. https://doi.org/10.1149/2.0671501jes.
[7] Khorasany RMH, Singh Y, Sadeghi Alavijeh A, Kjeang E, Wang GG, Rajapakse RKND. Fatigue properties of catalyst coated membranes for fuel cells: ex-situ measurements supported by numerical simulations. Int J Hydrogen Energy 2016;41:8992–9003. https://doi.org/10.1016/j.ijhydene.2016.04.042.
[8] Healy J, Hayden C, Xie T, Olson K, Waldo R, Brundage M, et al. Aspects of the chemical degradation of PFSA ionomers used in PEM fuel cellsx. Fuel Cell 2005;5:302–8. https://doi.org/10.1002/fuce.200400050.
[9] Rodgers MP, Bonville LJ, Kunz HR, Slattery DK, Fenton JM. Fuel cell perfluorinated sulfonic acid membrane degradation correlating accelerated stress testing and lifetime. Chem Rev 2012;112:6075–103. https://doi.org/10.1021/cr200424d.
[10] Büchi FN, Srinivasan S. Operating proton exchange membrane fuel cells without external humidification of the reactant gases. J Electrochem Soc 1997;144:2767. https://doi.org/10.1149/1.1837893.
[11] Knights SD, Colbow KM, St-Pierre J, Wilkinson DP. Aging mechanisms and lifetime of PEFC and DMFC. J Power Sources 2004;127:127–34. https://doi.org/10.1016/j.jpowsour.2003.09.033.
[12] Sadeghi Alavijeh A, Goulet MA, Khorasany RMH, Ghataurah J, Lim C, Lauritzen M, et al. Decay in mechanical properties of catalyst coated membranes subjected to combined chemical and mechanical membrane degradation. Fuel Cell 2015;15:204–13. https://doi.org/10.1002/fuce.201400040.
[13] Kundu S, Fowler MW, Simon LC, Grot S. Morphological features (defects) in fuel cell membrane electrode assemblies. J Power Sources 2006;157:650–6. https://doi.org/10.1016/j.jpowsour.2005.12.027.
[14] Kusoglu A, Santare MH, Karlsson AM. Aspects of fatigue failure mechanisms in polymer fuel cell membranes. J Polym Sci B Polym Phys 2011;49:1506–17. https://doi.org/10.1002/polb.22336.
[15] Kreitmeier S, Schuler GA, Wokaun A, Büchi FN. Investigation of membrane degradation in polymer electrolyte fuel cells using local gas permeation analysis. J Power Sources 2012;212:139–47. https://doi.org/10.1016/j.jpowsour.2012.03.071.
[16] Zhu X, Zhang H, Liang Y, Zhang Y, Luo Q, Bi C, et al. Challenging reinforced composite polymer electrolyte membranes based on disulfonated poly(arylene ether sulfone)-impregnated expanded PTFE for fuel cell applications. J Mater Chem 2007;17:386–97. https://doi.org/10.1039/b611690f.
[17] Shi S, Weber AZ, Kusoglu A. Structure/Property relationship of nafion XL composite membranes. J Membr Sci 2016;516:123–34. https://doi.org/10.1016/j.memsci.2016.06.004.
[18] Yu L, Lin F, Xu L, Xi J. Structure-property relationship study of Nafion XL membrane for high-rate, long-lifespan, and all-climate vanadium flow batteries. RSC Adv 2017;7:31164–72. https://doi.org/10.1039/c7ra04996j.
[19] Tang Y, Kusoglu A, Karlsson AM, Santare MH, Cleghorn S, Johnson WB. Mechanical properties of a reinforced composite polymer electrolyte membrane and its simulated performance in PEM fuel cells. J Power Sources 2008;175:817–25. https://doi.org/10.1016/j.jpowsour.2007.09.093.
[20] Tang Y, Karlsson AM, Santare MH, Gilbert M, Cleghorn S, Johnson WB. An experimental investigation of humidity and temperature effects on the mechanical properties of perfluorosulfonic acid membrane. Mater Sci Eng, A 2006;425:297–304. https://doi.org/10.1016/j.msea.2006.03.055.
[21] Cleghorn SJC, Mayfield DK, Moore DA, Moore JC, Rusch G, Sherman TW, et al. A polymer electrolyte fuel cell life test: 3 years of continuous operation. J Power Sources 2006;158:446–54. https://doi.org/10.1016/j.jpowsour.2005.09.062.
[22] Li Y, Dillard DA, Case SW, Ellis MW, Lai Y-H, Gittleman CS, et al. Fatigue and creep to leak tests of proton exchange membranes using pressure-loaded blisters. J Power Sources 2009;194:873–9. https://doi.org/10.1016/j.jpowsour.2009.06.083.
[23] Grohs JR, Li Y, Dillard DA, Case SW, Ellis MW, Lai Y-H, et al. Evaluating the time and temperature dependent biaxial strength of Gore-Select® series 57 proton exchange membrane using a pressure loaded blister test. J Power Sources 2010;195:527–31. https://doi.org/10.1016/j.jpowsour.2009.07.054.
[24] Tang HL, Pan M, Wang F. A mechanical durability comparison of various perfluocarbon proton exchange membranes. J Appl Polym Sci 2008;109:2671–8. https://doi.org/10.1002/app.28343.
[25] Rodgers MP, Bonville LJ, Mukundan R, Borup R, Ahluwalia R, Beattie P, et al. Perfluorinated sulfonic acid membrane and membrane electrode assembly degradation correlating accelerated stress testing and lifetime testing. ECS Transactions 2013;58:129–48. https://doi.org/10.1149/05801.0129ecst. Electrochemical Society Inc.
[26] Lai Y-H, Mittelsteadt CK, Gittleman CS, Dillard DA. Viscoelastic stress analysis of constrained proton exchange membranes under humidity cycling. J Fuel Cell Sci Technol 2009;6. https://doi.org/10.1115/1.2971045. 021002.
[27] Huang X, Solasi R, Zou Y, Feshler M, Reifsnider K, Condit D, et al. Mechanical endurance of polymer electrolyte membrane and PEM fuel cell durability. J Polym Sci B Polym Phys 2006;44:2346–57. https://doi.org/10.1002/polb.20863.
[28] Alavijeh AS, Khorasany RMH, Nunn Z, Habisch A, Lauritzen M, Rogers E, et al. Microstructural and mechanical characterization of catalyst coated membranes subjected to in situ hygrothermal fatigue. J Electrochem Soc 2015;162:F1461–9. https://doi.org/10.1149/2.0471514jes.
[29] Panha K, Fowler M, Yuan X-Z, Wang H. Accelerated durability testing via reactants relative humidity cycling on PEM fuel cells. Appl Energy 2012;93:90–7. https://doi.org/10.1016/j.apenergy.2011.05.011.
[30] Zhang S, Yuan X-Z, Ng J, Hin C, Wang H, Wu J, et al. Effects of open-circuit operation on membrane and catalyst layer degradation in proton exchange membrane fuel cells. J Power Sources 2010;195:1142–8. https://doi.org/10.1016/j.jpowsour.2009.08.070.
[31] Wu B, Zhao M, Shi W, Liu W, Liu J, Xing D, et al. The degradation study of Nafion/PTFE composite membrane in

PEM fuel cell under accelerated stress tests. Int J Hydrogen Energy 2014;39:14381–90. https://doi.org/10.1016/j.ijhydene.2014.02.142.
[32] Zhang Z, Shi S, Lin Q, Wang L, Liu Z, Li P, et al. Exploring the role of reinforcement in controlling fatigue crack propagation behavior of perfluorosulfonic-acid membranes. Int J Hydrogen Energy 2018;43:6379–89. https://doi.org/10.1016/j.ijhydene.2018.02.034.
[33] Andisheh-Tadbir M, Orfino FP, Kjeang E. Three-dimensional phase segregation of micro-porous layers for fuel cells by nano-scale X-ray computed tomography. J Power Sources 2016;310:61–9. https://doi.org/10.1016/j.jpowsour.2016.02.001.
[34] Odaya S, Phillips RK, Sharma Y, Bellerive J, Phillion AB, Hoorfar M. X-ray tomographic analysis of porosity distributions in gas diffusion layers of proton exchange membrane fuel cells. Electrochim Acta 2015;152:464–72. https://doi.org/10.1016/j.electacta.2014.11.143.
[35] James JP, Choi H-W, Pharoah JG. X-ray computed tomography reconstruction and analysis of polymer electrolyte membrane fuel cell porous transport layers. Int J Hydrogen Energy 2012;37:18216–30. https://doi.org/10.1016/j.ijhydene.2012.08.077.
[36] Pokhrel A, Hannach M El, Orfino FP, Dutta M, Kjeang E. Failure analysis of fuel cell electrodes using three-dimensional multi-length scale X-ray computed tomography. 2016. https://doi.org/10.1016/j.jpowsour.2016.08.092.
[37] Litster S, Epting WK, Wargo EA, Kalidindi SR, Kumbur EC. Morphological analyses of polymer electrolyte fuel cell electrodes with nano-scale computed tomography imaging. Fuel Cell 2013;13:935–45. https://doi.org/10.1002/fuce.201300008.
[38] Pfrang A, Veyret D, Janssen GJM, Tsotridis G. Imaging of membrane electrode assemblies of proton exchange membrane fuel cells by X-ray computed tomography. J Power Sources 2011;196:5272–6. https://doi.org/10.1016/j.jpowsour.2010.09.020.
[39] Markötter H, Alink R, Haußmann J, Dittmann K, Arlt T, Wieder F, et al. Visualization of the water distribution in perforated gas diffusion layers by means of synchrotron X-ray radiography. Int J Hydrogen Energy 2012;37:7757–61. https://doi.org/10.1016/j.ijhydene.2012.01.141.
[40] Krüger P, Markötter H, Haußmann J, Klages M, Arlt T, Banhart J, et al. Synchrotron X-ray tomography for investigations of water distribution in polymer electrolyte membrane fuel cells. J Power Sources 2011;196:5250–5. https://doi.org/10.1016/j.jpowsour.2010.09.042.
[41] Zenyuk IV, Parkinson DY, Connolly LG, Weber AZ. Gas-diffusion-layer structural properties under compression via X-ray tomography. J Power Sources 2016;328:364–76. https://doi.org/10.1016/j.jpowsour.2016.08.020.
[42] Tötzke C, Gaiselmann G, Osenberg M, Bohner J, Arlt T, Markötter H, et al. Three-dimensional study of compressed gas diffusion layers using synchrotron X-ray imaging. J Power Sources 2014;253:123–31. https://doi.org/10.1016/j.jpowsour.2013.12.062.
[43] Holzer L, Pecho O, Schumacher J, Marmet P, Stenzel O, Büchi FN, et al. Microstructure-property relationships in a gas diffusion layer (GDL) for Polymer Electrolyte Fuel Cells, Part I: effect of compression and anisotropy of dry GDL. Electrochim Acta 2017;227:419–34. https://doi.org/10.1016/j.electacta.2017.01.030.
[44] Kulkarni N, Kok MDR, Jervis R, Iacoviello F, Meyer Q, Shearing PR, et al. The effect of non-uniform compression and flow-field arrangements on membrane electrode assemblies - X-ray computed tomography characterisation and effective parameter determination. J Power Sources 2019;426:97–110. https://doi.org/10.1016/j.jpowsour.2019.04.018.
[45] Meyer Q, Mansor N, Iacoviello F, Cullen PL, Jervis R, Finegan D, et al. Investigation of hot pressed polymer electrolyte fuel cell assemblies via X-ray computed tomography. Electrochim Acta 2017;242:125–36. https://doi.org/10.1016/j.electacta.2017.05.028.
[46] Hack J, Heenan TMM, Iacoviello F, Mansor N, Meyer Q, Shearing P, et al. A structure and durability comparison of membrane electrode assembly fabrication methods: self-assembled versus hot-pressed. J Electrochem Soc 2018;165:3045–52. https://doi.org/10.1149/2.0051806jes.
[47] Singh Y, Orfino FP, Dutta M, Kjeang E. 3D visualization of membrane failures in fuel cells. J Power Sources 2017;345:1–11. https://doi.org/10.1016/j.jpowsour.2017.01.129.
[48] Singh Y, Orfino FP, Dutta M, Kjeang E. 3D failure analysis of pure mechanical and pure chemical degradation in fuel cell membranes. J Electrochem Soc 2017;164:1331–41. https://doi.org/10.1149/2.0451713jes.
[49] Ramani D, Singh Y, Orfino FP, Dutta M, Kjeang E. Characterization of membrane degradation growth in fuel cells using X-ray computed tomography. J Electrochem Soc 2018;165:F3200–8. https://doi.org/10.1149/2.0251806jes.
[50] White RT, Wu A, Najm M, Orfino FP, Dutta M, Kjeang E. 4D in situ visualization of electrode morphology changes during accelerated degradation in fuel cells by X-ray computed tomography. J Power Sources 2017;350:94–102. https://doi.org/10.1016/j.jpowsour.2017.03.058.
[51] White RT, Orfino FP, Hannach M El, Luo O, Dutta M, Young AP, et al. 3D printed flow field and fixture for visualization of water distribution in fuel cells by X-ray computed tomography. J Electrochem Soc 2016;163:F1337–43. https://doi.org/10.1149/2.0461613jes.
[52] Young AP, Stumper J, Gyenge E. Characterizing the structural degradation in a PEMFC cathode catalyst layer: carbon corrosion. J Electrochem Soc 2009;156:B913. https://doi.org/10.1149/1.3139963.
[53] Singh Y, White RT, Najm M, Haddow T, Pan V, Orfino FP, et al. Tracking the evolution of mechanical degradation in fuel cell membranes using 4D in situ visualization. J Power Sources 2019;412:224–37. https://doi.org/10.1016/j.jpowsour.2018.11.049.
[54] White RT, Najm M, Dutta M, Orfino FP, Kjeang E. Communication—effect of micro-XCT X-ray exposure on the performance of polymer electrolyte fuel cells. J Electrochem Soc 2016;163:1206–8. https://doi.org/10.1149/2.0751610jes.
[55] Roth J, Eller J, Buchi FN. Effects of synchrotron radiation on fuel cell materials. J Electrochem Soc 2012;159:F449–55. https://doi.org/10.1149/2.042208jes.
[56] ImageJ. ImageJ. https://imagej.net; 2017.
[57] White RT, Eberhardt SH, Singh Y, Haddow T, Dutta M, Orfino FP, et al. Four-dimensional joint visualization of electrode degradation and liquid water distribution inside operating polymer electrolyte fuel cells. Sci Rep 2018:1–12. https://doi.org/10.1038/s41598-018-38464-9.
[58] Dragonfly 2.0, Object Research systems. (ORS) Inc.; 2017. http://www.theobjects.com/dragonfly.
[59] Khorasany RMH, Kjeang E, Wang GG, Rajapakse RKND. Simulation of ionomer membrane fatigue under mechanical and hygrothermal loading conditions. J Power Sources 2015;279:55–63. https://doi.org/10.1016/j.jpowsour.2014.12.133.
[60] Khorasany RMH, Singh Y, Alavijeh AS, Rajapakse RKND, Kjeang E. In-situ simulation of membrane fatigue in polymer electrolyte fuel cells. 2017. https://doi.org/10.1016/j.ijhydene.2017.01.173.

[61] Moukheiber E, Bas C, Flandin L. Understanding the formation of pinholes in PFSA membranes with the essential work of fracture (EWF). Int J Hydrogen Energy 2014;39:2717–23. https://doi.org/10.1016/j.ijhydene.2013.03.031.
[62] Mukundan R, Baker AM, Kusoglu A, Beattie P, Knights S, Weber AZ, et al. Membrane accelerated stress test development for polymer electrolyte fuel cell durability validated using field and drive cycle testing. J Electrochem Soc 2018;165:F3085–93. https://doi.org/10.1149/2.0101806jes.
[63] Jung A, Kong IM, Yun CY, Kim MS. Characteristics of hydrogen crossover through pinhole in polymer electrolyte membrane fuel cells. J Membr Sci 2017;523:138–43. https://doi.org/10.1016/j.memsci.2016.09.009.
[64] Hu M, Cao G. Research on the long-term stability of a PEMFC stack: analysis of pinhole evolution. Int J Hydrogen Energy 2014;39:7940–54. https://doi.org/10.1016/j.ijhydene.2014.03.072.
[65] Venkatesan S, Lim C, Holdcroft S, Kjeang E. Progression in the morphology of fuel cell membranes upon conjoint chemical and mechanical degradation. J Electrochem Soc 2016;163:637–43. https://doi.org/10.1149/2.0671607jes.

Appendix D.

Mitigation of Mechanical Membrane Degradation in Fuel Cells – Part 1: Gas Diffusion Layers with Low Surface Roughness

This is a preprint version of accepted article with Elsevier– *Journal of Power Sources* (Aug. 2021) reproduced with permission for the present thesis.

Mitigation of Mechanical Membrane Degradation in Fuel Cells – Part 1: Gas Diffusion Layers with Low Surface Roughness

D. Ramani[a], N.S. Khattra[a], Y. Singh[a,b], A. Mohseni-Javid[a], F.P. Orfino[a], M. Dutta[b] and E. Kjeang[a,*]

[a] *Fuel Cell Research Lab (FCReL), Simon Fraser University, 250-13450 102 Ave, Surrey, BC V3T 0A3, Canada*

[b] *Ballard Power Systems, 9000 Glenlyon Pkwy, Burnaby, BC V5J 5J8, Canada*

*ekjeang@sfu.ca

Abstract

Hygrothermal variations that arise during dynamic fuel cell operation are known to generate mechanical stresses in the ionomer membrane. Previous research has indicated that membrane electrode assembly (MEA) interaction effects may influence membrane degradation under such loads. The present objective is therefore to evaluate novel MEA design strategies for mitigating mechanical membrane degradation in fuel cells. In this case (Part 1), a gas diffusion layer (GDL) with low surface roughness is applied to suppress buckling-driven membrane failures. Laboratory-based X-ray computed tomography is used in a customized, time-resolved workflow for non-invasive four-dimensional characterization of membrane damage evolution during accelerated stress testing. Membrane crack development is the key failure mode preceded by fracture of the cathode catalyst layer. In comparison to high surface roughness GDL, the severity of membrane buckling is substantially reduced by adoption of the smoother GDL, contributing 2x greater lifetime. Accompanying finite element simulations of the unit fuel cell assembly show plastic strain accumulation in the buckled membrane and identified a critical range of GDL void sizes that influence membrane buckling. Overall, the improvement in GDL surface demonstrates substantial mitigation effect against fatigue-driven mechanical membrane degradation and failure, which is also corroborated by the numerical simulation results.

Keywords: fuel cell; membrane; durability; X-ray computed tomography; mitigation; mechanical degradation.

Introduction

Polymer electrolyte membrane fuel cells (PEMFCs) are considered as a promising zero-emission replacement of internal combustion (IC) engines in transportation applications, owing to their high-power density and low temperature operation. The overall life of the operational fuel cell is strongly governed by the membrane endurance and lifetime [1,2]. The key functions of the membrane are to enable high proton conduction, provide electronic insulation, act as a combustion barrier between the reactant species, and contribute high chemical and mechanical robustness [3,4]. During dynamic fuel cell (FC) operation, the ionomer membrane undergoes two major types of degradation mechanisms, namely chemical [5–7] and mechanical degradation [8]. The chemical degradation is caused by radical attack (•OH, •OOH) on the main and side chains of the ionomer molecule, leading to decrease in proton conductivity and thickness reduction from material loss [9]. The mechanical degradation is induced by varying relative humidity (RH). The varying RH leads to repetitive swelling and shrinking of the membrane that introduces recurrent stress and strain on the membrane. This mechanism leads to destructive membrane failure modes such as fractures [10–12], creep [13], and pinholes [14]. These mechanically induced features can facilitate gas crossover across the membrane and thereby compromising its functionality inside the FC.

Accelerated stress test (AST) is an experimental technique designed to expedite the rate of degradation and thus shorten the time to failure of a device compared to its use conditions. This approach can also isolate the individual stressors to reproduce desired degradation mechanisms and study any associated mitigation approaches. Typically, to achieve mechanical membrane degradation in a FC, the RH is cycled at high temperature. The RH cycling significantly weakens the membrane strength [15]. Several works have adopted this approach to achieve pure mechanical membrane degradation within the membrane electrode assembly (MEA) [16–18]. Defects and irregularities within the MEA could also be sources of local membrane degradation. Tavassoli *et al.* [19] studied the influence of artificial catalyst layer (CL) defects on membrane degradation and reported

that electrode delamination may amplify local membrane degradation. Hizir *et al.* [20] speculated that microporous layer (MPL) cracks cause degradation effects during freeze/thaw cycles. Uchiyama *et al.* [21,22] performed systematic buckling tests to study CL crack formation and membrane deformation under humidity cycling. Circular holes were fabricated in a thin polyimide film and wrapped between gas diffusion layers (GDLs) to create artificial clearances into which the membrane could expand. Improper contact during assembly, possibly due to GDL fibers and MPL surfaces [20,23], could lead to clearances between catalyst coated membrane (CCM) and GDL. The cracks/voids in the MPL layer can be beneficial to FC performance as they may reduce GDL liquid water saturation [24] and enhance water management in the MEA. However, these irregular locations could also make the adjoining components vulnerable to local damage.

Traditionally, failure analysis of FC components has been conducted using 2D imaging techniques such as scanning electron microscopy (SEM) [12,25,26]. However, the SEM methodology is destructive in nature and requires elaborate sample preparation and vacuum operation. Furthermore, this procedure could introduce additional artifacts, thereby compromising the quality of the results. Recently, X-ray computed tomography (XCT) has acquired growing interest for characterization of FC components. XCT methodology allows for non-destructive 3D visualization of internal parts and analysis of their properties. XCT systems have been used to characterize the different FC MEA parts, such as GDLs [27–31] and CLs [32–36], and also to study liquid water distribution within an operational cell [37–39]. This technique was also extensively used by our group to perform detailed 3D *ex-situ* failure analysis of the membrane [40–42]. Moreover, 4D *in-situ* visualization studies, which involved periodic identical location imaging of degrading MEAs, showed that both reinforced [43] and non-reinforced membranes [44] experience non-linear crack initiation and growth that intensifies during the later stages of a humidity cycling AST. Pre-existing MEA features, such as CL cracks and delamination, were shown to have a critical role in the local membrane crack formation process. In a recent work, Singh *et al.* [45] utilized this approach to demonstrate the effectiveness of a lower CL crack density in suppressing the rate of mechanical membrane degradation. They also showed the dominant role of local buckling deformation on the membrane fracture when GDLs/MPLs containing large void spaces are utilized in an MEA.

In light of these recent findings, the present work is a focused investigation on the impact of GDL/MPL morphologies in mitigation of membrane degradation in fuel cells. The

objective of this work (Part 1) is to adopt 4D *in-situ* XCT visualization to evaluate the mitigation of mechanical membrane degradation using a GDL with low surface roughness. The present study aims to enhance the fundamental understanding of membrane degradation evolution and its interaction with the GDL morphology. This investigation is facilitated by the 3D visualization of the same MEA locations within a custom small-scale fuel cell assembly during different stages of a wet/dry cycling AST. This miniature fuel cell fixture [46] is designed for non-destructive periodic visualization using a laboratory-based XCT system that enables 4D characterization of membrane degradation and its associated interaction with the GDL [34]. Furthermore, a numerical finite element model is developed to simulate the contact interaction at the CL|MPL interface. The XCT findings are correlated with the finite element results to perceive the specific impact of MPL surface features on the development and distribution of membrane failures.

Methodology

Materials

The MEAs were fabricated using CCMs and GDLs. The CCM consisted of a central Nafion® NR211 membrane along with anode and cathode CLs with 50:50 Pt/C ratio and respective Pt loading of 0.1 and 0.4 mg cm^{-2}. SGL Sigracet® 29BC GDL having a smooth MPL with low surface roughness (LSR) was used on both anode and cathode sides without bonding. The LSR GDL displayed MPL crack features, whereas the comparable GDL with high surface roughness (HSR) featured surface pores (or voids), as previously reported [45]. The LSR GDL had an estimated average crack width of ~37 µm with frequency of ~7 cracks per mm^2 and ~1% surface coverage, whereas the HSR GDL had an estimated average surface pore size of ~95 µm with frequency of ~21 pores per mm^2 and ~9% surface coverage. The HSR metrics given are representative of the anode GDL, which was the most influential for buckling deformation. A cathode catalyst layer (CCL) with a low crack density was adopted for the present work, given its focus on membrane-GDL interactions. The MEAs had an active area of 9x4 mm^2 and were framed and sealed using Kapton® polyimide adhesive sheets. Furthermore, these sheets were used to cap the compression to 20±5% of the nominal GDL thickness during fuel cell assembly. Further details of the materials used are given in our previous work [45], and the only component different in the present work is the LSR GDLs.

Test apparatus and operation

To enable AST operation and periodic *in-situ* XCT imaging, a small-scale FC hardware was developed, as illustrated in **Figure 1** [47]. This miniature fixture comprised of a single cell FC featuring graphitic flow field plates with two parallel, 1 mm wide, semi-circular channels on both anode and cathode sides operated in co-flow mode. The X-ray transparent fixture housed an operational small sized MEA with electrical, heating, and tubing connections embedded in the plates. The material used for the plates was compressed resin impregnated graphite/carbon, which facilitated good transmission of X-rays while allowing adequate resolution and facilitating good conduction of heat and electricity. Prior to the operation, external and internal leak tests were performed by pressurizing the FC under impassable channels with air. Leaks within the FC compartments and out of the cell were checked. Detailed descriptions of the parts, capabilities, and connections of the small fixture are elaborated in our previous works [34,46,47]. The FC was operated using a custom designed Greenlight Innovation® G40 fuel cell test station, which was calibrated for the reduced flows required for this small scale MEA [44].

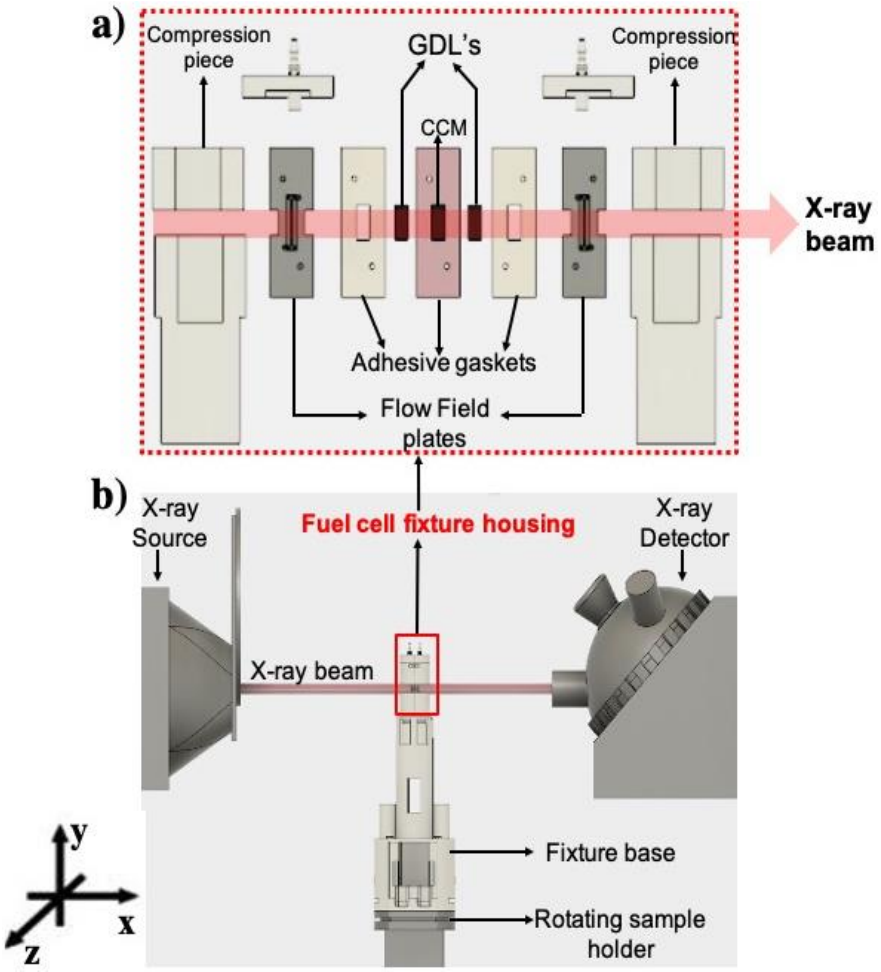

Figure 1: Expanded view of the miniature fuel cell fixture showing the dissection of various components, based on Ref. [48]. b) Representative contour of the small fixture housed within the XCT system.

Accelerated stress testing

For the present study, a modified version of accelerated mechanical stress test (AMST) protocol was used to achieve pure mechanical membrane degradation [43,44]. Briefly, the protocol consists of two-minute wet (super saturated) and two-minute dry (0% inlet gas RH) phases with 0.5 slpm N_2 flow on both anode and cathode sides. The inlet cell temperature was maintained at 80°C through the entire AMST procedure. No *in-situ* cell conditioning or diagnostics were done to avoid introduction of chemical stress, and thus maintaining a purely mechanical form of degradation throughout the test.

X-ray computed tomography

The internal features of the MEA components within the small-scale fixture were visualized using a ZEISS Xradia 520 Versa® XCT system (**Figure 1b**). The XCT system was operated at 80 kV and 7 W rating, using a low energy X-ray filter. The small-scale fixture was mounted on the rotating sample stage at 27 mm and 30 mm from the X-ray source and detector, respectively. This configuration enabled a pixel resolution of 1.59 µm. To obtain sufficient intensity around the membrane section, each XCT projection was obtained for 5 s interval and a total of 1601 projections were obtained in each scan. In addition, high aspect ratio tomography (HART) feature was adopted to enhance the overall image quality in the extremities of the angular rotation. After obtaining the XCT projections, ZEISS XMReconstructor® software was used to reconstruct the tomographic data sets. A field of view (FOV) of 3.2 mm × 3.2 mm was captured around the inlet section of the MEA at various stages of the mechanical membrane degradation AMST. Prior to starting the imaging acquisitions, the fuel cell fixture inside the XCT scanner was equilibrated under constant ambient dew point (DP) N_2 gas purge for 2 h at ambient room temperature. Five separate XCT scans of identical MEA locations were obtained from beginning of life (BOL) until the end of test (EOT), *i.e.*, 4000 AMST cycles, at an interval of every 1000 cycles. In addition, the BOL and EOT states were imaged under wet conditions to study the membrane's hydration dependent dynamics. Further details of this imaging procedure are elaborated elsewhere [43].

Finite Element Model

To understand the interaction between the CCM and a void in the GDL, a multi-physics finite element model (FEM) was employed to simulate the hygro-thermo-mechanical fuel cell operation. The model used here was adapted from our recent work [49] and has been modified to consider the effect of contact interaction between the CCM and GDL. The simulation domain of the model consists of a two-dimensional plane strain representation of one half of the miniaturized fuel cell geometry, considering the cell symmetry, as illustrated in **Figure 2**. The model consists of the polymer membrane sandwiched between the catalyst and gas diffusion layers from both sides. The material properties used for the membrane are based on a previously developed modified version of constitutive G'Sell-Jonas model, which takes into consideration the viscoelastic-plastic constitutive response of the membrane and further accounts for its time, temperature, and

humidity dependent behavior. The CLs were modeled as linear elastic and assumed to be bonded with the membrane. The GDLs were modeled as linear elastic orthotropic and the interface between the GDL and CCM permitted relative sliding (non bonded). The GDL substrate and MPL was modeled as a single entity with uniform mechanical properties. Thermal expansion was considered for all components, whereas membrane was the only component assumed to incur hygral swelling. The physical behavior along with appropriate references to various properties used for the modeled components are summarized in **Table 1**.

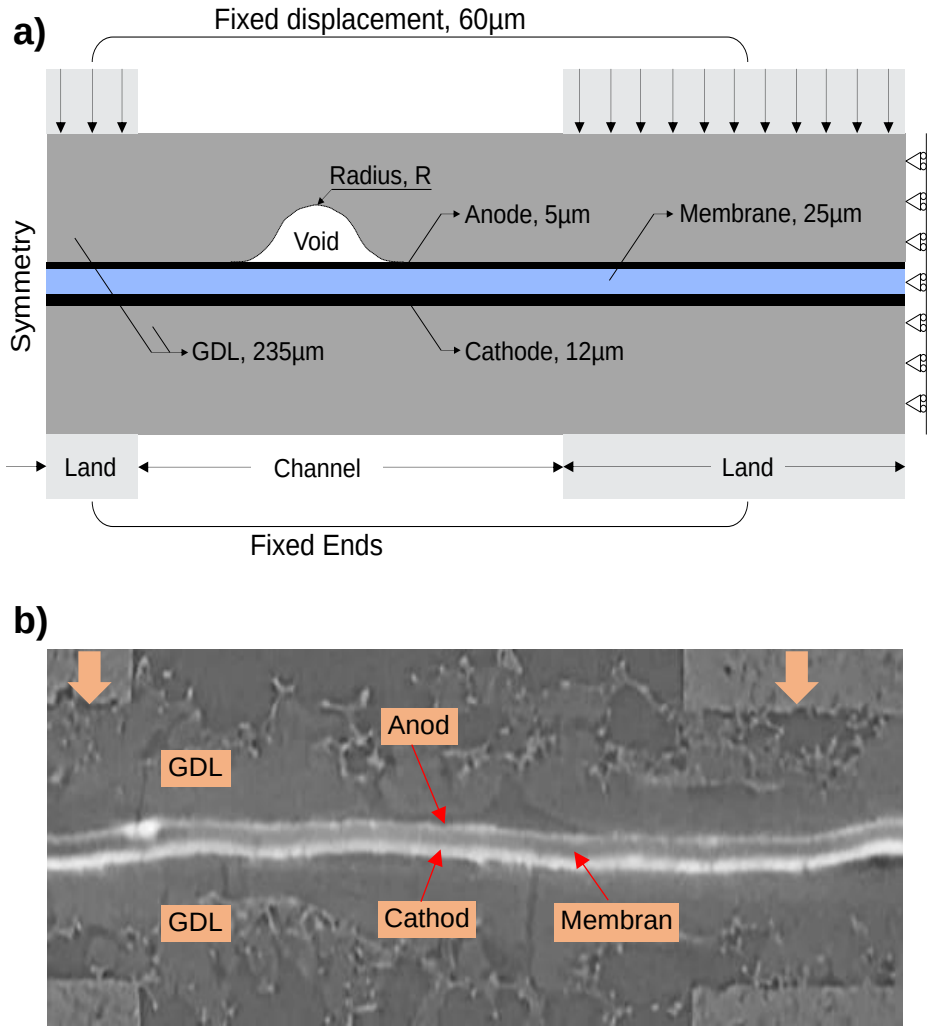

Figure 2: a) Representative 2D cross-sectional geometry for the finite element fuel cell model and b) cross-sectional image of the MEA as observed during XCT visualization.

Based on the microstructural observations from XCT, an imperfection in the form of a void was introduced in the anode-side GDL to investigate its effect on the behavior of the

membrane under the test conditions. The effect of different void sizes was then investigated to understand the critical behavior that leads to membrane deformation near a void. To simulate fuel cell operation, the model assembly was first compressed at the land region by a known displacement of around 60 µm. A single wet/dry cycle based on the AMST conditions consistent with the experiments was simulated for the model. The resulting mechanical response is discussed in the upcoming section.

Table 1: Physical properties of various components in the finite element model.

Properties	**Component**		
	Membrane	CL	GDL
Mechanical	Viscoelastic-Plastic [49]	Linear Elastic [50]	Linear Elastic, Orthotropic [51,52]
Hygral	Isotropic [53] $\in_{hygral} = \ln\left({}^{1}/_{1-\phi_w}\right)\frac{T}{T_{ref}}$	Assumed not to swell	Assumed not to swell
Thermal	Isotropic α= 3.4x10^{-4} K^{-1} [53]	Isotropic α= 3.4x10^{-4} K^{-1} [53]	Isotropic α= 0.8x10^{-6} K^{-1} [53]

Results and Discussion

The pure mechanical AMST protocol was applied to the MEA housed inside the small-scale FC fixture which was periodically scanned using the XCT system. This enabled 4D (*i.e.*, three spatial and one time dimensions) tracking of the same MEA locations to monitor the membrane damage initiation and growth over the cycling time. XCT scans were collected in a relatively dry state at BOL and after 1000, 2000, 3000, and 4000 (EOT) AMST cycles. Previous work with high surface roughness (HSR) GDL had

shown significant through-thickness membrane crack development after 2000 cycles of the same wet/dry cycling AMST [45]. In contrast, the present work with LSR GDL did not reveal any membrane cracks up to 2000 cycles, and accordingly, the AMST was continued until sufficient development of membrane cracks by 4000 cycles. In addition, to understand the swelling and shrinking behavior of the membrane at the initial and degraded states, the hydrated state of the membrane was visualized at both BOL and EOT. The upcoming sections elaborate the results obtained from the experimental 4D visualization approach and correlate those with the finite element simulations.

Membrane crack development

Representative planar views of the membrane extracted from the XCT scans at BOL and after 4000 cycles are shown in **Figure 3**. As expected, the membrane at BOL was free of any damage. With wet/dry cycling, the planar view at EOT revealed significant membrane cracks, which is known to be the predominant failure mode in an ionomer membrane during pure mechanical degradation [41,44]. Crack frequency within the MEA can be quantified as crack density, *i.e.*, number of cracks per unit planar area [42]. The membrane crack density after 4000 cycles was found to be 8 cracks/mm^2. Most of the membrane cracks exhibited I-shaped morphology, which typifies the underlying pure mechanical degradation and absence of any major chemical stressors [41]. Spatially, over 90% of the through-thickness membrane cracks were confined primarily under the channel regions and, in agreement with published literature, suggests intensified mechanical membrane degradation in these regions [44]. Previous modeling works [14,16,54,55] have also shown that the uncompressed channel regions are prone to membrane crack formation during the RH cycling. Similar micro-cracks have also been reported in a large-scale technical cell after undergoing a similar RH cycling AMST in the absence of chemical stressors [12]. The planar views show the location and distribution of membrane cracks, whereas cross-sectional slices facilitate identification of the through-plane crack reach and their interaction with the adjacent components in *x* and *y* directions. **Figure 3c** shows periodic tracking of an identical cross-section under the channel region during various life stages of the cycling procedure, as per the location indicated in **Figure 3a**. The cross-sectional views show early crack development in the CCL after the first 1000 wet/dry cycles. Multiple CCL cracks developed, which grew in both in-plane and through-plane directions between 1000 and 3000 cycles and then initiated a few partial membrane cracks at the end of 3000 cycles. With progressive cycling, these partial membrane cracks grew

in size and formed through-thickness membrane cracks at EOT. This observation agrees with the theory that the crack development process occurs in two steps inside the ionomer membranes, namely: (i) crack initiation; and (ii) crack propagation [17,55,56]. The through-thickness membrane cracks are known to contribute to membrane failure as they facilitate gas crossover across the membrane, thereby compromising the overall lifetime and durability of an operational fuel cell [57]. Furthermore, the non-linear crack growth in time that accelerates during the later stages of RH cycling, as observed in the present work, agrees with previous published results for both large-scale cells [16] and similar miniature cells [43,44].

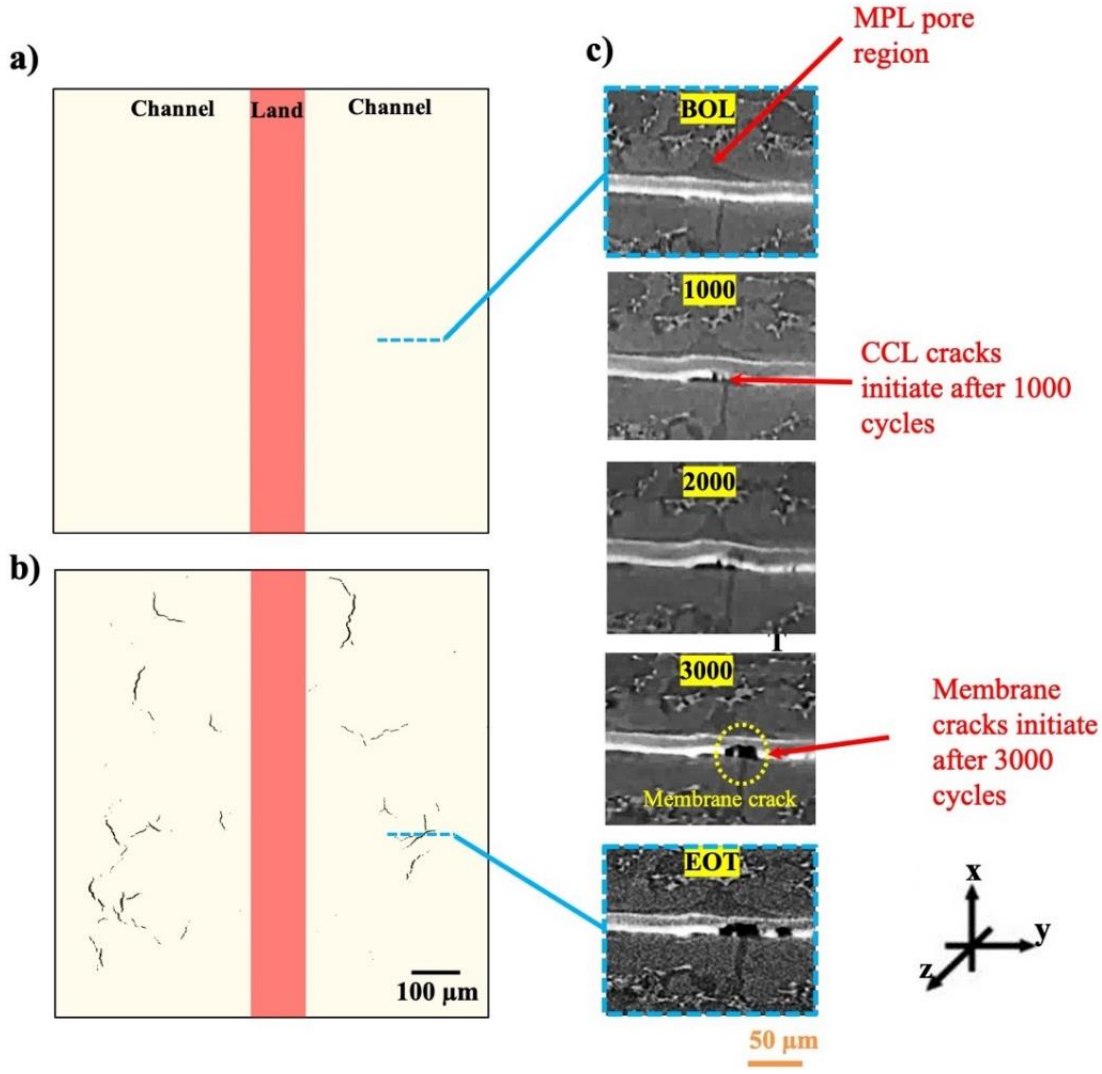

Figure 3: Virtually extracted planar views of the membrane at a) BOL and b) EOT (4000 cycles), i.e., before and after the wet/dry cycling AMST, respectively. c) Periodic identical-

location cross-sectional views of the MEA at the indicated location during various stages of cycling.

In situ characterization capability allows to visualize the MEA under wet state which aids understanding of the hydration-induced structural changes of the ionomer membrane [43]. **Figure 4** shows the cross-sectional images of the EOT dry and wet structure of the MEAs with LSR and HSR GDLs, respectively. In both MEAs at EOT, *i.e.*, after membrane crack formation, the membrane swelled due to water sorption leading to increase in thickness and reduced crack area along with wrinkling into adjacent GDL pore cavities. This wrinkle deformation is caused by membrane/CCM buckling due to its in-plane expansion during the wet phase. While both MEAs demonstrate swelling that caused the CCMs to buckle into the GDL voids, the buckling effect for the HSR MEA was more pronounced as compared to the LSR MEA. This difference is likely due to the wider and deeper pores as well as the thinner MPL in the HSR GDL. Previous works have also shown that the gaps at the interface between the CCL and MPL, which are shown to influence the CCM deformation herein, are governed by variations in the MPL surface profile [20,58,59].

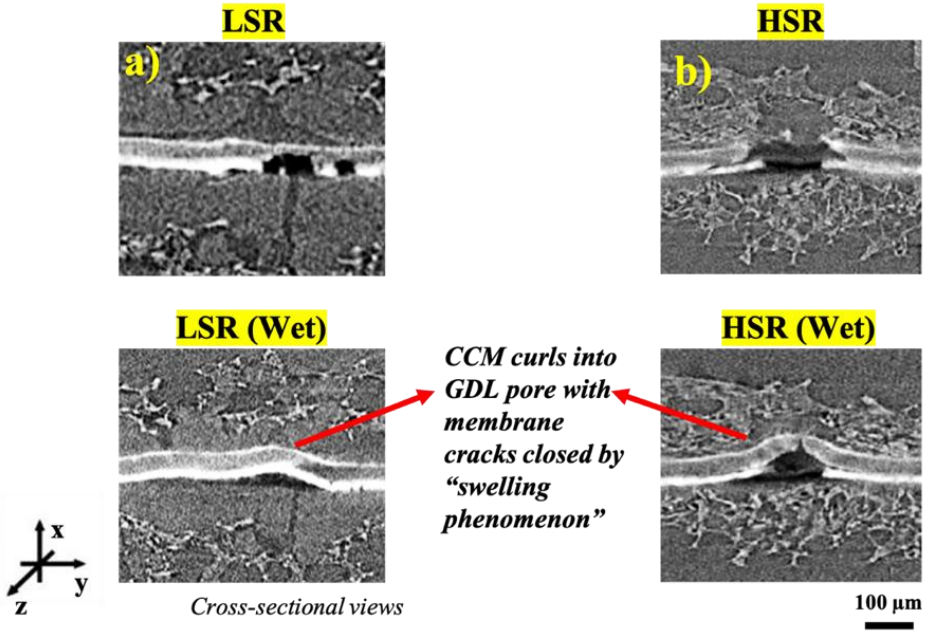

Figure 4: Cross-sections of MEAs with a) LSR GDL and b) HSR GDL [45] imaged during ambient and wet conditions after EOT. The EOT for LSR MEA was 4000 wet/dry cycles, while that for HSR MEA was 2000 wet/dry cycles.

Membrane crack interaction with catalyst layers

The 3D XCT approach enables in-depth investigation of the interactions between different components of the MEA during degradation [43,44]. In the present work, this is achieved by tracking the damage densities of individual MEA layers during the wet/dry cycling process, as shown in **Figure 5a**. As mentioned earlier, no membrane cracks were observed up to 2000 cycles. At BOL, the fresh membrane is expected to be free of damage or deformities. However, with progressive cycling, membrane cracks developed in the later stages of the applied AMST. The through-thickness membrane crack density was ~2 and ~8 cracks/mm^2 after 3000 and 4000 cycles, respectively. In contrast to the membrane, the CLs could develop cracks during the initial preparation and handling procedure. A low crack CCL was adopted here, and hence, the CCL crack density at pre-operational state was less than 2 cracks/mm^2. During the initial AMST phase, *i.e.*, up to 2000 cycles, there was a major rise in the CCL crack density to 23 cracks/mm^2 as a result of wet/dry cycling. With further cycling from 2000 to 3000 cycles, the CCL crack density doubled to 48 cracks/mm^2 along with initial membrane crack formation during the same period. It is thus evident that CCL crack development preceded the membrane crack formation and was more extensive than that of the membrane. By comparison, the HSR MEA developed ~5 membrane cracks/mm^2 after 2000 wet/dry cycles, which is significantly higher than in the LSR MEA at the same AMST stage [45]. This suggests that although the membrane cracks were the primary failure mode due to mechanical degradation in both studies, the membrane through-thickness crack initiation and subsequent development was significantly delayed with the use of LSR GDLs.

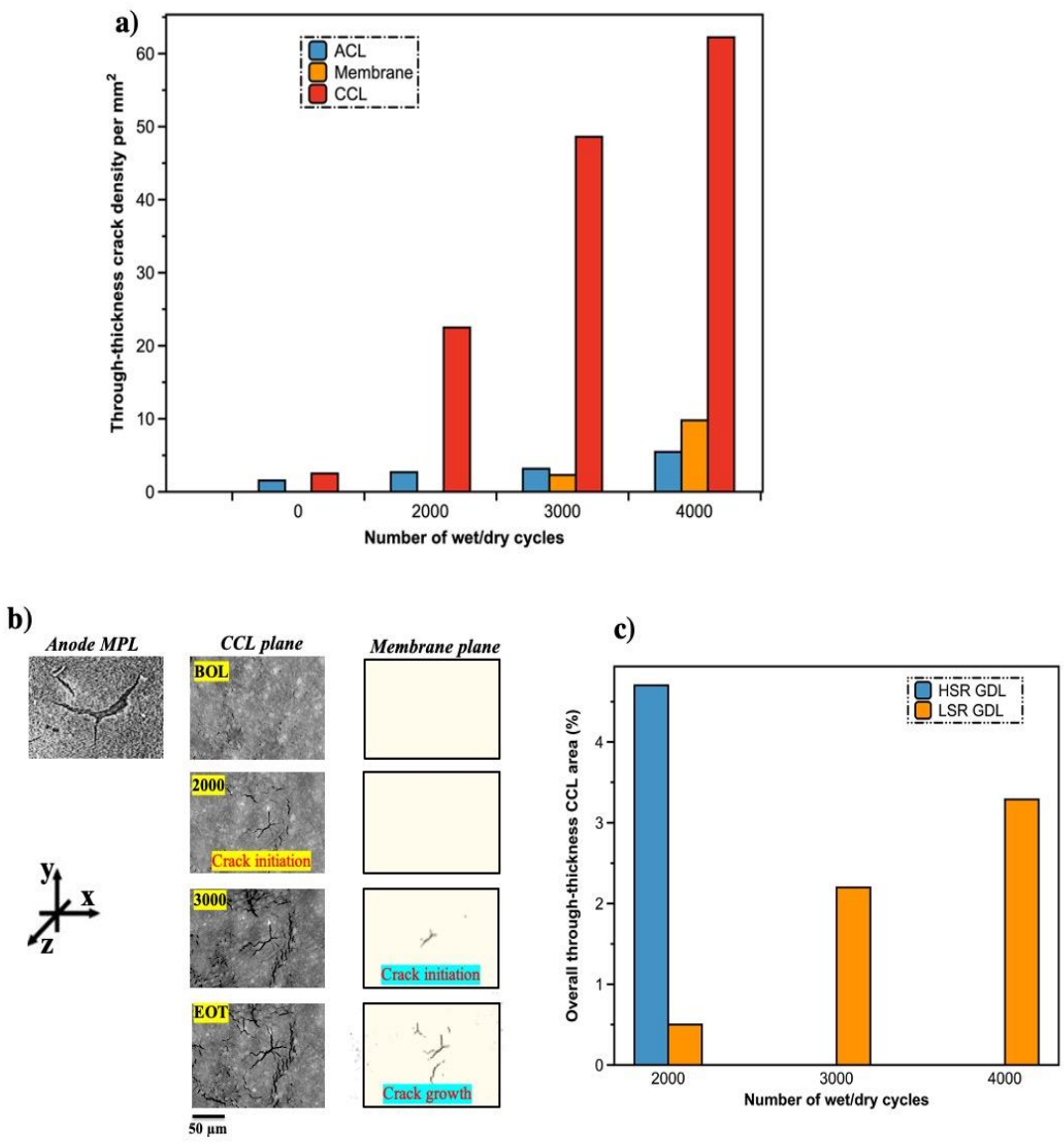

Figure 5: Tracking of through-thickness crack densities within the individual layers of the MEA made with LSR GDLs from BOL to 4000 wet/dry AMST cycles. (ACL: anode catalyst layer, CCL: cathode catalyst layer) b) Planar slices of the anode MPL, CCL, and corresponding membrane plane taken from a particular location under the channel region at different life stages of wet/dry cycling for the LSR GDL MEA. c) Overall through-thickness CCL crack area relative to the total active area at different cycling stages for both HSR and LSR GDL based MEAs.

Visualizing the same location in different MEA layers enables the tracking of the membrane crack initiation, development, and interaction process with the adjacent layers

at critical life stages. **Figure 5b** shows the identical planar locations of the CCL and membrane planes during the cycling procedure until 4000 cycles (EOT). As mentioned earlier, the CCL cracks at BOL were negligible. Up to 2000 cycles, no membrane cracks were observed in the membrane plane; however, several crack clusters had developed in the CCL within that timeframe. In other words, predominant CCL crack initiation occurred in the early cycling phase. With progressive cycling, the originated CCL cracks propagated into the membrane plane, as indicated by the identical crack geometries in both layers at EOT. It is inferred that the initial crack formation on the CCL surface had created favorable conditions for membrane crack development in the later stages of cycling. This is likely due to the local stress concentration effects at CL crack sites where membrane cracks tend to initiate and develop over time. Similar observation was also reported by Singh *et al.* [44] for a gas diffusion electrode (GDE)-based MEA, where the crack geometry on the membrane surface resembled that of propagated damage features in the CCL. The membrane cracks which penetrate through the adjacent CLs facilitate gas crossover, and thus compromise the overall fuel cell performance and durability. Given the strong interaction between CL and membrane cracks, as discussed above, this crossover development is influenced by the CL crack coverage area, which is a function of the crack density along with the individual crack lengths and widths. For instance, **Figure 5c** shows the overall through-thickness CCL crack coverage area at different life stages for MEAs made with LSR and HSR GDLs. At BOL, the CCL crack areas for both MEA configurations were negligible, and hence, not shown here. For the MEA with LSR GDL, the CCL crack area after the initial cycling phase, *i.e.*, 2000 cycles, was less than 1% of the total active area. With progressive cycling, there was a gradual rise to around 3% of the active area by EOT. This CCL crack growth is significantly slower and less severe than the corresponding observations for the HSR MEA, wherein over 4% crack area was observed after merely 2000 cycles. In addition, the membrane crack area for HSR MEA was around 2% after 2000 AMST cycles, while no membrane cracks were observed in the present work. This observation reaffirms the mitigating role of LSR GDLs against the mechanical degradation of the MEA, not only in the membrane but also in the CLs. Overall, the linear trend in the crack area growth correlates with the crack density rise in the CCL during the AMST cycling.

Impact of MPL features on membrane crack development

The relevance of structural features within the MEA layers on its degradation can be characterized using the XCT technique, which enables improved understanding of the damage development process. An XCT-based 4D visualization approach was adopted herein to investigate the mitigatory effect of using a GDL with LSR, as compared to a HSR GDL, on the membrane mechanical degradation process. **Figure 6** shows cross-sectional and planar views of representative membrane fracture sites within the LSR and HSR MEAs at EOT. Both MEA configurations showed interaction of membrane crack development process with the location of adjoining anode GDL features; specifically, membrane cracks were formed at or near pre-existing anode GDL features. For the HSR GDL, Singh *et al.* [45] have shown that the GDL voids facilitate membrane fracture through localized buckling of CCM into these irregularities. The relatively lower density and different geometry of MPL cracks in the LSR GDL was observed to reduce the severity of CCM buckling (and associated membrane fracture) as its bulge height in the MPL cracks is lower, as observed in the wet images of **Figure 4**. In addition, the thicker MPL utilized in the LSR GDL likely acted as a buffer layer and provided structural rigidity to prevent/delay the onset of membrane cracks, as shown in the cross-sectional images of **Figure 6a**. Furthermore, the LSR GDL likely enabled a greater uniformity of the compressive pressure on the MEA, and thereby delayed its onset of crack initiation since the smoother MPL can simultaneously minimize the contact resistance and reduce mechanical pressure peaks leading to a reduced MEA crack formation. The contact resistance can be reduced by maintaining high contact pressure between the plates and GDLs. However, inhomogeneous compression could interfere with the key properties of GDL such as diffusivity, thermal conductivity, and porosity [60–63].

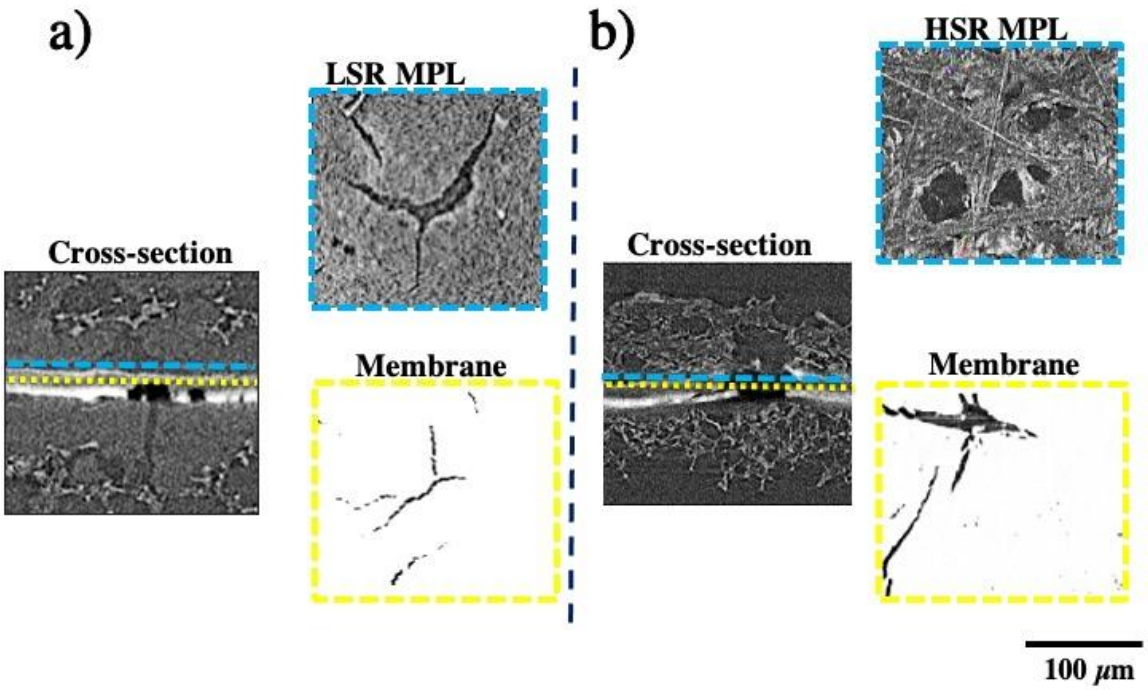

Figure 6: Representative membrane fracture sites at EOT of the MEAs with a) LSR and b) HSR GDLs. The planar views show the anode MPL and membrane planes indicated in the corresponding cross sections. Both images are sub-sections extracted from locations under the channel.

The CCM buckling also had a direct influence on the CL crack formation. For instance, CCL cracks were induced under pre-existing anode GDL cracks and pores for both LSR and HSR MEAs. These CL cracks subsequently expanded into membrane cracks upon further wet/dry cycling, *i.e.*, sustained cyclic membrane swelling and contraction and associated dynamic buckling events. It is noteworthy that membrane cracks formed via CCL cracks due to buckling into anode GDL voids were far more frequent than membrane cracks formed via ACL cracks due to buckling into cathode GDL voids, despite both GDLs being the same material. This suggests that the CCL has a more influential role than the ACL in the mechanical stability of the MEA in the context of buckling induced failure, presumably due to its greater thickness.

FEM simulation results

The results obtained from simulating the finite element fuel cell model using the relevant AMST conditions are presented in this section. The initial clamping displacement

compresses the GDLs at the land regions and introduces compressive stresses in the membrane. With the increase in the membrane water content from the reference dry condition to saturated conditions during the AMST, the ionomer membrane swells in both in-plane and through-thickness directions. Due to the planar constraints at the two edges, the compressive stresses in the membrane increase. This is accompanied by a reduction in the membrane stiffness which is defined as a function of relative humidity and temperature in the model. At a certain critical value of the compressive stresses, the membrane is observed to buckle into the anode-side GDL void as shown in **Figure 7a**. This is accompanied by an increase in the effective plastic strain, especially in the regions where the membrane deformation is highest. Upon dehydration, the membrane retracts from the buckled state towards the initial state, except for the irreversible inelastic deformation that it accumulates over the load cycle. The membrane buckling leads to a state of tension-compression in the two opposite surfaces of CCM at the point of maximum buckling displacement as shown in **Figure 7c**. On the concave side, the CCL is crushed due to high compressive stresses that develop as a result of buckling. As the membrane retracts from the buckling state, the compressive stresses are relaxed. The CCM's repeated buckling in and out of the GDL void is likely responsible for the development of cracks in the CL [21,22] that propagate over time into the membrane through the interface, as validated through the experimental observations.

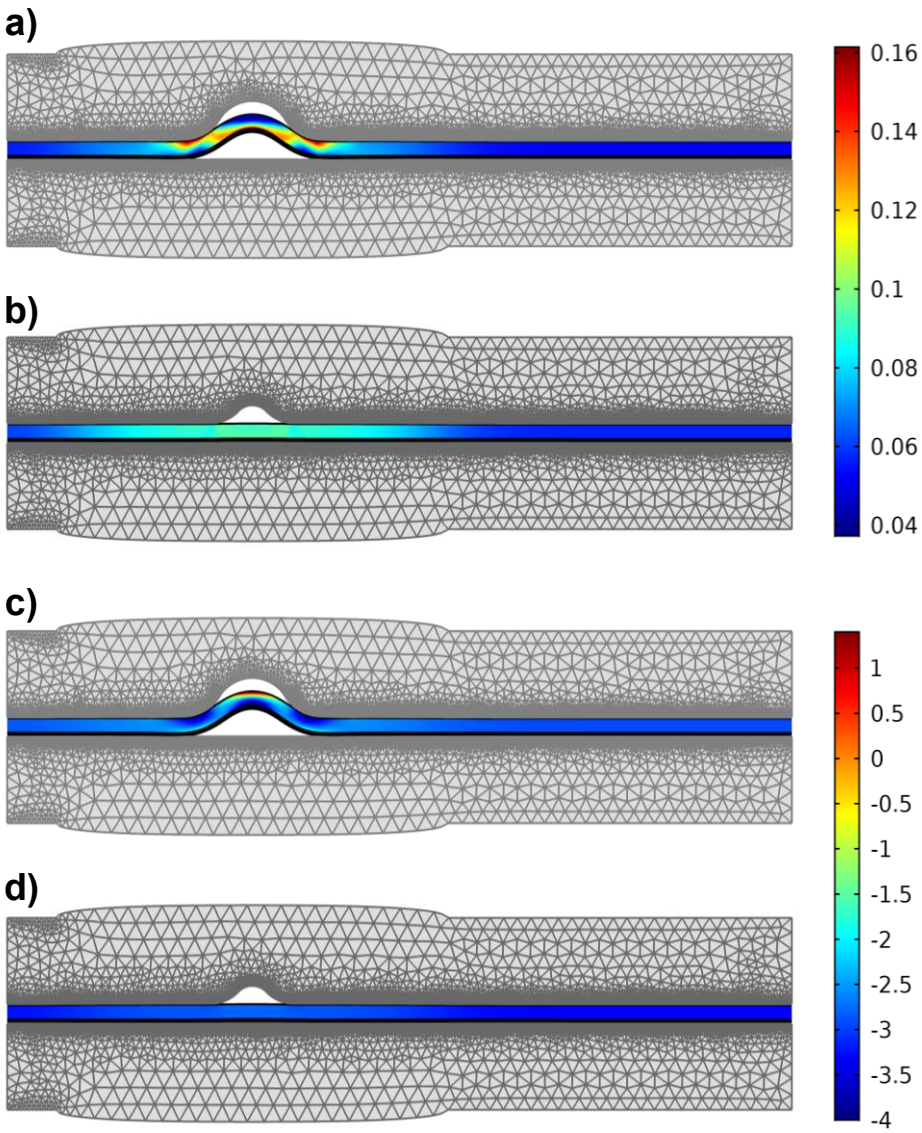

Figure 7: Finite element simulation of the miniature fuel cell subjected to an AMST cycle, showing the effective plastic strain in the membrane at the end of the wet phase for a) large and b) small anode GDL voids located under the channel. a) Membrane buckles-in when the void size is greater than a critical size, whereas in b) the membrane does not buckle-in when the void size is smaller than the critical size. Also shown are the contours for the in-plane stress in the membrane (c-d) for c) large and d) small void, highlighting the state of tension and compression in the membrane. The unit for the stress scale is in MPa.

The effect of GDL void size is investigated by repeating the simulations for several different void dimensions. It is observed that below a certain void size, the membrane does not buckle into the void when subjected to the same hygral conditions (see **Figure 7b, d**). This is expected because for a planar structure to buckle under given compressive forces, the critical state is a function of the geometry (in addition to material stiffness). Specifically, the ratio between the unsupported length and the thickness determines whether buckling takes place or not. The bulge height (or the maximum buckling displacement) and the maximum effective plastic strain increase with an increase in void dimensions, with a certain critical zone that defines the transition to buckling behavior of the membrane, as shown in **Figure 8a**. The state of tension-compression in the membrane at the point of maximum buckling displacement (that occurs at the end of wet phase) is shown through the magnitude of maximum in-plane stress in **Figure 7c**. Furthermore, in **Figure 8b,** the results show that for smaller void sizes, the membrane stresses are compressive with a much smaller gradient between top and bottom regions. As the void size is increased beyond the critical dimensions, the difference in the stress at the anode and cathode sides also increases and tensile stresses appear on the convex side of the membrane. The maximum compressive stresses in the CCL are also observed to increase non-linearly in the same critical fashion beyond certain void dimensions, as shown in **Figure 8c**. Although only elastic properties were used for the CL but based on the semi-empirically deduced nominal yield behavior of the electrode material as reported in literature [64], it could be construed that the CL incurs plastic deformation and ultimately fractures over several cycles of loading and unloading. These observations from the model correlate with the experimental findings, as the HSR MEA with an average pore diameter of around ~100 µm had demonstrated enhanced buckling that led to CL fracture followed by membrane fracture. On the contrary, the lower bulge height and reduced MPL crack coverage, meaning better contact within the LSR MEA delayed CL fracture and mitigated the overall membrane crack development. In addition, it could be speculated that the low MPL crack width directly reduced the CCM buckling.

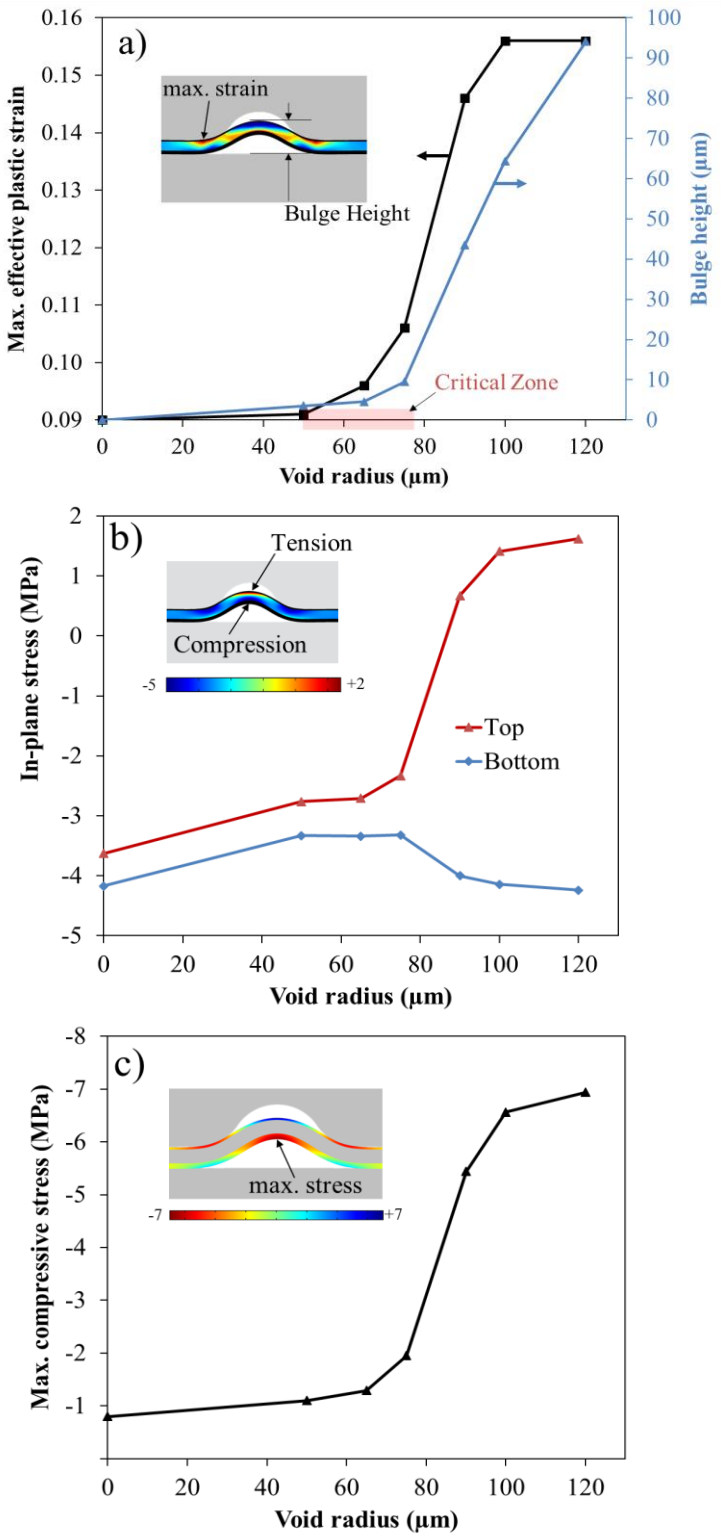

Figure 8: Compiled results from the finite element simulations obtained at the end of the wet phase (or maximum buckling displacement) for various anode GDL void sizes. a)

Maximum value of the effective plastic strain in the membrane and the bulge height of the buckled membrane. The zone of critical void size is highlighted on the *x*-axis and the bulge height is defined as shown in the inset. b) Maximum in-plane stress at the anode and cathode side of the buckled membrane. c) Maximum compressive stress in the CCL.

Conclusions

4D *in-situ* visualization of pure mechanical membrane degradation was carried out using a small-scale fuel cell fixture which enables same-location tracking of the membrane degradation process at different life stages. This novel methodology demonstrated that low surface roughness GDLs have significant mitigatory impact on mechanical membrane degradation in fuel cells. Specifically, a doubling of the AMST lifetime was achieved compared to the baseline high surface roughness GDL. The primary membrane failure mode during the wet/dry cycling AMST was membrane fracture preceded by CCL fracture associated with locally elevated stress and strain. The membrane crack formation occurred preferentially under the uncompressed channel regions while strongly interacting with the structural deformities in the MPL region of the GDL. Buckling deformation of the MEA with low surface roughness was significantly suppressed compared to the high surface roughness MEA, owing to the thick and smooth MPL of the low surface roughness MEA. In addition, the CCL had a more dominant role than the ACL to maintain the mechanical stability with respect to the CCM buckling effect. Complementary FEM simulations showed that cyclic CCM buckling onto the GDL cavities led to a state of tension-compression, causing crack development at the CL and membrane surfaces. In addition, the membrane's simulated bulge height and effective plastic strain were found to be related to the critical geometry-dependent buckling behavior of the membrane. The simulation results also revealed that the critical GDL pore radius for CCM buckling to occur was ~80 μm, which is consistent with the experimental observations of membrane crack formation under the adopted AMST conditions. Overall, the new findings from this work illustrate the unique advantage of XCT visualization methodology in gaining an extensive understanding of various degradation mitigation factors through capturing of critical failure mechanisms at their different developmental stages.

Acknowledgements

Funding for this research was provided by the Natural Sciences and Engineering Research Council of Canada, Canada Foundation for Innovation, British Columbia Knowledge Development Fund, and Ballard Power Systems through an Automotive Partnership Canada grant. This research was undertaken, in part, thanks to funding from the Canada Research Chairs program. We credit Dr. Robin T. White for development of the small-scale fuel cell fixture. We also acknowledge Mike Xu and Matthew Wegener for experimental assistance.

References

[1] Mench MM. Fuel Cell Engines. John Wiley and Sons; 2008. doi:10.1002/9780470209769.

[2] Wang Y, Chen KS, Mishler J, Cho SC, Adroher XC. A review of polymer electrolyte membrane fuel cells: Technology, applications, and needs on fundamental research. Applied Energy 2011;88:981–1007. doi:10.1016/j.apenergy.2010.09.030.

[3] Gittleman CS, Coms FD, Lai YH. Membrane Durability: Physical and Chemical Degradation. In: Mench M, Kumbur EC, Veziroglu TN, editors. Polymer Electrolyte Fuel Cell Degradation, Cambridge MA: Academic Press; 2012, p. 15–88.

[4] Coms FD. The Chemistry of Fuel Cell Membrane Chemical Degradation Frank D. Coms General Motors Corporation, Fuel Cell Research Labs, 10 Carriage Street, Honeoye Falls, NY 14472, USA. ECS Trans 2008;16:235–55. doi:10.1149/1.2981859.

[5] Rodgers MP, Bonville LJ, Kunz HR, Slattery DK, Fenton JM. Fuel cell perfluorinated sulfonic acid membrane degradation correlating accelerated stress testing and lifetime. Chemical Reviews 2012;112:6075–103. doi:10.1021/cr200424d.

[6] Wu J, Yuan XZ, Martin JJ, Wang H, Zhang J, Shen J, et al. A review of PEM fuel cell durability: Degradation mechanisms and mitigation strategies. Journal of Power Sources 2008;184:104–19. doi:10.1016/j.jpowsour.2008.06.006.

[7] Zhang S, Yuan X-Z, Ng J, Hin C, Wang H, Wu J, et al. Effects of open-circuit operation on membrane and catalyst layer degradation in proton exchange membrane fuel cells. Journal of Power Sources 2010;195:1142–8. doi:10.1016/j.jpowsour.2009.08.070.

[8] Aindow TT, O'Neill J. Use of mechanical tests to predict durability of polymer fuel cell membranes under humidity cycling. J Power Sources 2011;196:3851–4.

[9] Lim C, Ghassemzadeh L, Van Hove F, Lauritzen M, Kolodziej J, Wang GG, et al. Membrane degradation during combined chemical and mechanical accelerated stress testing of polymer electrolyte fuel cells. Journal of Power Sources 2014;257:102–10. doi:10.1016/j.jpowsour.2014.01.106.

[10] Patil YP, Jarrett WL, Mauritz KA. Deterioration of mechanical properties: A cause for fuel cell membrane failure. Journal of Membrane Science 2010;356:7–13. doi:10.1016/j.memsci.2010.02.060.

[11] Sadeghi Alavijeh A, Goulet MA, Khorasany RMH, Ghataurah J, Lim C, Lauritzen M, et al. Decay in mechanical properties of catalyst coated membranes subjected to combined chemical and mechanical membrane degradation. Fuel Cells 2015;15:204–13. doi:10.1002/fuce.201400040.

[12] Alavijeh AS, Khorasany RMH, Nunn Z, Habisch A, Lauritzen M, Rogers E, et al. Microstructural and Mechanical Characterization of Catalyst Coated Membranes Subjected to In Situ Hygrothermal Fatigue. Journal of The Electrochemical Society 2015;162:F1461–9. doi:10.1149/2.0471514jes.

[13] Sadeghi Alavijeh A, Khorasany RMH, Habisch A, Wang GG, Kjeang E. Creep properties of catalyst coated membranes for polymer electrolyte fuel cells. Journal of Power Sources 2015;285:16–28. doi:10.1016/j.jpowsour.2015.03.082.

[14] Khorasany RMH, Goulet M-A, Alavijeh AS, Kjeang E, Wang GG, Rajapakse RKND. On the constitutive relations for catalyst coated membrane applied to in-situ fuel cell modeling. Journal of Power Sources 2014;252:176–88. doi:10.1016/j.jpowsour.2013.11.087.

[15] Goulet M-A, Khorasany RMH, De Torres C, Lauritzen M, Kjeang E, Wang GG, et al. Mechanical properties of catalyst coated membranes for fuel cells. Journal of Power Sources 2013;234:38–47. doi:10.1016/j.jpowsour.2013.01.128.

[16] Lai Y-H, Mittelsteadt CK, Gittleman CS, Dillard DA. Viscoelastic Stress Analysis of Constrained Proton Exchange Membranes Under Humidity Cycling. Journal of Fuel Cell Science and Technology 2009;6:021002. doi:10.1115/1.2971045.

[17] Khorasany RMH, Kjeang E, Wang GG, Rajapakse RKND. Simulation of ionomer membrane fatigue under mechanical and hygrothermal loading conditions. Journal of Power Sources 2015;279:55–63. doi:10.1016/j.jpowsour.2014.12.133.

[18] Sadeghi Alavijeh A, Venkatesan SV, Khorasany RMH, Kim WHJ, Kjeang E. Ex-situ tensile fatigue-creep testing: A powerful tool to simulate in-situ mechanical degradation in fuel cells. Journal of Power Sources 2016;312:123–7.

[19] Tavassoli A, Lim C, Kolodziej J, Lauritzen M, Knights S, Wang GG, et al. Effect of catalyst layer defects on local membrane degradation in polymer electrolyte fuel cells. Journal of Power Sources 2016;322:17–25. doi:10.1016/j.jpowsour.2016.05.016.

[20] Hizir FE, Ural SO, Kumbur EC, Mench MM. Characterization of interfacial morphology in polymer electrolyte fuel cells: Micro-porous layer and catalyst layer surfaces. Journal of Power Sources 2010;195:3463–71. doi:10.1016/j.jpowsour.2009.11.032.

[21] Uchiyama T, Kato M, Yoshida T. Buckling deformation of polymer electrolyte membrane and membrane electrode assembly under humidity cycles. Journal of Power Sources 2012;206:37–46. doi:10.1016/j.jpowsour.2012.01.073.

[22] Uchiyama T, Kumei H, Yoshida T. Catalyst layer cracks by buckling deformation of membrane electrode assemblies under humidity cycles and mitigation methods. Journal of Power Sources 2013;238:403–12. doi:10.1016/j.jpowsour.2013.04.026.

[23] Lai YH, Li Y, Rock JA. A novel full-field experimental method to measure the local compressibility of gas diffusion media. Journal of Power Sources 2010;195:3215–23. doi:10.1016/j.jpowsour.2009.11.122.

[24] Gostick JT, Ioannidis MA, Fowler MW, Pritzker MD. On the role of the microporous layer in PEMFC operation. Electrochemistry Communications 2009;11:576–9. doi:10.1016/j.elecom.2008.12.053.

[25] Huang X, Solasi R, Zou YUE, Feshler M, Reifsnider K, Condit D, et al. Mechanical Endurance of Polymer Electrolyte Membrane and PEM Fuel Cell Durability. J Polym Sci Part B Polym Physics 2006;44:2346–57.

[26] Kang J, Kim J. Membrane electrode assembly degradation by dry/wet gas on a PEM fuel cell. International Journal of Hydrogen Energy 2010;35:13125–30. doi:10.1016/j.ijhydene.2010.04.077.

[27] Andisheh-Tadbir M, Orfino FP, Kjeang E. Three-dimensional phase segregation of micro-porous layers for fuel cells by nano-scale X-ray computed tomography. Journal of Power Sources 2016;310:61–9. doi:10.1016/j.jpowsour.2016.02.001.

[28] Zenyuk I V., Parkinson DY, Connolly LG, Weber AZ. Gas-diffusion-layer structural properties under compression via X-ray tomography. Journal of Power Sources 2016;328:364–76. doi:10.1016/j.jpowsour.2016.08.020.

[29] Tötzke C, Gaiselmann G, Osenberg M, Bohner J, Arlt T, Markötter H, et al. Three-dimensional study of compressed gas diffusion layers using synchrotron X-ray imaging. Journal of Power Sources 2014;253:123–31. doi:10.1016/j.jpowsour.2013.12.062.

[30] Odaya S, Phillips RK, Sharma Y, Bellerive J, Phillion AB, Hoorfar M. X-ray Tomographic Analysis of Porosity Distributions in Gas Diffusion Layers of Proton Exchange Membrane Fuel Cells. Electrochimica Acta 2015;152:464–72. doi:10.1016/j.electacta.2014.11.143.

[31] James JP, Choi H-W, Pharoah JG. X-ray computed tomography reconstruction and analysis of polymer electrolyte membrane fuel cell porous transport layers. International Journal of Hydrogen Energy 2012;37:18216–30. doi:10.1016/j.ijhydene.2012.08.077.

[32] Litster S, Epting WK, Wargo EA, Kalidindi SR, Kumbur EC. Morphological analyses of polymer electrolyte fuel cell electrodes with nano-scale computed tomography imaging. Fuel Cells 2013;13:935–45. doi:10.1002/fuce.201300008.

[33] Pfrang A, Veyret D, Janssen GJM, Tsotridis G. Imaging of membrane electrode assemblies of proton exchange membrane fuel cells by X-ray computed tomography. Journal of Power Sources 2011;196:5272–6. doi:10.1016/j.jpowsour.2010.09.020.

[34] White RT, Wu A, Najm M, Orfino FP, Dutta M, Kjeang E. 4D in situ visualization of electrode morphology changes during accelerated degradation in fuel cells by X-ray computed tomography. Journal of Power Sources 2017;350:94–102. doi:10.1016/j.jpowsour.2017.03.058.

[35] White RT, Ramani D, Eberhardt S, Najm M, Orfino FP, Dutta M, et al. Correlative X-ray Tomographic Imaging of Catalyst Layer Degradation in Fuel Cells 2019;166:914–25. doi:10.1149/2.0121913jes.

[36] Pokhrel A, El Hannach M, Orfino FP, Dutta M, Kjeang E. Failure analysis of fuel cell electrodes using three-dimensional multi-length scale X-ray computed tomography. Journal of Power Sources 2016;329:330–8. doi:10.1016/j.jpowsour.2016.08.092.

[37] Markötter H, Alink R, Haußmann J, Dittmann K, Arlt T, Wieder F, et al. Visualization of the water distribution in perforated gas diffusion layers by means of synchrotron X-ray radiography. International Journal of Hydrogen Energy 2012;37:7757–61. doi:10.1016/j.ijhydene.2012.01.141.

[38] Krüger P, Markötter H, Haußmann J, Klages M, Arlt T, Banhart J, et al. Synchrotron X-ray tomography for investigations of water distribution in polymer electrolyte membrane fuel cells. Journal of Power Sources 2011;196:5250–5. doi:10.1016/j.jpowsour.2010.09.042.

[39] White RT, Eberhardt SH, Singh Y, Haddow T, Dutta M, Orfino FP, et al. Four-dimensional joint visualization of electrode degradation and liquid water distribution inside operating polymer electrolyte fuel cells. Scientific Reports 2018:1–12. doi:10.1038/s41598-018-38464-9.

[40] Singh Y, Orfino FP, Dutta M, Kjeang E. 3D visualization of membrane failures in fuel cells. Journal of Power Sources 2017;345:1–11. doi:10.1016/j.jpowsour.2017.01.129.

[41] Singh Y, Orfino FP, Dutta M, Kjeang E. 3D Failure Analysis of Pure Mechanical and Pure Chemical Degradation in Fuel Cell Membranes. Journal of The Electrochemical Society 2017;164:1331–41. doi:10.1149/2.0451713jes.

[42] Ramani D, Singh Y, Orfino FP, Dutta M, Kjeang E. Characterization of Membrane Degradation Growth in Fuel Cells Using X-ray Computed Tomography. Journal of The Electrochemical Society 2018;165:F3200–8. doi:10.1149/2.0251806jes.

[43] Ramani D, Singh Y, White RT, Wegener M, Orfino FP, Dutta M, et al. 4D in situ visualization of mechanical degradation evolution in reinforced fuel cell membranes. International Journal of Hydrogen Energy 2020;45:10089–103. doi:10.1016/j.ijhydene.2020.02.013.

[44] Singh Y, White RT, Najm M, Haddow T, Pan V, Orfino FP, et al. Tracking the evolution of mechanical degradation in fuel cell membranes using 4D in situ visualization. Journal of Power Sources 2019:224–37. doi:10.1016/j.jpowsour.2018.11.049.

[45] Y. Singh, R. T. White, M. Najm , A. Boswell, F. P. Orfino MD and EK. Mitigation of Mechanical Membrane Degradation in Fuel Cells by Controlling Electrode Morphology — a 4D in-situ Structural Characterization. Journal of The Electrochemical Society 2021;168.

[46] White RT, Najm M, Dutta M, Orfino FP, Kjeang E. Communication—Effect of Micro-XCT X-ray Exposure on the Performance of Polymer Electrolyte Fuel Cells. Journal of The Electrochemical Society 2016;163:1206–8. doi:10.1149/2.0751610jes.

[47] White RT, Orfino FP, Hannach M El, Luo O, Dutta M, Young AP, et al. 3D Printed Flow Field and Fixture for Visualization of Water Distribution in Fuel Cells by X-ray Computed Tomography. Journal of The Electrochemical Society 2016;163:F1337–43. doi:10.1149/2.0461613jes.

[48] White RT, Wu A, Najm M, Orfino FP, Dutta M, Kjeang E. 4D in situ visualization of electrode morphology changes during accelerated degradation in fuel cells by X-ray computed tomography. Journal of Power Sources 2017;350:94–102. doi:10.1016/j.jpowsour.2017.03.058.

[49] Singh N, Bhattacharya S, Lauritzen M V, Kjeang E. Residual fatigue life modeling of fuel cell membranes. Journal of Power Sources 2020;477:228714. doi:10.1016/j.jpowsour.2020.228714.

[50] Khattra NS, Karlsson AM, Santare MH, Walsh P, Busby FC. Effect of time-dependent material properties on the mechanical behavior of PFSA membranes subjected to humidity cycling. Journal of Power Sources 2012;214:365–76. doi:https://doi.org/10.1016/j.jpowsour.2012.04.065.

[51] Khattra NS, Lu Z, Karlsson AM, Santare MH, Busby FC, Schmiedel T. Time-dependent mechanical response of a composite PFSA membrane. Journal of Power Sources n.d.;228:256–69. doi:10.1016/j.jpowsour.2012.11.116.

[52] Lu Z, Kim C, Karlsson AM, Cross JC, Santare MH. Effect of gas diffusion layer modulus and land–groove geometry on membrane stresses in proton exchange membrane fuel cells. Journal of Power Sources 2011;196:4646–54. doi:https://doi.org/10.1016/j.jpowsour.2011.01.028.

[53] Kusoglu A, Weber AZ. New Insights into Perfluorinated Sulfonic-Acid Ionomers. Chemical Reviews 2017;117:987–1104. doi:10.1021/acs.chemrev.6b00159.

[54] Kusoglu A, Santare MH, Karlsson AM. Aspects of fatigue failure mechanisms in polymer fuel cell membranes. J Polym Sci Part B Polym Physics 2011;49:1506–17.

[55] Khorasany RMH, Singh Y, Alavijeh AS, Rajapakse RKND, Kjeang E. In-situ simulation of membrane fatigue in polymer electrolyte fuel cells 2017. doi:10.1016/j.ijhydene.2017.01.173.

[56] Khorasany RMH, Sadeghi Alavijeh A, Kjeang E, Wang GG, Rajapakse RKND. Mechanical degradation of fuel cell membranes under fatigue fracture tests. Journal of Power Sources 2015;274:1208–16. doi:10.1016/j.jpowsour.2014.10.135.

[57] Kreitmeier S, Schuler GA, Wokaun A, Büchi FN. Investigation of membrane degradation in polymer electrolyte fuel cells using local gas permeation analysis. Journal of Power Sources 2012;212:139–47. doi:10.1016/j.jpowsour.2012.03.071.

[58] Swamy T, Hizir FE, Khandelwal M, Kumbur EC, Mench MM. Interfacial Morphology and Contact Resistance Model for Polymer Electrolyte Fuel Cells. vol. 25, n.d., p. 15–27. doi:10.1149/1.3210555.

[59] Daniel L, Bonakdarpour A, Sharman J, Wilkinson DP. New CCL|MPL Architecture Reducing Interfacial Gaps and Enhancing PEM Fuel Cell Performance. Fuel Cells 2020;20:224–8. doi:10.1002/fuce.201900171.

[60] Nitta I, Hottinen T, Himanen O, Mikkola M. Inhomogeneous compression of PEMFC gas diffusion layer. Journal of Power Sources 2007;171:26–36. doi:10.1016/j.jpowsour.2006.11.018.

[61] Hottinen T, Himanen O, Karvonen S, Nitta I. Inhomogeneous compression of PEMFC gas diffusion layer. Journal of Power Sources n.d.;171:113–21. doi:10.1016/j.jpowsour.2006.10.076.

[62] Chu H-S, Yeh C, Chen F. Effects of porosity change of gas diffuser on performance of proton exchange membrane fuel cell. Journal of Power Sources 2003;123:1–9. doi:10.1016/s0378-7753(02)00605-5.

[63] Ge J, Higier A, Liu H. Effect of gas diffusion layer compression on PEM fuel cell performance. Journal of Power Sources 2006;159:922–7. doi:10.1016/j.jpowsour.2005.11.069.

[64] Lu Z, Santare MH, Karlsson AM, Busby FC, Walsh P. Time-dependent mechanical behavior of proton exchange membrane fuel cell electrodes. Journal of Power Sources 2014;245:543–52. doi:10.1016/j.jpowsour.2013.07.013.

Appendix E.

Mitigation of Mechanical Membrane Degradation in Fuel Cells – Part 2: Bonded Membrane Electrode Assembly

This is a preprint version of accepted article with Elsevier– *Journal of Power Sources* (Aug. 2021) reproduced with permission for the present thesis.

Mitigation of Mechanical Membrane Degradation in Fuel Cells – Part 2: Bonded Membrane Electrode Assembly

D. Ramani[a], N.S. Khattra[a], Y. Singh[a,b], F.P. Orfino[a], M. Dutta[b] and E. Kjeang[a,*]

[a] *Fuel Cell Research Lab (FCReL), Simon Fraser University, 250-13450 102 Ave, Surrey, BC V3T 0A3, Canada*

[b] *Ballard Power Systems, 9000 Glenlyon Pkwy, Burnaby, BC V5J 5J8, Canada*

*ekjeang@sfu.ca

Abstract

Repetitive hygrothermal fluctuations cause mechanical membrane degradation in fuel cells, which requires mitigation for longevity. Part 1 of this work demonstrated that gas diffusion layers (GDLs) with low surface roughness can improve lifetime by reducing harmful buckling phenomena during wet/dry cycling. As a second novel mitigation approach in the present work (Part 2), the catalyst coated membrane (CCM) is bonded with the GDLs to eliminate relative motion and further curb mechanical degradation. A custom miniaturized fuel cell fixture is used within a laboratory-based X-ray computed tomography system to visualize the membrane degradation process during wet/dry cycling. Compared to a non-bonded baseline cell, membrane buckling is shown to be completely arrested with bonding and lead to a two-fold increase in lifetime. Membrane crack development is still observed as the key failure mode, preceded by cathode catalyst layer fracture. However, the root causes are related to bonding irregularities and compressive impingement of GDL fibers rather than membrane buckling. Complementary finite element simulations of a representative fuel cell assembly are carried out to fundamentally establish the favorable effect of improved CCM-GDL adhesion on membrane durability. Overall, the improved adhesion of the bonded cell provided substantial mitigation against fatigue-driven mechanical membrane degradation and failure.

Keywords: fuel cell; membrane; durability; X-ray computed tomography; adhesion; mechanical degradation.

Introduction

Fuel cell membranes under operational environment can undergo three main types of degradation, namely, i) chemical [1,2], ii) mechanical [3], and iii) thermal degradation [4]. Of these types, the mechanical membrane degradation is known to be commonly related to failure and significantly detrimental to fuel cell durability. This is primarily attributed to key failure modes such as cracks [5] and creep [6], which could lead to gas crossover through the membrane that compromises the overall cell performance and durability. The interaction with adjacent components is a key factor influencing the membrane mechanical degradation [7]. The proton exchange membrane tends to swell and shrink depending on hygrothermal fluctuations within the membrane electrode assembly (MEA). The membrane swelling/shrinkage process introduces interactions with the design and microstructure of adjoining catalyst layer (CL) and gas diffusion layer (GDL) components, such as non-uniform mechanical stress development [8–10], that could affect eventual membrane failure.

Failure analysis pertinent to fuel cell components using X-ray computed tomography (XCT) was introduced as an advantageous approach compared to the traditional methods of electron microscopy. Some of the key benefits of XCT are: i) it allows for three-dimensional (3D) investigation of material microstructure; ii) it is non-invasive in nature; and iii) it requires minimal sample preparation. XCT was successfully used to perform *post mortem* 3D failure analysis of the fuel cell components such as CL [11,12], GDL [13–15], and ionomer membrane [16–18]. More recently, our group developed a custom miniature fuel cell [19] compatible with non-destructive XCT imaging, which enables tracking of identical MEA locations over degradation time to achieve a 4D visualization workflow, *i.e.*, three dimensions in space and one in time [20,21]. 4D studies pertinent to mechanical degradation of ionomer membranes showed the direct influence of CL cracks and interfacial delamination on membrane damage initiation and propagation [9,10]. A recent 4D study with a non-reinforced membrane captured membrane buckling phenomena, wherein the hygrally expanding catalyst coated membrane (CCM) displaced into the adjoining GDL pore spaces during a wet/dry cycling protocol [7], and significant membrane failures were found to develop at these buckling sites.

The most common MEA preparation technique is direct coating or decal transfer of catalyst layers onto the membrane to form a CCM followed by layered assembly of GDLs on either side. This method is amenable to mass production and known to improve the ionic conductivity between CL and membrane [22]. Otherwise, poor interfacial contact between the CL and membrane may reduce overall cell performance [23,24] and facilitate membrane degradation leading to early failure. Goulet *et al*. [25] showed that membrane expansion and contraction is controlled by its confinement within the MEA. Adoption of mechanical reinforcements has shown to improve membrane stability by reducing the in-plane expansion in favor of through-plane swelling [26–28]. Another approach to reduce in-plane expansion is by adopting MEA bonding, most commonly through a hot-pressing procedure that applies mechanical compression at elevated temperature. For instance, Hack *et al*. [29] compared hot-pressed and self-assembled MEAs [30] and observed improved lamination but no major changes in cell performance or catalyst layer durability, whereas membrane durability was not evaluated. Several works in literature studied the impact of different hot-pressing conditions [31–34] such as temperature, time, and pressure and on the MEA structure and performance [35]. Furthermore, Uchiyama *et al*. [36] demonstrated that the compression related static friction force within the MEA may influence the extent of deformation upon swelling.

The present work is a two-part series on mitigation of mechanical membrane degradation in fuel cells, focusing on component interaction effects within an MEA with non-reinforced membrane. In the first part of this series [8], an MEA comprising of GDLs with low surface roughness was evaluated as a novel strategy to mitigate mechanical membrane degradation. In the present work (Part 2), a second mitigation technique is proposed by establishing uniform CL-GDL bonding via CCM lamination through decal transfer to evade delamination and CCM buckling. Since crack initiation and propagation are known to be influenced by free movement of the CCM [7,8], this technique aims to mitigate or delay the membrane crack formation during an accelerated mechanical stress test (AMST) for membrane degradation. Similar to Part 1 [8], XCT enabled 4D identical-location tracking within a miniature fuel cell is utilized in order to understand the membrane degradation modes and mechanisms over time. Detailed analysis is performed to evaluate the impact of adopting the present mitigation approach against a non-bonded, self-assembled baseline cell. Furthermore, fundamental support of the experimental findings is provided with complementary finite element (FE)-based numerical simulations.

Experimental

Materials

Each MEA used in this work comprised of a CCM and two GDLs. The CCM was made of a non-reinforced Nafion® NRE211 perfluorosulfonic acid (PFSA) ionomer membrane coated with catalyst layers consisting of 50/50% Pt/carbon ratio and PFSA ionomer [7,8]. A cathode catalyst layer (CCL) with a low crack density was adopted in the present work due to the adverse impact of such cracks on membrane mechanical durability [7]. The anode and cathode GDLs were made up of teflonated Avcarb® carbon paper substrate coated with a microporous layer (MPL). The lamination of the MEA components was improved by hot-pressing using Instron® 5569 apparatus at 150ºC under 1.4 MPa compression pressure for 3 min [10]. **Figure 1** shows cross-sectional XCT views of the MEA before and after the bonding process, wherein the post bonded MEA shows improved CCM-GDL lamination and contact, including localized membrane creep into adjacent GDL voids. These images do not represent identical locations.

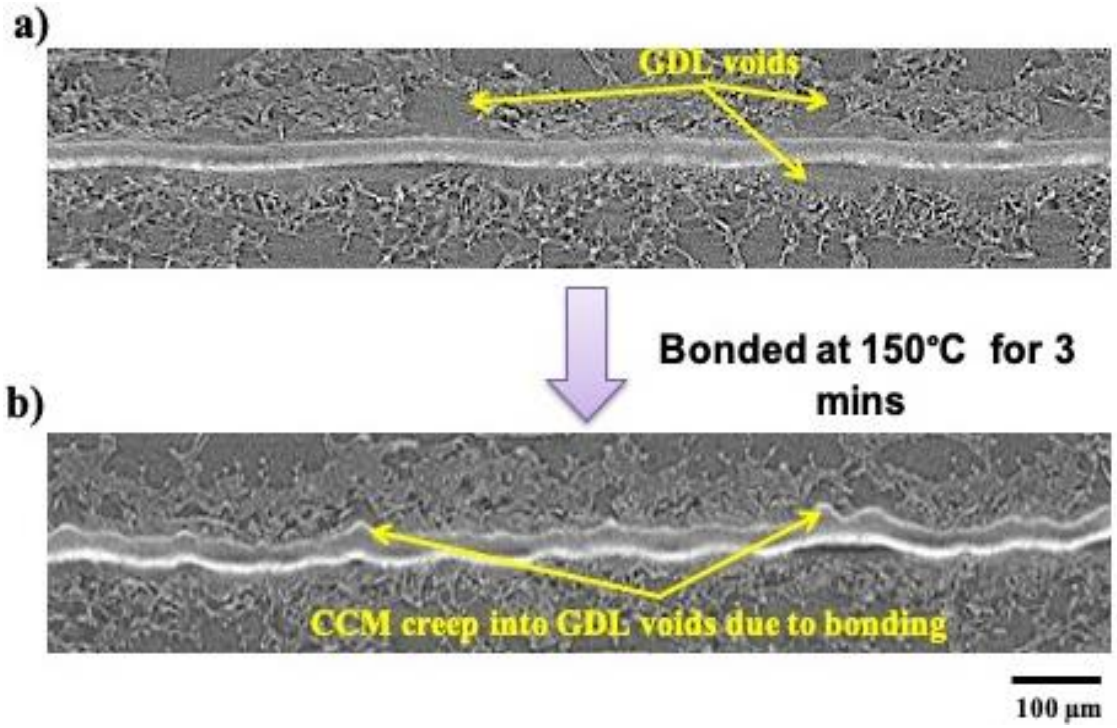

Figure 1: Cross sectional XCT views of the MEA a) before and b) after the bonding procedure. The cross-sectional images shown are representative of the general microstructure but are not acquired at identical locations.

Fuel cell operation

A small-scale fuel cell hardware was used to enable AMST operation and periodic *in situ* XCT imaging. This miniature fixture comprised of a single fuel cell of 9 mm x 4 mm active area with gases flowing in co-flow mode through two parallel, straight, semi-circular channels of graphitic flow field plates on both anode and cathode sides. The fixture housing the small MEA is X-ray transparent and equipped with electrical, heating, and tubing connections to enable complete fuel cell operation. The material used for the plates was compressed graphite/carbon impregnated with resin, which enabled an efficient transmission of X-rays, adequate XCT imaging resolution, and high thermal and electrical conduction. Before operation, external and internal leak tests were performed by pressurizing the setup under impassable channels with air. Detailed description of the parts, capabilities, and connections of the experimental setup are elaborated in our previous works [19,37,38]. The fuel cell was operated using a Greenlight Innovation® G40 fuel cell test station which was calibrated for the reduced flows required for this small scale MEA [9]. A modified AMST protocol [3] was adopted in the present work to achieve pure mechanical membrane degradation through relative humidity (RH) cycling [9,10]. The AMST protocol was performed at 80°C cell temperature with each RH cycle consisting of two-minute wet (150% inlet gas RH) and two-minute dry (0% inlet gas RH) phases, respectively, of 0.5 slpm N_2 flow on both anode and cathode sides. To maintain pure mechanical form of degradation, no electrochemical conditioning or diagnostics were performed in order to completely eliminate any chemical stressor development during the AMST [9,10].

XCT imaging

A Zeiss Xradia 520 Versa® micro-XCT system was used to achieve identical location imaging facilitated by the small-scale fuel cell setup. The fuel cell hardware was mounted on a rotating sample base at a distance of 27 mm and 30 mm from the X-ray source and detector, respectively, to obtain a pixel resolution of 1.59 µm. To obtain sufficient intensity around the membrane section, each XCT projection was acquired over a 5 s interval and a total of 1601 projections were obtained in each tomography scan. After obtaining the XCT projections, Zeiss XMReconstructor® software was used to reconstruct the tomographic data sets. A field of view (FOV) of 3.2 mm × 3.2 mm was captured around the inlet section of the MEA at various stages of the mechanical membrane degradation

protocol. Prior to starting the imaging acquisitions, the fuel cell fixture inside the XCT scanner was equilibrated under constant ambient temperature and dew point N_2 gas flow for 2 h. Separate, periodic XCT scans of identical MEA locations were obtained from the beginning of life (BOL) until the end of test (EOT), *i.e.*, 4500 AMST cycles. Furthermore, the fresh MEA at BOL and the degraded MEA at EOT were also imaged under highly saturated conditions to study the hydration dependent microstructural dynamics within the MEA. Further details of this imaging procedure and related image processing steps are elaborated in [10].

Finite Element Model

The effect of adhesion at the CCM-GDL interfaces on the membrane's *in situ* mechanical response was investigated using a multi-physics FE based fuel cell model, similar to the one discussed in Part 1 [8]. While the overall miniature fuel cell geometry, material properties of various components, and applied load in the FE model were unchanged from the previous investigation on GDL surface roughness in Part 1, the additional role of adhesion at the CCM-GDL interfaces was simulated here using various magnitudes of surface friction, as shown in **Figure 2**. The GDLs were modeled as linear elastic orthotropic material with a thickness of 150 µm (compared to 235 µm for the SGL Sigracet® 29BC GDL used in Part 1). The GDL (including the MPL) was modeled as a single entity with homogeneous mechanical properties. The CLs were modeled as linear elastic and assumed to be bonded with the viscoelastic-plastic membrane to make the CCM. Thermal expansion was considered for all components, whereas membrane was the only component assumed to incur hygral swelling.

Based on the microstructural observations from XCT, imperfections in the form of a void were introduced in the anode GDL to investigate their impact on the behavior of the membrane under the test conditions. The simulations were carried out for various CCM-GDL interface conditions ranging from a slip-free condition (frictional coefficient, $\mu = 0$) to a perfectly bonded configuration, with several intermediate values. The hygral displacement of membrane under RH modulation within the fuel cell assembly was investigated for all selected surface friction coefficients in the presence of anode GDL voids. The tendency of the membrane to buckle under such conditions was investigated and the critical condition for buckling was determined. To simulate fuel cell operation, the model assembly was first compressed at the land region by a known displacement of

around 60 µm. The membrane was then subjected to a single wet/dry cycle with conditions similar to the experimental AMST protocol, and the resulting mechanical response is discussed in the next section.

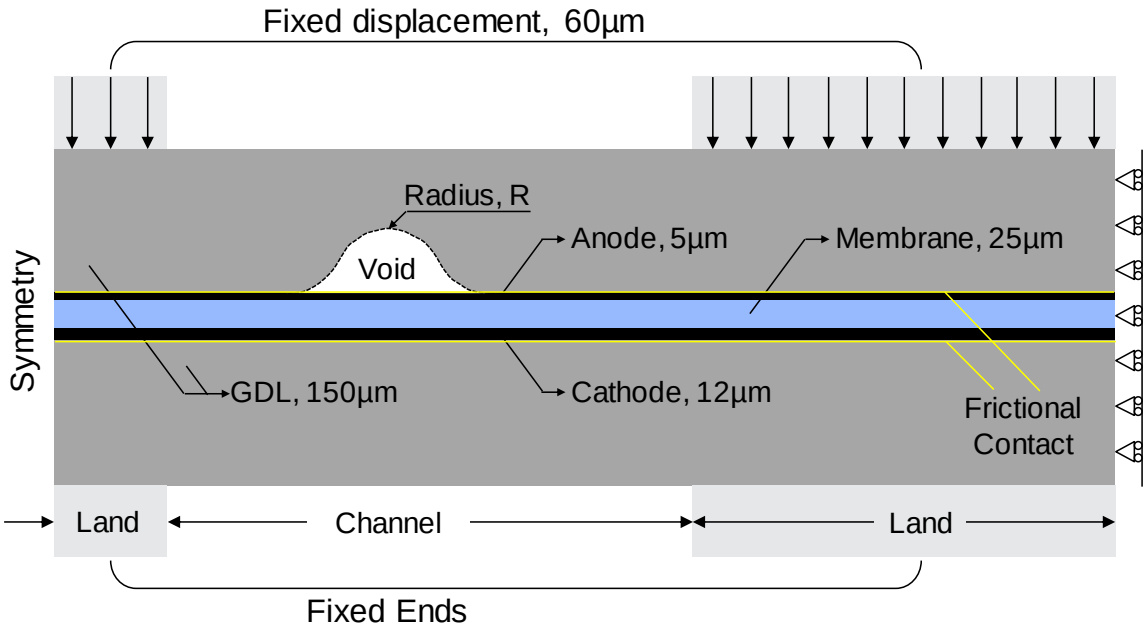

Figure 2: Representative 2D cross-sectional geometry for the finite element fuel cell model.

Results and Discussion

The use of the small-scale, X-ray transparent fuel cell fixture facilitated 4D *in situ* XCT tracking of the identical MEA location during various life stages of the applied AMST protocol. Complete tomographic scans were collected at BOL and after 2000, 3000, 4000, and 4500 (EOT) wet/dry cycles of the AMST. In order to establish the impact of the adopted CCM-GDL bonding approach in mitigating mechanical membrane degradation, the present observations were compared against a previously reported work on non-bonded, self-assembled MEAs [7] which underwent a similar AMST procedure. The following sections also compare the findings obtained from XCT microstructural characterization with FE simulation of representative scenarios.

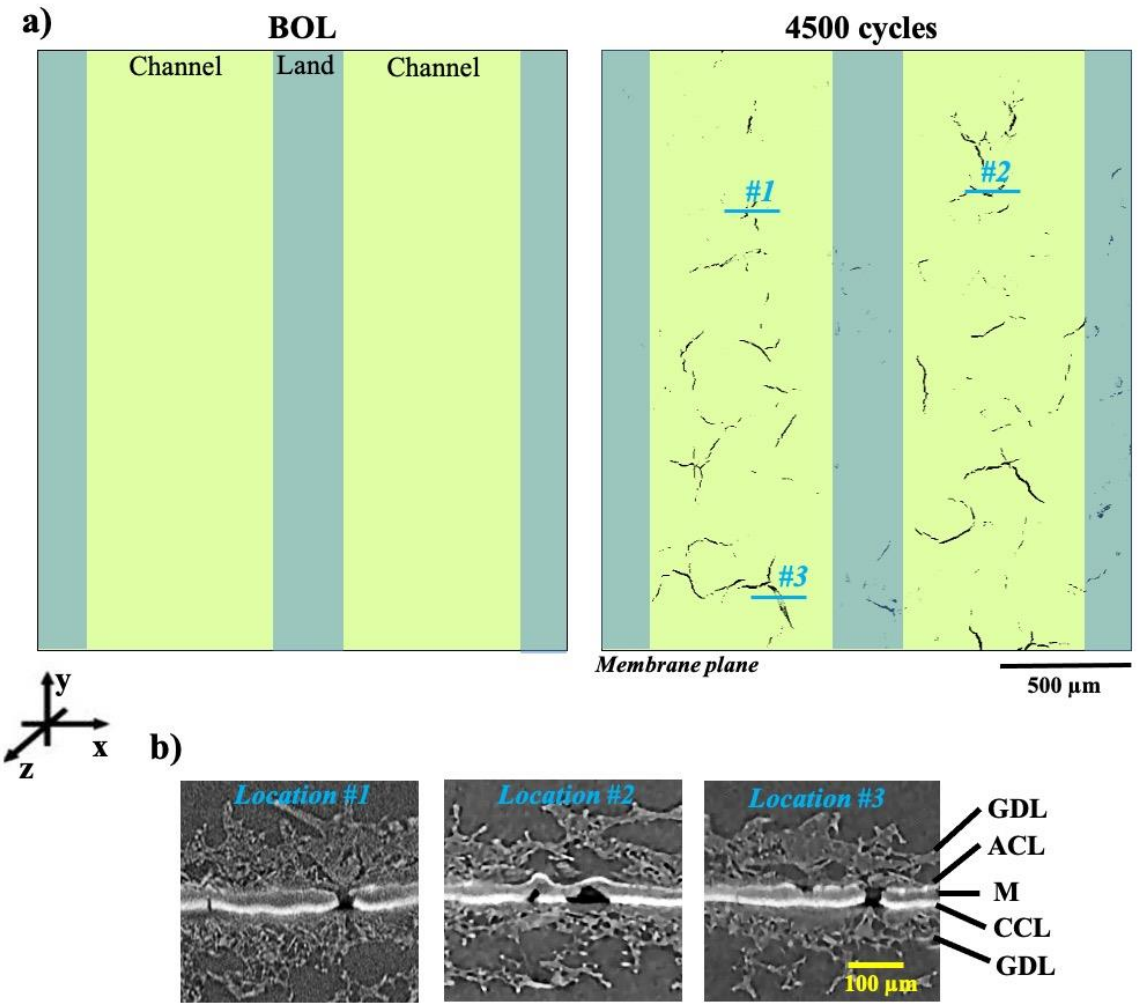

Figure 3: a) Planar XCT views of the membrane at BOL and after 4500 cycles (EOT) of the wet/dry cycling AMST. b) Cross-sectional XCT views of the MEA at three selected locations under the channel regions, as indicated in (a), measured at EOT. The gas diffusion layer (GDL), anode catalyst layer (ACL), membrane (M), and cathode catalyst layer (CCL) components are indicated in the cross-sectional view. (For interpretation of the references to color, the reader is referred to the web version of the article.)

Membrane crack development

The 3D XCT method allows to visualize the concurrent planar and cross-sectional views of the internal MEA features. **Figure 3** shows the representative planar slices of the membrane at BOL and upon completion of 4500 wet/dry cycles at EOT. As expected, the membrane at BOL was a defect-free, blank canvas across the entire FOV. The EOT membrane, however, showed significant through-thickness membrane crack development

throughout most of the FOV under the channel regions and less frequently under the land regions (**Figure 3b)**. Membrane fracture is known to be the main failure mode during mechanical degradation induced through wet/dry cycling, as seen in our previous works with both reinforced [10] and non-reinforced [3,7,9,16] membranes. A recent work with non-bonded CCM-GDL interface but similar MEA configuration and material composition had demonstrated ~2% membrane crack area post 2000 cycles of the same wet/dry cycling AMST [7]. However, the present work done with the additional CCM-GDL lamination step during MEA fabrication did not show any membrane cracks after 2000 cycles. The cycling was continued until a substantial development of membrane cracks had occurred by 4500 cycles which was deemed as EOT. Membrane crack formation occurred most frequently under the channel regions. This observation is consistent with that in Part 1 as well with our earlier works involving both CCM and gas diffusion electrode (GDE) based MEA designs [9,10]. Modeling works based on mechanical degradation via the RH cycling protocol have also predicted the susceptibility of channel regions to membrane crack formation due to increased stress [39–42].

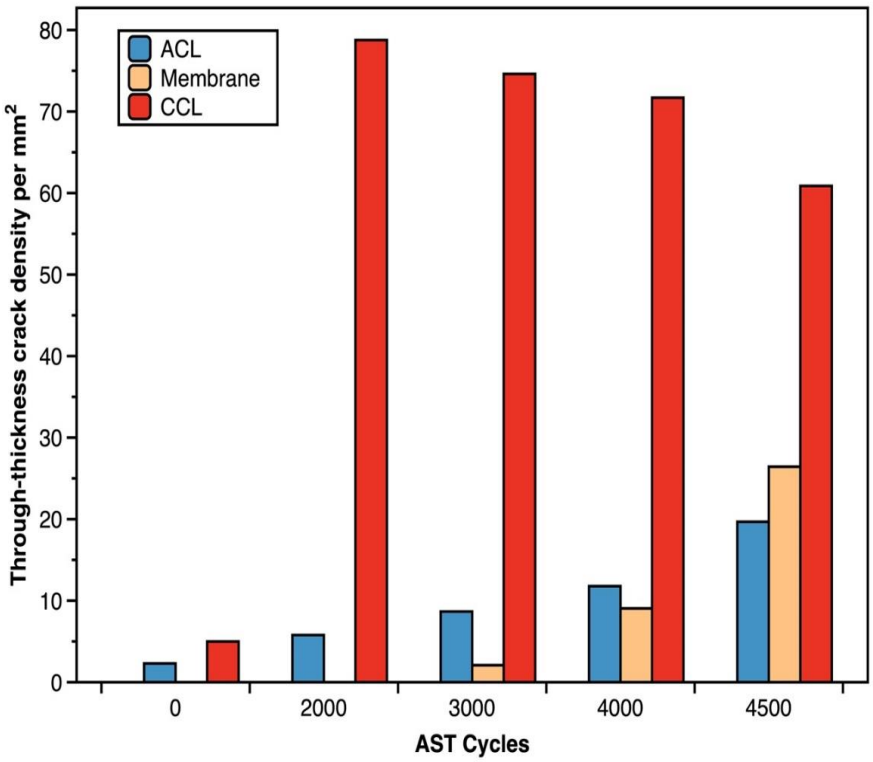

Figure 4: Evolution of through-thickness crack density in each layer of the MEA during the AMST cycling from BOL to 4500 cycles. (ACL: anode catalyst layer, CCL: cathode catalyst layer)

The 3D XCT datasets acquired at various life stages enable a detailed numerical analysis of damage features, such as cracks, within each individual MEA layer. Crack density is one of the metrics to represent mechanical damage and is defined as the number of through-thickness cracks per unit examined area of the MEA [10]. For the MEA analyzed in the present work, **Figure 4** shows the evolution of through-thickness crack density of each CCM layer across various cycling stages. As expected, the membrane was crack-free at BOL, while the ACL and CCL also had negligible number of BOL cracks due to the use of low crack density electrodes in this work. With wet/dry cycling, the central membrane did not show any through-thickness cracks up to 2000 cycles. Between 2000-3000 cycles, the first few membrane cracks were detected, with a membrane crack density of 2 cracks/mm^2 after 3000 cycles. With further cycling, an exponential increase in membrane crack density was observed resulting in 26 cracks/mm^2 after 4500 cycles. Crack development in both CLs initiated during the first cycling phase, *i.e.*, between BOL and 2000 cycles, with more than 90% of the cracks forming on the cathode side. Albeit

significant, the CCL crack area fraction of ~1% was still relatively modest compared to the 4% crack area reported in [7]. The slightly decreasing trend of CCL crack density after 2000 cycles was predominantly due to merging of existing cracks. Interestingly, this trend was inversely related to ACL and membrane cracks, as the densities of both ACL and membrane cracks increased with decreasing CCL crack density.

The 4D XCT visualization workflow allows for tracking complementary planar and cross-sectional perspectives of identical locations which helps to unravel the membrane failure mechanism process at various AMST life stages. For instance, **Figure 5** shows the identical location cross-sectional views of two particular membrane crack sites under the channel regions. *Location #1* demonstrates a membrane location with slightly lower local thickness at BOL (**Figure 5a**) resulting from the MEA fabrication process as described in the 'Experimental' section. After 2000 cycles, a micro crack had initiated on the CCL surface. With further cycling up to 4000 cycles, a through-thickness membrane crack developed that spanned the entire CCM thickness. Such through-thickness CCM cracks are deemed to be fatal to fuel cell durability, as they could facilitate convective gas crossover, thus compromising the overall performance and lifetime of the fuel cell [43]. With further application of 500 more wet/dry cycles, the through-thickness cracks had grown wider by the EOT. However, during the saturated wet condition, the membrane crack closed likely from the ionomer's hygral expansion. Similar swelling and crack closure phenomena have been previously demonstrated with the 4D *in situ* XCT technique [7,9,10]. On the other hand, *Location #2* displays an MEA location bearing a relatively greater local membrane thickness at BOL. This is owing to the CCM creep during the MEA bonding process, as shown in **Figure 1**. Similar to *Location #1*, several CCL cracks had developed by 2000 wet/dry cycles. While membrane surface cracks initiated after ~3000 cycles and grew in size with continuous cycling, this location did not form a through-thickness membrane crack, possibly due to the greater local thickness, and may have required more AMST cycles for the cracks to fully span the membrane thickness. Another novel observation of *Location #2*, specifically in the wet state, is that full crack closure is feasible with this degradation mode despite asymmetric cracking, *i.e.*, only partially through the CCM (cathode side) as opposed to previously discussed through-thickness CCM cracks.

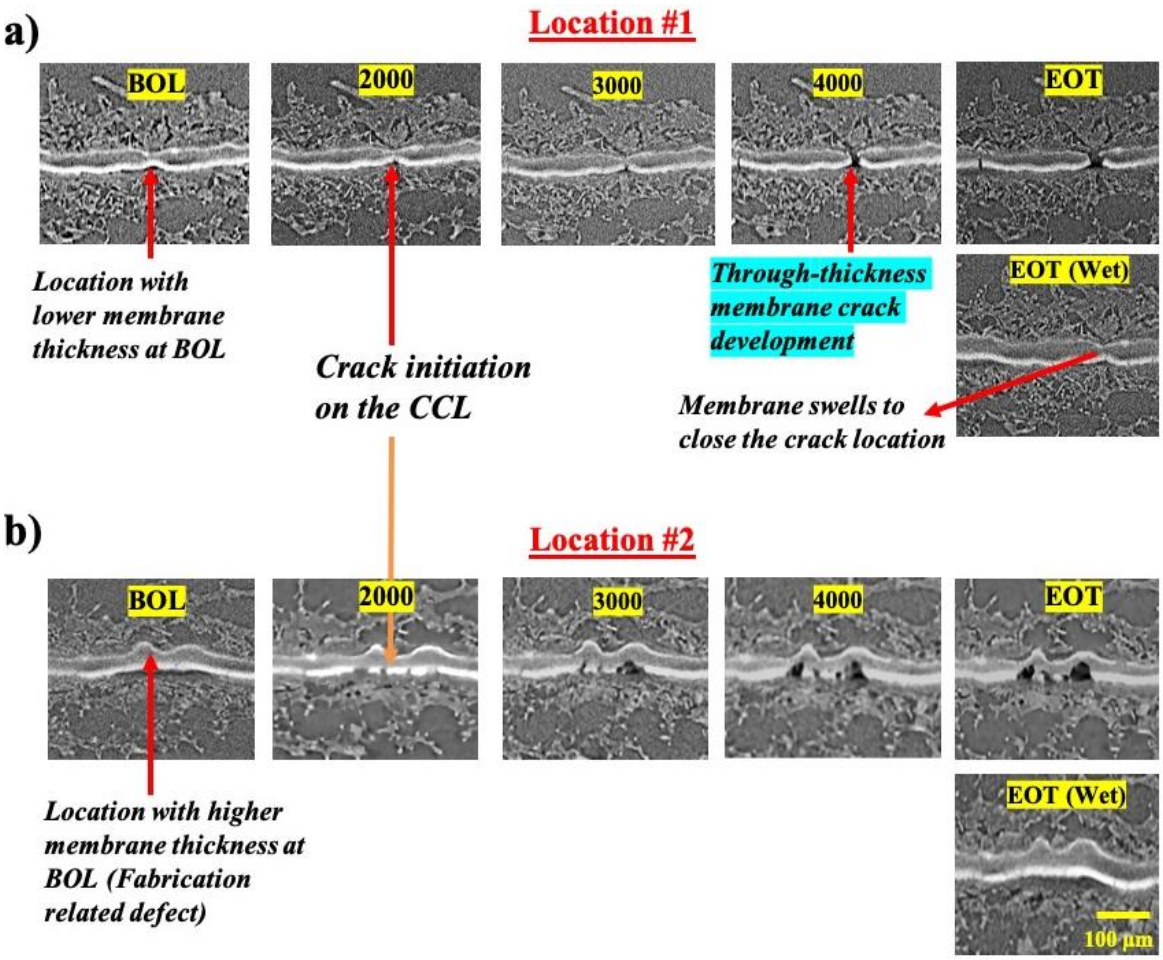

Figure 5: Membrane crack initiation and development as observed by identical location cross-sectional XCT views of a) Location #1 and b) Location #2 (indicated in Figure 3) after various life stages of the AMST cycling process. (EOT = 4500 cycles)

The XCT data also facilitates the understanding of crack reach within different layers of the MEA. **Figure 6** shows the cross-sectional and planar views of *Location #3* during the AMST cycling procedure. The cross-sectional views show the identical location at BOL and upon application of 4500 cycles or EOT. The BOL location shows a slight GDL intrusion on the cathode side and the membrane also appears locally thin at the same location. Post 4500 cycles, a through-thickness CCM crack developed at this location. The XCT also allows to perform slice-by-slice inspection of the planar views, which enables investigation of damage reach within each CCM layer. **Figure 6b** shows the planar views of different CCM layers after 4500 cycles. The membrane crack shape was similar to the adjacent CCL crack. A closer examination revealed that the CCL crack was formed due to cathode GDL fiber impingement that influenced the eventual CCL and membrane crack

shapes. This observation is partly similar to that reported in our previous work done with GDE-based MEAs [9], wherein the membrane crack geometry resembled that of adjacent damage features developing in the CCL, while the role of GDL fiber impingement in CCL cracking is a new finding.

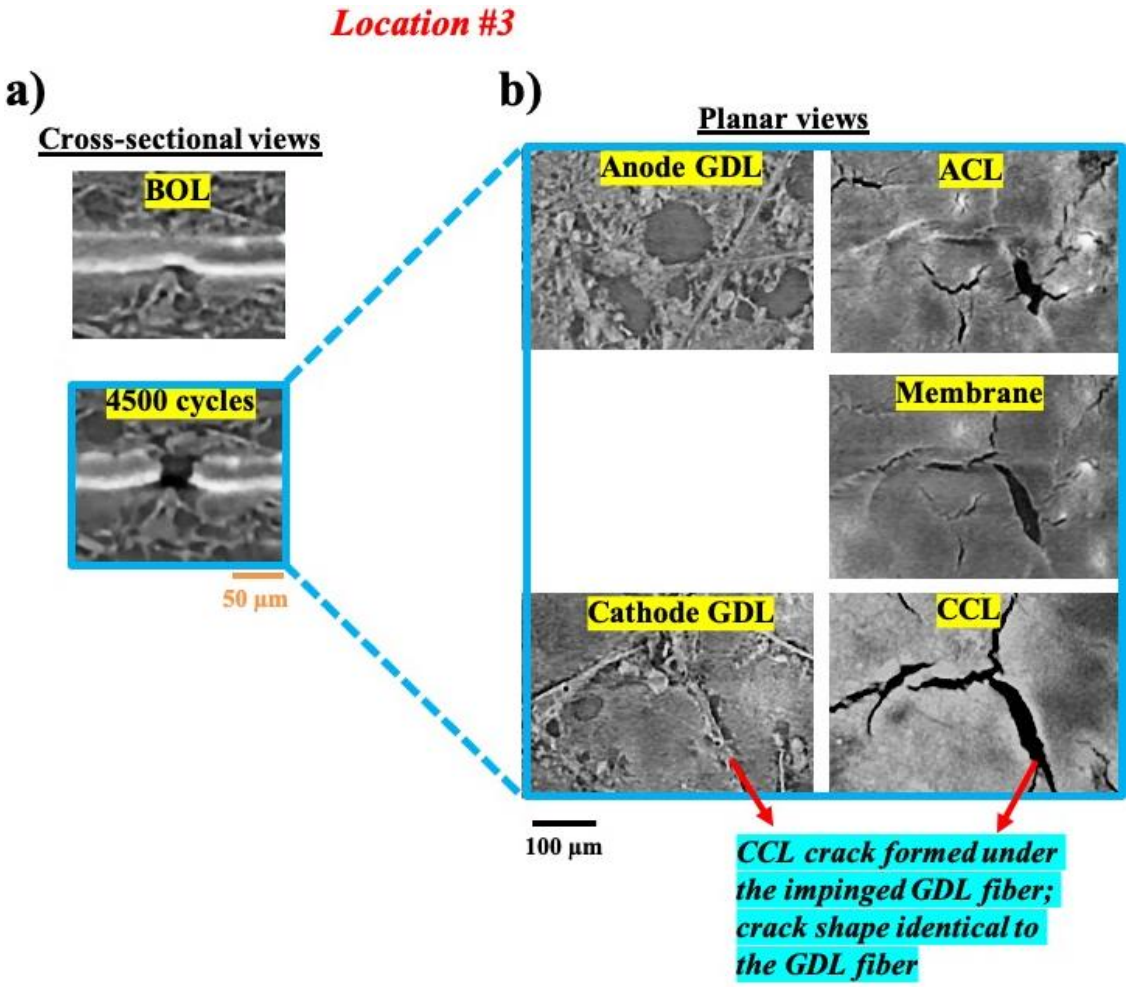

Figure 6: a) Cross-sectional views of Location #3 (indicated in Figure 3) at BOL and 4500 AMST cycles. b) Planar views of Location #3 at 4500 cycles. The planar views show the slices within different MEA components at 4500 cycles. (ACL: Anode catalyst layer, CCL: Cathode catalyst layer)

Mitigation of mechanical membrane degradation

The CCM is known to swell due to water absorption and may undergo buckling to occupy the clearance/gaps in the adjoining GDLs within the MEA. This leads to crack formation in the CLs [9] due to its brittle nature and simultaneously the membrane accumulates plastic strain, as documented in Part 1 of this research [8]. Improving lamination and bonding quality between the CCM and GDL is one approach attempted in this work to mitigate or delay the membrane cracking by improving the interfacial contact between these MEA components. **Figure 7** shows the membrane planes within three different MEA configurations, *i.e.*, high crack density CCL without bonding, low crack density CCL without bonding, and low crack density CCL with bonding designs, after undergoing 2000 wet/dry cycles of a similar AMST protocol. Observations reported previously by Singh *et al.* [7] showed that the high crack density CCL without bonding led to 12% membrane crack area coverage after 2000 cycles. Membrane locations with a high crack coverage area are typically characterized by a higher length and width of the individual cracks and are thus capable of facilitating high convective gas crossover [10]. The strong influence of CL cracks on membrane crack development is well understood, and to overcome this, an MEA made with a low crack density CCL was further investigated by Singh *et al.* [7] through application of the similar mechanical degradation process. Their results demonstrated nearly six times reduction (or mitigation) in membrane crack area with the use of low crack density CCLs after 2000 wet/dry cycles, which was attributed to the lower *ab initio* defect density of the CCL design. The membrane failure process in their study was predominantly linked to buckling deformations of the non-bonded CCM into anode GDL void spaces and was also accompanied by CCL cracking at such sites likely due to the asymmetric nature of strain accumulation across the buckled CCM. To mitigate this failure-inducing buckling phenomenon, the present work combined into the MEA design the known benefit of low crack density CCL along with an additional bonding step between the CCM and GDLs. XCT results showed negligible membrane damage after 2000 AMST cycles and even with continued cycling, less than 1% membrane crack coverage developed by 4500 cycles (**Figure 7d)**. Therefore, the present work clearly demonstrated the added mitigatory impact of the CCM-GDL bonding step compared to the previous non-bonded MEA configurations.

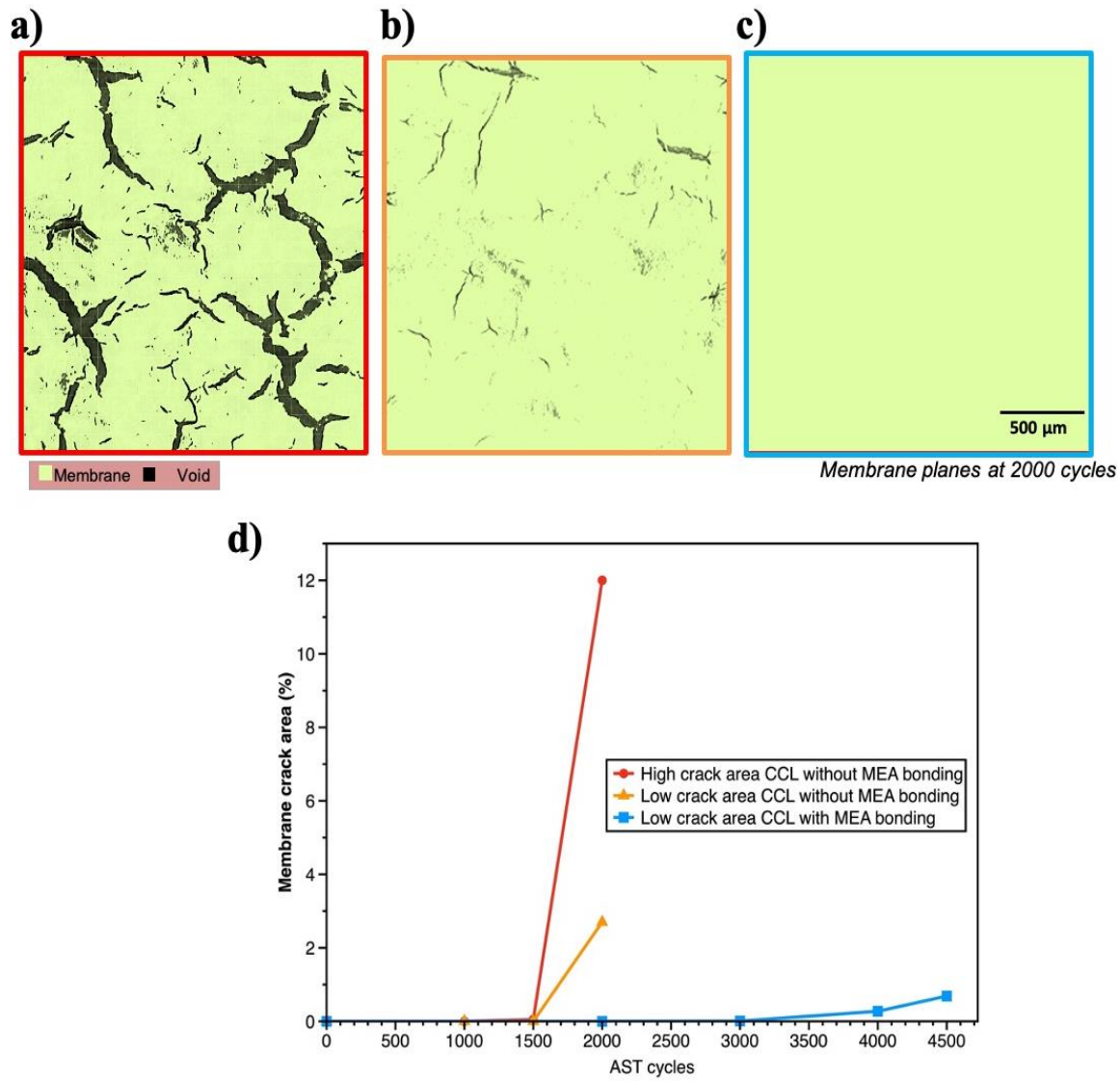

Figure 7: Planar membrane slices of separate MEA configurations having a) high crack CCL without bonding [7], b) low crack CCL without bonding, and c) low crack CCL with bonding process after 2000 wet/dry AMST cycles. d) Evolution of membrane crack areas of all three MEA configurations during the AMST. The two non-bonded MEAs were cycled up to 2000 cycles, while the present bonded MEA was cycled up to 4500 cycles.

FEM simulation results

The results obtained from finite element simulations of the multi-physics fuel cell model under the action of relevant AMST conditions are presented in this section. The displacement of the membrane under the assembly conditions was investigated in the presence of various void sizes implemented at the MPL side of the anode GDL. For each

void size, various values of frictional coefficient for the CCM-GDL interface were used to understand its impact on the resulting deformations. The compiled results from all simulations are shown in **Figure 8**. The basic mechanism of membrane deformation remains similar as discussed in Part 1 because of the similarity of external assembly constraints. The initial compression applied through the lands introduces compressive stresses in the membrane. Upon introduction of humidification, the membrane absorbs water and swells, giving rise to more compressive in-plane stresses owing to constraints at both planar ends. Therefore, in correspondence with the results shown in **Figure 8** of Part 1, the membrane develops plastic deformation during a complete load swing from dry to saturated condition, even when there is no void in the GDL. However, upon introducing an MPL-side anode GDL void of successively increasing size, the effective plastic strain in the membrane increases significantly beyond a critical void size. This critical condition reflects buckling of the membrane into the GDL void. For the results corresponding to lack of CCM-GDL adhesion (or frictionless, $\mu = 0$) there is a marked increase in the developed plastic strain in the membrane for larger void sizes beyond a certain critical value. Upon incremental increase of the adhesion at the CCM-GDL surface ($\mu = 0.05$), the effective plastic strain was found to decrease significantly for all void sizes. This indicates that even with the slight introduction of frictional forces, the displacement of the membrane and hence its propensity to buckle into the GDL void is reduced. With further increase in the surface adhesion ($\mu = 0.10$ and 0.90), the effective plastic strain was found to decrease further contributing to a potential mitigation of the crack development process. In the case of full adhesion (completely bonded) the membrane does not slide at the CCM-GDL interface and hence does not incur any additional plastic strain with increasing void sizes, beyond the plastic strain induced due to swelling. Thus, according to this simulation study, it is evident that higher adhesion reduces the ability of the membrane to slide at the CCM-GDL interface and eventually prevents buckling into the GDL void. The reduction in the effective plastic strain in the CCM, when carried over multiple wet-dry cycles, could delay the onset of appearance of cracks on the outer CLs of the CCM. This delay leads to a late occurrence of the CL cracks entering the membrane that was also observed experimentally in this work for the MEA fabricated with CCM-GDL bonding.

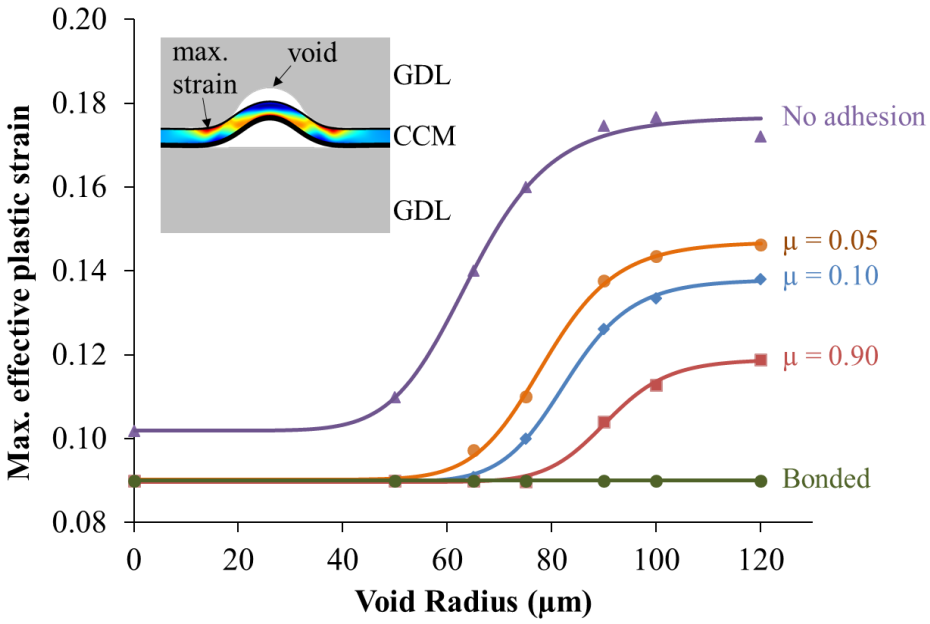

Figure 8: Maximum value of the effective plastic strain in the membrane at the end of the wet phase in the presence of various sizes of a single MPL-side anode GDL void. Full simulation results are presented for five different CCM-GDL surface friction coefficients ranging from no adhesion (non-bonded) through three partial adhesion levels to full adhesion (bonded).

Conclusions

Using a miniature fuel cell fixture, a 4D *in situ* visualization workflow was achieved, which allowed non-destructive XCT monitoring of identical MEA locations at different stages of a wet/dry cycling AMST. The adopted approach enabled understanding of the mitigatory effect of using an MEA having both low crack CCL and bonded CCM-GDL interfaces against the mechanical membrane degradation process. The key membrane failure mode associated with the repetitive wet/dry cycles was development of through-thickness membrane cracks. The membrane crack locations were generally associated with mild creep related MEA defects introduced during the CCM-GDL bonding step, that is, locally high and low membrane thickness sites. A strong interaction between membrane and electrode cracks was observed which is characteristic of the wet/dry cycling AMSTs, with dominant crack growth from CCL to membrane. In addition, the GDL fiber intrusion at the CCM surface was discovered to induce CCL crack and ultimately leading to membrane cracks. In comparison to a self-assembled MEA without CCM-GDL bonding, the bonded MEA showed 2X longer AMST lifetime which was attributed to the improved interfacial contact and arresting of the CCM buckling facilitated by the lamination procedure. Complementary FE simulations showed that an increase in the CCM-GDL frictional coefficient, which is representative of the interfacial adhesion quality, substantially decreases the effective plastic strain within the membrane during CCM swelling and buckling into the adjacent GDL void spaces. Therefore, the formation of CL cracks and henceforth membrane cracks are delayed or possibly even evaded, depending on the bonding quality. Future work could focus on optimizing the bonding process to minimize unintended defects, thereby offering further potential improvements in membrane durability and lifetime. Overall, the new findings reported herein were enabled through the considerable advantage of lab based XCT imaging technology in gaining an improved fundamental understanding of critical fuel cell failure modes and mechanisms across different developmental stages, which is recommended for future durability research in electrochemical systems.

Acknowledgements

Funding for this research was provided by the Natural Sciences and Engineering Research Council of Canada, Canada Foundation for Innovation, British Columbia Knowledge Development Fund, and Ballard Power Systems through an Automotive Partnership Canada grant. This research was undertaken, in part, thanks to funding from the Canada Research Chairs program. We acknowledge Dr. Robin T. White for development of the miniature fuel cell fixture and Mike Xu for experimental assistance.

References

[1] Macauley N, Alavijeh AS, Watson M, Kolodziej J, Lauritzen M, Knights S, et al. Accelerated membrane durability testing of heavy duty fuel cells. Journal of the Electrochemical Society 2015;162:F98–107. doi:10.1149/2.0671501jes.

[2] Mukundan R, Baker AM, Kusoglu A, Beattie P, Knights S, Weber AZ, et al. Membrane Accelerated Stress Test Development for Polymer Electrolyte Fuel Cell Durability Validated Using Field and Drive Cycle Testing. Journal of The Electrochemical Society 2018;165:F3085–93. doi:10.1149/2.0101806jes.

[3] Alavijeh AS, Khorasany RMH, Nunn Z, Habisch A, Lauritzen M, Rogers E, et al. Microstructural and Mechanical Characterization of Catalyst Coated Membranes Subjected to In Situ Hygrothermal Fatigue. Journal of The Electrochemical Society 2015;162:F1461–9. doi:10.1149/2.0471514jes.

[4] Kusoglu A, Weber AZ. New Insights into Perfluorinated Sulfonic-Acid Ionomers. Chemical Reviews 2017;117:987–1104. doi:10.1021/acs.chemrev.6b00159.

[5] Patil YP, Jarrett WL, Mauritz KA. Deterioration of mechanical properties: A cause for fuel cell membrane failure. Journal of Membrane Science 2010;356:7–13. doi:10.1016/j.memsci.2010.02.060.

[6] Sadeghi Alavijeh A, Khorasany RMH, Habisch A, Wang GG, Kjeang E. Creep properties of catalyst coated membranes for polymer electrolyte fuel cells. Journal of Power Sources 2015;285:16–28. doi:10.1016/j.jpowsour.2015.03.082.

[7] Y. Singh, R. T. White, M. Najm , A. Boswell, F. P. Orfino MD and EK. Mitigation of Mechanical Membrane Degradation in Fuel Cells by Controlling Electrode Morphology — a 4D in-situ Structural Characterization. Journal of The Electrochemical Society 2021;168.

[8] Ramani D, Khattra NS, Singh Y, Mohseni-Javid A, Orfino FP, Dutta M and KE. Mitigation of Mechanical Membrane Degradation in Fuel Cells – Part 1: Gas Diffusion Layers with Low Surface Roughness. Under Review 2021.

[9] Singh Y, White RT, Najm M, Haddow T, Pan V, Orfino FP, et al. Tracking the evolution of mechanical degradation in fuel cell membranes using 4D in situ visualization. Journal of Power Sources 2019:224–37. doi:10.1016/j.jpowsour.2018.11.049.

[10] Ramani D, Singh Y, White RT, Wegener M, Orfino FP, Dutta M, et al. 4D in situ visualization of mechanical degradation evolution in reinforced fuel cell membranes. International Journal of Hydrogen Energy 2020;45:10089–103. doi:10.1016/j.ijhydene.2020.02.013.

[11] Pokhrel A, El Hannach M, Orfino FP, Dutta M, Kjeang E. Failure analysis of fuel cell electrodes using three-dimensional multi-length scale X-ray computed tomograp1. A. Pokhrel, M. El Hannach, F. P. Orfino, M. Dutta, and E. Kjeang, J. Power Sources, 329, 330–338 (2016).hy. Journal of Power Sources 2016;329:330–8. doi:10.1016/j.jpowsour.2016.08.092.

[12] Litster S, Epting WK, Wargo EA, Kalidindi SR, Kumbur EC. Morphological analyses of polymer electrolyte fuel cell electrodes with nano-scale computed tomography imaging. Fuel Cells 2013;13:935–45. doi:10.1002/fuce.201300008.

[13] Andisheh-Tadbir M, Orfino FP, Kjeang E. Three-dimensional phase segregation of micro-porous layers for fuel cells by nano-scale X-ray computed tomography. Journal of Power Sources 2016;310:61–9. doi:10.1016/j.jpowsour.2016.02.001.

[14] Odaya S, Phillips RK, Sharma Y, Bellerive J, Phillion AB, Hoorfar M. X-ray Tomographic Analysis of Porosity Distributions in Gas Diffusion Layers of Proton Exchange Membrane Fuel Cells. Electrochimica Acta 2015;152:464–72. doi:10.1016/j.electacta.2014.11.143.

[15] James JP, Choi H-W, Pharoah JG. X-ray computed tomography reconstruction and analysis of polymer electrolyte membrane fuel cell porous transport layers. International Journal of Hydrogen Energy 2012;37:18216–30. doi:10.1016/j.ijhydene.2012.08.077.

[16] Singh Y, Orfino FP, Dutta M, Kjeang E. 3D Failure Analysis of Pure Mechanical and Pure Chemical Degradation in Fuel Cell Membranes. Journal of The Electrochemical Society 2017;164:1331–41. doi:10.1149/2.0451713jes.

[17] Ramani D, Singh Y, Orfino FP, Dutta M, Kjeang E. Characterization of Membrane Degradation Growth in Fuel Cells Using X-ray Computed Tomography. Journal of The Electrochemical Society 2018;165:F3200–8. doi:10.1149/2.0251806jes.

[18] Singh Y, Orfino FP, Dutta M, Kjeang E. 3D visualization of membrane failures in fuel cells. Journal of Power Sources 2017;345:1–11. doi:10.1016/j.jpowsour.2017.01.129.

[19] White RT, Orfino FP, Hannach M El, Luo O, Dutta M, Young AP, et al. 3D Printed Flow Field and Fixture for Visualization of Water Distribution in Fuel Cells by X-ray Computed Tomography. Journal of The Electrochemical Society 2016;163:F1337–43. doi:10.1149/2.0461613jes.

[20] White RT, Eberhardt SH, Singh Y, Haddow T, Dutta M, Orfino FP, et al. Four-dimensional joint visualization of electrode degradation and liquid water distribution inside operating polymer electrolyte fuel cells. Scientific Reports 2018:1–12. doi:10.1038/s41598-018-38464-9.

[21] White RT, Wu A, Najm M, Orfino FP, Dutta M, Kjeang E. 4D in situ visualization of electrode morphology changes during accelerated degradation in fuel cells by X-ray computed tomography. Journal of Power Sources 2017;350:94–102. doi:10.1016/j.jpowsour.2017.03.058.

[22] Wilson MS, Gottesfeld S. High Performance Catalyzed Membranes of Ultra-low Pt Loadings for Polymer Electrolyte Fuel Cells. Journal of The Electrochemical Society 1992;139:L28–30. doi:10.1149/1.2069277.

[23] Prass S, Hasanpour S, Sow PK, Phillion AB, Mérida W. Microscale X-ray tomographic investigation of the interfacial morphology between the catalyst and micro porous layers in proton exchange membrane fuel cells. Journal of Power Sources 2016;319:82–9. doi:10.1016/j.jpowsour.2016.04.031.

[24] Kundu S, Fowler MW, Simon LC, Grot S. Morphological features (defects) in fuel cell membrane electrode assemblies. Journal of Power Sources 2006;157:650–6. doi:10.1016/j.jpowsour.2005.12.027.

[25] Goulet M-A, Arbour S, Lauritzen M, Kjeang E. Water sorption and expansion of an ionomer membrane constrained by fuel cell electrodes. Journal of Power Sources 2015;274:94–100. doi:10.1016/j.jpowsour.2014.10.040.

[26] Shi S, Weber AZ, Kusoglu A. Structure/property relationship of Nafion XL composite membranes. Journal of Membrane Science 2016;516:123–34. doi:10.1016/j.memsci.2016.06.004.

[27] Khattra NS, Lu Z, Karlsson AM, Santare MH, Busby FC, Schmiedel T. Time-dependent mechanical response of a composite PFSA membrane. Journal of Power Sources n.d.;228:256–69. doi:10.1016/j.jpowsour.2012.11.116.

[28] Tang Y, Kusoglu A, Karlsson AM, Santare MH, Cleghorn S, Johnson WB. Mechanical properties of a reinforced composite polymer electrolyte membrane and its simulated performance in PEM fuel cells. Journal of Power Sources 2008;175:817–25. doi:https://doi.org/10.1016/j.jpowsour.2007.09.093.

[29] Hack J, Heenan TMM, Iacoviello F, Mansor N, Meyer Q, Shearing P, et al. A structure and durability comparison of membrane electrode assembly fabrication methods: Self-assembled versus hot-pressed. Journal of the Electrochemical Society 2018;165:3045–52. doi:10.1149/2.0051806jes.

[30] Fuel USD, Tech C. Appendix A : FCTT AST and Polarization Curve Protocols for PEMFCs 2013.

[31] Andersen SM, Dhiman R, Larsen MJ, Skou E. Importance of electrode hot-pressing conditions for the catalyst performance of proton exchange membrane fuel cells. Applied Catalysis B: Environmental 2015;172–173:82–90. doi:10.1016/j.apcatb.2015.02.023.

[32] Bayrakçeken A, Erkan S, Türker L, Eroğlu I. Effects of membrane electrode assembly components on proton exchange membrane fuel cell performance. International Journal of Hydrogen Energy 2008;33:165–70. doi:10.1016/j.ijhydene.2007.08.021.

[33] Tang Y, Zhang J, Song C, Liu H, Zhang J, Wang H, et al. Temperature Dependent Performance and In Situ AC Impedance of High-Temperature PEM Fuel Cells Using the Nafion-112 Membrane. Journal of The Electrochemical Society 2006;153:A2036. doi:10.1149/1.2337008.

[34] Martemianov S, Raileanu Ilie VA, Coutanceau C. Improvement of the proton exchange membrane fuel cell performances by optimization of the hot pressing process for membrane electrode assembly. Journal of Solid State Electrochemistry 2014;18:1261–9. doi:10.1007/s10008-013-2273-2.

[35] Meyer Q, Mansor N, Iacoviello F, Cullen PL, Jervis R, Finegan D, et al. Investigation of Hot Pressed Polymer Electrolyte Fuel Cell Assemblies via X-ray Computed Tomography. Electrochimica Acta 2017;242:125–36. doi:10.1016/j.electacta.2017.05.028.

[36] Uchiyama T, Kumei H, Yoshida T, Ishihara K. Static friction force between catalyst layer and micro porous layer and its effect on deformations of membrane electrode assemblies under swelling. Journal of Power Sources 2014;272:522–30. doi:10.1016/j.jpowsour.2014.08.103.

[37] White RT, Wu A, Najm M, Orfino FP, Dutta M, Kjeang E. 4D in situ visualization of electrode morphology changes during accelerated degradation in fuel cells by X-ray computed tomography. Journal of Power Sources 2017;350:94–102. doi:10.1016/j.jpowsour.2017.03.058.

[38] White RT, Najm M, Dutta M, Orfino FP, Kjeang E. Communication—Effect of Micro-XCT X-ray Exposure on the Performance of Polymer Electrolyte Fuel Cells. Journal of The Electrochemical Society 2016;163:1206–8. doi:10.1149/2.0751610jes.

[39] Kusoglu A, Santare MH, Karlsson AM. Aspects of fatigue failure mechanisms in polymer fuel cell membranes. J Polym Sci Part B Polym Physics 2011;49:1506–17.

[40] Khorasany RMH, Singh Y, Alavijeh AS, Rajapakse RKND, Kjeang E. In-situ simulation of membrane fatigue in polymer electrolyte fuel cells 2017. doi:10.1016/j.ijhydene.2017.01.173.

[41] Lai Y-H, Mittelsteadt CK, Gittleman CS, Dillard DA. Viscoelastic Stress Analysis of Constrained Proton Exchange Membranes Under Humidity Cycling. Journal of Fuel Cell Science and Technology 2009;6:021002. doi:10.1115/1.2971045.

[42] Khorasany RMH, Goulet M-A, Alavijeh AS, Kjeang E, Wang GG, Rajapakse RKND. On the constitutive relations for catalyst coated membrane applied to in-situ fuel cell modeling. Journal of Power Sources 2014;252:176–88. doi:10.1016/j.jpowsour.2013.11.087.

[43] Kreitmeier S, Schuler GA, Wokaun A, Büchi FN. Investigation of membrane degradation in polymer electrolyte fuel cells using local gas permeation analysis. Journal of Power Sources 2012;212:139–47. doi:10.1016/j.jpowsour.2012.03.071.